

CONTINUOUS VARIABLE QUANTUM TRANSDUCTION AND QUANTUM
ERROR CORRECTION

by

Jing Wu

Copyright © Jing Wu 2024

A Dissertation Submitted to the Faculty of the

JAMES C. WYANT COLLEGE OF OPTICAL SCIENCES

In Partial Fulfillment of the Requirements

For the Degree of

DOCTOR OF PHILOSOPHY

In the Graduate College

THE UNIVERSITY OF ARIZONA

2024

THE UNIVERSITY OF ARIZONA
GRADUATE COLLEGE


As members of the Dissertation Committee, we certify that we have read the dissertation
prepared by: **Jing Wu**
titled:

and recommend that it be accepted as fulfilling the dissertation requirement for the Degree of
Doctor of Philosophy.


Linran Fan (Apr 3, 2024 13:26 CDT)


Linran Fan

Date: Apr 3, 2024


Daniel Soh (Apr 3, 2024 11:27 PDT)

Daniel Soh

Date: Apr 3, 2024



Christos Gagatsos (Apr 5, 2024 15:54 PDT)

Christos Gagatsos

Date: Apr 5, 2024

Final approval and acceptance of this dissertation is contingent upon the candidate's submission
of the final copies of the dissertation to the Graduate College.

I hereby certify that I have read this dissertation prepared under my direction and recommend
that it be accepted as fulfilling the dissertation requirement.


Linran Fan (Apr 3, 2024 13:26 CDT)

Linran Fan

Date: Apr 3, 2024

Defense committee chair
College of optical sciences

Contents

Abstract	5
1 Continuous Variable Quantum Systems	6
1.1 Preliminaries	6
1.1.1 Mathematical Tools	6
1.1.2 Gaussian Transform	9
1.1.3 Characteristic Function and Wigner Function	10
1.1.4 Gaussian Channel	12
1.2 Capacity of Gaussian Channels	14
1.2.1 Entropy of Continuous Variables	15
1.2.2 Entanglement-Assisted Classical Capacity	16
1.2.3 Quantum Capacity	17
1.3 General Theorems on Quantum Information	18
2 Continuous Variable Quantum Teleportation	20
2.1 Teleportation with Two Oscillators	20
2.2 Teleportation with Many Oscillators	24
2.3 A Decomposition of Symplectic Transform	26
2.4 Metrics for Evaluating the Teleportation	30
2.4.1 Fidelity	31
2.4.2 Capacity	32
3 Microwave-optical Transduction	36
3.1 Cavity Electro-optics	36
3.2 Direct Conversion Channel	39
3.3 Teleportation Channel	41
3.4 Comparison between Direct Conversion and Teleportation Channel	45
3.4.1 Additive Noise Analysis	45
3.4.2 Fidelity	47
3.4.3 Capacity	50
4 Squeezing Enhanced Quantum Teleportation	54
4.1 Direct Conversion and Teleportation Scheme	54
4.1.1 Cavity Electro-Optics involving Squeezing	55
4.1.2 Stability Condition	56
4.2 Direct Conversion Channel	59
4.3 Teleportation Channel	61
4.3.1 Choice of Squeezing Based on Direction of Transduction	63
4.4 Fidelity Comparison	64

4.5	Capacity Comparison	65
4.5.1	Ideal Extraction Efficiency Case	65
4.5.2	Practical Extraction Efficiency Case	66
4.6	Enhance Entanglement for Teleportation	72
4.6.1	Upper Bound of Teleportation Channel	72
4.6.2	Entanglement Generation by Concatenation	72
4.6.3	Capacity Boost by Concatenation	74
4.6.4	Three Mode Teleportation	75
5	Continuous-Variable Quantum Error Correction	77
5.1	Stabilizer Formalism	78
5.1.1	Stabilizer Formalism on Discrete Qubits	78
5.1.2	Stabilizer Formalism on GKP Qubits	80
5.1.3	$[[n,k]]$ GKP Qubit Code	86
5.2	Error Model	87
5.3	Quantum Error Correction on Oscillators	90
5.3.1	GKP-Gaussian Error Correction and the Lower Bound	91
5.3.2	Concatenated TMS and SR Code with Linear Estimator	92
5.3.3	Mode-wise Decomposition and MMSE Estimation	109
5.4	Quantum Error Correction on GKP Qubit	124
5.4.1	Code Distance	124
5.4.2	Distributed Two Mode Squeezing Code	126
	Bibliography	133

Abstract

Quantum transduction and error correction are pivotal for advancing quantum communication, particularly in the optical frequency domain. Coherent transduction between microwave and optical frequencies is essential for connecting superconducting quantum processors over long distances. Additionally, quantum error correction plays a vital role in safeguarding the fidelity of quantum information during transmission through noisy communication channels.

This dissertation explores an electro-optic transduction system based on continuous-variable quantum teleportation, proposing and formulating a general continuous-variable quantum teleportation channel within this context. The advantages and limitations of the teleportation-based quantum transduction are analyzed, highlighting its robust performance in practical levels of cooperativity and extraction coefficients, common in electro-optic transduction systems. The study also examines new methods to enhance the performance of teleportation based quantum transduction, offering feasible near-term experimental solutions. Compared to the standard direct conversion approach under the same conditions, the teleportation-based scheme demonstrates superior, while limited, efficacy.

In parallel, the dissertation delves into continuous variable quantum error correction utilizing Gottesman-Kitaev-Preskill (GKP) states, focusing on error correction under the stabilizer formalism framework. Two primary models are explored: safeguarding oscillators with GKP states and safeguarding GKP qubits with GKP states. For safeguarding oscillators, new encoding methods are presented, considering general symplectic transform matrices and channel properties. A novel estimation approach is proposed, outperforming traditional linear estimation method and slightly extending the error correction threshold. Furthermore, the dissertation discusses potential code reduction and evaluates the bounds of quantum capacity and ultimate noise reduction when the squeezing is limited. The optimal strategy for protecting a single oscillator with another GKP state is identified.

Regarding GKP qubit encoding, a new family of codes – the distributed two-mode squeezing code – is proposed, which is effective in low dimensions and simpler in design compared to existing codes. This code family, leveraging the concept of distributing entanglement among multiple oscillators, shows promise for application in higher dimensions in future quantum error correction studies.

Chapter 1

Continuous Variable Quantum Systems

This chapter delves into the realm of continuous variable (CV) quantum systems, a cornerstone in the field of quantum mechanics and quantum information theory. CV systems, characterized by quantum states in infinite-dimensional Hilbert spaces, are fundamental for understanding a wide range of quantum phenomena. These include quantum harmonic oscillators, quantum transduction, quantum entanglement in CV systems, and CV error correction.

The chapter is organized to first introduce the mathematical theorems and tools, as well as basic definitions and properties of Gaussian Transforms. Then the Gaussian channel is discussed, along with the capacity of the channel. These concepts and tools are well-known and form a well-formulated quantum mechanical description.

1.1 Preliminaries

1.1.1 Mathematical Tools

Definition 1 (Symplectic Form) *A symplectic form on a real vector space V is a bilinear map $\psi : V \times V \rightarrow \mathbb{R}$ such that:*

- ψ is skew-symmetric, meaning $\psi(v_1, v_2) = -\psi(v_2, v_1)$ for all $v_1, v_2 \in V$.
- ψ is non-degenerate, which implies that if $\psi(v, w) = 0$ for all $w \in V$, then $v = 0$.

Lemma 2 *Let ψ be a symplectic form on a real vector space V of finite dimension. Define $V^\perp = \{u \in V \mid \psi(u, v) = 0, \forall v \in V\}$. Then V^\perp is a subspace of V , and we have $V = W \oplus V^\perp$.*

Proof. V^\perp comprises all vectors in V that are symplectically orthogonal to every vector in V . It forms a subspace of V , as for any $v_1, v_2 \in V^\perp$, any linear combination of v_1 and v_2 also belongs to V^\perp . According to linear algebra, every subspace of a finite-dimensional vector space is complemented (refer to [1]). Thus, we can express V as the direct sum $V = W \oplus V^\perp$. ■

Lemma 3 (Gram-Schmidt) *Let V be a finite-dimensional vector space over a field F with a skew-symmetric form $\psi : V \times V \rightarrow F$. Then there exists a basis B in*

V such that the matrix representation of ψ under B , denoted $[\psi]_B$, is $(\oplus_{i=1}^n \omega) \oplus \mathbf{0}^m$, where $\omega = \begin{pmatrix} 0 & 1 \\ -1 & 0 \end{pmatrix}$.

Proof. The theorem can be proved by induction. Let $V = W \oplus V^\perp$, where $\psi|_{V^\perp \times V} = 0$. If $\psi|_{W \times W}$ is a zero form, then $n = 0$ and we are done. Otherwise, there exists $v_1, v_2 \in W$ such that $\psi(v_1, v_2) \neq 0$. Since F is a field, we can assume $\psi(v_1, v_2) = 1$ by applying a nonzero scaling factor to v_1 or v_2 . Moreover, v_1 and v_2 are linear independent otherwise $v_2 = av_1$ for some nonzero $a \in F$ and $\psi(v_1, v_2) = \psi(v_1, av_2) = 0$.

Let $W_1 = \text{span}(v_1, v_2)$ be the vector space spanned by v_1 and v_2 . Define $W_1^\perp = \{v \in W | \psi(v, w_1) = 0, \forall w_1 \in W_1\}$, which is also a subspace of W . Observe that $W_1 \cap W_1^\perp = \{0\}$. If $v \in W$, $\psi(v, v_1) = c$ and $\psi(v, v_2) = d$, there exists $w_1 = dv_1 - cv_2 \in W_1$ such that $v - w_1 \in W_1^\perp$. Thus $W = W_1 \oplus W_1^\perp$. $\psi|_{W_1 \times W_1}$ has representation ω and $\psi|_{W_1 \times W_1^\perp} = 0$. By induction, we have $W = W_n^\perp \oplus \dots \oplus W_1^\perp$ and a corresponding set of vectors $B = \{v_1, v_2, \dots, v_{2n}\}$ such that $[\psi]_B = (\oplus_{i=1}^n \omega) \oplus \mathbf{0}^m$. ■

Definition 4 (Standard Forms) The standard form 1, ψ_1 and the standard form 2, ψ_2 on \mathbb{R}^{2n} are defined as follows:

$$\psi_1(v_1, v_2) = v_1^\top \Omega_{2n} v_2, \quad (1.1)$$

$$\psi_2(v_1, v_2) = v_1^\top J_{2n} v_2, \quad (1.2)$$

where $\Omega_{2n} = \oplus_{i=1}^n \omega$ and $J_{2n} = \begin{pmatrix} 0 & I_n \\ -I_n & 0 \end{pmatrix}$, and ω is as previously defined.

Definition 5 (Symplectic Matrices) The group of symplectic matrices on the real vector space \mathbb{R}^{2n} with respect to Ω_{2n} is defined as

$$\text{Sp}(\mathbb{R}^{2n}, \Omega_{2n}) = \{S \mid S^\top \Omega_{2n} S = \Omega_{2n}\}. \quad (1.3)$$

For simplicity, this group is denoted as $\text{Sp}(2n) = \text{Sp}(\mathbb{R}^{2n}, \Omega_{2n})$.

Note that if $S \in \text{Sp}(2n)$, then S^{-1} and S^\top are also in the group of symplectic matrices.

Lemma 6 (Extension of Symplectic Basis) Let V be a subspace of \mathbb{R}^{2n} , and suppose there exists a basis B of V such that $B^\top \Omega_{2n} B = \Omega_{2m}$, where $m \leq n$ and B is the matrix with columns formed by the vectors in B . Then B can be extended to \bar{B} as a basis of \mathbb{R}^{2n} such that $\bar{B}^\top \Omega_{2n} \bar{B} = \Omega_{2n}$. Two extensions \bar{B}_1 and \bar{B}_2 are unique up to local symplectic transform, i.e. $\bar{B}_1 = \bar{B}_2(I_{2m} \oplus S)$.

Proof. The existence of the extension \bar{B} is guaranteed by Lemma 3. Consider two such extensions \bar{B}_1 and \bar{B}_2 . We have

$$\bar{B}_1^\top \Omega_{2n} \bar{B}_1 = \Omega_{2n} = \bar{B}_2^\top \Omega_{2n} \bar{B}_2.$$

This equality implies that $\bar{B}_1 = \bar{B}_2 \bar{S}$ for some matrix $\bar{S} \in \text{Sp}(2n)$. On the other hand, \bar{B}_1 and \bar{B}_2 have the same first $2m$ columns. Then \bar{S} must have the block form

$$\bar{S} = \begin{pmatrix} I_{2m} & C \\ 0 & S \end{pmatrix}.$$

From $\bar{\mathbf{S}}^\top \boldsymbol{\Omega}_{2n} \bar{\mathbf{S}} = \boldsymbol{\Omega}_{2n}$, we get $\mathbf{S}^\top \boldsymbol{\Omega}_{2n-2m} \mathbf{S} = \boldsymbol{\Omega}_{2n-2m}$ and $\mathbf{C} = \mathbf{0}$. ■

A special subgroup of $\text{Sp}(2n)$ is the intersection of $\text{Sp}(2n)$ and the real orthogonal group $O(2n)$. This subgroup represents passive operations or general beam splitters in quantum mechanics, as it does not alter the system's total energy. Remarkably, there is a correspondence between this subgroup and the complex unitary group of dimension n , as described in [1]:

$$U(n) \cong \text{Sp}(2n) \cap O(2n), \quad (1.4)$$

where \cong denotes group isomorphism. Similar to singular value decomposition of a real matrix, a real symplectic matrix \mathbf{S} can be diagonalized by two matrices \mathbf{O}_1 and \mathbf{O}_2 in $\text{Sp}(2n) \cap O(2n)$, which is called Bloch-Messiah decomposition [2]

$$\mathbf{S} = \mathbf{O}_1 \text{Sq}(\mathbf{r}) \mathbf{O}_2, \quad (1.5)$$

where $\text{Sq}(\mathbf{r}) = \text{Diagonal}(r_1, 1/r_1, \dots, r_n, 1/r_n)$ is a diagonal matrix representing squeezing operation. The squeezing operation is active because it changes the system's total energy. Since $U(n)$ has dimension n^2 , we have dimension of $\text{Sp}(2n)$:

$$\dim \text{Sp}(2n) = 2n^2 + n. \quad (1.6)$$

Definition 7 A symplectic form on an R -module M is a bilinear mapping $\psi : M \times M \rightarrow R$ with the following property:

- *Skew-symmetry:* $\psi(m_1, m_2) = -\psi(m_2, m_1)$ for all $m_1, m_2 \in M$.

In this dissertation, the base ring R is the set of integer \mathbb{Z} and M is finitely generated by $\{m_1, \dots, m_s\}$, thus is a free module. Similarly, a skew-symmetric form can be block-diagonalized.

Lemma 8 Let M be an n -dimensional free module over a principal ideal domain \mathbb{Z} and $\psi : M \times M \rightarrow \mathbb{Z}$ is a skew-symmetric form. Then there exists a basis B in M such that under the basis representation $[\psi]_B$, we have

$$[\psi]_B = \left[\bigoplus_{i=1}^k \begin{pmatrix} 0 & d_i \\ -d_i & 0 \end{pmatrix} \right] \oplus \mathbf{0}_{n-2k},$$

where d_i are elements of \mathbb{Z} .

Proof. Since M is isomorphic to \mathbb{Z}^n , where n is the dimension, we can consider M as \mathbb{Z}^n with the basis $\{m_1, \dots, m_n\}$. Viewing \mathbb{Z}^n as a ring, the map $\psi(m_1, M)$ is a from \mathbb{Z}^n to \mathbb{Z} . Thus, $\psi(m_1, M)$ forms a subring of \mathbb{Z} . Since for all $r \in \mathbb{Z}$, $r\psi(m_1, M) = \psi(m_1, rM) \subseteq \psi(m_1, M)$, $\psi(m_1, M)$ is an ideal of principle ideal domain \mathbb{Z} as well. Then $\psi(m_1, M) = \langle d_1 \rangle$. If $d_1 = 0$, then m_1 is orthogonal to $\{m_2, \dots, m_n\}$. We set $M = \text{span}(m_1) \oplus \text{span}(m_1)^\perp$ and consider a smaller module $\text{span}(m_1)^\perp$.

If $d_1 \neq 0$, there exists $b_1 \in M$ such that $\psi(m_1, b_1) = d_1$. Then the ideal $\psi(b_1, M) = \langle d_2 \rangle$, with $d_2 | d_1$. And we have ascending chain $\langle d_1 \rangle \subseteq \langle d_2 \rangle \subseteq \dots \subseteq \langle d_k \rangle$. There exists k such that $d_k = d_{k+1} = d$ since \mathbb{Z} is Noetherian. We have a pair of elements of M such that $\psi(b_k, M) = \langle d \rangle = \psi(b_{k+1}, M)$ and $\psi(b_k, b_{k+1}) = d$ by construction. b_k and b_{k+1} are linear independent otherwise $d = 0$. Let $\alpha = b_k$ and $\beta = b_{k+1}$, the module

generated by $\{\alpha, \beta\}$ is a free submodule of M . From basis theorem of free module, there exists a basis of M , $\{\alpha', \beta', \gamma_1, \dots\}$ such that $\alpha = r_1\alpha'$ and $\beta = r_2\beta'$. Since $\psi(\alpha, \beta)|\psi(\alpha, \beta')$, $r_2\psi(\alpha, \beta')|\psi(\alpha, \beta')$. Then $r_2 = \pm 1$. Similarly $r_1 = \pm 1$. So we find a basis $\{\alpha, \beta, \gamma_1, \dots\}$ of M such that $\psi(\alpha, \gamma_k) = r_k d$ and $\psi(\beta, \gamma_k) = r'_k d$ for some r_k and r'_k in \mathbb{Z} . Replacing γ_k by $\gamma'_k = \gamma_k - r_k\beta + r'_k\alpha$, then $\psi(\alpha, \gamma'_k) = \psi(\beta, \gamma'_k) = 0$. We find a basis $\{\alpha, \beta, \gamma'_1, \dots\}$ such that $M = \text{span}(\alpha, \beta) \oplus [\text{span}(\alpha, \beta)]^\perp$. By mathematical induction, $M = [\oplus_{i=1}^k \text{span}(\alpha_i, \beta_i)] \oplus_{i=1}^{n-2k} \text{span}(m_i)$ and under this basis $[\psi]_B = \left[\oplus_{i=1}^k \begin{pmatrix} 0 & d_i \\ -d_i & 0 \end{pmatrix} \right] \oplus \mathbf{0}_{n-2k}$. ■

1.1.2 Gaussian Transform

The quantum harmonic oscillator is characterized by position and momentum operators, denoted as $\hat{\mathbf{x}} = (\hat{q}, \hat{p})^\top$, which possess continuous spectra over the real numbers. The fundamental canonical commutation relation, given by $[\hat{q}, \hat{p}] = i\hbar$, leads to the following matrix representation:

$$[\hat{\mathbf{x}}, \hat{\mathbf{x}}^\top] = \begin{pmatrix} 0 & i\hbar \\ -i\hbar & 0 \end{pmatrix} = i\omega,$$

with the unit

$$\hbar = 1.$$

This formulation lays the groundwork for exploring the properties of quantum harmonic oscillators in the realm of quantum mechanics. The annihilation and creation operators are defined by

$$\hat{a} = (\hat{q} + i\hat{p})/\sqrt{2}, \quad (1.7)$$

$$\hat{a}^\dagger = (\hat{q} - i\hat{p})/\sqrt{2}, \quad (1.8)$$

which satisfy the commutation relation

$$[\hat{a}, \hat{a}^\dagger] = 1.$$

For n oscillators, we use the vector of operators $\hat{\mathbf{x}} = (\hat{q}_1, \hat{p}_1, \dots, \hat{q}_n, \hat{p}_n)^\top$ and $\hat{\mathbf{a}} = (\hat{a}_1, \hat{a}_1^\dagger, \dots, \hat{a}_n, \hat{a}_n^\dagger)$. The Weyl operator is defined as

$$\hat{W}(\boldsymbol{\xi}) = e^{i\hat{\mathbf{x}}^\top \boldsymbol{\Omega} \boldsymbol{\xi}}, \quad (1.9)$$

where $\boldsymbol{\Omega} = \oplus_{i=1}^n \omega$. Let $\mathbf{t} = \boldsymbol{\Omega} \boldsymbol{\xi}$, we may also write $\hat{W}(\mathbf{t}) = e^{i\hat{\mathbf{x}}^\top \mathbf{t}}$. The orthogonality of Weyl operators is

$$\text{Tr}[e^{-i\hat{\mathbf{x}}^\top \boldsymbol{\Omega} \boldsymbol{\xi}_1} e^{i\hat{\mathbf{x}}^\top \boldsymbol{\Omega} \boldsymbol{\xi}_2}] = (2\pi)^n \delta(\boldsymbol{\xi}_1 - \boldsymbol{\xi}_2),$$

$$\text{Tr}[e^{-i\hat{\mathbf{x}}^\top \mathbf{t}_1} e^{i\hat{\mathbf{x}}^\top \mathbf{t}_2}] = (2\pi)^n \delta(\mathbf{t}_1 - \mathbf{t}_2).$$

An operator $\hat{U}_{\mathbf{S}, \mathbf{d}}$ is Gaussian if in Heisenberg picture it transforms the canonical operator $\hat{\mathbf{x}}$ to

$$\hat{\mathbf{x}}' = \hat{U}_{\mathbf{S}, \mathbf{d}}^\dagger \hat{\mathbf{x}} \hat{U}_{\mathbf{S}, \mathbf{d}} = \mathbf{S} \hat{\mathbf{x}} + \mathbf{d}. \quad (1.10)$$

By commutation relation, we have $[\hat{\mathbf{x}}, \hat{\mathbf{x}}^\top] = i\mathbf{\Omega}$ and $[\hat{\mathbf{x}}', \hat{\mathbf{x}}'^\top] = i\mathbf{\Omega}$. Therefore \mathbf{S} has to be symplectic for a quantum valid operation,

$$\mathbf{S}\mathbf{\Omega}\mathbf{S}^\top = \mathbf{\Omega}.$$

On the other hand, from $[e^{i\mathbf{d}^\top\mathbf{\Omega}\hat{\mathbf{x}}}, \hat{\mathbf{x}}] = \mathbf{d}$ and the Baker-Campbell-Hall formula [3],

$$e^X Y e^{-X} = Y + [X, Y] + \frac{1}{2!}[X, [X, Y]] + \dots, \quad (1.11)$$

$$e^{i\mathbf{d}^\top\mathbf{\Omega}\hat{\mathbf{x}}} \hat{\mathbf{x}} e^{-i\mathbf{d}^\top\mathbf{\Omega}\hat{\mathbf{x}}} = \hat{\mathbf{x}} + \mathbf{d}.$$

So the displacement operator is given by

$$\hat{D}(\mathbf{d}) = e^{-i\mathbf{d}^\top\mathbf{\Omega}\hat{\mathbf{x}}}. \quad (1.12)$$

From Eq. (1.10), we obtain the transform of Wely operator under a Gaussian transform.

$$\hat{U}_{\mathbf{S},\mathbf{d}}^\dagger \hat{W}(\boldsymbol{\xi}) \hat{U}_{\mathbf{S},\mathbf{d}} = \hat{W}(\mathbf{S}^{-1}\boldsymbol{\xi}) e^{i\mathbf{d}^\top\mathbf{\Omega}\boldsymbol{\xi}}, \quad (1.13)$$

$$\hat{U}_{\mathbf{S},\mathbf{d}}^\dagger \hat{W}(\mathbf{t}) \hat{U}_{\mathbf{S},\mathbf{d}} = \hat{W}(\mathbf{S}^\top \mathbf{t}) e^{i\mathbf{d}^\top \mathbf{t}}. \quad (1.14)$$

1.1.3 Characteristic Function and Wigner Function

The characteristic function $\chi_{\hat{O}}(\boldsymbol{\xi})$ of an operator \hat{O} describes its statistics in real space. It is defined by the inner product

$$\chi_{\hat{O}}(\boldsymbol{\xi}) = \text{Tr}(\hat{O} \hat{W}(\boldsymbol{\xi})). \quad (1.15)$$

A state $\hat{\rho}$ is defined as a Gaussian state with mean \mathbf{m} and variance $\boldsymbol{\sigma}$ if it has a characteristic function of the form

$$\chi_{\hat{\rho}}(\boldsymbol{\xi}) = \exp\left(i\mathbf{m}^\top(\mathbf{\Omega}\boldsymbol{\xi}) - \frac{1}{2}(\mathbf{\Omega}\boldsymbol{\xi})^\top \boldsymbol{\alpha}(\mathbf{\Omega}\boldsymbol{\xi})\right), \quad (1.16)$$

$$\chi_{\hat{\rho}}(\mathbf{t}) = \exp\left(i\mathbf{m}^\top \mathbf{t} - \frac{1}{2}\mathbf{t}^\top \boldsymbol{\alpha} \mathbf{t}\right). \quad (1.17)$$

The Gaussian state is generated by the second order of $\hat{\mathbf{x}}$. By inverting Eq. (1.15), one can obtain [4]

$$\hat{\rho} = \exp\{-\hat{\mathbf{x}}^\top \boldsymbol{\epsilon} \hat{\mathbf{x}}\},$$

where $\boldsymbol{\epsilon}$ is a certain real matrix. This relationship highlights the connection between the Gaussian states and quadratic forms in the operators $\hat{\mathbf{x}}$. From the inequality $\text{Tr}((\hat{\mathbf{x}} - \mathbf{m})^\top \hat{\rho} (\hat{\mathbf{x}} - \mathbf{m})) \geq 0$, it can be derived that the covariance matrix of a Gaussian state must satisfy [5]

$$\boldsymbol{\alpha} \pm i\mathbf{\Omega}/2 \geq 0, \quad (1.18)$$

which is a manifestation of the quantum uncertainty principle in the context of Gaussian states.

For example, the thermal state $\hat{\rho}_{th}(\bar{n})$ is a Gaussian state with mean $\mathbf{0}$ and covariance matrix $\boldsymbol{\sigma} = (\bar{n} + 1/2)\mathbf{I}_2$, where $\bar{n} \geq 0$ is the thermal background. In Fock basis, the thermal state has expression

$$\hat{\rho}_{th}(\bar{n}) = \frac{1}{\bar{n} + 1} \sum_{k=0}^{\infty} \left(\frac{\bar{n}}{\bar{n} + 1} \right)^k |k\rangle\langle k|. \quad (1.19)$$

Another example is coherent state $|\alpha\rangle$, where $\alpha = \alpha_R + i\alpha_I$ is a complex number. The coherent state has mean $\mathbf{d} = \sqrt{2}(\alpha_R, \alpha_I)^\top$ and covariance matrix $\boldsymbol{\alpha} = 1/2\mathbf{I}_2$. By Williamson's theorem [6], a covariance matrix $\boldsymbol{\alpha}$ can be diagonalized by a symplectic transform \mathbf{S} . Suppose that $\mathbf{S}\boldsymbol{\alpha}\mathbf{S}^\top = \text{diag}(\alpha_1, \alpha_1, \dots, \alpha_n, \alpha_n)$, where α_i are the symplectic eigenvalues. Then, Eq. (1.18) is equivalent to stating that the symplectic eigenvalues α_i must be greater than $1/2$. Let $\alpha_i = \bar{n}_i + 1/2$, a Gaussian state with mean \mathbf{m} can always be decomposed as

$$\hat{\rho} = \hat{U}_{\mathbf{S}^{-1}, \mathbf{m}} \left(\otimes_{i=1}^n \hat{\rho}_{th}(\bar{n}_i) \right) \hat{U}_{\mathbf{S}^{-1}, \mathbf{m}}^\dagger. \quad (1.20)$$

A Gaussian state is pure if and only if $\bar{n}_i = 0$. This implies that all pure Gaussian states can be generated from the vacuum state by applying a bosonic transform \mathbf{S} and displacement \mathbf{d} . In other words, for a pure Gaussian state, the covariance matrix satisfies $\boldsymbol{\alpha} = \mathbf{S}\mathbf{S}^\top/2$. Any Gaussian state can be purified by some Gaussian state in a higher dimension. From the decomposition rule, it is sufficient to demonstrate that a single-mode thermal state can be obtained from a pure state in a composite system AB . This process of purification is essential for understanding the structure and behavior of Gaussian states in quantum systems. The covariance matrix

$$\boldsymbol{\alpha}_{AB} = \begin{pmatrix} (\bar{n} + 1/2)\mathbf{I}_2 & \sqrt{\bar{n}(\bar{n} + 1)}\mathbf{Z}_2 \\ \sqrt{\bar{n}(\bar{n} + 1)}\mathbf{Z}_2 & (\bar{n} + 1/2)\mathbf{I}_2 \end{pmatrix}, \quad (1.21)$$

where $\mathbf{Z}_2 = \text{diag}(1, -1)$, represents a pure Gaussian state in AB . The subsystem A is a thermal state. It is worth to mention that this is a two-mode squeezed vacuum state, which is defined by its covariance matrix

$$\boldsymbol{\pi}(r) = \frac{1}{2} \begin{pmatrix} \cosh r \mathbf{I}_2 & \sinh r \mathbf{Z}_2 \\ \sinh r \mathbf{Z}_2 & \cosh r \mathbf{I}_2 \end{pmatrix}. \quad (1.22)$$

The Wigner function of a Gaussian state is obtained by the Fourier transform of its characteristic function:

$$W_{\hat{\rho}}(\mathbf{x}) = \frac{1}{(2\pi)^{2n}} \int_{\mathbb{R}^{2n}} d^{2n}\mathbf{t} e^{-i\mathbf{t}^\top \mathbf{x}} \chi_{\hat{\rho}}(\mathbf{t}), \quad (1.23)$$

which results in a Gaussian function. By integration, the following properties of

Wigner function and characteristic function can be verified.

$$\int_{\mathbb{R}^{2n}} d^{2n}\mathbf{x} W_{\hat{\rho}}(\mathbf{x}) = 1, \quad (1.24a)$$

$$\chi_{\hat{\rho}}(\mathbf{0}) = 1, \quad (1.24b)$$

$$W_{\hat{\rho}_1 \otimes \hat{\rho}_2}(\mathbf{x}) = W_{\hat{\rho}_1}(\mathbf{x}_1) W_{\hat{\rho}_2}(\mathbf{x}_2), \quad (1.24c)$$

$$\chi_{\hat{\rho}_1 \otimes \hat{\rho}_2}(\mathbf{t}) = \chi_{\hat{\rho}_1}(\mathbf{t}_1) \chi_{\hat{\rho}_2}(\mathbf{t}_2), \quad (1.24d)$$

$$\text{Tr}(\hat{\rho} \hat{\sigma}) = (2\pi)^n \int d^{2n}\mathbf{x} W_{\hat{\rho}}(\mathbf{x}) W_{\hat{\sigma}}(\mathbf{x}), \quad (1.24e)$$

$$\text{Tr}(\hat{\rho} \hat{\sigma}) = 1/(2\pi)^n \int d^{2n}\mathbf{t} \chi_{\hat{\rho}}(\mathbf{t}) \chi_{\hat{\sigma}}(-\mathbf{t}), \quad (1.24f)$$

$$W_{\text{Tr}_B(\hat{\rho}_{AB})}(\mathbf{x}_A) = \int d^2\mathbf{x}_B W_{\hat{\rho}_{AB}}(\mathbf{x}_A, \mathbf{x}_B), \quad (1.24g)$$

$$\chi_{\text{Tr}_B(\hat{\rho}_{AB})}(\mathbf{t}_A) = \chi_{\hat{\rho}_{AB}}(\mathbf{t}_A, \mathbf{x}_B = \mathbf{0}). \quad (1.24h)$$

If $\hat{\rho}' = \hat{U}_{S,d} \hat{\rho} \hat{U}_{S,d}^\dagger$, then

$$\begin{aligned} \chi_{\hat{\rho}'}(\boldsymbol{\xi}) &= \text{Tr}(\hat{U}_{S,d} \hat{\rho} \hat{U}_{S,d}^\dagger \hat{W}(\boldsymbol{\xi})) \\ &= \text{Tr}(\hat{\rho} \hat{W}(\mathbf{S}^{-1} \boldsymbol{\xi}) e^{i\mathbf{d}^\top \Omega \boldsymbol{\xi}}) \\ &= \chi_{\hat{\rho}}(\mathbf{S}^{-1} \boldsymbol{\xi}) e^{i\mathbf{d}^\top \Omega \boldsymbol{\xi}}, \end{aligned} \quad (1.25a)$$

$$\chi_{\hat{\rho}'}(\mathbf{t}) = \chi_{\hat{\rho}}(\mathbf{S}^\top \mathbf{t}) e^{i\mathbf{d}^\top \mathbf{t}}. \quad (1.25b)$$

1.1.4 Gaussian Channel

A quantum channel Φ transforms a state $\hat{\rho}$ to another state $\Phi(\hat{\rho})$. To be a valid channel, if the input state $\hat{\rho}$ is a valid quantum state, then the output $\Phi(\hat{\rho})$ must also be a quantum state adhering to the axioms of quantum mechanics. Thus, Φ is a trace-preserving and completely positive map (CPTP). The trace-preserving condition is derived from the fact that $\text{Tr}(\Phi(\hat{\rho})) = 1$ when $\text{Tr}(\hat{\rho}) = 1$. The complete positivity comes from the consideration that if an auxiliary system R is introduced to our quantum system $Q : \hat{\rho} \rightarrow \Phi(\hat{\rho})$, the channel $\mathbf{1}_R \otimes \Phi$ outputs a valid quantum state (positive operator) for any input state $\hat{\rho}_{QR}$ of the combined system. According to Stinespring dilation theorem [7, 8], any CPTP map Φ can be represented on some auxiliary Hilbert space. Specifically, for a quantum system Q and an environment E , we have

$$\Phi(\hat{\rho}) = \text{Tr}_E[U_{QE}(|0\rangle_E \langle 0| \otimes \hat{\rho}_Q) U_{QE}^\dagger], \quad (1.26)$$

where U_{QE} is some unitary operator. A Gaussian channel, as illustrated in Fig. 1.1, involves an input state which is a direct product of a state $\hat{\rho}$ in system A and an environmental Gaussian state $\hat{\rho}_G$ in system D . It is important to note that the environmental Gaussian state $\hat{\rho}_G$ can be purified as outlined in Eq. (1.21) by Stinespring dilation. During the interaction process, which occurs over a specific time interval, the state $\hat{\rho}_G$ is linearly coupled with the environment by Gaussian unitary.

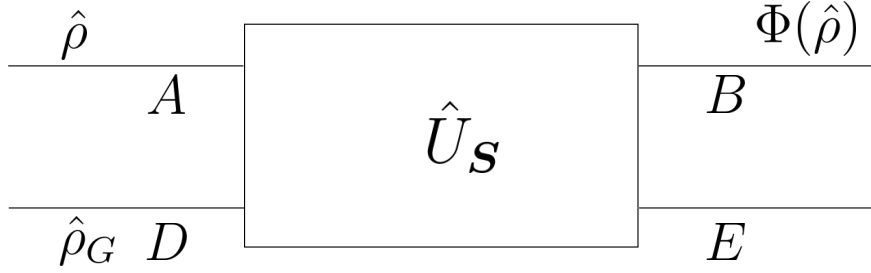


Figure 1.1: Illustration of a Gaussian channel. An input state is linearly coupled to a Gaussian state by \hat{U}_S . The output is obtained by tracing out the environment.

The output of the channel is then obtained by tracing out the environment E from the combined system BE . As a result, the transformation of states from system A to system B becomes a Gaussian channel

$$\Phi(\hat{\rho}) = \text{Tr}_E[\hat{U}_S(\hat{\rho} \otimes \hat{\rho}_G)\hat{U}_S^\dagger].$$

Let

$$\mathbf{S} = \begin{pmatrix} \mathbf{T} & \mathbf{T}_D \\ \mathbf{L} & \mathbf{L}_D \end{pmatrix}.$$

Then from Eq. (1.25b), the characteristic function of the output is

$$\begin{aligned} \chi_{\hat{\rho}}(\mathbf{t}_B, \mathbf{t}_E) &= \chi_{\hat{\rho} \otimes \hat{\rho}_G}(\mathbf{S}^\top(\mathbf{t}_A, \mathbf{t}_D)) \\ &= \chi_{\hat{\rho}}(\mathbf{T}^\top \mathbf{t}_B + \mathbf{L}^\top \mathbf{t}_D) \chi_{\hat{\rho}_G}(\mathbf{T}_D^\top \mathbf{t}_B + \mathbf{L}_D^\top \mathbf{t}_D). \end{aligned}$$

Tracing out the environment E as in Eq. (1.24h), the characteristic function of the final state in system B is

$$\chi_{\hat{\rho}}(\mathbf{T}^\top \mathbf{t}_B) \chi_{\hat{\rho}_G}(\mathbf{T}_D^\top \mathbf{t}_B) = \chi_{\hat{\rho}}(\mathbf{T}^\top \mathbf{t}_B) \exp\left(i\mathbf{d}^\top \mathbf{t}_B - \frac{1}{2}\mathbf{t}_B^\top \mathbf{N} \mathbf{t}_B\right),$$

where $\mathbf{N} = \mathbf{T}_D \boldsymbol{\alpha}_D \mathbf{T}_D^\top$ and $\mathbf{d} = \mathbf{T}_D \mathbf{m}_D$ and Gaussian state $\hat{\rho}_G$ has covariance matrix $\boldsymbol{\alpha}_D$ and mean \mathbf{m}_D . In general, a Gaussian channel is determined by \mathbf{T} , \mathbf{N} and \mathbf{d} and it transforms the Gaussian state with mean \mathbf{m} and covariance matrix $\boldsymbol{\alpha}$ to another Gaussian state with

$$\mathbf{m}' = \mathbf{T}\mathbf{m} + \mathbf{d}, \quad (1.27a)$$

$$\boldsymbol{\sigma}' = \mathbf{T}\boldsymbol{\sigma}\mathbf{T}^\top + \mathbf{N}. \quad (1.27b)$$

The transform in terms of characteristic function is given by

$$\chi_{\Phi(\hat{\rho})}(\mathbf{t}) = \chi_{\hat{\rho}}(\mathbf{T}^\top \mathbf{t}) \exp\left(i\mathbf{d}^\top \mathbf{t} - \frac{1}{2}\mathbf{t}^\top \mathbf{N} \mathbf{t}\right). \quad (1.28)$$

Lemma 9 ([4]) *A channel defined by Eq. (1.27a) and Eq. (1.27b) is Gaussian if and only if*

$$\mathbf{N} \pm \frac{i}{2}(\boldsymbol{\Omega}_B - \mathbf{T}\boldsymbol{\Omega}_A\mathbf{T}^\top) \geq 0. \quad (1.29)$$

Proof. Without the loss of generality, we can assume $\mathbf{d} = \mathbf{0}$. If the channel is Gaussian, then there exists a Gaussian state α_D and a symplectic transform \mathbf{S} such that $\mathbf{N} = \mathbf{T}_D \alpha_D \mathbf{T}_D^\top$ and $\Omega_B = \mathbf{T} \Omega_A \mathbf{T}^\top + \mathbf{T}_D \Omega_D \mathbf{T}_D^\top$. By uncertainty relation of Gaussian state α_D ,

$$\mathbf{N} = \mathbf{T}_D \alpha_D \mathbf{T}_D^\top \geq \pm i/2 \mathbf{T}_D \Omega_D \mathbf{T}_D^\top = \pm i/2 (\Omega_B - \mathbf{T} \Omega_A \mathbf{T}^\top).$$

On the other hand, if Eq. (1.29) is satisfied, we need to find a symplectic extension of \mathbf{T} from the system A to AD so that \mathbf{T} is the transform $A \rightarrow B$. One can construct such a symplectic transform \mathbf{S} given the condition $\Omega_B = \mathbf{T} \Omega_A \mathbf{T}^\top + \mathbf{T}_D \Omega_D \mathbf{T}_D^\top$ such that the first n rows of \mathbf{S} is $(\mathbf{T}, \mathbf{T}_D)$. This is due to

$$(\mathbf{T}, \mathbf{T}_D) \begin{pmatrix} \Omega_A & \mathbf{0} \\ \mathbf{0} & \Omega_D \end{pmatrix} \begin{pmatrix} \mathbf{T}^\top \\ \mathbf{T}_D^\top \end{pmatrix} = \Omega_B,$$

and Lemma 6. The proof is now equivalent to given \mathbf{T} find a Gaussian state $\alpha_D \geq \pm i/2 \Omega_D$ and a real matrix \mathbf{T}_D such that $\mathbf{T}_D \alpha_D \mathbf{T}_D^\top = \mathbf{N}$ and $\Omega_B = \mathbf{T} \Omega_A \mathbf{T}^\top + \mathbf{T}_D \Omega_D \mathbf{T}_D^\top$. Since $\Omega_B - \mathbf{T} \Omega_A \mathbf{T}^\top$ is a real anti-symmetric matrix, by Lemma 3, there exists a basis \mathbf{B} such that $\mathbf{B} \Omega_D \mathbf{B}^\top = \Omega_B - \mathbf{T} \Omega_A \mathbf{T}^\top$. So we find $\mathbf{T}_D = \mathbf{B}$ and $\alpha_D = \mathbf{T}_D^{-1} \mathbf{N} \mathbf{T}_D^{-\top}$ to satisfy the above conditions. α_D is positive since \mathbf{N} is positive. $\alpha_D \geq \pm i/2 \Omega_D$ is equivalent to $\mathbf{N} \geq \pm i/2 \mathbf{T}_D \Omega_D \mathbf{T}_D^\top = \pm i/2 (\Omega_B - \mathbf{T} \Omega_A \mathbf{T}^\top)$, which completes the proof. ■

Given two Gaussian channels Φ_1 characterized by \mathbf{T}_1 , \mathbf{N}_1 and \mathbf{d}_1 and Φ_2 characterized by \mathbf{T}_2 , \mathbf{N}_2 and \mathbf{d}_2 , the concatenated channel $\Phi_2 \circ \Phi_1$ is Gaussian with

$$\mathbf{T} = \mathbf{T}_2 \mathbf{T}_1, \tag{1.30a}$$

$$\mathbf{N} = \mathbf{T}_2 \mathbf{N}_1 \mathbf{T}_2^\top + \mathbf{N}_2, \tag{1.30b}$$

$$\mathbf{d} = \mathbf{T}_2 \mathbf{d}_1 + \mathbf{d}_2. \tag{1.30c}$$

When both system A and B have dimension $n = 1$, the channel is a single-mode Gaussian channel. With a suitable symplectic transform applied before the input state $\hat{\rho}$ and after the output state $\Phi(\hat{\rho})$, a single-mode Gaussian channel can be simplified to a form where \mathbf{T} and \mathbf{N} are diagonal and $\mathbf{d} = \mathbf{0}$. The simplified channel can then be classified into different classes based on the structure of $\mathbf{T} \Omega \mathbf{T}^\top$ [9]. In this dissertation, we encounter three such classes: the thermal-loss channel, the thermal-amplification channel, and the Gaussian additive-noise channel. The transmissivity and noise characteristics of these channels are given by:

$$k^2 = \det[\mathbf{T}], \tag{1.31}$$

$$N = (\bar{n} + \frac{1}{2}) |k^2 - 1| = \sqrt{\det[\mathbf{N}]}, \tag{1.32}$$

where $k^2 \geq 0$ is the transmissivity, N is the additive noise, and \bar{n} is the mean photon number of the thermal background. When $k < 1$, the channel is a thermal-loss channel. When $k = 1$, the channel is an additive noise channel with $\bar{n} |k^2 - 1| \rightarrow \sqrt{\det[\mathbf{N}]}$. When $k > 1$, the channel is a thermal-amplification channel.

1.2 Capacity of Gaussian Channels

In this section, I briefly review the quantum information rate and the capacity of Gaussian channels. While the exact quantum capacity of Gaussian channels remains

an open question, there are established methods for determining both upper and lower bounds of capacity. These bounds provide crucial insights into the efficiency and limitations of information transmission through Gaussian channels in quantum communication systems.

1.2.1 Entropy of Continuous Variables

Similar to classical information theory, the entropy of a state $\hat{\rho}$ is given by

$$H(\hat{\rho}) = -\text{Tr}(\hat{\rho} \log \hat{\rho}). \quad (1.33)$$

According to the source theorem [4], the entropy defined in Eq. (1.33) represents the amount of information encoded in the quantum state $\hat{\rho}$. The entropy is 0 if a state is a pure state. Since $\hat{\rho}$ is a positive operator, it has positive eigenvalues λ_i with eigenvectors $|i\rangle\langle i|$ as pure state. Then $\hat{\rho} = \sum_i \lambda_i |i\rangle\langle i|$ and

$$H(\hat{\rho}) = -\sum_i \lambda_i \log \lambda_i. \quad (1.34)$$

Since $H(\hat{\rho}) = H(\hat{U}\hat{\rho}\hat{U}^\top)$, the entropy is independent of unitary transformation. From Eq. (1.20), the entropy of a Gaussian state depends only on its symplectic eigenvalues $\alpha_i = \bar{n}_i + 1/2$. From the Eq. (1.19), the eigenvalues of a thermal state $\hat{\rho}_{th}(\bar{n})$ is $\lambda_k = \bar{n}^k / (\bar{n} + 1)^{k+1}$ therefore by Eq. (1.34), the entropy of the thermal state is given by

$$g(\bar{n}) = (\bar{n} + 1) \log(\bar{n} + 1) - \bar{n} \log(\bar{n}). \quad (1.35)$$

From the decomposition in Eq. (1.20), the entropy of a Gaussian state is the sum $\sum_{i=1}^n g(\bar{n}_i)$.

Definition 10 (Complementary Channel) *Given a channel Φ with representation by Stinespring dilation theorem*

$$\Phi(\hat{\rho}) = \text{Tr}_E[U_{QE}(|0\rangle\langle 0|_E \otimes \hat{\rho}_Q)U_{QE}^\dagger],$$

the complementary channel of Φ is defined as

$$\Phi^C(\hat{\rho}) = \text{Tr}_Q[U_{QE}(|0\rangle\langle 0|_E \otimes \hat{\rho}_Q)U_{QE}^\dagger]. \quad (1.36)$$

Let $|\chi\rangle\langle\chi|_{RQ}$ be a purification of $\hat{\rho}$. The entropy exchange is the amount of quantum information of the state after the channel:

$$\begin{aligned} H(\hat{\rho}, \Phi) &= H(\hat{\mathbf{1}} \otimes \Phi(|\chi\rangle\langle\chi|_{RQ})), \\ \hat{\rho} &= \text{Tr}(|\chi\rangle\langle\chi|_{RQ}). \end{aligned}$$

The entropy of $\Phi^C(\hat{\rho})$ is the same as the entropy exchange. Since after the interaction, the $\hat{\rho}_{RQE}$ is a pure state Then $H(\Phi^C[\hat{\rho}]) = H(E) = H(RQ) = H(\hat{\rho}, \Phi)$. The capacity refers to a channel's information rate. In quantum information science, depending on how we use the quantum channel Φ , we have different quantities to describe the information rate. Below I summarize some known theorems about different capacities and their results on Gaussian channel. The classical capacity of a

quantum channel Φ refers to its capability to transfer classical information. In this context, classical information is encoded in an ensemble $\{\pi_i, \hat{\rho}_i\}$, where π_i denotes a probability distribution satisfying $\sum_i \pi_i = 1$, and each $\hat{\rho}_i$ corresponds to a quantum state source. The classical capacity of the channel is quantified by the Holevo capacity C_χ , as established in the seminal work by Holevo [10].

$$C_\chi(\Phi) = \sup_{\pi_i, \hat{\rho}_i} \left[H \left(\sum_i \pi_i \Phi(\hat{\rho}_i) \right) - \sum_i \pi_i H(\Phi(\hat{\rho}_i)) \right]. \quad (1.37)$$

It is possible to introduce a constraint \hat{F} on the ensemble for a certain quantity $E > 0$. Then, the condition is given by $\text{Tr} \left(\hat{F} \sum_i \pi_i \hat{\rho}_i \right) \leq E$. For instance, in the case of an energy constraint, we have $\text{Tr} (\hat{n} \sum_i \pi_i \hat{\rho}_i) \leq \bar{n}$, where \bar{n} represents the average photon number of the ensemble.

For a Gaussian channel Φ , calculating the Holevo capacity $C_\chi(\Phi)$ is challenging. There is a conjecture that the maximization can be achieved by using coherent states $|\alpha_i\rangle$ [4]. This conjecture holds true for Gaussian channels when the environmental state D , denoted as $\hat{\rho}_G$, is initially in the vacuum state with $\bar{n} = 0$. In this case,

$$C_\chi(\Phi) = g(k^2 E), \quad (1.38)$$

where $k^2 = \det[\mathbf{T}]$ and E is the energy constraint. A lower bound of C_χ can be obtained by taking $\hat{\rho} = |\alpha\rangle\langle\alpha|$ as input with probability distribution $p(\alpha) \propto e^{-|\alpha|^2/E}$ [11] and

$$C_\chi(\Phi) = g(k^2 E + \bar{n}) - g(\bar{n}). \quad (1.39)$$

1.2.2 Entanglement-Assisted Classical Capacity

Another strategy for transmitting classical information from Alice to Bob involves utilizing entanglement. Initially, Alice and Bob share an entangled state $\hat{\rho}_{AB}$ before using the channel. Alice performs an operation \mathcal{E}_A on her part of the state, $\hat{\rho}_A$, and then sends the state through the channel to Bob. Upon receiving it, Bob performs a combined measurement on $\mathcal{E}_A \otimes \mathbb{I}_B(\hat{\rho}_{AB})$ to retrieve the information. The maximum information rate achievable in this scenario is defined as the entanglement-assisted classical capacity $C_{ea}(\Phi)$. It has been shown that the classical capacity is the maximum of quantum mutual information $I(\rho, \Phi)$ [12]

$$C_{ea}(\Phi) = \sup_{\hat{\rho}} H(\hat{\rho}) + H(\Phi[\hat{\rho}]) - H(\Phi^C[\hat{\rho}]). \quad (1.40)$$

In general $C_\chi(\Phi) \leq C_{ea}(\Phi) \leq \log(d) + C_\chi(\Phi)$. And for a Gaussian channel Φ , $C_{ea}(\Phi)$ is attained by Gaussian state $\hat{\rho}$ with $\text{Tr}\{\hat{\rho}\hat{n}\} = E$. The analytical expression exists and can be calculated by $H(\hat{\rho})$, $H(\Phi[\hat{\rho}])$ and $H(\hat{\rho}, \Phi) = H(\Phi^C[\hat{\rho}])$. First of all from Eq. (1.35) $H(\hat{\rho}) = g(E)$. And from Eq. (1.27b), one can get the mean photon number N' at output by

$$N' = \begin{cases} k^2 E + (1 - k^2)\bar{n}, & \text{if } k < 1; \\ \sqrt{\det[N]}, & \text{if } k = 1; \\ k^2 E + (k^2 - 1)(\bar{n} + 1), & \text{if } k > 1. \end{cases} \quad (1.41)$$

The purification of $\hat{\rho}$ can be obtained by Eq. (1.21). The entropy exchange $H(\hat{\rho}, \Phi)$ can be calculated by symplectic eigenvalues of matrix

$$\begin{pmatrix} (N' + 1/2)\mathbf{I}_2 & k\sqrt{E(E+1)}\mathbf{Z}_2 \\ k\sqrt{E(E+1)}\mathbf{Z}_2 & (N' + 1/2)\mathbf{I}_2 \end{pmatrix}.$$

The symplectic eigenvalues are $D \pm (N' - E)$, where

$$D = \sqrt{(E + N' + 1) - 4k^2E(E+1)}.$$

1.2.3 Quantum Capacity

The quantum capacity of a channel refers to the maximum rate of quantum information (qubits) that can be transmitted through the channel, with the aid of quantum error correction. This process involves both encoding and decoding. A nonzero quantum capacity is crucial for the existence of effective encoding and decoding schemes that enable faithful qubit transmission. If quantum capacity is zero, the quantum information is invariably lost, even though classical information might still be transmitted successfully.

Given that $S(\Phi(\hat{\rho}))$ represents the quantum information retrievable from the output of the channel, and $S(\Phi^C(\hat{\rho}))$ denotes the inaccessible portion of quantum information, the coherent information is defined as

$$I_c(\hat{\rho}, \Phi) = S(\Phi(\hat{\rho})) - S(\Phi^C(\hat{\rho})), \quad (1.42)$$

which has been proven to be the rate of quantum information for a single use of the channel [13, 14]. Since the channel can be utilized multiple times and an entangled state can be used as the input, the quantum capacity is given by

$$Q(\Phi) = \max_{\hat{\rho}^{\otimes n}} \lim_{n \rightarrow \infty} \frac{1}{n} I_c(\hat{\rho}^{\otimes n}, \Phi^{\otimes n}). \quad (1.43)$$

In general, obtaining quantum capacity of a channel is hard due to the difficulty of evaluating $I_c(\hat{\rho}, \Phi)$ and the entanglement-assisted enhancement of multiple uses of channel. However, there are known theorems and lower and upper bounds that help with evaluating the quantum capacity of single-mode Gaussian channel [11, 15, 16]. The lower bound is obtained by considering the Gaussian state $\hat{\rho}$.

$$Q_{\text{LB}}(\eta, N) \equiv \max \left[\log \left(\frac{\eta}{|1 - \eta|} \right) - g(\bar{n}), 0 \right], \quad (1.44)$$

where $\eta = k^2$ and \bar{n} is the mean photon number of thermal background as in Eq. (1.41). The upper bounds are obtained by two-way assisted quantum capacity and the degradable extensions.

$$Q_{\text{UP}} = \min[Q_{\text{PLOB}}(\eta, \bar{n}), Q_{\text{DE}}(\eta, \bar{n})]. \quad (1.45)$$

Here the capacities are given by

$$Q_{\text{PLOB}}(\eta, \bar{n}) \equiv \begin{cases} \max[-\log_2[(1 - \eta)\eta^{\bar{n}}] - g(\bar{n}), 0], & \text{if } \eta < 1; \\ \max\left[\log_2\left(\frac{\eta^{\bar{n}+1}}{\eta-1}\right) - g(\bar{n}), 0\right], & \text{if } \eta > 1; \\ \log_2(1/N_{\text{add}}) - 1/\ln(2) + N_{\text{add}}/\ln(2), & \text{if } \eta = 1, (1 - \eta)\bar{n} \rightarrow N_{\text{add}}. \end{cases} \quad (1.46)$$

$$Q_{\text{DE}}(\eta, \bar{n}) \equiv \begin{cases} \max \left\{ \log_2 \left(\frac{\eta}{1-\eta} \right) + h[(1-\eta)(2\bar{n}+1) + \eta] \right. \\ \quad \left. - h[\eta(2\bar{n}+1) + 1 - \eta], 0 \right\}, & \text{if } \eta < 1; \\ \max \left[\log_2 \left(\frac{1}{(\eta-1)\bar{n}} \right) - 1/\ln 2 \right. \\ \quad \left. + 2h \left(\sqrt{1 + (\eta-1)^2 \bar{n}^2} \right), 0 \right], & \text{if } \eta > 1; \\ \max \left[\log_2 \left(\frac{1}{N_{\text{add}}} \right) - 1/\ln 2 + 2h \left(\sqrt{1 + N_{\text{add}}^2} \right), 0 \right], & \text{if } \eta = 1, (1-\eta)\bar{n} \rightarrow N_{\text{add}}. \end{cases} \quad (1.47)$$

1.3 General Theorems on Quantum Information

This section is dedicated to organize some general theorems and concepts that are pivotal in evaluating the quantum capacity of a channel. These foundational ideas not only provide a theoretical underpinning for understanding quantum information rate but also offer practical insights into their analysis and optimization.

Consider the direct composition of two channels $\Phi_1 \otimes \Phi_2$. It admits a general input state $\hat{\rho}_{12}$. When $\hat{\rho}_{12} = \hat{\rho}_1 \otimes \hat{\rho}_2$ is separable, the output is equivalent to $\Phi_1(\hat{\rho}_1) \otimes \Phi_2(\hat{\rho}_2)$. And the information rate is $Q(\Phi_1) + Q(\Phi_2)$. However, the potential for greater classical and quantum information rates arises when $\hat{\rho}_{12}$ is an entangled state. Consequently, the single-shot capacity values provided earlier should be regarded as lower bounds for these channels.

Definition 11 (Entanglement Breaking Channel) *A channel Φ is defined as entanglement breaking if, for any input state $|\chi\rangle\langle\chi|_{RQ}$, the output $\mathbb{I}_R \otimes \Phi(|\chi\rangle\langle\chi|_{RQ})$ is separable.*

It is noteworthy that this definition is equivalent to stating that if the input $|\chi\rangle\langle\chi|_{RQ}$ is maximally entangled, the output will always be separable. This implies that if a channel Φ is entanglement breaking, then the single-shot classical and quantum capacity is the true capacity, as any entangled state becomes separable after multiple uses of the channel. While this characteristic simplifies the analysis of the classical capacity of the quantum channel, it is important to note that the quantum capacity of entanglement-breaking channels is zero. This concept can be further generalized to anti-degradable and degradable channels.

Definition 12 (Degradable and Anti-Degradable Channels) *A channel Φ is defined as degradable if there exists a completely positive and trace-preserving (CPTP) map D such that $\Phi^C = D \circ \Phi$. Conversely, a channel is anti-degradable if $\Phi = D \circ \Phi^C$.*

In the case of a degradable channel, the receiver can effectively simulate the environment $\Phi^C(\hat{\rho})$ using the degradable map D . Conversely, for an anti-degradable channel, the environment can simulate the received state $\Phi(\hat{\rho})$. It can be shown that the coherent information defined in Eq. (1.42) is additive if Φ is degradable and equals zero if Φ is anti-degradable [4]. Thus, an entanglement-breaking channel, being anti-degradable, has zero quantum capacity. Another important result is that if Φ^C is entanglement-breaking, then Φ is degradable. For single-mode Gaussian channels characterized by k^2 and \bar{n} , the channel is anti-degradable when the transmissivity $\eta = k^2 \leq 1/2$ and degradable when $\bar{n} = 0$ [17].

Despite the general difficulty in evaluating the true capacity of a channel, the data processing inequality provides a means to compare the capacities of two channels.

The inequalities of mutual information and coherent information are consequence of the Strong Subadditive property. Following from these iniqualities, one can also deduce the data inequality of capacity, considering that capacity is the supremum of the channel's information rate.

Theorem 13 (Data Processing Inequality) *The data processing inequality in quantum information theory states the following:*

$$I(\hat{\rho}, \Phi_2 \circ \Phi_1) \leq \min\{I(\hat{\rho}, \Phi_1), I(\hat{\rho}, \Phi_2)\}, \quad (1.48a)$$

$$I_c(\hat{\rho}, \Phi_2 \circ \Phi_1) \leq \min\{I_c(\hat{\rho}, \Phi_1), I_c(\hat{\rho}, \Phi_2)\}, \quad (1.48b)$$

$$C_{ea}(\Phi_2 \circ \Phi_1) \leq \min\{C_{ea}(\Phi_1), C_{ea}(\Phi_2)\}, \quad (1.48c)$$

$$Q(\Phi_2 \circ \Phi_1) \leq \min\{Q(\Phi_1), Q(\Phi_2)\}. \quad (1.48d)$$

One can evaluate the lower and upper bounds of quantum capacity by concatenating channels with known capacities. The quantum version of the data processing inequality, derived from the strong subadditivity of quantum entropy, allows for a closer evaluation if the auxiliary channel is chosen appropriately. Consider two single-mode Gaussian channels Φ_1 with $\mathbf{T}_1 = \text{diag}(k_1, k_1)$ and $\mathbf{N}_1 = \text{diag}(N_1, N_1)$, and Φ_2 with $\mathbf{T}_2 = \text{diag}(k_2, k_2)$ and $\mathbf{N}_2 = \text{diag}(N_2, N_2)$. If there exists a Gaussian channel $\Phi_{2 \leftarrow 1}(\mathbf{T}, \mathbf{N})$ such that $\Phi_2 = \Phi_{2 \leftarrow 1} \circ \Phi_1$, then $Q(\Phi_2) \leq Q(\Phi_1)$. Consequently, we have

Corollary 14 *For single-mode Gaussian channels Φ_1 with $\mathbf{T}_1 = \text{diag}(k_1, k_1)$ and $\mathbf{N}_1 = \text{diag}(N_1, N_1)$, and Φ_2 with $\mathbf{T}_2 = \text{diag}(k_2, k_2)$ and $\mathbf{N}_2 = \text{diag}(N_2, N_2)$, if*

$$N_2 - \frac{N_1}{k_1^2} - \frac{1}{2} \left| \frac{k_2^2}{k_1^2} - 1 \right| \geq 0, \quad (1.49)$$

then $Q(\Phi_2) \leq Q(\Phi_1)$.

Proof. The channel with $\mathbf{T} = \mathbf{T}_2 \mathbf{T}_1^{-1} = \text{diag}(k_2/k_1, k_2/k_1)$ and

$$\mathbf{N} = \mathbf{N}_2 - (\mathbf{T}_2 \mathbf{T}_1^{-1}) \mathbf{N}_1 (\mathbf{T}_2 \mathbf{T}_1^{-1})^\top = \text{diag}(N_2 - k_2^2 N_1 / k_1^2, N_2 - k_2^2 N_1 / k_1^2),$$

is Gaussian if they satisfy Eq. (1.29). Then we impose

$$\mathbf{N} + \frac{i}{2}(\boldsymbol{\Omega} - \mathbf{T} \boldsymbol{\Omega} \mathbf{T}^\top) = \begin{pmatrix} N_2 - N_1 k_2^2 / k_1^2 & \frac{1}{2} i (1 - k_2^2 / k_1^2) \\ -\frac{1}{2} i (1 - k_2^2 / k_1^2) & N_2 - N_1 k_2^2 / k_1^2 \end{pmatrix} \geq 0. \quad (1.50)$$

The eigenvalues are $N_2 - N_1 / k_1^2 \pm \frac{1}{2} (k_2^2 / k_1^2 - 1)$. The matrix is positive if $N_2 - N_1 / k_1^2 - \frac{1}{2} |k_2^2 / k_1^2 - 1| \geq 0$. Therefore, with the condition as Eq. (1.49), we can find a Gaussian channel Φ such that $\Phi_2 = \Phi \circ \Phi_1$, which complete the proof by data processing inequality in Eq. (1.48d). ■

Chapter 2

Continuous Variable Quantum Teleportation

Quantum teleportation refers to the process of transferring a quantum state from one location to another using an entangled pair and classical communication. For discrete variables, qubit teleportation has been demonstrated using Bell states and Bell measurements [18]. In contrast, in the continuous-variable regime, quantum teleportation has been successfully achieved with two-mode squeezed vacuum states, utilizing beam splitters and homodyne detection [19]. These analyses traditionally focus on a single entangled pair. However, if entanglement is established among more than two parties, additional information can be obtained by measuring a third state, potentially enhancing the teleportation process. Quantum teleportation involving more than two entangled states is often referred to as a quantum teleportation network or entanglement-assisted quantum teleportation.

This section delves into the specifics of quantum teleportation with n oscillators. I first generalize the definition of continuous-variable quantum teleportation channels, focusing on restrictions involving Gaussian operations and homodyne measurements. It is notable that an arbitrary Gaussian measurement can be implemented by first applying a Gaussian operation followed by homodyne detection. Input state is an arbitrary single-mode oscillator. Regarding on entanglement, it is essential to have at least one partition of the composite oscillators AB being inseparable, i.e., $\hat{\rho}_{AB}$ cannot be expressed as $\sum_i \lambda_i \hat{\rho}_A \otimes \hat{\rho}_B$. Otherwise, it can be shown that the teleportation channel is entanglement breaking. Thus high-fidelity transfer of arbitrary quantum states (non-zero quantum capacity) is not feasible. Finally, I present a simplified yet equivalent version of the teleportation channel, along with a series of sub-operations that can optimally enhance the performance of quantum teleportation with n oscillators. These sub-operations include single-mode and two-mode operations, specifically between adjacent oscillators.

2.1 Teleportation with Two Oscillators

We begin by exploring continuous variable quantum teleportation with two oscillators and extend the framework to teleportation involving multiple oscillators. Within teleportation, there are two primary schemes: deterministic teleportation and heralded teleportation. In the deterministic teleportation scheme, all measurement outcomes are utilized for the teleportation process. Here, I focus on the de-

terministic teleportation scheme. Through careful calculations, we establish equivalence between the general definition and a simplified form, which is referred as the reduced teleportation scheme. This reduced scheme aligns with the conventional approach, utilizing a 50/50 beam splitter.

Furthermore, when the entangled state involved in the teleportation is Gaussian, the resulting teleportation channel can be characterized as a Gaussian channel. This allows us to integrate the framework of continuous variable quantum teleportation with that of Gaussian channels, thereby leveraging the results and insights gained from the study of Gaussian channels in the context of quantum teleportation.

Definition 15 (Teleportation with Two Oscillators) *Consider a scenario where two parties, A and B, share a pair of entangled oscillators $\hat{\rho}_{AB}$. The procedure for continuous-variable quantum teleportation involving Gaussian unitary operations and measurements is given by the following steps:*

1. *At site A, the input state $\hat{\rho}_{in}$ is mixed with the state $\hat{\rho}_A$ using a Gaussian operation corresponding to a symplectic matrix in $Sp(4)$.*
2. *Homodyne measurements are performed at site A, to measure \hat{q}_+ and \hat{q}_- after the mixing, yielding measurements outcome $\tilde{\mathbf{x}} = (q_+, q_-)^\top$.*
3. *Classical information $\tilde{\mathbf{x}}$ is transmitted to B. To get the output state, a conditional displacement $\hat{D}(\mathbf{K}\tilde{\mathbf{x}})$ is applied to $\hat{\rho}_B$, where \mathbf{K} is a 2×2 linear estimation matrix.*

Now, I will characterize the teleportation channel by calculating the characteristic function of the output state. Consider that the Gaussian unitary operation in step 1 corresponds to the following transformation in block form:

$$\begin{pmatrix} \mathbf{x}_{in} \\ \mathbf{x}_A \end{pmatrix} = \begin{pmatrix} \mathbf{A} & \mathbf{B} \\ \mathbf{C} & \mathbf{D} \end{pmatrix} \begin{pmatrix} \tilde{\mathbf{x}} \\ \mathbf{x} \end{pmatrix}, \quad (2.1)$$

where $\tilde{\mathbf{x}} = (q_+, q_-)^\top$ and $\mathbf{x} = (p_+, p_-)^\top$. According to Eq. (1.24g), the Wigner function of the output state conditioned on the measured results $\tilde{\mathbf{x}}$ is given by

$$W(\mathbf{x}_B | \tilde{\mathbf{x}}) = \int_{\mathbb{R}^2} d^2\mathbf{x} W^{in}(\mathbf{A}\tilde{\mathbf{x}} + \mathbf{B}\mathbf{x}) W^{AB}(\mathbf{C}\tilde{\mathbf{x}} + \mathbf{D}\mathbf{x}, \mathbf{x}_B + \mathbf{K}\tilde{\mathbf{x}}),$$

where W^{in} and W^{AB} are the Wigner functions of the input state and the entangled Gaussian state, respectively. The teleportation process can be categorized into two schemes: deterministic and heralded. In the deterministic scheme, all measurement outcomes $\tilde{\mathbf{x}}$ are accepted. By averaging over the measurement outcomes $\tilde{\mathbf{x}}$ in the deterministic scheme, we obtain the Wigner function of the output state of the teleportation channel \mathcal{E} :

$$W_{\mathcal{E}(\hat{\rho})}(\mathbf{x}_B) = \int_{\mathbb{R}^4} d^2\mathbf{x} d^2\tilde{\mathbf{x}} W^{in}(\mathbf{A}\tilde{\mathbf{x}} + \mathbf{B}\mathbf{x}) W^{AB}(\mathbf{C}\tilde{\mathbf{x}} + \mathbf{D}\mathbf{x}, \mathbf{x}_B + \mathbf{K}\tilde{\mathbf{x}}).$$

The above integral can be expressed by characteristic functions of input and entangled oscillators.

$$\begin{aligned}
W_{\mathcal{E}(\hat{\rho})}(\mathbf{x}_B) &= \frac{1}{(2\pi)^6} \int_{\mathbb{R}^6} d^2\mathbf{t}_1 d^2\mathbf{t}_2 d^2\mathbf{t}_3 \chi^{\text{in}}(\mathbf{t}_1) \chi^{AB}(\mathbf{t}_2, \mathbf{t}_3) \times \\
&\quad \int_{\mathbb{R}^4} d^2\mathbf{x} d^2\tilde{\mathbf{x}} e^{-i\mathbf{t}_1^\top (\mathbf{A}\tilde{\mathbf{x}} + \mathbf{B}\mathbf{x})} e^{-i\mathbf{t}_2^\top (\mathbf{C}\tilde{\mathbf{x}} + \mathbf{D}\mathbf{x})} e^{-i\mathbf{t}_3^\top (\mathbf{x}_B + \mathbf{K}\tilde{\mathbf{x}})} \\
&= \frac{1}{(2\pi)^2} \int_{\mathbb{R}^2} d^2\mathbf{t}_1 e^{i\mathbf{t}_1^\top (\mathbf{A} - \mathbf{B}\mathbf{D}^{-1}\mathbf{C})\mathbf{K}^{-1}\mathbf{x}_B} \times \\
&\quad \chi^{\text{in}}(\mathbf{t}_1) \chi^{AB} [-\mathbf{D}^{-\top} \mathbf{B}^\top \mathbf{t}_1, -\mathbf{K}^{-\top} (\mathbf{A}^\top - \mathbf{C}^\top \mathbf{D}^{-\top} \mathbf{B}^\top) \mathbf{t}_1].
\end{aligned}$$

The characteristic function of output state can be obtained by

$$\begin{aligned}
\chi_{\mathcal{E}(\hat{\rho})}(\mathbf{t}_B) &= \int_{\mathbb{R}^2} d^2\mathbf{x}_B e^{i\mathbf{t}_B^\top \mathbf{x}_B} W_{\mathcal{E}(\hat{\rho})}(\mathbf{x}_B) \\
&= \chi^{\text{in}}(\mathbf{K}'^\top \mathbf{t}_B) \chi^{AB} [-(\mathbf{K}' \mathbf{B} \mathbf{D}^{-1})^\top \mathbf{t}_B, \mathbf{t}_B], \tag{2.2}
\end{aligned}$$

$$\mathbf{K}' = -\mathbf{K}(\mathbf{A} - \mathbf{B}\mathbf{D}^{-1}\mathbf{C})^{-1}. \tag{2.3}$$

Comparing with Eq. (1.28), we see that the channel is Gaussian when χ^{AB} is Gaussian. Moreover, it can be shown that $\mathbf{B}\mathbf{D}^{-1} = \mathbf{Z}_2 \mathbf{S}_A$, where $\mathbf{Z}_2 = \text{Diag}(1, -1)$ for some 2-by-2 symplectic transform \mathbf{S}_A . The block form in Eq. (2.1) must satisfies the canonical commutation relation:

$$\begin{pmatrix} \mathbf{A} & \mathbf{B} \\ \mathbf{C} & \mathbf{D} \end{pmatrix} \mathbf{J} \begin{pmatrix} \mathbf{A} & \mathbf{B} \\ \mathbf{C} & \mathbf{D} \end{pmatrix}^\top = \Omega,$$

So we obtain the equations:

$$\mathbf{A}\mathbf{B}^\top - \mathbf{B}\mathbf{A}^\top = \omega, \tag{2.4a}$$

$$\mathbf{C}\mathbf{D}^\top - \mathbf{D}\mathbf{C}^\top = \omega, \tag{2.4b}$$

$$\mathbf{A}\mathbf{D}^\top - \mathbf{B}\mathbf{C}^\top = 0. \tag{2.4c}$$

From Eq. (2.4c), $\mathbf{C}^\top = \mathbf{B}^{-1}\mathbf{A}\mathbf{D}^\top$ and substituting this into Eq. (2.4b) we have

$$\mathbf{D}\mathbf{A}^\top \mathbf{B}^{-\top} \mathbf{D}^\top - \mathbf{D}\mathbf{B}^{-1} \mathbf{A}\mathbf{D}^\top = \omega. \tag{2.5}$$

From Eq. (2.4a), we get $\mathbf{A}^\top \mathbf{B}^{-\top} = \mathbf{B}^{-1} \mathbf{A} - \mathbf{B}^{-1} \omega \mathbf{B}^{-\top}$ and combining with Eq. (2.5) we get $-\mathbf{D}\mathbf{B}^{-1} \omega \mathbf{B}^{-\top} \mathbf{D}^\top = \omega$. Since $\mathbf{Z}_2 \omega \mathbf{Z}_2 = -\omega$, then $\mathbf{D}\mathbf{B}^{-1} \mathbf{Z}_2$ is symplectic. Since if a matrix is symplectic, its inverse is symplectic as well. Then $\mathbf{Z}_2 \mathbf{B}\mathbf{D}^{-1} = \mathbf{S}_A$ for some symplectic transform \mathbf{S}_A and therefore $\mathbf{B}\mathbf{D}^{-1} = \mathbf{Z}_2 \mathbf{S}_A$. From the calculations presented above, we establish the following theorem:

Theorem 16 *In the deterministic teleportation channel, as defined in Definition 15, the characteristic function transforms according to the formula:*

$$\chi_{\mathcal{E}(\hat{\rho})}(\mathbf{t}) = \chi_{\hat{\rho}}(\mathbf{K}_1^\top \mathbf{t}) \cdot \chi_{\hat{\rho}_{AB}}(-\mathbf{S}_A^\top \mathbf{Z}_2 \mathbf{K}_1^\top \mathbf{t}, \mathbf{t}), \tag{2.6}$$

where \mathbf{K}_1 and \mathbf{S}_A are determined by the Gaussian transformation in Eq. (2.1) and the estimation matrix \mathbf{K} :

$$\mathbf{K}_1 = -\mathbf{K}(\mathbf{A} - \mathbf{B}\mathbf{D}^{-1}\mathbf{C})^{-1}, \tag{2.7}$$

$$\mathbf{S}_A = \mathbf{Z}_2 \mathbf{B}\mathbf{D}^{-1}. \tag{2.8}$$

Definition 17 (Reduced Teleportation Scheme) Consider a scenario where two parties, A and B , share a pair of entangled oscillators $\hat{\rho}_{AB}$. The reduced quantum teleportation procedure is given by the following steps:

1. At site A , the input state $\hat{\rho}_{in}$ is combined with state $\hat{\rho}_A$ using a 50/50 beam splitter.
2. Homodyne measurements are performed at site A , to measure \hat{q}_- and \hat{p}_+ after the mixing, yielding measurements outcome $\tilde{\mathbf{x}} = \sqrt{2}(q_-, -_+)$.
3. To get the output state, a conditional displacement $\hat{D}(\mathbf{K}\tilde{\mathbf{x}})$ is applied to $\hat{\rho}_B$ at site B , where \mathbf{K} is a 2×2 linear estimation matrix.

From Theorem 16, it can be shown that in this reduced case, the characteristic function transforms as

$$\chi_{\mathcal{E}(\hat{\rho})}(\mathbf{t}) = \chi_{\hat{\rho}}(\mathbf{K}^\top \mathbf{t}) \cdot \chi_{\hat{\rho}_{AB}}(-\mathbf{Z}_2 \mathbf{K}^\top \mathbf{t}, \mathbf{t}). \quad (2.9)$$

By equating \mathbf{K} in Definition 17 with \mathbf{K}_1 from Theorem 16, we arrive at the following corollary:

Corollary 18 The deterministic teleportation channel, as defined in Definition 15, is equivalent to first applying some local operation \mathbf{S}_A on $\hat{\rho}_{AB}$ and then utilizing the reduced teleportation channel detailed in Definition 17. This channel becomes a Gaussian channel when $\hat{\rho}_{AB}$ is Gaussian. If $\hat{\rho}_{AB}$ has a mean of $\mathbf{0}$ and a covariance matrix

$$\boldsymbol{\sigma}_{AB} = \begin{pmatrix} \boldsymbol{\sigma}_{11} & \boldsymbol{\sigma}_{12} \\ \boldsymbol{\sigma}_{21} & \boldsymbol{\sigma}_{22} \end{pmatrix}, \quad (2.10)$$

then the parameters of the Gaussian channel are given by

$$\mathbf{T} = \mathbf{K}, \quad (2.11)$$

$$\mathbf{N} = \mathbf{K} \mathbf{Z}_2 \mathbf{S}_A \boldsymbol{\sigma}_{11} \mathbf{S}_A^\top \mathbf{Z}_2 \mathbf{K}^\top - 2 \mathbf{K} \mathbf{Z}_2 \mathbf{S}_A \boldsymbol{\sigma}_{12} + \boldsymbol{\sigma}_{22}. \quad (2.12)$$

Next, I address the redundancy of local operations in the teleportation channel. While the analysis initially focuses on two-mode entangled Gaussian states, it can be extended to general two-mode oscillators. We start with the following lemma:

Lemma 19 Let $\mathbf{S}^Z = \mathbf{Z}_2 \mathbf{S} \mathbf{Z}_2$. Then \mathbf{S}^Z is symplectic if and only if \mathbf{S} is symplectic.

Consider \mathbf{S}_E , \mathbf{S}_D , \mathbf{S}_1 , and \mathbf{S}_2 as 2×2 symplectic matrices corresponding to local operations on the input, output, local oscillators A and B , respectively. \mathbf{S}_E and \mathbf{S}_D are interpreted as encoding and decoding matrices. Without loss of generality, we can assume $\mathbf{S}_A = \mathbf{I}_2$ in the teleportation channel, as it can be incorporated through \mathbf{S}_1 . Let \mathbf{K} be the estimation matrix. Through calculations, we obtain:

$$\begin{aligned} \mathbf{T} &= \mathbf{S}_D \mathbf{K} \mathbf{S}_E, \\ \mathbf{N} &= \mathbf{S}_D \mathbf{K} \mathbf{Z}_2 \mathbf{S}_1 \boldsymbol{\sigma}_{11} (\mathbf{S}_D \mathbf{K} \mathbf{Z}_2 \mathbf{S}_1)^\top - 2 \mathbf{S}_D \mathbf{K} \mathbf{Z}_2 \mathbf{S}_1 \boldsymbol{\sigma}_{12} \mathbf{S}_2^\top \mathbf{S}_D^\top + \\ &\quad \mathbf{S}_D \mathbf{S}_2 \boldsymbol{\sigma}_{22} (\mathbf{S}_D \mathbf{S}_2)^\top. \end{aligned}$$

Simplifying, we find:

$$\begin{aligned} \mathbf{T} &= \mathbf{K}', \\ \mathbf{N} &= \mathbf{K}' \mathbf{Z}_2 \mathbf{S}'_1 \boldsymbol{\sigma}_{11} (\mathbf{K}' \mathbf{Z}_2 \mathbf{S}'_1)^\top - 2 \mathbf{K}' \mathbf{Z}_2 \mathbf{S}'_1 \boldsymbol{\sigma}_{12} \mathbf{S}'_2{}^\top + \mathbf{S}'_2 \boldsymbol{\sigma}_{22} \mathbf{S}'_2{}^\top, \end{aligned}$$

where $\mathbf{K}' = \mathbf{S}_D \mathbf{K} \mathbf{S}_E$, $\mathbf{S}'_1 = (\mathbf{S}_E^{-1})^Z \mathbf{S}_1$, and $\mathbf{S}'_2 = \mathbf{S}_D \mathbf{S}_2$. Thus, encoding \mathbf{S}_E and decoding \mathbf{S}_D in the teleportation channel are equivalent to performing local operations on oscillators A and B , respectively.

Theorem 20 *In two-mode quantum teleportation, performing both encoding \mathbf{S}_E and decoding \mathbf{S}_D on the input and output is equivalent to performing the local operation $(\mathbf{S}_E^{-1})^Z$ on oscillator A , \mathbf{S}_D on oscillator B , and using a new estimation matrix $\mathbf{S}_D \mathbf{K} \mathbf{S}_E$.*

2.2 Teleportation with Many Oscillators

Moving forward, I extend the discussion to encompass the general case of teleportation with n oscillators. The definitions and methodologies applied here are analogous to those used in the two-oscillator scenario, but they are adapted to accommodate an n -oscillator system. I will demonstrate that the definitions for n oscillators are equivalent to the simpler two-oscillator case, as elucidated by Corollary 24. This equivalence plays a crucial role in understanding and analyzing teleportation schemes in larger quantum systems.

Definition 21 (General Teleportation Scheme) *Consider a scenario where two parties, A and B , share n entangled oscillators $\hat{\rho}_{AB}$, with $\hat{\rho}_A$ consisting of $n - 1$ oscillators and $\hat{\rho}_B$ being a single oscillator. A general continuous-variable quantum teleportation procedure involving Gaussian unitary operations and measurements is given by the following steps:*

1. At site A , the input state $\hat{\rho}_{in}$ is combined with state $\hat{\rho}_A$ using a Gaussian operation corresponding to a symplectic matrix in $Sp(2n)$.
2. Homodyne measurements are performed at site A , yielding measurements outcome $\hat{\mathbf{x}} = (q_1, \dots, q_n)$ after the mixing.
3. To get the output state, a conditional displacement $\hat{D}(\mathbf{K}\hat{\mathbf{x}})$ is applied at site B , where \mathbf{K} is a $2 \times n$ linear estimation matrix.

Definition 22 (Reduced Teleportation Scheme) *Consider a scenario where two parties, A and B , share n entangled oscillators $\hat{\rho}_{AB}$, with $\hat{\rho}_A$ consisting of $n - 1$ oscillators and $\hat{\rho}_B$ being a single oscillator. The reduced teleportation procedure is given by the following steps:*

1. Applying a local operation $\bar{\mathbf{S}}_A \in Sp(2n - 2)$ on the $n - 1$ oscillators $\hat{\rho}_A$.
2. Executing the reduced teleportation process as in Definition 17 between the first oscillator of $\hat{\rho}_A$ and the input state.

The adaptation of the reduction process to a larger number of oscillators of $\hat{\rho}_A$ is achieved through similar calculations. The dimensions of the sub-block matrices are indicated by subscripts, and the inverse of a matrix is to be interpreted as a pseudo-inverse. The commutation relations yield:

$$\begin{aligned} \mathbf{A}_{2 \times n} \mathbf{B}_{n \times 2}^\top - \mathbf{B}_{2 \times n} \mathbf{A}_{n \times 2}^\top &= \omega, \\ \mathbf{C}_{(2n-2) \times n} \mathbf{D}_{n \times (2n-2)}^\top - \mathbf{D}_{(2n-2) \times n} \mathbf{C}_{n \times (2n-2)}^\top &= \Omega_{2n-2}, \\ \mathbf{A}_{2 \times n} \mathbf{D}_{n \times (2n-2)}^\top - \mathbf{B}_{2 \times n} \mathbf{C}_{n \times (2n-2)}^\top &= \mathbf{0}. \end{aligned}$$

From the above relation, the $2 \times (2n - 2)$ matrix $\mathbf{Z}_2 \mathbf{B} \mathbf{D}^{-1}$ satisfies

$$\mathbf{Z}_2 \mathbf{B} \mathbf{D}^{-1} \Omega_{2n-2} (\mathbf{B} \mathbf{D}^{-1} \mathbf{Z}_2)^\top = \omega.$$

Thus $\mathbf{S}_A = \mathbf{Z}_2 \mathbf{B} \mathbf{D}^{-1}$ can be extended to a symplectic transform $\bar{\mathbf{S}}_A \in \text{Sp}(2n - 2)$ by Lemma 6. The Theorem 16 is generalized to

Theorem 23 *In the deterministic teleportation channel as defined in Definition 21, the characteristic function transforms according to:*

$$\chi_{\mathcal{E}(\hat{\rho})}(\mathbf{t}) = \chi_{\hat{\rho}}(\mathbf{K}_1^\top \mathbf{t}) \cdot \chi_{\hat{\rho}_{AB}}(-\mathbf{S}_A^\top \mathbf{Z}_2 \mathbf{K}_1^\top \mathbf{t}, \mathbf{t}), \quad (2.13)$$

where \mathbf{K}_1 and \mathbf{S}_A are $2 \times n$ and $2 \times (2n - 2)$ matrices, respectively, as specified by the Gaussian transform in Eq. (2.1) and the $2 \times n$ estimation matrix \mathbf{K} :

$$\mathbf{K}_1 = -\mathbf{K}(\mathbf{A} - \mathbf{B} \mathbf{D}^{-1} \mathbf{C})^{-1}, \quad (2.14)$$

$$\mathbf{S}_A = \mathbf{Z}_2 \mathbf{B} \mathbf{D}^{-1}. \quad (2.15)$$

Corollary 24 *The deterministic teleportation channel defined in Definition 21 is equivalent to the reduced teleportation scheme outlined in Definition 22 by extending the symplectic basis from \mathbf{S}_A to $\bar{\mathbf{S}}_A$. The channel is a Gaussian channel when $\hat{\rho}_{AB}$ is Gaussian. If $\hat{\rho}_{AB}$ has a mean of $\mathbf{0}$ and a covariance matrix:*

$$\boldsymbol{\sigma}_{AB} = \begin{pmatrix} \boldsymbol{\sigma}_{11} & \boldsymbol{\sigma}_{12} \\ \boldsymbol{\sigma}_{21} & \boldsymbol{\sigma}_{22} \end{pmatrix}, \quad (2.16)$$

then the parameters of the Gaussian channel are:

$$\mathbf{T} = \mathbf{K}, \quad (2.17)$$

$$\mathbf{N} = \mathbf{K} \mathbf{Z}_2 \mathbf{S}_A \boldsymbol{\sigma}_{11} \mathbf{S}_A^\top \mathbf{Z}_2 \mathbf{K}^\top - 2 \mathbf{K} \mathbf{Z}_2 \mathbf{S}_A \boldsymbol{\sigma}_{12} + \boldsymbol{\sigma}_{22}. \quad (2.18)$$

Next, I discuss the optimization of the teleportation network. Given that the teleportation process involves transferring a state from a single oscillator to another single oscillator via an entangled network of n oscillators, the primary objective of optimization is to find the optimal transformation $\bar{\mathbf{S}}_A$ between the first $n - 1$ oscillators. This transformation should maximize the entanglement between the first and last oscillators among the n oscillators. Once this optimal entanglement is achieved, the first and the last oscillator can be used as effectively as teleportation with n oscillators.

2.3 A Decomposition of Symplectic Transform

In optical quantum networks, a general beam splitter transform, denoted by \mathbf{O} , cannot be realized by a single device. Instead, it is typically decomposed into a series of beam splitters that interconnect pairs of adjacent oscillators, as illustrated in [20]. In practical applications, there is also an interest in constructing a symplectic transform \mathbf{S} through local operations that similarly connect nearby oscillators. In this dissertation, a method for decomposing \mathbf{S} to adjacent interactions is provided. If $\mathbf{S} \in U(n)$, then this decomposition becomes the same as the decomposition of a general beam splitter in [20]. The local operations involved in this decomposition are a combination of two-mode and single-mode operations, providing a practical approach for implementing symplectic transforms in quantum networks.

Definition 25 (Single-mode Transform and Two-mode Transform) *Let $k \in \mathbb{R}$, a two-mode transform $\mathbf{S}_{ij}(k) \in Sp(2n)$ between i and j is given by*

$$\begin{pmatrix} \mathbf{I}_{2i-2} & \mathbf{0} & \mathbf{0} & \mathbf{0} & \mathbf{0} \\ \mathbf{0} & \sqrt{k}\mathbf{I}_2 & \mathbf{0} & -\sqrt{1-k}\mathbf{I}_2 & \mathbf{0} \\ \mathbf{0} & \mathbf{0} & \mathbf{0} & \mathbf{0} & \mathbf{0} \\ \mathbf{0} & \sqrt{1-k}\mathbf{I}_2 & \mathbf{0} & \sqrt{k}\mathbf{I}_2 & \mathbf{0} \\ \mathbf{0} & \mathbf{0} & \mathbf{0} & \mathbf{0} & \mathbf{I}_{2n-2j} \end{pmatrix}, \text{ when } 0 < k < 1 \quad (2.19a)$$

$$\begin{pmatrix} \mathbf{I}_{2i-2} & \mathbf{0} & \mathbf{0} & \mathbf{0} & \mathbf{0} \\ \mathbf{0} & \sqrt{k}\mathbf{I}_2 & \mathbf{0} & \sqrt{k-1}\mathbf{Z}_2 & \mathbf{0} \\ \mathbf{0} & \mathbf{0} & \mathbf{0} & \mathbf{0} & \mathbf{0} \\ \mathbf{0} & \sqrt{k-1}\mathbf{Z}_2 & \mathbf{0} & \sqrt{k}\mathbf{I}_2 & \mathbf{0} \\ \mathbf{0} & \mathbf{0} & \mathbf{0} & \mathbf{0} & \mathbf{I}_{2n-2j} \end{pmatrix}, \text{ when } k > 1 \quad (2.19b)$$

$$\begin{pmatrix} \mathbf{I}_{2i-2} & \mathbf{0} & \mathbf{0} & \mathbf{0} & \mathbf{0} \\ \mathbf{0} & \sqrt{-k}\mathbf{Z}_2 & \mathbf{0} & \sqrt{1-k}\mathbf{I}_2 & \mathbf{0} \\ \mathbf{0} & \mathbf{0} & \mathbf{0} & \mathbf{0} & \mathbf{0} \\ \mathbf{0} & \sqrt{1-k}\mathbf{I}_2 & \mathbf{0} & \sqrt{-k}\mathbf{Z}_2 & \mathbf{0} \\ \mathbf{0} & \mathbf{0} & \mathbf{0} & \mathbf{0} & \mathbf{I}_{2n-2j} \end{pmatrix}, \text{ when } k < 0 \quad (2.19c)$$

$$\begin{pmatrix} \mathbf{I}_{2i-2} & \mathbf{0} & \mathbf{0} & \mathbf{0} & \mathbf{0} \\ \mathbf{0} & \mathbf{L}_1 & \mathbf{0} & \mathbf{I}_2 & \mathbf{0} \\ \mathbf{0} & \mathbf{0} & \mathbf{0} & \mathbf{0} & \mathbf{0} \\ \mathbf{0} & \mathbf{I}_2 & \mathbf{0} & \omega\mathbf{L}_1^\top\omega & \mathbf{0} \\ \mathbf{0} & \mathbf{0} & \mathbf{0} & \mathbf{0} & \mathbf{I}_{2n-2j} \end{pmatrix}, \text{ when } k = 0, \text{ and } \mathbf{L}_1 = \begin{pmatrix} a & b \\ 0 & 0 \end{pmatrix} \quad (2.19d)$$

$$\begin{pmatrix} \mathbf{I}_{2i-2} & \mathbf{0} & \mathbf{0} & \mathbf{0} & \mathbf{0} \\ \mathbf{0} & \mathbf{I}_2 & \mathbf{0} & \mathbf{L}_2 & \mathbf{0} \\ \mathbf{0} & \mathbf{0} & \mathbf{0} & \mathbf{0} & \mathbf{0} \\ \mathbf{0} & \omega\mathbf{L}_2^\top\omega & \mathbf{0} & \mathbf{I}_2 & \mathbf{0} \\ \mathbf{0} & \mathbf{0} & \mathbf{0} & \mathbf{0} & \mathbf{I}_{2n-2j} \end{pmatrix}, \text{ when } k = 1 \text{ and } \mathbf{L}_2 = \begin{pmatrix} a & 0 \\ b & 0 \end{pmatrix} \quad (2.19e)$$

A single-mode operation $\mathbf{S}_i(r, \theta, \phi)$ on i is $\mathbf{R}_i(\theta)Sq[(1, \dots, r, 1, \dots, 1)]\mathbf{R}_i(\phi)$, where $r \geq 0$ is the single-mode squeezing parameter and $\mathbf{R}_i(\theta) = \mathbf{I}_{2i-2} \oplus \begin{pmatrix} \cos \theta & -\sin \theta \\ \sin \theta & \cos \theta \end{pmatrix} \oplus \mathbf{I}_{2n-2i}$.

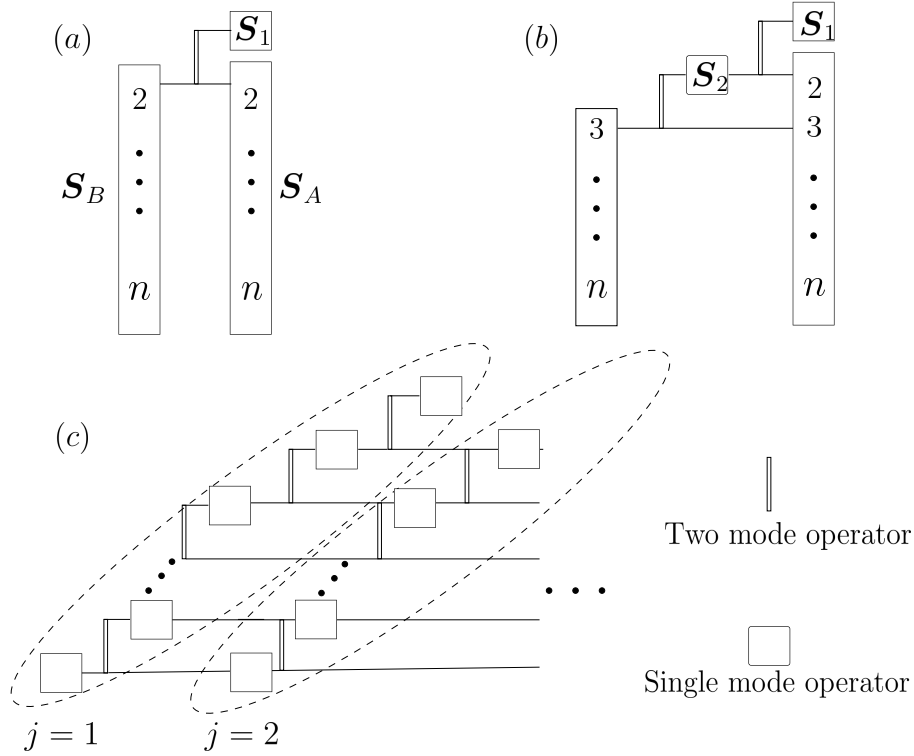


Figure 2.1: Decomposition of a symplectic transform \mathbf{S} . (a) Decompose $\mathbf{S} \in \text{Sp}(2n)$ to two mode operator and local operators $\mathbf{S}_{A,B} \in \text{Sp}(2n-2)$. (b) Decompose \mathbf{S} to two mode operators and local operators in lower dimension. (c) A full decomposition of \mathbf{S} .

Theorem 26 Let $\mathbf{S} \in \text{Sp}(2n)$. As illustrated in Fig. 2.1 (c), a general symplectic transform \mathbf{S} can be decomposed into a series of adjacent two-mode transforms and single-mode transforms as

$$\mathbf{S} = \Pi_{j=1}^{n-1} \left[\mathbf{S}_j^{(j)} \left(\Pi_{i=n}^{i=j+1} \mathbf{S}_{i-1,i}^{(j)} \mathbf{S}_i^{(j)} \right) \right], \quad (2.20)$$

where $\mathbf{S}_i^{(j)}$ is a single-mode transform on i -th mode in j -th layer and $\mathbf{S}_{i,i+1}^{(j)}$ is a two-mode transform in j -th layer as in the Definition 25. And the product of transforms is written as $\Pi_{i=1}^n \mathbf{S}_i = \mathbf{S}_n \dots \mathbf{S}_2 \mathbf{S}_1$.

Proof. Consider the first two rows of \mathbf{S} in the block form

$$\begin{pmatrix} \mathbf{A}_{2 \times 2} & \mathbf{B}_{2 \times (2n-2)} \end{pmatrix}$$

From $\mathbf{S} \Omega_{2n} \mathbf{S}^\top = \Omega_{2n}$, we have

$$\mathbf{A} \omega \mathbf{A}^\top + \mathbf{B} \Omega_{2n-2} \mathbf{B}^\top = \omega.$$

Since \mathbf{A} is a 2-by-2 matrix, we can assume that $\mathbf{A} \omega \mathbf{A}^\top = k \omega$ and $\mathbf{B} \Omega_{2n-2} \mathbf{B}^\top = (1-k) \omega$. If $1 > k > 0$, then $\mathbf{A} / \sqrt{k} = \mathbf{S}_1$ is a symplectic matrix. And the matrix $\mathbf{S}'_B = \mathbf{S}_1^{-1} \mathbf{B} / \sqrt{1-k}$ satisfies $\mathbf{S}'_B \Omega_{2n-2} \mathbf{S}'_B{}^\top = \omega$. So there exists a basis extension

\mathbf{S}_B such that the first two rows of \mathbf{S}_B is \mathbf{S}'_B . Thus we have

$$\begin{aligned} (\mathbf{A}_{2 \times 2} \quad \mathbf{B}_{2 \times (2n-2)}) &= (\mathbf{S}_1 \sqrt{k} \quad \mathbf{S}_1 \mathbf{S}'_B \sqrt{1-k}) \\ &= \mathbf{S}_1 (\sqrt{k} \mathbf{I}_2 \quad \sqrt{1-k} \mathbf{S}'_B) \begin{pmatrix} \mathbf{I}_2 & \mathbf{0} \\ \mathbf{0} & \mathbf{S}_B \end{pmatrix}^{-1} \begin{pmatrix} \mathbf{I}_2 & \mathbf{0} \\ \mathbf{0} & \mathbf{S}_B \end{pmatrix} \\ &= \mathbf{S}_1 (\sqrt{k} \mathbf{I}_2 \quad \sqrt{1-k} \mathbf{I}_2 \quad \mathbf{0}) \begin{pmatrix} \mathbf{I}_2 & \mathbf{0} \\ \mathbf{0} & \mathbf{S}_B \end{pmatrix}. \end{aligned}$$

Then we do an arbitrary basis extension on both sides. On the right hand side, we take the extension in the form

$$\begin{pmatrix} \mathbf{S}_1 & \mathbf{0} \\ \mathbf{0} & \mathbf{I}_{2n-2} \end{pmatrix} \begin{pmatrix} \sqrt{k} \mathbf{I}_2 & \sqrt{1-k} \mathbf{I}_2 & \mathbf{0} \\ \sqrt{1-k} \mathbf{I}_2 & \sqrt{k} \mathbf{I}_2 & \mathbf{0} \\ \mathbf{0} & \mathbf{0} & \mathbf{I}_{2n-4} \end{pmatrix} \begin{pmatrix} \mathbf{I}_2 & \mathbf{0} \\ \mathbf{0} & \mathbf{S}_B \end{pmatrix}.$$

From Lemma 6, the above extension is different from \mathbf{S} only by a local symplectic transform \mathbf{S}_A :

$$\mathbf{S} = \begin{pmatrix} \mathbf{S}_1 & \mathbf{0} \\ \mathbf{0} & \mathbf{S}_A \end{pmatrix} \begin{pmatrix} \sqrt{k} \mathbf{I}_2 & \sqrt{1-k} \mathbf{I}_2 & \mathbf{0} \\ \sqrt{1-k} \mathbf{I}_2 & \sqrt{k} \mathbf{I}_2 & \mathbf{0} \\ \mathbf{0} & \mathbf{0} & \mathbf{I}_{2n-4} \end{pmatrix} \begin{pmatrix} \mathbf{I}_2 & \mathbf{0} \\ \mathbf{0} & \mathbf{S}_B \end{pmatrix}.$$

Similarly, this will hold when $k \geq 1$ and $k \leq 0$. Therefore we have the decomposition as shown in Fig. 2.1 (a). We can express \mathbf{S} as

$$\mathbf{S} = \begin{pmatrix} \mathbf{S}_1 & \mathbf{0} \\ \mathbf{0} & \mathbf{S}_A \end{pmatrix} \begin{pmatrix} \mathbf{S}_{12}^{(k)} & \mathbf{0} \\ \mathbf{0} & \mathbf{I}_{2n-4} \end{pmatrix} \begin{pmatrix} \mathbf{I}_2 & \mathbf{0} \\ \mathbf{0} & \mathbf{S}_B \end{pmatrix}.$$

Next, we take the first two rows of \mathbf{S}_B and do the same decomposition above. The decomposition is shown in Fig. 2.1 (b). The \mathbf{S}'_A part of the decomposition of \mathbf{S}_B is absorbed into \mathbf{S}_A . Then we have

$$\begin{aligned} \mathbf{S} &= \begin{pmatrix} \mathbf{S}_1 & \mathbf{0} \\ \mathbf{0} & \mathbf{S}_A \end{pmatrix} \begin{pmatrix} \mathbf{S}_{12}^{(k)} & \mathbf{0} \\ \mathbf{0} & \mathbf{I}_{2n-4} \end{pmatrix} \begin{pmatrix} \mathbf{I}_2 & \mathbf{0} & \mathbf{0} \\ \mathbf{0} & \mathbf{S}_2 & \mathbf{0} \\ \mathbf{0} & \mathbf{0} & \mathbf{S}'_A \end{pmatrix} \begin{pmatrix} \mathbf{I}_2 & \mathbf{0} & \mathbf{0} \\ \mathbf{0} & \mathbf{S}_{23}^{(k')} & \mathbf{0} \\ \mathbf{0} & \mathbf{0} & \mathbf{I}_{2n-6} \end{pmatrix} \\ &\quad \cdot \begin{pmatrix} \mathbf{I}_2 & \mathbf{0} & \mathbf{0} \\ \mathbf{0} & \mathbf{I}_2 & \mathbf{0} \\ \mathbf{0} & \mathbf{0} & \mathbf{S}'_B \end{pmatrix} \\ &= \begin{pmatrix} \mathbf{S}_1 & \mathbf{0} \\ \mathbf{0} & \mathbf{S}_A (\mathbf{I}_2 \oplus \mathbf{S}'_A) \end{pmatrix} \begin{pmatrix} \mathbf{S}_{12}^{(k)} & \mathbf{0} \\ \mathbf{0} & \mathbf{I}_{2n-4} \end{pmatrix} \begin{pmatrix} \mathbf{I}_2 & \mathbf{0} & \mathbf{0} \\ \mathbf{0} & \mathbf{S}_2 & \mathbf{0} \\ \mathbf{0} & \mathbf{0} & \mathbf{I}_{2n-4} \end{pmatrix} \\ &\quad \cdot \begin{pmatrix} \mathbf{I}_2 & \mathbf{0} & \mathbf{0} \\ \mathbf{0} & \mathbf{S}_{23}^{(k')} & \mathbf{0} \\ \mathbf{0} & \mathbf{0} & \mathbf{I}_{2n-6} \end{pmatrix} \begin{pmatrix} \mathbf{I}_2 & \mathbf{0} & \mathbf{0} \\ \mathbf{0} & \mathbf{I}_2 & \mathbf{0} \\ \mathbf{0} & \mathbf{0} & \mathbf{S}'_B \end{pmatrix}. \end{aligned}$$

So in the first layer we get

$$\begin{aligned} \mathbf{S} &= (\mathbf{I}_2 \oplus \mathbf{S}_{(2n-2) \times (2n-2)}) \left[\mathbf{S}_1^{(1)} \mathbf{S}_{1,2}^{(1)} \mathbf{S}_2^{(1)} \mathbf{S}_{2,3}^{(1)} \dots \mathbf{S}_{n-1}^{(1)} \mathbf{S}_{n-1,n}^{(1)} \right] \mathbf{S}_n^{(1)} \\ &= (\mathbf{I}_2 \oplus \mathbf{S}_{(2n-2) \times (2n-2)}) \mathbf{S}_1^{(1)} \prod_{i=n}^{i=1} \left[\mathbf{S}_{i-1,i}^{(1)} \mathbf{S}_i^{(1)} \right], \end{aligned}$$

where $\mathbf{S}_{1,2}^{(1)} = \mathbf{S}_{12}(k)$, ..., $\mathbf{S}_1^{(1)} = \mathbf{S}_1$, ..., and $\mathbf{S}_{(2n-2) \times (2n-2)} \in \text{Sp}(2n-2)$. The theorem is proved by decomposing $\mathbf{S}_{(2n-2) \times (2n-2)}$ recursively. ■

There are 3 parameters to characterize a single-mode symplectic transform. For two-mode operations, we can introduce a single-mode operation to simplify \mathbf{L}_1 and \mathbf{L}_2 so that $a = 1$ and $b = 0$ or $a = 0$ and $b = 0$. When $a = 1$ and $b = 0$, the Eq. (2.19d) and Eq. (2.19e) correspond to general sum gates. The two-mode symplectic transform has 1 parameter. When $\mathbf{S} \in \text{Sp}(2n)$, the dimension of $\text{span}(v_1, v_2)$ with restriction $v_1^\top \Omega_{2n} v_2 = 1$ is $4n - 1$, which is the same as dimension of the first layer (n single-mode operations and $n - 1$ two-mode operations). In general, from the first layer with dimension $4n - 1$, to the last layer with dimension 3, the total dimension is $\sum_{k=1}^n 4k - 1 = 2n^2 + n = \dim \text{Sp}(2n)$.

Using the same underlying principles, we can also prove the decomposition of a general beam splitter. The decomposition of a general beam splitter, much like the earlier discussed symplectic transformations, can be sufficiently constructed by a series of two-mode beam splitters and single phase rotations in the same style as in Fig. 2.1 (c). Below, the theorem is stated within the group $U(n)$. Because $U(n)$ is isomorphic to $\text{Sp}(2n) \cap O(2n)$ by isomorphism μ

$$\mu(\mathbf{U}) = \begin{pmatrix} \mathbf{A} & -\mathbf{B} \\ \mathbf{B} & \mathbf{A} \end{pmatrix}, \quad (2.21)$$

where $\mathbf{U} = \mathbf{A} + i\mathbf{B} \in U(n)$ and \mathbf{A} and \mathbf{B} are real matrices. $\mu(\mathbf{U}) \in \text{Sp}(2n) \cap O(2n)$, is symplectic in the second standard from $\mu(\mathbf{U})\mathbf{J}\mu(\mathbf{U})^\top = \mathbf{J}$.

Theorem 27 *A general unitary $\mathbf{U} \in U(n)$ can be decomposed into a series of adjacent two-mode beam splitters and phase transforms as*

$$\mathbf{U} = \Pi_{j=1}^{n-1} \left[\mathbf{U}_j^{(j)} \left(\Pi_{i=n}^{j+1} \mathbf{U}_{i-1,i}^{(j)} \mathbf{U}_i^{(j)} \right) \right], \quad (2.22)$$

where \mathbf{U}_i is a single-mode phase transform and $\mathbf{U}_{i,i+1}$ is a two-mode beam splitter given by

$$\begin{aligned} \mathbf{U}_i &= \begin{pmatrix} e^{i\phi} & 0 \\ 0 & 1 \end{pmatrix}, \\ \mathbf{U}_{i,i+1} &= \begin{pmatrix} \cos \theta & -\sin \theta \\ \sin \theta & \cos \theta \end{pmatrix}. \end{aligned}$$

Proof. Let a be the first element of the first row of \mathbf{U} , (a, \mathbf{B}) . Since $\mathbf{U}\mathbf{U}^\dagger = \mathbf{I}$, $aa^* + \mathbf{B}\mathbf{B}^\dagger = 1$. Therefore we can take $a = \cos \theta e^{i\phi}$ and $\mathbf{B} = -\sin \theta e^{i\phi} \tilde{\mathbf{B}}$, with $\tilde{\mathbf{B}}\tilde{\mathbf{B}}^\dagger = 1$. The first row can be expressed as

$$\begin{aligned} (a, \mathbf{B}) &= e^{i\phi} (\cos \theta \quad -\sin \theta \tilde{\mathbf{B}}) \\ &= e^{i\phi} (\cos \theta \quad -\sin \theta \quad 0) \begin{pmatrix} 1 & 0 \\ 0 & \tilde{\mathbf{B}} \end{pmatrix}, \end{aligned}$$

where $\tilde{\mathbf{B}} \in U(n-1)$, is the unitary that inverts the extension of $\tilde{\mathbf{B}}$. The next step is extending (a, \mathbf{B}) to \mathbf{U} . Since any two extensions of (a, \mathbf{B}) are different only by local unitary of remaining transforms in $n-1$. There exists $\mathbf{A} \in U(n-1)$ such that

$$\mathbf{U} = \begin{pmatrix} e^{i\phi} & 0 \\ 0 & \mathbf{A} \end{pmatrix} \begin{pmatrix} \cos \theta & -\sin \theta & 0 \\ \sin \theta & \cos \theta & 0 \\ 0 & 0 & \mathbf{I}_{n-2} \end{pmatrix} \begin{pmatrix} 1 & 0 \\ 0 & \tilde{\mathbf{B}} \end{pmatrix}.$$

The above expression is exactly the same as in Fig. 2.1 (a), replacing \mathbf{S}_A by \mathbf{A} , \mathbf{S}_B by $\bar{\mathbf{B}}$, \mathbf{S}_1 by $e^{i\phi}$ and two-mode transform $\mathbf{U}_{1,2}$. Applying the decomposition recursively, we finally get a decomposition in Fig. 2.1 (c). ■

We can verify the decomposition by counting the dimension. In the first layer, we have $n-1$ two-mode beam transforms and n phases, leading to $2n-1$ in total. While in the last layer, there is only 1 phase. The dimension is given by $\sum_{k=1}^n 2k-1 = n^2$, which is $\dim U(n)$. With the isomorphism μ in Eq. (2.21), we can obtain the two-mode beam splitter transform in the first standard form $\mathbf{S}\mathbf{\Omega}\mathbf{S}^\top = \mathbf{\Omega}$ as

$$\begin{pmatrix} \cos \theta \mathbf{I}_2 & -\sin \theta \mathbf{I}_2 \\ \sin \theta \mathbf{I}_2 & \cos \theta \mathbf{I}_2 \end{pmatrix}.$$

The symplectic matrix of phase rotation $e^{i\phi}$ is written as

$$\begin{pmatrix} \cos \phi & -\sin \phi \\ \sin \phi & \cos \phi \end{pmatrix}.$$

In the teleportation network, the channel can effectively be reduced to a choice of estimation matrix \mathbf{K} and a local symplectic transform $\bar{\mathbf{S}}_A \in \text{Sp}(2n-2)$. But only first two rows of $\bar{\mathbf{S}}_A$ play a role in the teleportation. Hence, by the above theorem, it is sufficient to consider only the first layer of the decomposition:

$$\bar{\mathbf{S}}_A = \mathbf{S}_1^{(1)} \prod_{i=n}^{i=1} \left[\mathbf{S}_{i-1,i}^{(1)} \mathbf{S}_i^{(1)} \right]. \quad (2.23)$$

The physical intuition behind this approach is that the teleportation process effectively becomes a two-mode quantum teleportation between the first oscillator and the input. For cases where $n \geq 3$, local transforms between oscillators $2, \dots, n-1$ do not influence the teleportation protocol since we discard the oscillators $2, \dots, n-1$ after applying $\bar{\mathbf{S}}_A$ that concentrates the entanglement between the first and n -th oscillator. The symplectic transform involving the $2, \dots, n-1$ oscillators does not affect the measurement outcome or the output state at n -th oscillator as they are eventually discarded.

2.4 Metrics for Evaluating the Teleportation

In the previous sections, we formulated the process of continuous variable quantum teleportation utilizing Gaussian unitary operations and homodyne measurements. The efficacy of the teleportation channel depends on the estimation matrix \mathbf{K} and the entangled oscillators $\hat{\rho}_{AB}$. Since the estimation matrix can be arbitrarily chosen and it also constitutes a form of classical data processing, we can optimize \mathbf{K} . Optimizing the estimation matrix is crucial for enhancing the performance of the quantum teleportation. However, before proceeding with optimization, it is essential to establish a metric to quantify the performance of the teleportation channel. Different metrics will yield different optimal choices for \mathbf{K} .

In this section, we focus on quantum teleportation using a two-mode entangled Gaussian state as teleportation with n oscillators can be reduced to utilizing two oscillators concentrating entanglement. We assume that the two-mode Gaussian state has mean $\mathbf{0}$ and is characterized by its covariance matrix $\boldsymbol{\alpha}$. So the notation

$\Phi(\mathbf{K}, \boldsymbol{\alpha})$ is employed to indicate the teleportation channel that uses the Gaussian state $\boldsymbol{\alpha}$ and the estimation matrix \mathbf{K} . Two key quantifiers are considered: fidelity and quantum capacity. The analytical expression of the quantum capacity for an arbitrary single-mode Gaussian channel is not fully understood to date. However, the estimation matrix \mathbf{K} , being a 2×2 matrix, can be simplified to a diagonal form. Conversely, fidelity can be calculated analytically through integrals with a given input state, although in this case, the estimation matrix \mathbf{K} may not admit simplification.

2.4.1 Fidelity

The Uhlmann fidelity between two states $\hat{\rho}_1$ and $\hat{\rho}_2$ is defined as

$$\mathcal{F}(\hat{\rho}_1, \hat{\rho}_2) = \left(\text{tr} \sqrt{\sqrt{\hat{\rho}_1} \hat{\rho}_2 \sqrt{\hat{\rho}_1}} \right)^2. \quad (2.24)$$

If one of the states is a pure state, the fidelity $\mathcal{F}(\hat{\rho}_1, \hat{\rho}_2) = \text{tr}(\hat{\rho}_1 \hat{\rho}_2)$. For a single-mode Gaussian channel characterized by parameters $(\mathbf{K}, \mathbf{N}, \mathbf{d})$, the fidelity between the input state $\hat{\rho}^{\text{in}}$ and the output state $\hat{\rho}^{\text{out}}$ can be determined from their Wigner functions or their characteristic functions:

$$\begin{aligned} \mathcal{F}(\hat{\rho}^{\text{in}}, \hat{\rho}^{\text{out}}) &= (2\pi) \int_{\mathbb{R}^2} d^2 \mathbf{x} W^{\text{out}}(\mathbf{x}) W^{\text{in}}(\mathbf{x}) \\ &= \frac{1}{(2\pi)^3} \int_{\mathbb{R}^4} d^2 \mathbf{t}_1 d^2 \mathbf{t}_2 \chi_{\hat{\rho}^{\text{in}}}(\mathbf{t}_1) \chi_{\hat{\rho}^{\text{out}}}(\mathbf{t}_2) \int_{\mathbb{R}^2} d^2 \mathbf{x} e^{-i \mathbf{t}_1^\top \mathbf{x}} e^{-i \mathbf{t}_2^\top \mathbf{x}} \\ &= \frac{1}{2\pi} \int_{\mathbb{R}^2} d^2 \mathbf{t}_2 \chi_{\hat{\rho}^{\text{in}}}(-\mathbf{t}_2) \chi_{\hat{\rho}^{\text{out}}}(\mathbf{K}^\top \mathbf{t}_2) e^{i \mathbf{d}^\top \mathbf{t}_2 - \frac{1}{2} \mathbf{t}_2^\top \mathbf{N} \mathbf{t}_2}. \end{aligned} \quad (2.25)$$

If the input state is a mixed state, the fidelity cannot be simplified to $\text{tr}(\hat{\rho}_1 \hat{\rho}_2)$. However, for two Gaussian states, fidelity can be calculated analytically. This is facilitated by leveraging the decomposition outlined in Eq. (1.20) and the expression for a thermal state as specified in Eq. (1.19). These equations provide a framework for analytically deriving the fidelity between Gaussian states, even when dealing with the complexities inherent in mixed states. For two single mode Gaussian states with mean \mathbf{d}_1 and \mathbf{d}_2 and covariance matrix \mathbf{V}_1 and \mathbf{V}_2 , we have

$$\mathcal{F} = \frac{1}{\sqrt{\det[\mathbf{V}_1 + \mathbf{V}_2] + \delta} - \sqrt{\delta}} \exp \left\{ -\frac{1}{2} (\mathbf{d}_1 - \mathbf{d}_2)^\top (\mathbf{V}_1 + \mathbf{V}_2)^{-1} (\mathbf{d}_1 - \mathbf{d}_2) \right\}, \quad (2.26)$$

where $\delta = 4(\det[\mathbf{V}_1] - 1/4)(\det[\mathbf{V}_2] - 1/4)$. If we teleport a Gaussian state with mean \mathbf{d}_1 and variance \mathbf{V} , the output state is a Gaussian state with $\mathbf{d}_2 = \mathbf{K} \mathbf{d}_1$ and $\mathbf{V}_2 = \mathbf{K} \mathbf{V} \mathbf{K}^\top$. Because fidelity decrease exponentially with $\mathbf{d}_2 - \mathbf{d}_1 = \mathbf{K} \mathbf{d}_1 - \mathbf{d}_1$. If we have a prior knowledge of \mathbf{d}_1 , we can apply an additional constant displacement \mathbf{d} in the teleportation so that $\mathbf{K} \mathbf{d}_1 + \mathbf{d} - \mathbf{d}_1 = \mathbf{0}$. Therefore to teleport a Gaussian state with covariance matrix \mathbf{V} , we optimize \mathbf{K} to maximize

$$\mathcal{F} = \frac{1}{\sqrt{\det[\mathbf{V} + \mathbf{K} \mathbf{V} \mathbf{K}^\top + \mathbf{N}] + \delta} - \sqrt{\delta}}, \quad (2.27)$$

where $\delta = 4(\det[\mathbf{V}] - 1/4)(\det[\mathbf{K} \mathbf{V} \mathbf{K}^\top + \mathbf{N}] - 1/4)$. In summary, to maximize the fidelity with pure state as the input, we need to optimize (\mathbf{K}, \mathbf{d}) to maximize

the known expression in Eq. (2.25). If the state is Gaussian and \mathbf{d}_1 is unknown, for example, coherent state, we need to optimize \mathbf{K} to maximize the expression in Eq. (2.26). While if the state is Gaussian and \mathbf{d}_1 is deterministic, for example, squeezed state, we need to optimize \mathbf{K} to maximize the expression in Eq. (2.27).

2.4.2 Capacity

We assume a stable generation of the entanglement source, which leads to a fixed Gaussian state α during the quantum teleportation process. We define the capacity of a teleportation channel $\Phi(\mathbf{K}, \alpha)$ as the maximal rate achieved by optimizing \mathbf{K} . Then, we have the following definitions:

$$C_\chi(\Phi(\alpha)) = \sup_{\mathbf{K}} C_\chi(\Phi(\mathbf{K}, \alpha)), \quad (2.28a)$$

$$C_{ea}(\Phi(\alpha)) = \sup_{\mathbf{K}} C_{ea}(\Phi(\mathbf{K}, \alpha)), \quad (2.28b)$$

$$Q(\Phi(\alpha)) = \sup_{\mathbf{K}} Q(\Phi(\mathbf{K}, \alpha)). \quad (2.28c)$$

Although the exact expression for the quantum capacity of a single-mode Gaussian channel remains unknown, the process of optimization can still be simplified. The simplification is crucial for practical applications in quantum information processing, where optimizing the performance of quantum channels is often necessary even in the absence of a complete theoretical understanding of their capacities. An additional encoding process in a quantum channel can be represented as a transformation of the input state $\hat{\rho}$ to $\hat{U}_E \hat{\rho} \hat{U}_E^\dagger$. Since the capacity is the maximization of all encoded states, the additional encoding process does not change the capacity. On the other hand, the decoding process involves appending a decoding unitary \hat{U}_D to the channel Φ . This can be understood through the following relations:

$$\begin{aligned} H(\hat{U}_D \Phi[\hat{\rho}] \hat{U}_D^\dagger) &= H(\Phi[\hat{\rho}]), \\ \Phi^C &\rightarrow \hat{\mathbf{1}} \otimes \Phi^C, \end{aligned} \quad (2.29)$$

where H denotes the entropy of the state. As a result, the application of a decoding operation \hat{U}_D does not change the capacity of the channel Φ . Therefore classical capacity and quantum capacity in Eq. (1.37), (1.40) and (1.43) do not change with arbitrary additional encoding and decoding. By the equivalence between encoding (decoding) and local symplectic transform on A (B) in the Theorem (20), utilizing an entangled Gaussian state α in a quantum teleportation protocol is equivalent to using the transformed Gaussian state $(\mathbf{S}_A \otimes \mathbf{S}_B) \alpha (\mathbf{S}_A \otimes \mathbf{S}_B)^\top$. This equivalence highlights the flexibility in manipulating Gaussian states for teleportation purposes through symplectic transformations. When α is a 4-by-4 covariance matrix, it can be reduced to the Simon's normal form

$$\alpha(u, v_q, v_p, w) = \begin{pmatrix} u \mathbf{I}_2 & \text{diag}(v_q, -v_p) \\ \text{diag}(v_q, -v_p) & w \mathbf{I}_2 \end{pmatrix}, \quad (2.30)$$

where u , w , v_q and v_p are positive for non-separable Gaussian state.

Lemma 28 $\mathbf{K} = \text{diag}(k_q, k_p)$ maximizes the capacity of the teleportation channel $\Phi(\mathbf{K}, \alpha)$ given α in Eq. (2.30).

Proof. We can show that if $\det[\mathbf{K}]$ is fixed, the teleportation channel with non-diagonal \mathbf{K} has larger noise than with diagonal \mathbf{K} . By singular value decomposition, let

$$\mathbf{K} = \begin{pmatrix} \cos \theta & -\sin \theta \\ \sin \theta & \cos \theta \end{pmatrix} \begin{pmatrix} k_q & 0 \\ 0 & k_p \end{pmatrix} \begin{pmatrix} \cos \phi & -\sin \phi \\ \sin \phi & \cos \phi \end{pmatrix},$$

where $k_q > 0$ and $k_p > 0$ without the loss of generality. From Eq. (2.18), we have

$$\begin{aligned} \det[\mathbf{N}] &= k_q k_p (k_q k_p u^2 + 4v_q v_p) + (k_q^2 + k_p^2)uw + w^2 \\ &\quad - 2[k_q k_p u(k_q v_p + k_p v_q) + (k_p v_p + k_q v_q)w] \cos \theta \cos \phi \\ &\quad + 2[k_q k_p u(k_p v_p + k_q v_q) + (k_q v_p + k_p v_q)w] \sin \theta \sin \phi \\ &= p - p_1 \cos \theta \cos \phi + p_2 \sin \theta \sin \phi, \end{aligned}$$

where p, p_1 and p_2 are positive. The capacity is maximized if the noise is minimized for fixed $k^2 = k_q k_p$. Since if the noise is larger, the channel with larger noise can be obtained by the channel with less noise by concatenating additive Gaussian noise channel. So we impose $\frac{\partial \det[\mathbf{N}]}{\partial \theta} = 0$ and $\frac{\partial \det[\mathbf{N}]}{\partial \phi} = 0$ to get the minimum noise. If $p_1 \neq p_2$, then $\cos \theta \sin \phi = 0$ and $\sin \theta \cos \phi = 0$. The minimum can be obtained when $\theta = 0$ and $\phi = 0$. If $p_1 = p_2$, then we impose $\cos(\theta + \phi) = 1$ to minimize $\det[\mathbf{N}]$. $\theta = \phi = 0$ satisfies the condition and minimize the noise. Thus diagonal \mathbf{K} sufficiently maximizes the capacity of the teleportation channel. ■

Based on our definition, the capacity is the maximized value obtained by optimizing \mathbf{K} . Thus, it is possible to compare the capacities $Q(\Phi(\alpha_1))$ and $Q(\Phi(\alpha_2))$ by directly comparing α_1 and α_2 . The underlying physical intuition is that if α_2 exhibits higher noise levels compared to α_1 , the teleportation channel will consequently introduce more noise as well.

Theorem 29 *If $\alpha_2 = \alpha_1 + \varphi$, where $\varphi \geq 0$. Then*

$$Q(\Phi(\alpha_2)) \leq \min\{Q(\Phi(\alpha_1)), Q(\Phi(\mathbf{T} = \mathbf{I}_2, \mathbf{N} = \tilde{\varphi}\mathbf{I}_2))\},$$

where $\tilde{\varphi} = \inf_{\mathbf{K}} \sqrt{\det[(\mathbf{K}\mathbf{Z}_2, \mathbf{I})\varphi(\mathbf{K}\mathbf{Z}_2, \mathbf{I}_2)^\top]}$.

Proof. If $\alpha_2 = \alpha_1 + \varphi$, then there exists an additive Gaussian noise channel $\Phi(\mathbf{T} = \mathbf{I}_2, \mathbf{N}_2 - \mathbf{N}_1)$ so that $\Phi(\mathbf{K}, \alpha_2) = \Phi(\mathbf{T} = \mathbf{I}_2, \mathbf{N} = \tilde{\varphi}) \circ \Phi(\mathbf{K}, \alpha_1)$. To see this, from Eq. (2.18) we have

$$\mathbf{N}_2 - \mathbf{N}_1 = \mathbf{K}\mathbf{Z}_2\varphi_{11}\mathbf{Z}_2\mathbf{K}^\top - 2\mathbf{K}\mathbf{Z}_2\varphi_{12} + \varphi_{22}.$$

Since $\varphi \geq 0$, then

$$(\mathbf{K}\mathbf{Z}_2 \quad \mathbf{I}_2) \begin{pmatrix} \varphi_{11} & \varphi_{12} \\ \varphi_{12}^\top & \varphi_{22} \end{pmatrix} (\mathbf{K}\mathbf{Z}_2 \quad \mathbf{I}_2)^\top = \mathbf{N}_2 - \mathbf{N}_1 \geq 0.$$

By data processing inequality in Eq. (1.48d)

$$\begin{aligned} Q(\Phi(\alpha_2)) &= \sup_{\mathbf{K}} Q(\Phi(\mathbf{K}, \alpha_2)) = Q(\Phi(\mathbf{K}^*, \alpha_2)) \\ &\leq \min\{Q(\Phi(\mathbf{K}^*, \alpha_1)), Q(\Phi(\mathbf{I}_2, \mathbf{N}_2 - \mathbf{N}_1))\}. \end{aligned}$$

Since $Q(\Phi(\mathbf{K}^*, \alpha_1)) \leq Q(\Phi(\alpha_1))$ and $Q(\Phi(\mathbf{I}_2, \mathbf{N}_2 - \mathbf{N}_1)) \leq Q(\Phi(\mathbf{T} = \mathbf{I}_2, \mathbf{N} = \tilde{\varphi}\mathbf{I}_2))$, where $\tilde{\varphi}$ is the minimum additive noise by some \mathbf{K} . Therefore the inequality holds. ■

Next we discuss the relation between the entanglement and the capacity of the teleportation channel. The intuition is that the larger entanglement the better the teleportation. The entanglement of formation (EoF) quantifies the entanglement of a state. It is the entropy of entanglement of the least entangled pure state $\pi(r)$ needed to prepare it. The EoF for two-mode Gaussian state has analytical expression [21] and has been shown additive when it is symmetric [22].

Definition 30 (Entanglement of Formation) *The EoF of a pure Gaussian state $\pi(r)$ is*

$$E_f(\pi(r)) = g(\sinh r) = \cosh^2 r \log_2 \cosh^2 r - \sinh^2 r \log_2 \sinh^2 r. \quad (2.31)$$

The EoF of a two-mode Gaussian state α is

$$E_f(\alpha) = \inf_{\pi(r)} \{E_f(\pi(r)) | \alpha = \pi(r) + \varphi\}, \quad (2.32)$$

where φ is a classical Gaussian state. A Gaussian state is classical if $\varphi > \pi(0)$.

Corollary 31 *Among all the Gaussian state with the same EoF, the quantum teleportation with pure state has the largest quantum capacity.*

Proof. From the definition of the EoF, $\alpha \geq \pi(r)$ where $\pi(r)$ is the decomposition in Eq. (2.32). By theorem (29), $Q(\alpha) \leq Q(\pi(r))$. ■

For nonzero quantum capacity of a teleportation channel $\Phi(\mathbf{K}, \alpha)$, it is necessary that the entangled state α has some entanglement characterized by $\pi(r)$ and finite amount of noise $\tilde{\varphi}$ according to the decomposition $\alpha = \pi(r) + \varphi$. Since the Theorem 29 does not require φ to be classical. So it is easier to find φ in the Theorem 29 than the decomposition in Eq. (2.32). Before proceeding, it can be shown that the additive noise $\tilde{\varphi} < 1$ for non-zero quantum capacity. If $\tilde{\varphi} \geq 1$, the additive Gaussian noise channel is entanglement-breaking.

Lemma 32 *Quantum teleportation channel with separable state is entanglement breaking.*

Lemma 33 *The channel $\Phi(\mathbf{T} = k\mathbf{I}_2, \mathbf{N} = N\mathbf{I}_2)$ is entanglement-breaking if $N > (k^2 + 1)/2$.*

Proof. Consider the quantum teleportation channel with $\mathbf{K} = k\mathbf{I}_2$ and Gaussian state $\pi(r)$. The channel is Gaussian channel with $N = \frac{1}{2}(k^2 \cosh r - 2k \sinh r + \cosh r)$. It is entanglement-breaking when $r \rightarrow 0$. When $N > (k^2 + 1)/2$, the channel can be stimulated by quantum teleportation with separable state concatenated by additive noise channel with noise $N - (k^2 + 1)/2$. By Lemma 32, and that concatenating entanglement breaking channel with any channel is entanglement breaking, we conclude that the channel $\Phi(\mathbf{T} = k\mathbf{I}_2, \mathbf{N} = N\mathbf{I}_2)$ is entanglement-breaking if $N > (k^2 + 1)/2$. ■

Taking $k = 1$ in the above Lemma, we see that the additive Gaussian noise channel is entanglement-breaking if $\tilde{\varphi} \geq 1$.

Let's consider the teleportation channel $\Phi(\mathbf{K} = \mathbf{I}_2, \pi(r))$. The transmissivity $\eta = 1$. We observe that the channel $\Phi(\mathbf{K} = \mathbf{I}_2, \pi(r))$ has additive noise $N = e^{-r}$. In the limit as r approaches infinity, the additive noise decreases exponentially, and the

channel approaches an identical channel asymptotically. Thus, the channel has infinite quantum capacity when $r \rightarrow \infty$. If there is a mismatch between \mathbf{K} and \mathbf{I}_2 , the additive noise increases exponentially. In fact using the data processing inequality we can show that

Lemma 34 *The capacity of the teleportation channel $\Phi(\mathbf{K}, \boldsymbol{\pi}(r))$ is maximized when $\mathbf{K} = k\mathbf{I}_2$ and $2 \tanh(r/2) - 1 \leq k \leq 2 \coth(r/2) - 1$.*

Proof. First of all, the diagonal \mathbf{K} will maximize the capacity from the Lemma 28. Moreover, since $v_q = v_p$ for the state $\boldsymbol{\pi}(r)$, $\mathbf{K} = k\mathbf{I}_2$ by symmetry. If we take $\mathbf{T}_1 = \mathbf{I}_2$, $N_1 = e^{-r}$, $\mathbf{T}_2 = k\mathbf{I}_2$ and $N_2 = \frac{1}{2}[(1 + k^2) \cosh r - 2k \sinh r]$ in the Corollary 14, then $Q(\Phi_2) \leq Q(\Phi_1)$ if

$$\frac{1}{2}[(1 + k^2) \cosh r - 2k \sinh r] - e^{-r} - \frac{1}{2}|k^2 - 1| \geq 0.$$

When $k \geq 1$, the inequality holds when $k \geq 2 \coth(r/2) - 1$. And when $k < 1$, the inequality holds when $k \leq 2 \tanh(r/2) - 1$. Thus when the above inequality holds, $Q(\Phi(k\mathbf{I}_2, \boldsymbol{\pi}(r))) \leq Q(\Phi(\mathbf{I}_2, \boldsymbol{\pi}(r)))$. And we should take $k = 1$. When $2 \tanh(r/2) - 1 \leq k \leq 2 \coth(r/2) - 1$, it is possible that some k in this range has larger capacity than $k = 1$. So the capacity of the channel is maximized in the range. ■

As the parameter r tends to infinity, $2 \tanh(r/2) - 1$ asymptotically approaches to $1 - \epsilon$ and $2 \coth(r/2) - 1$ asymptotically approaches $1 + \epsilon$. This observation has significant implications in the realm of quantum teleportation with pure Gaussian states. Specifically, as the entanglement in a pure Gaussian state increases (indicated by increasing r), the optimal value of the parameter k , converges towards 1. This behavior reflects the relationship between the strength of entanglement in Gaussian states and the optimal settings for certain parameters in quantum teleportation protocols.

In the rest of the dissertation, the source generates the entangled Gaussian state with the covariance matrix as in the block form:

$$\boldsymbol{\alpha} = \frac{1}{2} \begin{pmatrix} u_q & 0 & v_q & 0 \\ 0 & u_p & 0 & -v_p \\ v_q & 0 & w_q & 0 \\ 0 & -v_p & 0 & w_p \end{pmatrix},$$

Therefore we take $\mathbf{K} = \text{diag}(k_q, k_p)$ when evaluating the performance of the teleportation channel. The noise matrix \mathbf{N} of the teleportation channel is given by

$$\mathbf{N} = \frac{1}{2} \text{diag}(u_q k_q^2 - 2v_q k_q + w_q, u_p k_p^2 - 2v_p k_p + w_p).$$

Chapter 3

Microwave-optical Transduction

Quantum networks are envisaged as high-performance quantum processors interconnected by efficient quantum communication channels. These quantum processors necessitate strong nonlinear interactions at the single-quanta level, which can be effectively achieved using the Josephson effect at microwave frequencies in superconducting circuits. However, the challenges of high attenuation and thermal noise at room temperature hinder the direct transmission of quantum states at microwave frequencies over long distances.

In contrast, optical photons are ideal candidates for long-distance quantum information transmission, owing to their low loss and ability to maintain quantum coherence at room temperature. Nonetheless, the weak optical nonlinearity means that quantum information processing is hard in optical frequency. To bridge the gap between microwave-based information processors and optical quantum communication links, quantum transduction is essential for inter-converting quantum states between different frequency domains.

In this chapter, the physical phenomena behind microwave and optical interactions is introduced, following the approach of Tsang [23, 24]. This examination lays the groundwork to generalize the interaction and introduces two potential approaches for quantum transduction: the direct conversion approach and the teleportation-based approach. Subsequently, I delve into the recent experimental parameters feasible for these models and provide a comparative analysis of their advantages and disadvantages.

3.1 Cavity Electro-optics

When light travels through a dense medium, its field undergoes scattering and re-scattering by the medium's atoms. This interaction alters the speed of light c , which is modified by the refractive index n of the medium. The electro-optic effect refers to the modulation of the refractive index in response to an applied electric field. If this change in refractive index is linearly proportional to the applied field, it is called the Pockels effect. Conversely, if the change is proportional to the square of the field, it is known as the Kerr effect. Thus, one can modulate light by applying a microwave field via the electro-optic effect. Conversely, the inverse process of the electro-optic effect, known as electro-optic rectification, is a nonlinear optical process where a strong pump light at frequency ω_p , a signal light at frequency ω_s , and the certain polarization of a microwave field are coupled as $P^{\text{NL}}(\omega = \omega_p \pm \omega_s, \omega_p, \omega_s)$.

Consequently, modulated optical fields can generate microwave fields in reverse.

To effectively implement a transducer utilizing these effects, factors such as the strength of the nonlinearity, mode coupling, optical loss, etc., must be considered. The popular materials are LiNbO₃ and KTP. In the subsequent analysis, the relationship between microwave and optical fields is explored without specifying the materials.

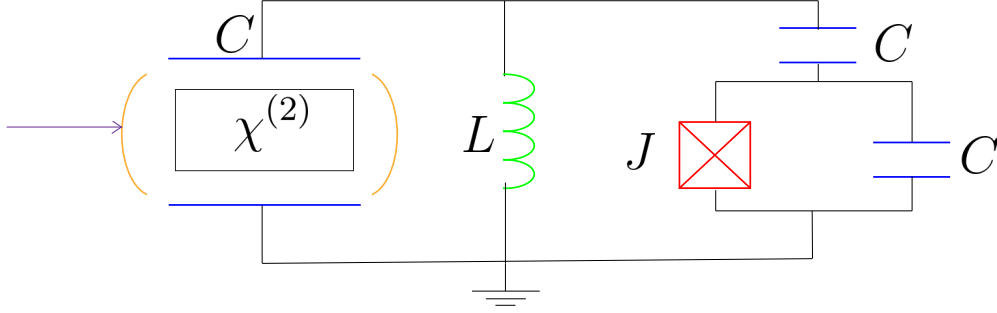


Figure 3.1: Electro-optic transduction system. C: capacitor, L: inductor, J: josephson junction. Microwave mode (LC circuit) is coupled to optical mode by optical cavity as shown on the left. And microwave quantum state is controlled by superconducting qubit (JC) as shown on the right.

As depicted in Fig. 3.1, the optical cavity is composed of materials possessing $\chi^{(2)}$ nonlinearity, such as lithium niobate or an electro-optic polymer. This cavity is situated between the capacitors of an LC microwave resonator. The modulation in this system utilizes the transverse electro-optic effect, with the microwave field applied perpendicularly to the light propagation vector. Additionally, the cavity can be configured as an on-chip ring cavity on chip that supports whispering-gallery modes.

The voltage V across the capacitor induces a phase shift ϕ in the resonating optical mode \hat{a} within the cavity during a single round trip time τ . This interaction is described by the following interaction Hamiltonian:

$$\hat{H}_I = -\frac{\hbar}{\tau} \hat{\phi} \hat{a}^\dagger \hat{a}. \quad (3.1)$$

The phase shift is proportional to the voltage V and it can be quantized as the position in the Lagrangian of the harmonic oscillator \hat{m} at frequency ω_m .

$$\begin{aligned} \phi &= \frac{\omega_a n^3 r l}{c d} V, \\ \hat{V} &= \left(\frac{\hbar \omega_m}{2C} \right)^{\frac{1}{2}} (\hat{m} + \hat{m}^\dagger), \end{aligned}$$

where r is the coefficient of the electro-optic effect, l is the length of the medium, c is the speed of light d is the thickness and C is capacitance of the microwave resonator. Thus the total Hamiltonian is

$$\hat{H} = \hbar \omega_a \hat{a}^\dagger \hat{a} + \hbar \omega_m \hat{m}^\dagger \hat{m} - \hbar g_{eo} (\hat{m}^\dagger + \hat{m}) (\hat{a}^\dagger \hat{a}),$$

where $g_{eo} = \frac{\omega_a n^3 r l}{\tau c d} \left(\frac{\hbar \omega_m}{2C} \right)^{\frac{1}{2}}$ is the electro-optic coupling constant. The optical cavity is specifically designed to have a free spectral range, denoted as $\Delta\omega$, that is closely

matched to the microwave frequency ω_m . This design allows for the generation of optical modes at frequencies $\omega_a \pm \omega_m$ within the cavity when it is pumped by an optical mode \hat{a} at frequency ω_a . The output optical mode \hat{a}_1 , with frequency $\omega_{o1} = \omega_a - \omega_m$, represents a down-conversion, while the optical mode \hat{a}_2 , at frequency $\omega_{o2} = \omega_a + \omega_m$, signifies an up-conversion. We can focus on these three optical modes as the higher-order modes experience greater loss than these modes. Various techniques can be employed to achieve this, such as ensuring that $|\Delta\omega - \omega_m|$ is larger than the linewidth of the output optical modes, introducing splitting in the ring cavity, and so on.

Including these three optical modes in the analysis, we can represent the system with the following Hamiltonian:

$$\begin{aligned}\hat{H} &= \hat{H}_0 - \hbar g_{eo}(\hat{m}^\dagger + \hat{m})(\hat{a} + \hat{a}_1 + \hat{a}_2)^\dagger(\hat{a} + \hat{a}_1 + \hat{a}_2), \\ \hat{H}_0 &= \hbar\omega_a\hat{a}^\dagger\hat{a} + \hbar\omega_{o1}\hat{a}_1^\dagger\hat{a}_1 + \hbar\omega_{o2}\hat{a}_2^\dagger\hat{a}_2 + \hbar\omega_m\hat{m}^\dagger\hat{m}.\end{aligned}$$

It is often convenient to work within the rotating frame to simplify the analysis of quantum systems. By employing the interaction picture, we can transform the operators using a time-dependent rotation. Specifically, we can rewrite the operators \hat{a} , \hat{a}_1 , \hat{a}_2 , and \hat{m} as follows:

$$e^{i\hat{H}_0 t/\hbar}\{\hat{a}, \hat{a}_1, \hat{a}_2, \hat{m}\}e^{-i\hat{H}_0 t/\hbar} = \{\hat{a}e^{-i\omega_a t}, \hat{a}_1e^{-i\omega_{o1} t}, \hat{a}_2e^{-i\omega_{o2} t}, \hat{m}e^{-i\omega_m t}\}, \quad (3.2)$$

where \hat{H}_0 is the Hamiltonian describing the free evolution of the system, and ω_a , ω_{o1} , ω_{o2} , and ω_m are the respective frequencies of the optical and microwave modes. This transformation effectively shifts the reference frame to the rotating frame. Discarding the fast rotating terms, the Hamiltonian with $\omega_a - \omega_{o1} - \omega_m = 0$ and $\omega_{o2} - \omega_a - \omega_m = 0$ remains. Then we have

$$\hat{H} = \hat{H}_0 - \hbar g_{eo}(\hat{a}^\dagger\hat{a}_1\hat{m} + \hat{a}\hat{a}_2^\dagger\hat{m} + \text{h.c.}).$$

The pump \hat{a} is strong thus can be treated classically as coherent state. Then $\hat{a} = \sqrt{N_p}e^{-i\omega_a t}$, where N_p is the number of mean photon number of the pump. Let $g_1 = g_{eo}\sqrt{N_p}$ and $g_2 = g_{eo}\sqrt{N_p}$ be the coupling coefficient of optical mode \hat{a}_1 and \hat{a}_2 , which can be different in general. The Hamiltonian is then

$$\hat{H} = \hat{H}_0 + \hbar g_1(\hat{a}_1^\dagger\hat{m}^\dagger + \hat{a}_1\hat{m}) + \hbar g_2(\hat{a}_2^\dagger\hat{m} + \hat{a}_2\hat{m}^\dagger), \quad (3.3)$$

$$\hat{H}_0 = \hbar\omega_{o1}\hat{a}_1^\dagger\hat{a}_1 + \hbar\omega_{o2}\hat{a}_2^\dagger\hat{a}_2 + \hbar\omega_m\hat{m}^\dagger\hat{m}. \quad (3.4)$$

where \hat{m} is replaced by $\hat{m}e^{i\pi} = -\hat{m}$ to get positive interaction term and the pump is absorbed into $g_{1/2}$ as a constant.

The interaction Hamiltonian can be divided into two parts based on the nature of the conversion processes. The first part corresponds to down-conversion, where a pump photon generates a pair of entangled optical and microwave photons. This process is significant for creating entanglement between different frequency domains. The second part of the Hamiltonian relates to up-conversion, wherein a pump photon and a microwave photon combine to form an optical photon. This up-conversion process is essential in transferring information from the microwave to the optical regime.

The Hamiltonian, including the effects of electro-optic rectification, can be similarly derived and is essentially the same as in Eq. (3.3). This similarity arises because

electro-optic rectification is the inverse process of the electro-optic effect. However, it is important to note that a nonlinearity characterized by $\chi^{(2)}$ is required in the coupling coefficients g_1 and g_2 , which are critical in these conversion processes.

3.2 Direct Conversion Channel

In the electro-optical quantum transduction, it is possible to selectively suppress either up-conversion or down-conversion by introducing high loss, as discussed in [25, 26, 27]. In the direct conversion scheme, the g_2 is suppressed. Referring to Eq. (3.3), the Hamiltonian for this process can be expressed as:

$$\hat{H} = \hbar\omega_o\hat{a}^\dagger\hat{a} + \hbar\omega_m\hat{m}^\dagger\hat{m} + \hbar g(\hat{a}\hat{m}^\dagger + \hat{a}^\dagger\hat{m}). \quad (3.5)$$

The operators in quantum mechanics are time-dependent. In the Heisenberg picture, the state of the system remains constant, the operators evolve with time. The time evolution of an operator \hat{O} can be expressed as:

$$\hat{O}(t) = e^{\hat{H}t/(-i\hbar)}\hat{O}(0)e^{\hat{H}t/(i\hbar)}, \quad (3.6)$$

$$\frac{d\hat{O}}{dt} = \frac{i}{\hbar}[\hat{H}, \hat{O}]. \quad (3.7)$$

Applying this to the operator \hat{a} , we obtain:

$$\frac{d\hat{a}}{dt} = \frac{i}{\hbar}[\hat{H}, \hat{a}] \quad (3.8)$$

$$= -i\omega_o\hat{a} - ig\hat{m}. \quad (3.9)$$

For the analysis of steady-state dynamics over a long period, it is beneficial to transform to the frequency domain, representing $\hat{a}(t)$ as $\hat{a}(\omega)$. The dynamics in the frequency domain are then given by:

$$\frac{d\hat{a}}{dt} = -i\Delta_o\hat{a} - ig\hat{m}, \quad (3.10)$$

where $\Delta_o = \omega_o - \omega_a$ represents the optical detuning, which is the frequency difference between the signal ω_a and its eigenmode in the optical cavity ω_o , as illustrated in Fig. 3.2 (b).

However, as the system under consideration is open, Eq. (3.10) does not account for the coupling of the system with the input field and background noise. To address this, the input-output relation is derived to describe the dynamics of the quantum system interacting with thermal reservoirs, as per the principles of quantum stochastic theory [28, 29]. The relation between the input field \hat{a}_{in} and the output field \hat{a}_{out} is given by:

$$\frac{d\hat{a}}{dt} = i\Delta_o\hat{a} - ig\hat{m} - \frac{\gamma_o}{2}\hat{a} + \sqrt{\gamma_{oc}}\hat{a}_{\text{in}} + \sqrt{\gamma_{oi}}\hat{a}^{(i)}, \quad (3.11)$$

$$\hat{a}_{\text{out}} = -\sqrt{\gamma_{oc}}\hat{a} + \hat{a}_{\text{in}}, \quad (3.12)$$

where γ_{oc} is the rate of the conduction band, γ_{oi} is the rate of intrinsic noise $\hat{a}^{(i)}$, and $\gamma_o = \gamma_{oc} + \gamma_{oi}$. The input and output relation, illustrating the interaction of the

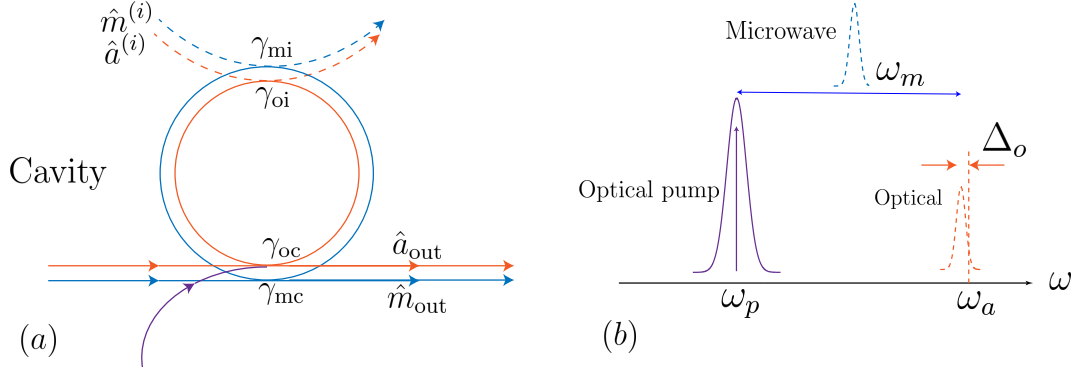


Figure 3.2: Direct conversion scheme. (a) Input-output relation of a ring cavity. (b) Spectrum of the direct conversion scheme.

quantum system with its environment, is depicted in Fig. 3.2 (a). The spectrum of the direct conversion scheme is shown in Fig. 3.2 (b).

We can obtain equation of $d\hat{m}/dt$ in the same way. The set of equations are called quantum Langevin equations in the Fourier domain.

$$0 = \frac{d\hat{\mathbf{a}}}{dt} = \mathbf{G}\hat{\mathbf{a}} + \mathbf{K}\hat{\mathbf{a}}_{in}, \quad (3.13)$$

$$\hat{\mathbf{a}}_{out} = -\mathbf{K}^T\hat{\mathbf{a}} + \hat{\mathbf{a}}_{in}, \quad (3.14)$$

where $\frac{d\hat{\mathbf{a}}}{dt} = 0$ is imposed for steady-state solution. Here we use the matrix form to represent the dynamics in the Fourier domain with optical frequency detuning Δ_o and microwave frequency detuning Δ_m . The notations are defined as the following

$$\begin{aligned} \hat{\mathbf{a}} &= (\hat{a}, \hat{a}^\dagger, \hat{m}, \hat{m}^\dagger)^T, \\ \hat{\mathbf{a}}_{in} &= (\hat{a}_{in}, \hat{a}_{in}^\dagger, \hat{a}^{(i)}, \hat{a}^{\dagger(i)}, \hat{m}_{in}, \hat{m}_{in}^\dagger, \hat{m}^{(i)}, \hat{m}^{\dagger(i)})^T, \\ \mathbf{G} &= \begin{pmatrix} -\frac{\gamma_o}{2} + i\Delta_o & 0 & -ig & 0 \\ 0 & -\frac{\gamma_o}{2} - i\Delta_o & 0 & ig \\ -ig & 0 & -\frac{\gamma_m}{2} + i\Delta_m & 0 \\ 0 & ig & 0 & -\frac{\gamma_m}{2} - i\Delta_m \end{pmatrix}, \\ \mathbf{K} &= \begin{pmatrix} \sqrt{\gamma_{oc}} & 0 & \sqrt{\gamma_{oi}} & 0 & 0 & 0 & 0 & 0 \\ 0 & \sqrt{\gamma_{oc}} & 0 & \sqrt{\gamma_{oi}} & 0 & 0 & 0 & 0 \\ 0 & 0 & 0 & 0 & \sqrt{\gamma_{mc}} & 0 & \sqrt{\gamma_{mi}} & 0 \\ 0 & 0 & 0 & 0 & 0 & \sqrt{\gamma_{mc}} & 0 & \sqrt{\gamma_{mi}} \end{pmatrix}. \end{aligned}$$

The output fields then relate to the input fields by

$$\hat{\mathbf{a}}_{out} = \mathbf{S}_a \hat{\mathbf{a}}_{in} = (\mathbf{K}^T \mathbf{G}^{-1} \mathbf{K} + \mathbf{I}_8) \hat{\mathbf{a}}_{in}.$$

By defining quadrature observables and the transform matrix as

$$\begin{aligned} \begin{pmatrix} \hat{q}^a \\ \hat{p}^a \end{pmatrix} &= \frac{1}{\sqrt{2}} \begin{pmatrix} 1 & 1 \\ -i & i \end{pmatrix} \begin{pmatrix} \hat{\mathbf{a}} \\ \hat{\mathbf{a}}^\dagger \end{pmatrix}, \\ \mathbf{Q} &= \mathbf{I}_4 \otimes \frac{1}{\sqrt{2}} \begin{pmatrix} 1 & 1 \\ -i & i \end{pmatrix}, \end{aligned}$$

we get the input-output quadrature relation

$$\begin{aligned}\hat{\mathbf{x}}_{\text{out}} &= \mathbf{S}_x \hat{\mathbf{x}}_{\text{in}} = \mathbf{Q} \mathbf{S}_a \mathbf{Q}^{-1} \hat{\mathbf{x}}_{\text{in}}, \\ \hat{\mathbf{x}}_{\text{in}} &= (\hat{q}_{\text{in}}^o, \hat{p}_{\text{in}}^o, \hat{q}^{o,(i)}, \hat{p}^{o,(i)}, \hat{q}_{\text{in}}^m, \hat{p}_{\text{in}}^m, \hat{q}^{m,(i)}, \hat{p}^{m,(i)})^T.\end{aligned}\quad (3.15)$$

As we have seen from above relation, the output is a linear combination of the input. Therefore the channel is Gaussian. In most scenario and for simplicity, it is assumed that $\Delta_o = \Delta_m = 0$, $\hat{a}^{(i)}$ is in the vacuum state $\hat{\rho}_{th}(\bar{n} = 0)$ and $\hat{m}^{(i)}$ is in thermal state $\hat{\rho}_{th}(\bar{n} = n_{\text{in}})$. In the scenario of microwave-to-optical transduction, we can deduce the parameters that characterize the channel as follows. The transmission matrix \mathbf{T} is obtained by selecting the rows 1, 2 and the columns 5, 6 of the symplectic matrix \mathbf{S}_x as specified in Eq. (3.15). The noise matrix \mathbf{N} is given by:

$$\mathbf{N} = \mathbf{T}_D \text{diag}(1/2, 1/2, 1/2 + n_{\text{in}}, 1/2 + n_{\text{in}}) \mathbf{T}_D^T, \quad (3.16)$$

where \mathbf{T}_D is derived by taking the rows 1, 2 and the columns 3, 4, 5, 6 of \mathbf{S}_x . The direct conversion channel is a single-mode Gaussian channel, and according to Eq. (1.31) and Eq. (1.32), we obtain [23]:

$$\eta_{\text{DC}} = \zeta_m \zeta_o \frac{4C}{(1+C)^2}, \quad (3.17)$$

$$\bar{n}_{\text{DC}} = \frac{1}{1 - \eta_{\text{DC}}} (1 - \zeta_m) \zeta_o \frac{4C}{(1+C)^2} n_{\text{in}}, \quad (3.18)$$

where $\zeta_m = \gamma_{mc}/\gamma_m$ and $\zeta_o = \gamma_{oc}/\gamma_o$ are the extraction coefficients, and $C_g = 4g^2/(\gamma_o\gamma_m)$ represents the cooperativity. Similar calculations reveal that the optical to microwave transduction yields the same transmissivity and noise as the microwave to optical transduction.

3.3 Teleportation Channel

In the teleportation-based transduction scheme, an optical pump photon generates an entangled pair consisting of an optical photon at a lower frequency and a microwave photon. Following the generation of entanglement, quantum teleportation is performed to convert the input state in microwave frequency to an output state in optical frequency, and vice versa. As depicted in Fig. 3.3, the entanglement between optical and microwave fields can be generated through a spontaneous parametric down-conversion (SPDC) process by pumping a triple-resonance device [26].

This electro-optical system, characterized by a coupling strength g , is modeled by the following total Hamiltonian:

$$\hat{H} = \hbar\omega_o \hat{a}^\dagger \hat{a} + \hbar\omega_m \hat{m}^\dagger \hat{m} + \hbar g (\hat{a}^\dagger \hat{m}^\dagger + \hat{a} \hat{m}), \quad (3.19)$$

where \hat{a} and \hat{m} are the annihilation operators for the optical and microwave fields, respectively, with resonances at frequencies ω_o and ω_m . The parameters such as intra-cavity pump power and the phase-matching condition have been incorporated into the coupling strength g .

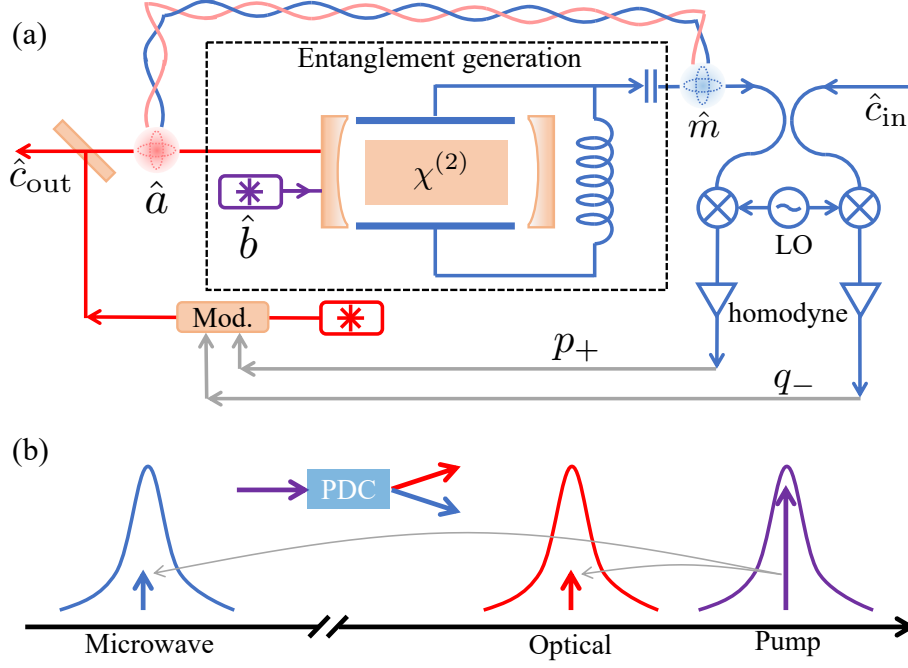


Figure 3.3: (a) Schematic of the teleportation based transduction scheme. The dashed box indicates the entanglement generation between the microwave mode \hat{m} and the optical mode \hat{a} , in a three-wave mixing described by Hamiltonian in Eq. (3.19) jointly with optical pump mode \hat{b} . (b) Entanglement generation between microwave and optical domains. Purple indicates the optical pump, blue indicates the microwave modes and red indicates optical modes. LO: local oscillator. Mod.: modulator. PDC: parametric down conversion.

The output fields can be derived by solving a group of Heisenberg-Langevin equations in the Fourier domain with the input-output relations in the same way as in the direct conversion.

$$0 = \mathbf{G}\hat{\mathbf{a}} + \mathbf{K}\hat{\mathbf{a}}_{in},$$

$$\hat{\mathbf{a}}_{out} = -\mathbf{K}^T\hat{\mathbf{a}} + \hat{\mathbf{a}}_{in}.$$

Here the notations are defined as the following

$$\hat{\mathbf{a}} = (\hat{a}, \hat{a}^\dagger, \hat{m}, \hat{m}^\dagger)^T,$$

$$\hat{\mathbf{a}}_{in} = (\hat{a}_{in}, \hat{a}_{in}^\dagger, \hat{a}^{(i)}, \hat{a}^{\dagger(i)}, \hat{m}_{in}, \hat{m}_{in}^\dagger, \hat{m}^{(i)}, \hat{m}^{\dagger(i)})^T,$$

$$\mathbf{G} = \begin{pmatrix} -\frac{\gamma_o}{2} + i\Delta_o & 0 & 0 & -ig \\ 0 & -\frac{\gamma_o}{2} - i\Delta_o & ig & 0 \\ 0 & -ig & -\frac{\gamma_m}{2} + i\Delta_m & 0 \\ ig & 0 & 0 & -\frac{\gamma_m}{2} - i\Delta_m \end{pmatrix},$$

$$\mathbf{K} = \begin{pmatrix} \sqrt{\gamma_{oc}} & 0 & \sqrt{\gamma_{oi}} & 0 & 0 & 0 & 0 & 0 \\ 0 & \sqrt{\gamma_{oc}} & 0 & \sqrt{\gamma_{oi}} & 0 & 0 & 0 & 0 \\ 0 & 0 & 0 & 0 & \sqrt{\gamma_{mc}} & 0 & \sqrt{\gamma_{mi}} & 0 \\ 0 & 0 & 0 & 0 & 0 & \sqrt{\gamma_{mc}} & 0 & \sqrt{\gamma_{mi}} \end{pmatrix}.$$

The relationship between the output and input fields in the quantum system can be

expressed as follows:

$$\mathbf{a}_{\text{out}} = \mathbf{S}_a \mathbf{a}_{\text{in}} = (\mathbf{K}^T \mathbf{G}^{-1} \mathbf{K} + \mathbf{I}_8) \mathbf{a}_{\text{in}}, \quad (3.20)$$

$$\hat{\mathbf{x}}_{\text{out}} = \mathbf{S}_x \hat{\mathbf{x}}_{\text{in}} = \mathbf{Q} \mathbf{S}_a \mathbf{Q}^{-1} \hat{\mathbf{x}}_{\text{in}}, \quad (3.21)$$

$$\hat{\mathbf{x}}_{\text{in}} = (\hat{q}_{\text{in}}^p, \hat{p}_{\text{in}}^p, \hat{q}^{p,(i)}, \hat{p}^{p,(i)}, \hat{q}_{\text{in}}^e, \hat{p}_{\text{in}}^e, \hat{q}^{e,(i)}, \hat{p}^{e,(i)})^T. \quad (3.22)$$

These equations describe how the output field operators are related to the input field operators. Subsequently, the input-output relation for the covariance matrix can be derived as:

$$\mathbf{V}_{\text{out}} = \mathbf{S}_x \mathbf{V}_{\text{in}} \mathbf{S}_x^T, \quad (3.23)$$

where \mathbf{V}_{in} is the input covariance matrix. This matrix encompasses vacuum noise from the optical modes and the input microwave mode, while the dissipation microwave mode is contaminated by thermal noise with a population n_{in} ,

$$\mathbf{V}_{\text{in}} = \text{Diag}(\mathbf{I}_6, (n_{\text{in}} + 1/2)\mathbf{I}_2).$$

Taking the input covariance matrix into consideration and assuming zero detune for both optical and microwave modes $\Delta_p = \Delta_e = 0$, the covariance matrix of two output fields finally shows in the form as [30]

$$\mathbf{V}_{\text{o,m}} = \frac{1}{2} \begin{pmatrix} w & 0 & v & 0 \\ 0 & w & 0 & -v \\ v & 0 & u & 0 \\ 0 & -v & 0 & u \end{pmatrix}, \quad (3.24)$$

where the parameters in Eq. (3.24) are as follows,

$$u = 1 + \frac{8\zeta_m[C + n_{\text{in}}(1 - \zeta_m)]}{(1 - C)^2}, \quad (3.25a)$$

$$v = \frac{4\sqrt{\zeta_o\zeta_m C}[1 + C + 2n_{\text{in}}(1 - \zeta_m)]}{(1 - C)^2}, \quad (3.25b)$$

$$w = 1 + \frac{8C\zeta_o[1 + n_{\text{in}}(1 - \zeta_m)]}{(1 - C)^2}. \quad (3.25c)$$

Here, we consider teleportation utilizing the entangled state $\hat{\rho}_{AB}$ between the microwave domain (A) and the optical domain (B), as depicted in Fig. 3.4. As previously established in the Theorem 23 and Corollary 24, this scheme is distinguished from general quantum teleportation only by a local operation on domain A. Additionally, based on Lemma 28 and the symmetry of the operators \hat{q} and \hat{p} , a scaling matrix $\mathbf{K} = \kappa \mathbf{I}_2$ is found to maximize the quantum capacity of the teleportation channel.

The model of the teleportation channel can now be derived from the equations provided in the Corollary 24. This model will account for the specificities of the microwave-optical entanglement and the optimized teleportation parameters, thereby providing a comprehensive understanding of the teleportation process in this context.

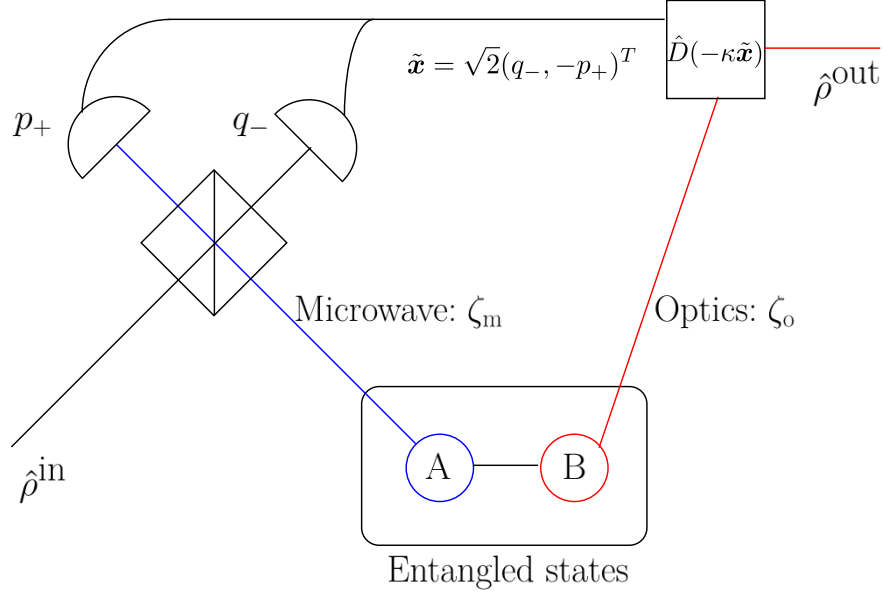


Figure 3.4: Schematic of the continuous-variable teleportation.

If $\kappa < 1$, the continuous-variable teleportation channel reduces to a thermal-attenuator channel $\mathcal{L}_{\eta, \bar{n}}$ with:

$$\eta = \kappa^2, \quad (3.26)$$

$$1 + 2\bar{n} = \frac{u\kappa^2 - 2v\kappa + w}{1 - \kappa^2}. \quad (3.27)$$

On the other hand when $\kappa > 1$, the continuous-variable teleportation channel can be modeled as a thermal-amplifier $\mathcal{A}_{G, \bar{n}}$ with:

$$G = \kappa^2, \quad (3.28)$$

$$1 + 2\bar{n} = \frac{u\kappa^2 - 2v\kappa + w}{\kappa^2 - 1}. \quad (3.29)$$

When $\kappa = 1$, it is an additive Gaussian noise channel with the noise variance $\frac{1}{2}(u\kappa^2 - 2v\kappa + w)$. The channel is shown in Fig. 3.5.

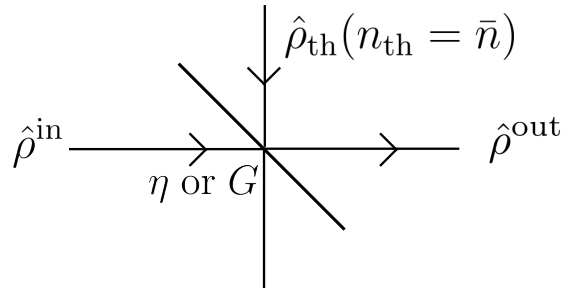


Figure 3.5: Schematic of an thermal-attenuator/amplifier channel. The thermal state $\hat{\rho}_{th}$ has mean photon number \bar{n} . η is the attenuator transmissivity and G is the amplifier gain.

3.4 Comparison between Direct Conversion and Teleportation Channel

The coherent transduction between microwave and optical frequencies plays a crucial role in connecting superconducting quantum processors over long distances. Although achieving such a quantum interface with high efficiency and minimal added noise is a challenge in the standard direct conversion scheme, the teleportation-based quantum transduction offers a promising alternative. This alternative scheme allows for reliable quantum information transmission even with small cooperativity, contrasting with the direct conversion scheme which necessitates a significantly higher minimum cooperativity.

This section demonstrates that the teleportation-based scheme consistently offers a substantial rate advantage, especially under practical conditions of thermal noise and low cooperativity. Additionally, the performance of this scheme in transducing complex quantum states, such as cat states and GKP states, is explored. It is found that higher fidelity can be achieved using the teleportation-based approach. By reducing device requirements, the teleportation scheme makes quantum transduction between microwave and optical frequencies a more feasible prospect in the near future.

3.4.1 Additive Noise Analysis

The direct conversion channel and the teleportation channel exhibit distinct transmissivity and noise characteristics under the same experimental conditions, denoted by ζ_s , C , and n_{in} . By employing the channel concatenation relations presented in Eq. (1.27a) and Eq. (1.27b), we can transform these transduction channels into additive Gaussian noise channels, thereby facilitating a comparison of their additive noise levels.

In the direct conversion scheme, we introduce a quantum-limited amplifier with a gain of $1/\eta_{\text{DC}}$ prior to the transduction process. On the other hand, for the teleportation-based scheme, we apply a quantum-limited amplifier with a gain of $1/\kappa$ before transduction when $\kappa < 1$. In cases where $\kappa > 1$, an attenuator with a transmissivity of $1/\kappa$ is used in post-processing. This approach effectively converts the transduction process into an additive Gaussian noise channel. It is important to note that the resultant additive noise level is not identical to the original noise levels N_{DT} or N_{TP} .

Specifically, in the direct conversion (DC) case, considering the transmissivity as outlined in Eq. (3.17) and the noise as described in Eq. (3.18), we can pre-amplify the signal before transduction to determine the additive noise variance:

$$\sigma_{\text{DC}}^2 = 1 + \frac{4C[n_{\text{in}}(1 - \zeta_m) - \zeta_m]\zeta_o}{(1 + C)^2}.$$

For the teleportation-based transduction approach, we need to consider different values of κ to obtain the minimum additive noise. When $\kappa \leq 1$, we can amplify prior to transduction to obtain an additive noise variance

$$\sigma_{\text{TP}}^2 = \frac{1}{2} [(u - 1)\kappa^2 - 2v\kappa + 1 + w],$$

where u, v, w are defined in Eqs. (3.25). In this case, σ_{TP}^2 is minimized when $\kappa = \min[1, v/(u-1)]$. Similarly, when $\kappa \geq 1$, we can append a pure-loss channel after transduction to obtain an additive noise variance

$$\sigma_{\text{TP}}^2 = \frac{1}{2} \left[(w-1) \frac{1}{\kappa^2} - 2v \frac{1}{\kappa} + 1 + u \right],$$

which is minimized when $\kappa = \max[1, (w-1)/v]$. The comparison between direct conversion and teleportation-based schemes can be done by evaluating these equations and the results are shown in Fig. 3.6. We find that the teleportation-based transduc-

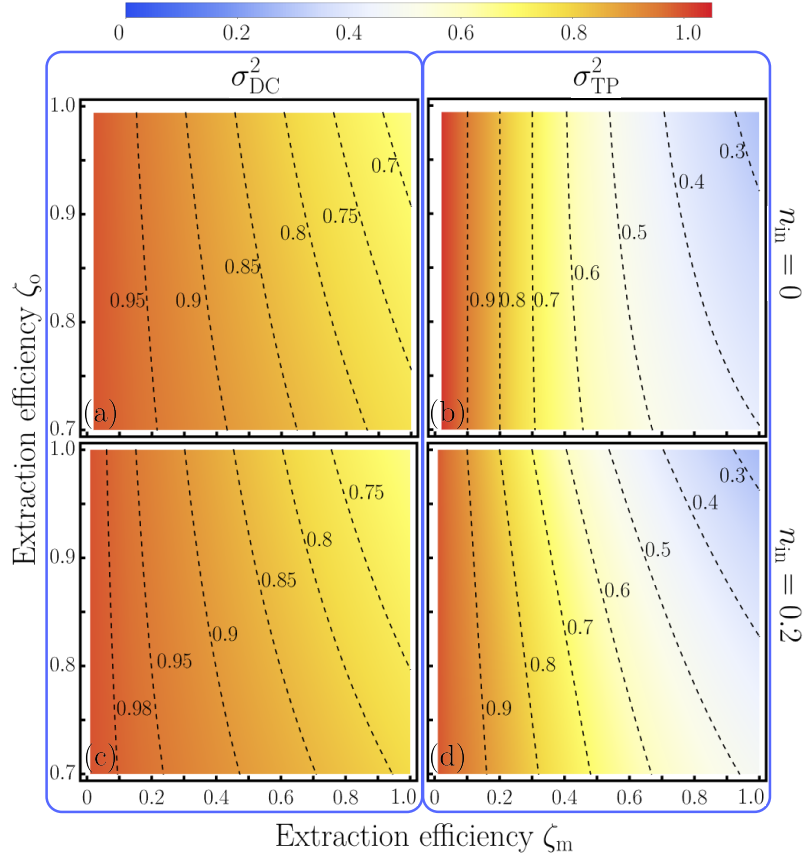


Figure 3.6: Contour plots of the additive noise variances for cooperativity $C = 0.1$ and (a)(b) $n_{\text{in}} = 0$ and (c)(d) $n_{\text{in}} = 0.2$.

tion offers a lower additive noise level across the entire parameter range. Notably, in the limit of large cooperativity ($C \rightarrow 1$), we obtain the following relationships:

$$\frac{v}{u-1} = \frac{w-1}{v} = \sqrt{\frac{\zeta_o}{\zeta_m}}. \quad (3.30)$$

If $\zeta_m > \zeta_o$, we set $\kappa = \frac{v}{u-1}$, leading to:

$$\sigma_{\text{TP}}^2 = \frac{1 - \zeta_o + n_{\text{in}}(1 - \zeta_m)}{1 + n_{\text{in}}(1 - \zeta_m)}. \quad (3.31)$$

Conversely, if $\zeta_m \leq \zeta_o$, we set $\kappa = \frac{w-1}{v}$, yielding:

$$\sigma_{\text{TP}}^2 = \frac{(1 + n_{\text{in}})(1 - \zeta_m)}{1 + n_{\text{in}}(1 - \zeta_m)}. \quad (3.32)$$

In both scenarios, we confirm that $\sigma_{\text{DC}}^2 \geq \sigma_{\text{TP}}^2$ for $C = 1$. The variation of the additive noise with extraction efficiencies ζ_{m} and ζ_{o} is depicted in Fig. 3.6. In the numerical simulation, we select practical parameters: $C = 0.1$ and $n_{\text{in}} = 0.2$. We observe that the additive noise for teleportation-based transduction is generally lower than that of the direct conversion, as seen in Fig. 3.6(a) and (b) for the ideal case of $n_{\text{in}} = 0$. For $n_{\text{in}} = 0.2$, corresponding to 0.2 Kelvin thermal background in a microwave cavity, the additive noise in teleportation-based transduction remains lower compared to the direct conversion, as illustrated in (c) and (d). Additionally, achieving equivalent noise levels via teleportation requires lower extraction efficiencies than direct conversion, thereby reducing the device requirements for near-future experiments in quantum transduction.

3.4.2 Fidelity

While quantum capacity indicates the ultimate rate of quantum information transfer, the performance of transduction can vary significantly depending on the specific quantum states involved. In this context, we focus on quantum states that are fundamentally important for quantum communication and computation. These include the coherent state $|\alpha\rangle$, the cat state $|\text{cat}_+\rangle \propto (|\alpha\rangle + |-\alpha\rangle)$, and finite-squeezed GKP states [31]:

$$|\tilde{k}\rangle_{\text{GKP}} \propto \int d^2\alpha \exp\left[-\frac{|\alpha|^2}{2\sigma_{\text{GKP}}^2}\right] \hat{D}(\alpha) |k\rangle_{\text{GKP}}, \quad k = 0, 1, \quad (3.33)$$

where $\hat{D}(\alpha)$ is the displacement operator characterized by complex number α and $|k\rangle_{\text{GKP}} = \sum_{n=-\infty}^{\infty} |\sqrt{\pi}(2n+k)\rangle_{\hat{q}}$ represents the ideal GKP qubit k .

The coherent state, as a Gaussian state, allows for an analytical evaluation of fidelity using Eq. (2.26). It should be noted that Eq. (2.27) may not be applicable unless additional displacement is performed based on prior knowledge of α .

The cat state, being a pure state, allows fidelity to be evaluated using Eq. (2.25). An analytical expression for this fidelity has been derived. Finally, the GKP state, known for its resistance to additive noise, requires numerical integration of Eq. (2.25) to determine its fidelity.

Coherent State

A coherent state $|\alpha\rangle$ is characterized by a complex number $\alpha = \alpha_R + i\alpha_I$. Defining $\boldsymbol{\alpha} = \sqrt{2}(\alpha_R, \alpha_I)^T$, the Wigner function of this state is given by:

$$W^{\text{in}}(\boldsymbol{x}; |\alpha\rangle) = \frac{1}{\pi} e^{-(\boldsymbol{x} - \sqrt{2}\boldsymbol{\alpha})^2}. \quad (3.34)$$

In the case of direct conversion (a thermal-attenuator characterized by η_{DC} and \bar{n}_{DC}), we get the fidelity

$$\mathcal{F} = \frac{1}{1 + \bar{n}_{\text{DC}}(1 - \eta_{\text{DC}})} \exp\left\{-\frac{2\boldsymbol{\alpha}^2(1 - \sqrt{\eta_{\text{DC}}})^2}{1 + \bar{n}_{\text{DC}}(1 - \eta_{\text{DC}})}\right\}. \quad (3.35)$$

It is the average fidelity between input and output states. In the case of teleportation, it is given by:

$$\mathcal{F} = \frac{2}{A(\kappa, u, v, w)} \exp\left\{-\frac{2\boldsymbol{\alpha}^2(\kappa - 1)^2}{A(\kappa, u, v, w)}\right\}, \quad (3.36)$$

where we define $A(\kappa, u, v, w) \equiv (u+1)\kappa^2 - 2v\kappa + w + 1$.

Cat State

The cat states are defined as $|cat_{\pm}\rangle \equiv N_{\pm}(|\alpha\rangle \pm |-\alpha\rangle)$, where $N_{\pm} = (2 \pm 2e^{-2\alpha^2})^{-1/2}$ are normalization constants. The Wigner functions corresponding to these states and the fidelity between the input and output states can be derived in a manner analogous to that used for coherent states.

$$W^{\text{in}}(\mathbf{x}; |cat_{\pm}\rangle) = N_{\pm}^2 \frac{1}{\pi} \left[e^{-(\mathbf{x}-\sqrt{2}\alpha)^2} + e^{-(\mathbf{x}+\sqrt{2}\alpha)^2} \pm 2e^{-\mathbf{x}^2} \cos[2\sqrt{2}(-q\alpha_I + p\alpha_R)] \right], \quad (3.37)$$

$$\mathcal{F} = \frac{4N_{\pm}^4}{1+a+b^2} \left(e^{-\frac{2\alpha^2(1-b)^2}{1+a+b^2}} + e^{-\frac{2\alpha^2(1+b)^2}{1+a+b^2}} \pm 2e^{-\frac{2\alpha^2(2+a)}{1+a+b^2}} \pm 2e^{-\frac{2\alpha^2(a+2b^2)}{1+a+b^2}} \right. \\ \left. \pm 2e^{-\frac{2\alpha^2(a+2b^2)}{1+a+b^2}} + e^{-\frac{2\alpha^2[2a+(1+b)^2]}{1+a+b^2}} + e^{-\frac{2\alpha^2[2a+(1-b)^2]}{1+a+b^2}} \right), \quad (3.38)$$

where $a = (1+2\bar{n}_{\text{DC}})(1-\eta_{\text{DC}})$ and $b = \sqrt{\eta_{\text{DC}}}$ for direct conversion; $a = u\kappa^2 - 2v\kappa + w$ and $b = \kappa$ for teleportation.

GKP state

An ideal GKP state is a sum of equal weighted eigenstates of position or momentum quadrature. For the qubit case, up to normalization, we have:

$$|0\rangle_{\text{GKP}} = \sum_{n=-\infty}^{\infty} |\sqrt{\pi}2n\rangle_{\hat{q}}, \quad (3.39)$$

$$|1\rangle_{\text{GKP}} = \sum_{n=-\infty}^{\infty} |\sqrt{\pi}(1+2n)\rangle_{\hat{q}}. \quad (3.40)$$

A GKP state with finite-squeezing can be modeled as an ideal GKP state with a Gaussian envelope of variance σ_{GKP}^2 . As shown in Ref. [32], the state is further reduced to an ideal GKP state with additive noise σ_{GKP} when $\sigma_{\text{GKP}} \ll \sqrt{\pi}$, via random shifts. The level of squeezing equals $1/\Delta$, where

$$\frac{1 - e^{-\Delta}}{1 + e^{-\Delta}} = \sigma_{\text{GKP}}^2. \quad (3.41)$$

We calculate the degree of squeezing in decibels (dB) using the formula $10 \log_{10}(1/\Delta)$. The explicit Wigner function for the state $|\tilde{0}\rangle$, corresponding to the single-qubit GKP code words in a $d = 2$ dimensional system, with a variance denoted as $\sigma_{\text{GKP}} = \sigma$, is detailed in [33].

$$W^{\text{GKP}}(q, p) = \frac{1}{N} \left\{ e^{-\frac{q^2+p^2}{2\Lambda/(4\sigma^2)}} \left[\sum_{n=-\infty}^{\infty} G_{\sigma^2}(q - n\Gamma) \right] \left[\sum_{n=-\infty}^{\infty} G_{\sigma^2}\left(p + n\frac{\pi\Lambda}{\Gamma}\right) \right] + \right. \\ \left. e^{-\frac{q^2+p^2}{2\Lambda/(4\sigma^2)}} \left[\sum_{n=-\infty}^{\infty} G_{\sigma^2}\left(q - (n + \frac{1}{2})\Gamma\right) \right] \left[\sum_{n=-\infty}^{\infty} (-1)^n G_{\sigma^2}\left(p + n\frac{\pi\Lambda}{\Gamma}\right) \right] \right\}, \quad (3.42)$$

where N is the normalized constant, $\Lambda = 1 - 4\sigma^4$ and $\Gamma = 2\sqrt{\pi}$. The fidelity between the input and the output states is given by Eq. (2.25). We set $\kappa = 1$ so that the overall teleportation channel is an additive noise channel and evaluate the fidelity numerically.

Numerical Results

In the preceding sections, we examined both the coherent state and the cat state. For these states, we directly compare the Uhlmann fidelity $\mathcal{F}(\rho, \sigma) = (\text{tr} \sqrt{\sqrt{\rho}\sigma\sqrt{\rho}})^2$ between the input and output states. In the teleportation-based transduction scheme, κ is optimized to obtain the highest fidelity between the input and output.

For GKP states, to maintain the phase space grid size invariant, we transform the overall channel into an additive noise channel. While GKP states and cat states both exhibit intrinsic error-correction capabilities, this dissertation focuses on a practical state transduction protocol for producing complex quantum states in the optical domain. Thus, we cannot assume the feasibility of performing error correction operations in the optical domain. For instance, the standard GKP error correction procedure post-noise channel involves the use of two ancilla GKP states. In our scenario, these ancilla GKP states in the optical domain would need to be generated via the same transduction protocol from microwave domain GKP states. Otherwise, one could directly produce the complex quantum states without the transduction. Consequently, the ancilla GKP states would have identical noise to the transduced GKP state, rendering them ineffective in reducing the additive noise during error correction.

For the reasons outlined above, we do not apply error correction operations at the output stage. Instead, we use fidelity to directly characterize the quality of the complex states produced.

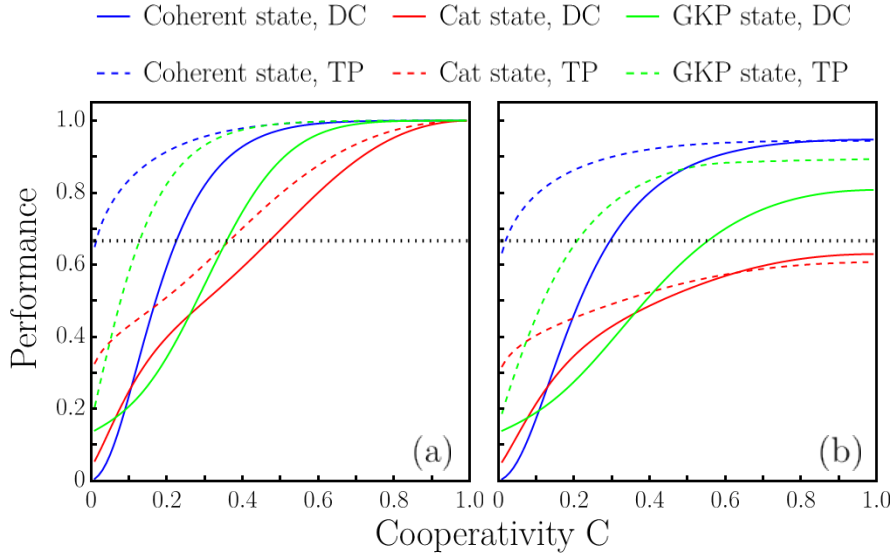


Figure 3.7: Fidelity for coherent state $|\alpha\rangle$, cat state $N_+(|\alpha\rangle + |-\alpha\rangle)$ (with $\alpha = 2$) and GKP state transduction. The GKP state has a finite squeezing noise $\sigma_{\text{GKP}} = 0.22$ (10dB). (a) $\zeta_m = 1$ and $\zeta_o = 1$, n_{in} is irrelevant. (b) $\zeta_m = 0.95$, $\zeta_o = 0.9$, and $n_{in} = 0.2$. The black dotted horizontal line indicates the fidelity threshold of $2/3$.

The ideal case with $\zeta_m = \zeta_o = 1$ is examined first. We present the fidelity for

coherent states, cat states, and GKP states, each with varying cooperativity values, in Fig. 3.7(a). In this figure, the teleportation-based transduction scheme (dashed lines) consistently outperforms the direct transduction scheme (solid lines) across all three states. As the cooperativity C nears unity, the fidelity similarly approaches unity, and the performance gap diminishes as anticipated. Additionally, the no-cloning threshold of $2/3$, as described in [34], is represented by black dotted horizontal lines in Fig. 3.7. With non-ideal extraction efficiencies ($\zeta_m = 0.95$, $\zeta_o = 0.9$) and non-zero noise $n_{\text{in}} = 0.2$, the GKP fidelity using the teleportation scheme (green dashed) consistently exceeds that of the direct conversion scheme (green solid), as depicted in Fig. 3.7(b). For coherent and cat states, the teleportation scheme offers superior fidelity over the direct conversion when cooperativity is low. Particularly, in the $C \rightarrow 0$ limit, the direct transmission scheme merely outputs noise, independent of the input, while the teleportation scheme still produces output containing some information about the input from the quadrature measurements. Conversely, at high cooperativity, direct conversion provides better fidelity. Notably, at the $C \rightarrow 1$ limit, even though the transmissivity κ of the teleportation-based scheme can be tuned close to unity, the additive noise mixed in is larger than that of the direct conversion scheme. When α is small, the states are close to vacuum, and lower transmissivity impacts the fidelity less than higher noise, explaining the observed behavior at large C . However, for larger α values, fidelity is mainly determined by transmissivity, and thus the teleportation scheme offers better fidelity.

We then vary the extraction efficiencies ζ_m and ζ_o for a practical experimental setting of $C = 0.1$ and $n_{\text{in}} = 0.2$. As expected, at relatively low cooperativity, the teleportation-based transduction outperforms direct transduction across all extraction efficiency values. As depicted in Fig. 3.8(a)(b), the fidelity of the coherent state is significantly higher with the teleportation-based scheme (b) compared to the direct conversion (a). Similar advantages for the cat state and GKP state are evident in Fig. 3.8(c)-(f), despite both schemes having overall lower fidelity for these states.

Overall, the fidelity of coherent-state transduction is much higher than that for cat states and GKP states. This is attributed to the coherent state having a positive Wigner function focused around the origin in phase space, making it more resilient to loss and noise. In contrast, GKP states and cat states, with their negative and positive Wigner function parts, do not benefit from their non-Gaussian nature without an optical domain error-correction procedure.

3.4.3 Capacity

The single mode Gaussian quantum channel, as described by Eq. (3.17) and Eq. (3.18), can only exhibit a nonzero quantum capacity if $\eta_{\text{DC}} > 1/2$. This establishes a threshold for the cooperativity in the direct conversion scheme,

$$C \geq -1 + 4\zeta_m\zeta_o - \sqrt{8\zeta_m\zeta_o(2\zeta_m\zeta_o - 1)} \geq 3 - 2\sqrt{2}. \quad (3.43)$$

This minimum value exceeds the capabilities demonstrated in state-of-the-art experiments, as reported in [26, 35], thereby precluding the reliable transduction of quantum states. This prerequisite for direct conversion is fundamental and cannot be bypassed by error-correction methods.

To surpass the limitations of direct conversion, transduction between microwave and optical frequencies can potentially be achieved through continuous-variable

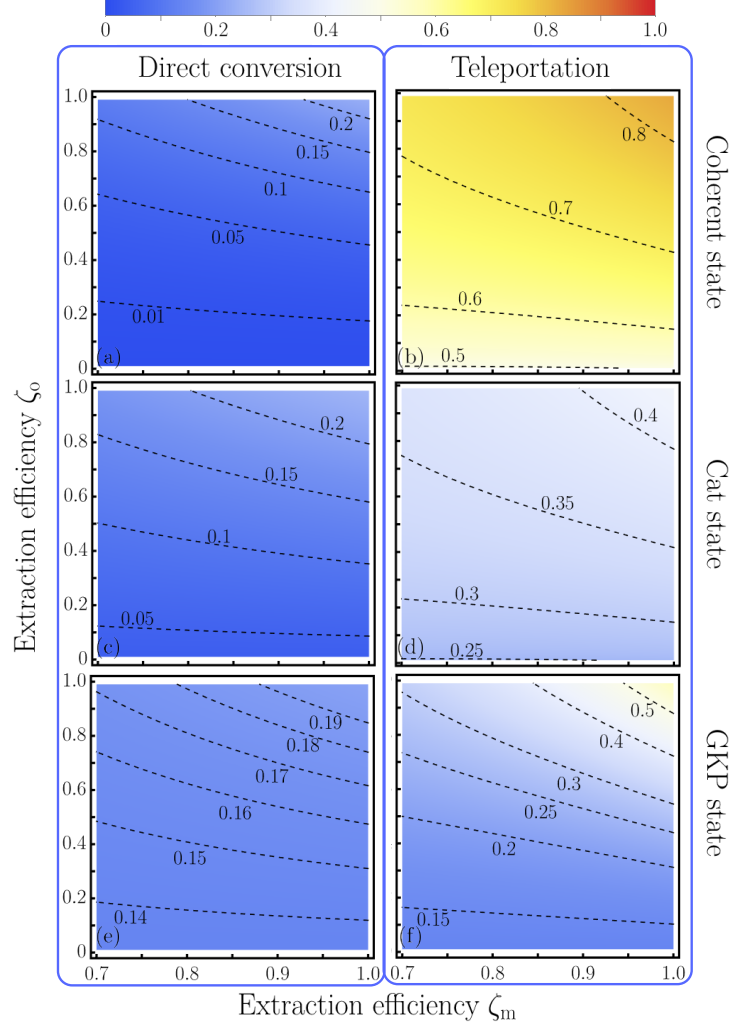


Figure 3.8: Performance of quantum state transfer: (a)(b) fidelity for coherent state $|\alpha = 2\rangle$, (c)(d) fidelity for cat state $|cat_+\rangle$ with $\alpha = 2$, and (e)(f) fidelity for GKP state. The GKP state has a finite squeezing noise $\sigma_{\text{GKP}} = 0.22$ (10 dB). The left column represents direct conversion, while the right column shows teleportation-based transduction. We choose $C = 0.1$ and $n_{\text{in}} = 0.2$ to represent state-of-the-art experimental conditions.

quantum teleportation. The underlying principle of teleportation-based transduction is that classical communication can enhance the quantum information transmission rate beyond the unassisted quantum capacity, as suggested by [36, 15].

The quantum capacities of the two schemes provide the ultimate bound of quantum information rates. We begin with the ideal case with ideal extraction efficiencies ($\zeta_o = \zeta_m = 1$) at zero temperature. Therefore, the thermal noise at microwave frequency vanishes and the quantum capacity of direct conversion can be calculated exactly [37]. However, the teleportation-based scheme can still have non-zero noise due to finite two-mode squeezing at $C < 1$. As the exact solution to quantum capacities for thermal-attenuator and thermal-amplifier with non-zero noise is unknown, we calculate the lower bound and upper bounds of quantum capacities as prescribed by Eq. (1.44) and Eq. (1.45).

As illustrated in Fig. 3.9(a), the upper (solid) and lower bound (dashed) coincide

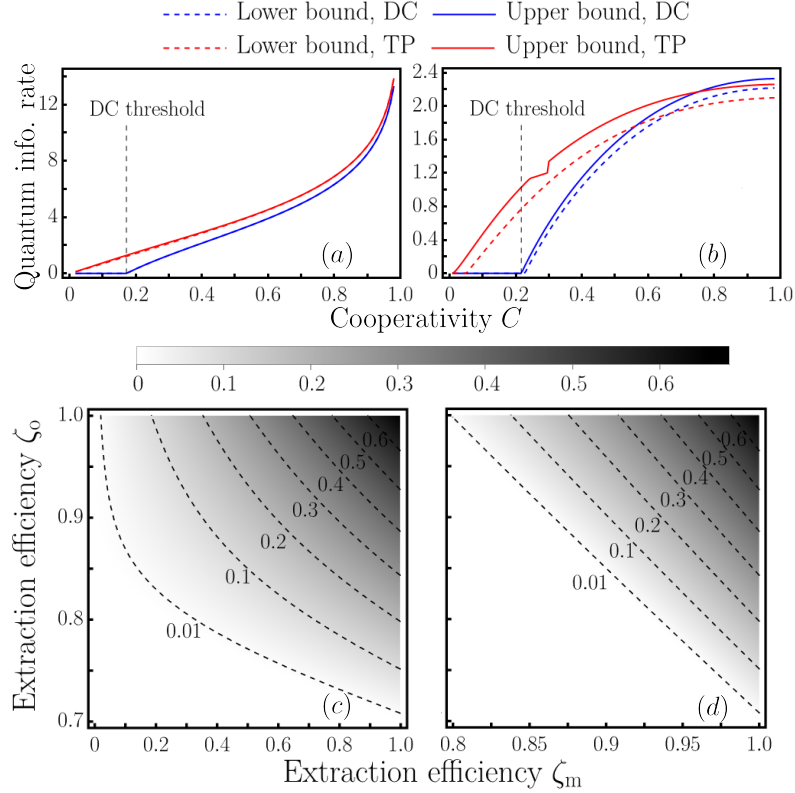


Figure 3.9: Quantum capacity comparison. (a)(b) Capacity bounds versus cooperativity C with extraction efficiencies (a) $\zeta_o = 1, \zeta_m = 1$ and (b) $\zeta_o = 0.9, \zeta_m = 0.95$. The noise is irrelevant in (a) and $n_{in} = 0.2$ in (b). The thresholds of the direct conversion in Eq. (3.43) are indicated by the vertical black dashed lines, with values around (a) $3 - 2\sqrt{2} \simeq 0.172$ and (b) 0.216. The multiple different upper bounds are combined as in Eq. (1.45). (c)(d) Contours of the capacity lower bound for the teleportation-based (TP) transduction scheme, with $C = 0.1$ and (c) $n_{in} = 0$ (d) $n_{in} = 0.2$. In these two cases, the capacity of the direct conversion (DC) scheme is all zero.

exactly for the direct conversion (blue), while a small gap persists for the teleportation scheme (red, see Fig. 3.10). The teleportation scheme exhibits a quantum capacity consistently higher than direct conversion for all C values. Notably, the direct conversion quantum capacity drops to zero below the threshold (Eq. (3.43)), unlike the teleportation scheme which maintains a non-zero quantum capacity at very low cooperativity. Fig. 3.9(c) presents the teleportation scheme's quantum capacity lower bound at experimentally demonstrated cooperativity of $C = 0.1$ [26, 35]. With non-ideal extraction efficiencies, the quantum capacity decreases only gradually, showing the robustness of the teleportation scheme.

Next, we explore the practical case with non-ideal extraction efficiencies at finite temperature. In this scenario, thermal noise at the microwave frequency is a crucial factor. Assuming a microwave resonator frequency of 8 GHz and an ambient temperature of 0.2 Kelvin, the thermal noise occupation is assumed to be $n_{in} = 0.2$. We adopt $\zeta_m = 0.95$ and $\zeta_o = 0.9$ for our analysis, aligning with experimentally feasible parameters as reported in [38, 39].

Despite these conditions, the quantum capacity lower bound of the teleportation

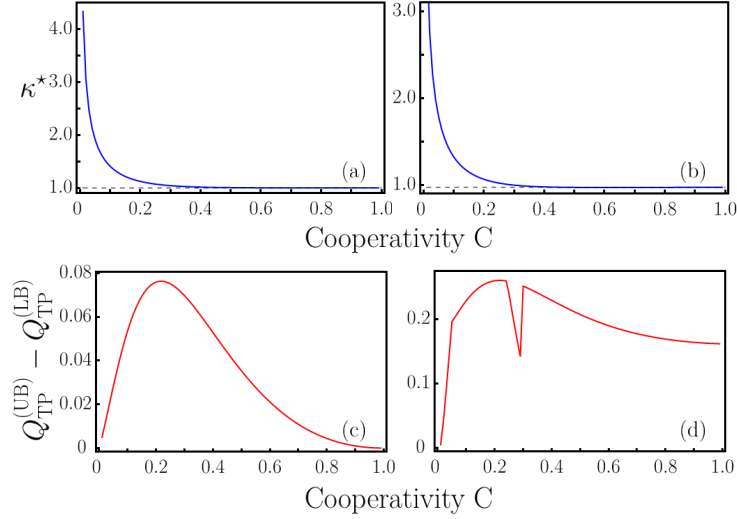


Figure 3.10: Optimum κ and difference between upper and lower bound. The black dashed lines are $\kappa = \sqrt{\zeta_o/\zeta_m}$. (a)(c) $\zeta_m = 1$ and $\zeta_o = 1$. (b)(d) $\zeta_m = 0.95$, $\zeta_o = 0.9$ and $n_{\text{in}} = 0.2$.

scheme remains above zero for any cooperativity C . In stark contrast, the quantum capacity upper bound of direct conversion drops to zero when cooperativity falls below the threshold set by Eq. (3.43). Notably, the lower bound of the teleportation scheme surpasses the upper bound of direct conversion in low cooperativity regions, indicating that the teleportation scheme is unequivocally superior to direct conversion in these cases.

We also examine the quantum capacity of the teleportation scheme under different extraction efficiencies, using conditions of $C = 0.1$ and $n_{\text{in}} = 0.2$. As before, direct transmission exhibits zero quantum capacity under these circumstances. Compared to the ideal scenario of $n_{\text{in}} = 0$ (as shown in Fig. 3.9(c)), the quantum capacity experiences a decline due to thermal noise interference (see Fig. 3.9(d)). Hence, to maintain a comparable quantum capacity, a higher microwave extraction efficiency becomes necessary.

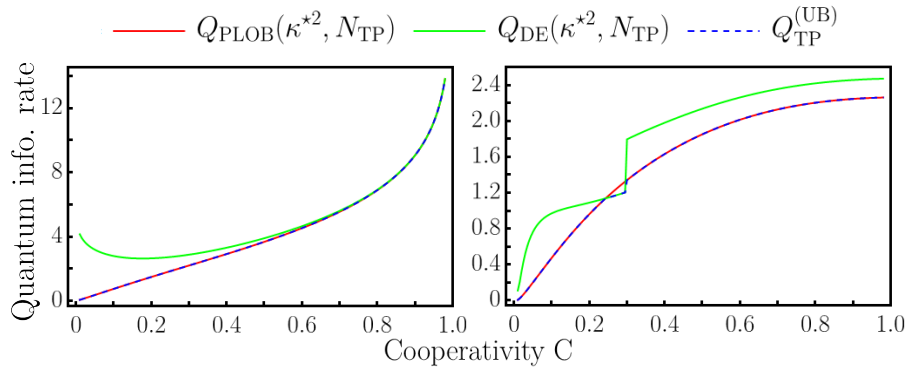


Figure 3.11: Different upper bounds for (a) $\zeta_o = 1$, $\zeta_m = 1$, and (b) $\zeta_o = 0.9$, $\zeta_m = 0.95$, and $n_{\text{in}} = 0.2$.

The capacity upper and lower bounds with κ^* are presented in Fig. 3.9. We also present different upper bounds in Fig. 3.11. As shown in Fig. 3.10, in the limit $C \rightarrow 1$, we need $\kappa = \sqrt{\zeta_o/\zeta_m}$ so that N_{TP} does not diverge.

Chapter 4

Squeezing Enhanced Quantum Teleportation

In this chapter, we begin by analyzing the role of single-mode squeezing in the continuous-variable teleportation-based transduction scheme [40]. The quantum Langevin equations are derived, incorporating squeezing and the associated stability conditions. The transmissivity and noise parameters for both direct conversion and the teleportation channel are derived similarly to the methods outlined in the previous chapter. Then we elucidate how single-mode squeezing can enhance the effectiveness of quantum teleportation by enhancing the entanglement. In the final section, additional methods are explored to enhance quantum teleportation. However, it's important to note that some approaches, such as three-mode teleportation and purifying electro-optical entanglement, are not currently feasible.

4.1 Direct Conversion and Teleportation Scheme

Despite the different systems, traditional schemes all utilize a direct conversion approach of transduction: the Hamiltonian can be directly modeled as a beam-splitter interaction between optical and microwave frequencies. The state-of-the-art performance of such schemes are far from satisfying in neither efficiency or noise level. The engineering challenge is that simply increasing the power of the pulsed pump to achieve high cooperativity will lead to heating that significantly reduces the repetition rate of transduction. For example, Refs. [41, 42, 43] can achieve high cooperativity when adopting a pump pulse of 100ns; however, they can only do so by reducing the repetition rate to $10 \sim 100\text{Hz}$ so that the average heating is low. This leads to a 3 ~ 4 orders of magnitude of reduction of transduction rates in terms of qubits-per-second. Therefore, in order to maintain a high transduction rate in qubits per second, low cooperativity is still the major issue to overcome.

Recently, microwave single-mode squeezing has been proposed to improve the performance of an electro-optical transduction system [44]. On the other hand, the teleportation-based approach generates optical-microwave entanglement from the transduction device and subsequently employs quantum teleportation to transmit quantum information, via the time-bin approach [45] or the continuous-variable approach [30]. In particular, the continuous-variable teleportation approach has shown performance advantages over the direct conversion scheme, especially in the low cooperativity region of near-term devices, thanks to its tunable efficiency and reduced

noise [30]. At the same time, experimental generation of optical-microwave entanglement on electro-optical devices has recently been demonstrated [43], showing great promise for the teleportation-based transduction.

4.1.1 Cavity Electro-Optics involving Squeezing

Despite that the analyses can be applied to different platforms, we focus on electro-optical systems, owing to their state-of-the-art performance [26, 41] and the simplicity of their interaction Hamiltonian. Notably, microwave-optical entanglement has recently been generated on such platforms [43], marking a significant advancement towards realizing teleportation-based transduction.

As shown in Fig. 4.1, an electro-optical system consists of an optical cavity with $\chi^{(2)}$ nonlinear materials placed between the capacitor of a LC microwave resonator. To enhance the performance, we can apply single-mode squeezing to the microwave side using the inductive nonlinearity in Josephson parametric amplifiers [46, 47, 48]. The interaction Hamiltonian of the cavity electro-optics is described by

$$\hat{H}_I/\hbar = g_0(\hat{a}^\dagger \hat{b} \hat{m}^\dagger + \hat{a} \hat{b}^\dagger \hat{m}) + v(e^{i\theta} \hat{m}^2 + e^{-i\theta} \hat{m}^{\dagger 2}), \quad (4.1)$$

where \hat{a} and \hat{b} are two optical modes and \hat{m} is the microwave mode. To characterize the interaction strength, the interaction cooperativity is defined as $C_g = 4g^2/(\gamma_o\gamma_m)$, where we have defined the rescaled coupling coefficient $g = \sqrt{N_p}g_0$ with N_p being the total intra-cavity pump photon number. Similarly, the squeezing level is defined as $C_v = 4v^2/\gamma_m^2$, where v is the squeezing parameter in Eq. (4.1). Alternatively,

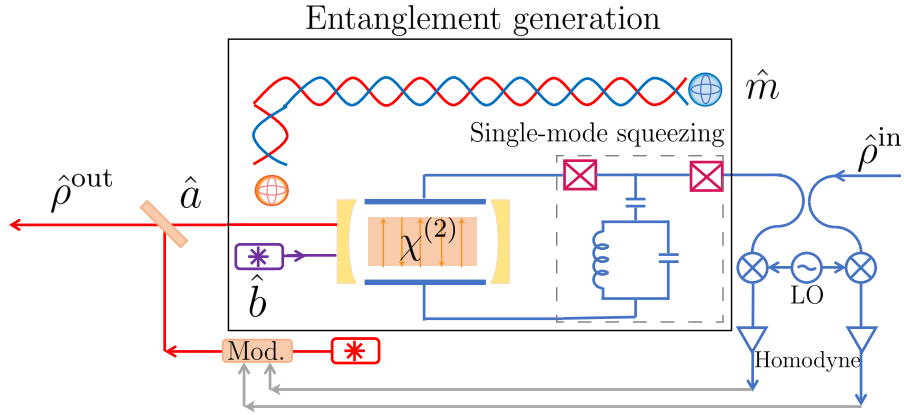


Figure 4.1: Schematic of the teleportation-based microwave-to-optical transduction scheme. The microwave single-mode squeezing is implemented by the parametric drive of superconducting inductance. The arrows inside the crystal indicate the optical axis of periodic poling structure for optical single-mode squeezing. The entanglement between microwave mode \hat{m} and optical mode \hat{a} is generated to teleport the state in microwave side $\hat{\rho}^{\text{in}}$ to optical side $\hat{\rho}^{\text{out}}$.

optical squeezing can be realized with parametric down-conversion using the same $\chi^{(2)}$ nonlinear materials between the capacitor. As shown in Fig. 4.1, the phase matching condition can be satisfied through geometric dispersion engineering or periodic poling [49]. For teleportation-based protocol, the interaction Hamiltonian is written as

$$\hat{H}_I/\hbar = g_0(\hat{a}^\dagger \hat{b} \hat{m}^\dagger + \hat{a} \hat{b}^\dagger \hat{m}) + v(e^{i\theta} \hat{a}^2 + e^{-i\theta} \hat{a}^{\dagger 2}), \quad (4.2)$$

with pumping mode \hat{b} . While for direct conversion,

$$\hat{H}_I/\hbar = g_0(\hat{a}^\dagger \hat{b} \hat{m}^\dagger + \hat{a} \hat{b}^\dagger \hat{m}) + v(e^{i\theta} \hat{b}^2 + e^{-i\theta} \hat{b}^{\dagger 2}), \quad (4.3)$$

with pumping mode \hat{a} and we can define the corresponding squeezing level $C_v = 4v^2/\gamma_o^2$. In both microwave and optical squeezing cases, we assume zero additive noise in the optical frequency and non-zero additive noise n_{in} in the microwave frequency. As according to the Bose-Einstein distribution, the room-temperature thermal photon at optical frequency is negligible, while the thermal photon $n_{\text{in}} \sim 10^{-1}$ for a typical 8 GHz microwave system cooled to $\sim 10^{-1}$ Kelvin.

4.1.2 Stability Condition

Let's consider the stability condition of the transduction system, which can be derived via the Laplace analysis as in Ref. [24]. For a linear time-invariant system, the stability condition is equivalent to that the poles of the transfer function are negative. Otherwise, the system output will be unbounded even when the initial input is bounded.

In a direct conversion transduction scheme, the optical mode \hat{a} is coherently pumped with mean photon number N_p , which leads to a beamsplitter interaction $g\hat{b}\hat{m}^\dagger$ in the first part of Eq. (4.1) or Eq. (4.2). The beam-splitter-like Hamiltonian is given by

$$\hat{H}_{\text{BS}} = g(\hat{b}^\dagger \hat{m} + \hat{b} \hat{m}^\dagger),$$

where the pumping photon number N_p of optical mode \hat{a} has been absorbed into g . Such a beamsplitter interaction enables coherent conversion between the optical mode \hat{b} and the microwave mode \hat{m} —achieving the required transduction. When squeezing is involved, the total Hamiltonian can be written as

$$\hat{H}_{\text{DC}}/\hbar = \omega_o \hat{b}^\dagger \hat{b} + \omega_m \hat{m}^\dagger \hat{m} + \hat{H}_{\text{BS}} + \hat{H}_{\text{MS/OS}}, \quad (4.4)$$

where \hat{H}_{MS} and \hat{H}_{OS} model the microwave squeezing and optical squeezing, respectively. They can be expressed as

$$\hat{H}_{\text{MS}} = v(e^{i\theta} \hat{m}^2 + e^{-i\theta} \hat{m}^{\dagger 2}),$$

$$\hat{H}_{\text{OS}} = v(e^{i\theta} \hat{b}^2 + e^{-i\theta} \hat{b}^{\dagger 2}),$$

where v and θ are real numbers describing the squeezing level and rotation, respectively. The quantum Langevin equations can be obtained from the Hamiltonian in Eq. (4.4). For example, for single-mode squeezing in microwave, they are

$$\frac{d\hat{b}(t)}{dt} = i\Delta_o \hat{b} - ig\hat{m} - \frac{\gamma_o}{2} \hat{b} + \sqrt{\gamma_{pc}} \hat{b}_{\text{in}} + \sqrt{\gamma_{pi}} \hat{b}^{(i)}, \quad (4.5a)$$

$$\begin{aligned} \frac{d\hat{m}(t)}{dt} = & i\Delta_m \hat{m} - ig\hat{b} - 2ve^{-i\theta} \hat{m}^\dagger - \\ & \frac{\gamma_m}{2} \hat{m} + \sqrt{\gamma_{ec}} \hat{m}_{\text{in}} + \sqrt{\gamma_{ei}} \hat{m}^{(i)}, \end{aligned} \quad (4.5b)$$

$$\hat{b}_{\text{out}} = -\sqrt{\gamma_{pc}} \hat{b} + \hat{b}_{\text{in}}, \quad (4.5c)$$

$$\hat{m}_{\text{out}} = -\sqrt{\gamma_{ec}} \hat{m} + \hat{m}_{\text{in}}, \quad (4.5d)$$

where \hat{b} , \hat{m} are time-dependent operators. The terms \hat{b}_{in} and $\hat{b}^{(i)}$ correspond to input and intrinsic loss of optical mode with $\gamma_o = \gamma_{pc} + \gamma_{pi}$. \hat{m}_{in} and $\hat{m}^{(i)}$ are input and intrinsic loss of microwave mode with $\gamma_m = \gamma_{ec} + \gamma_{ei}$. The detunings of the optical and microwave modes are denoted by Δ_o and Δ_m , respectively. The Laplace transform of function $f(t)$ is defined as

$$\tilde{f}(s) = \int_0^\infty dt f(t) \exp(-st), \quad (4.6)$$

which allows the replacement rule $\frac{df(t)}{dt} \rightarrow s\tilde{f}(s) - f(0)$. By taking the Laplace transform and assuming zero detuning, we obtain the following quantum Langevin equations in the complex domain,

$$0 = \mathbf{G}_{\text{DC,MS/OS}}(s)\tilde{\mathbf{b}} + \tilde{\mathbf{b}}(0) + \mathbf{K}\tilde{\mathbf{b}}_{\text{in}}, \quad (4.7a)$$

$$\tilde{\mathbf{b}}_{\text{out}}(s) = -\mathbf{K}^T\tilde{\mathbf{b}} + \tilde{\mathbf{b}}_{\text{in}}, \quad (4.7b)$$

$$\tilde{\mathbf{b}}_{\text{out}}(s) = \mathbf{F}(s)\tilde{\mathbf{b}}(0) + \mathbf{S}(s)\tilde{\mathbf{b}}_{\text{in}}(s). \quad (4.7c)$$

The vectors of operators are defined by

$$\tilde{\mathbf{b}} = \left(\tilde{b}, \tilde{b}^\dagger, \tilde{m}, \tilde{m}^\dagger \right)^T, \\ \tilde{\mathbf{b}}_{\text{in}} = \left(\tilde{b}_{\text{in}}, \tilde{b}_{\text{in}}^\dagger, \tilde{b}^{(i)}, \tilde{b}^{(i)\dagger}, \tilde{m}_{\text{in}}, \tilde{m}_{\text{in}}^\dagger, \tilde{m}^{(i)}, \tilde{m}^{(i)\dagger} \right)^T,$$

where the tilde version of operators denote the operators' Laplace transforms. And the matrices are given by

$$\mathbf{G}_{\text{DC,MS}}(s) = \begin{pmatrix} -\frac{\gamma_o}{2} - s & 0 & -ig & 0 \\ 0 & -\frac{\gamma_o}{2} - s^* & 0 & ig \\ -ig & 0 & -\frac{\gamma_m}{2} - s & -2ive^{-i\theta} \\ 0 & ig & 2ive^{i\theta} & -\frac{\gamma_m}{2} - s^* \end{pmatrix}, \\ \mathbf{G}_{\text{DC,OS}}(s) = \begin{pmatrix} -\frac{\gamma_o}{2} - s & -2ive^{-i\theta} & -ig & 0 \\ 2ive^{i\theta} & -\frac{\gamma_o}{2} - s^* & 0 & ig \\ -ig & 0 & -\frac{\gamma_m}{2} - s & 0 \\ 0 & ig & 0 & -\frac{\gamma_m}{2} - s^* \end{pmatrix}, \\ \mathbf{K} = \begin{pmatrix} \sqrt{\gamma_{pc}} & 0 & \sqrt{\gamma_{pi}} & 0 & 0 & 0 & 0 & 0 \\ 0 & \sqrt{\gamma_{pc}} & 0 & \sqrt{\gamma_{pi}} & 0 & 0 & 0 & 0 \\ 0 & 0 & 0 & 0 & \sqrt{\gamma_{ec}} & 0 & \sqrt{\gamma_{ei}} & 0 \\ 0 & 0 & 0 & 0 & 0 & \sqrt{\gamma_{ec}} & 0 & \sqrt{\gamma_{ei}} \end{pmatrix}, \\ \mathbf{F}(s) = \mathbf{K}^T \mathbf{G}_{\text{DC,MS/OS}}(s)^{-1}.$$

To get the stability of the system, we need to ensure that the poles of the transfer function $\mathbf{F}(s)$ are located in the left half-plane of the complex plane. This can be achieved by examining the roots of the equation $\det[\mathbf{G}_{\text{DC}}(\alpha)] = 0$, where α is a real variable. The stability condition is that the largest root of this equation must be negative. After solving the equation, we obtain the stability condition:

$$1 + C_g - 2\sqrt{C_v} > 0, \quad (4.8)$$

where $C_v = 4v^2/\gamma_{m/o}^2$ for microwave or optical squeezing respectively and $C_g = 4g^2/(\gamma_m\gamma_o)$ characterizes the strength of the beam-splitter interaction.

In the teleportation-based transduction scheme, the optical mode \hat{b} is coherently pumped with mean photon number N_p , Eq. (4.1) and Eq. (4.2) both lead to a two-mode-squeezing interaction $g\hat{a}^\dagger\hat{m}^\dagger$ between the optical mode \hat{a} and the microwave mode \hat{m} for entanglement generation. Thus, the total Hamiltonian \hat{H}_{TP} is

$$\hat{H}_{\text{TP}}/\hbar = \omega_o\hat{a}^\dagger\hat{a} + \omega_m\hat{m}^\dagger\hat{m} + \hat{H}_{\text{TMS}} + \hat{H}_{\text{MS/OS}}, \quad (4.9)$$

$$\hat{H}_{\text{TMS}} = g(\hat{a}^\dagger\hat{m}^\dagger + \hat{a}\hat{m}), \quad (4.10)$$

where \hat{H}_{MS} and \hat{H}_{OS} are single-mode squeezing in microwave and optical domain given by

$$\hat{H}_{\text{MS}} = v(e^{i\theta}\hat{m}^2 + e^{-i\theta}\hat{m}^{\dagger 2}),$$

$$\hat{H}_{\text{OS}} = v(e^{i\theta}\hat{a}^2 + e^{-i\theta}\hat{a}^{\dagger 2}),$$

where v is the level of squeezing. For entanglement generation, the stability condition can be derived in the same fashion. With Hamiltonian given by Eq. (4.10), the quantum Langevin equations are obtained in the teleportation scheme. Instead of the full equations, we directly provide the transition matrices as

$$\mathbf{G}_{\text{TP,MS}}(s) = \begin{pmatrix} -\frac{\gamma_o}{2} - s & 0 & 0 & -ig \\ 0 & -\frac{\gamma_o}{2} - s^* & ig & 0 \\ 0 & -ig & -\frac{\gamma_m}{2} - s & -2ive^{-i\theta} \\ ig & 0 & 2ive^{i\theta} & -\frac{\gamma_m}{2} - s^* \end{pmatrix}, \quad (4.11)$$

$$\mathbf{G}_{\text{TP,OS}}(s) = \begin{pmatrix} -\frac{\gamma_o}{2} - s & -2ive^{-i\theta} & 0 & -ig \\ 2ive^{i\theta} & -\frac{\gamma_o}{2} - s^* & ig & 0 \\ 0 & -ig & -\frac{\gamma_m}{2} - s & 0 \\ ig & 0 & 0 & -\frac{\gamma_m}{2} - s^* \end{pmatrix}. \quad (4.12)$$

The maximum root of the equation $\det[\mathbf{G}_{\text{TP}}(\alpha)] = 0$ has to be smaller than 0 to enable a stable system. Thus, for entanglement generation we have

$$1 - C_g - 2\sqrt{C_v} > 0, \quad (4.13)$$

where $C_v = \frac{4v^2}{\gamma_{m/o}^2}$ for microwave or optical squeezing, respectively.

4.2 Direct Conversion Channel

Under the stability condition, the input-output relations between the microwave (optical) input and the optical (microwave) output can be derived using the quantum Langevin equations in the frequency domain. Considering the general relation for the cavity modes, which includes the input modes $\hat{\mathbf{b}}_{\text{in}}$, output modes $\hat{\mathbf{b}}_{\text{out}}$ and cavity modes $\hat{\mathbf{b}}$ in frequency domain defined as

$$\begin{aligned}\hat{\mathbf{b}} &= (\hat{b}, \hat{b}^\dagger, \hat{m}, \hat{m}^\dagger)^T, \\ \hat{\mathbf{b}}_{\text{in}} &= (\hat{b}_{\text{in}}, \hat{b}_{\text{in}}^\dagger, \hat{b}^{(i)}, \hat{b}^{\dagger(i)}, \hat{m}_{\text{in}}, \hat{m}_{\text{in}}^\dagger, \hat{m}^{(i)}, \hat{m}^{\dagger(i)})^T, \\ \hat{\mathbf{b}}_{\text{out}} &= (\hat{b}_{\text{out}}, \hat{b}_{\text{out}}^\dagger, \hat{b}^{(i)}, \hat{b}^{\dagger(i)}, \hat{m}_{\text{out}}, \hat{m}_{\text{out}}^\dagger, \hat{m}^{(i)}, \hat{m}^{\dagger(i)})^T.\end{aligned}$$

Replacing s with $i\omega$ in the quantum Langevin equations within the complex domain, the output fields can be derived in the frequency domain for steady systems. By solving a set of Heisenberg-Langevin equations in the frequency domain, alongside utilizing the input-output relations below

$$\begin{aligned}0 &= \mathbf{G}_{\text{DC,OS/MS}}(i\omega)\hat{\mathbf{b}} + \mathbf{K}\hat{\mathbf{b}}_{\text{in}}, \\ \hat{\mathbf{b}}_{\text{out}} &= -\mathbf{K}^T\hat{\mathbf{b}} + \hat{\mathbf{b}}_{\text{in}},\end{aligned}$$

the output field is then given by

$$\hat{\mathbf{b}}_{\text{out}} = (\mathbf{K}^T\mathbf{G}^{-1}(i\omega)\mathbf{K} + \mathbf{I}_8)\hat{\mathbf{b}}_{\text{in}} \equiv \mathbf{S}(i\omega)\hat{\mathbf{b}}_{\text{in}}.$$

For the case of zero detuning, when $\omega = 0$, we use the shorter notations \mathbf{G} and \mathbf{S} . To transform the input-output relations from annihilation and creation operators $(\hat{a}, \hat{a}^\dagger)$ to quadrature operators $\hat{x} = (\hat{q}_a, \hat{p}_a)$, we introduce the transformation matrix as follows:

$$\mathbf{Q} = \mathbf{I}_4 \otimes \frac{1}{\sqrt{2}} \begin{pmatrix} 1 & 1 \\ -i & i \end{pmatrix}.$$

We obtain the relation between the input and output fields as

$$\begin{aligned}\hat{\mathbf{x}}_{\text{out}} &= \mathbf{S}_{\mathbf{x}}\hat{\mathbf{x}}_{\text{in}}, \\ \mathbf{S}_{\mathbf{x}} &= \mathbf{Q}\mathbf{S}\mathbf{Q}^{-1}, \\ \mathbf{V}_{\text{out}} &= \mathbf{S}_{\mathbf{x}}\mathbf{V}_{\text{in}}\mathbf{S}_{\mathbf{x}}^T,\end{aligned}$$

where $\hat{\mathbf{x}}_{\text{in}}$ and $\hat{\mathbf{x}}_{\text{out}}$ represent the quadrature operators of the input and output fields, and \mathbf{V}_{out} and \mathbf{V}_{in} are the covariance matrices of the output and input fields, respectively. By tracing out the other modes at the output, we obtain the reduced channel that describes the microwave-to-optical transduction:

$$\begin{pmatrix} \hat{q}_o \\ \hat{p}_o \end{pmatrix} = \mathbf{S}_{\mathbf{x}}^{<\{1,2\},\{5,6\}>} \begin{pmatrix} \hat{q}_m \\ \hat{p}_m \end{pmatrix} \equiv \mathbf{T} \begin{pmatrix} \hat{q}_m \\ \hat{p}_m \end{pmatrix}, \quad (4.14)$$

where $<\{1,2\},\{5,6\}>$ presents the row 1, 2 and column 5, 6 block of the matrix $\mathbf{S}_{\mathbf{x}}$. The transmissivity of the microwave-to-optical transduction can be calculated as:

$$\eta_{\text{DC,MS}}^{\text{m} \rightarrow \text{o}} = \det[\mathbf{T}] = \frac{4C_g\zeta_o\zeta_m}{(1 + C_g)^2 - 4C_v}. \quad (4.15)$$

The noise matrix for the microwave-to-optical transduction can be calculated as:

$$\mathbf{N}_{\text{DC,MS}}^{\text{m} \rightarrow \text{o}} = \mathbf{S}_{\mathbf{x}}^{<\{1,2\},\{1,2,3,4,7,8\}>} \mathbf{V}_{\text{in}} \mathbf{S}_{\mathbf{x}}^{<\{1,2\},\{1,2,3,4,7,8\}>^T}, \quad (4.16)$$

where we assume the microwave thermal noise n_{in} and zero optical thermal loss resulting in the input covariance matrix:

$$\mathbf{V}_{\text{in}} = \text{Diag} \left(\frac{1}{2}, \frac{1}{2}, \frac{1}{2}, \frac{1}{2}, \frac{1}{2} + n_{\text{in}}, \frac{1}{2} + n_{\text{in}} \right).$$

We can then calculate the noise $\bar{n}_{\text{DC,MS}}^{\text{m} \rightarrow \text{o}}$ and the noise mixed in $N_{\text{DC,MS}}^{\text{m} \rightarrow \text{o}}$ through the following expression,

$$\begin{aligned} N_{\text{DC,MS}}^{\text{m} \rightarrow \text{o}} &= \left(\frac{1}{2} + \bar{n}_{\text{DC,MS}}^{\text{m} \rightarrow \text{o}} \right) |1 - \eta_{\text{DC,MS}}^{\text{m} \rightarrow \text{o}}| \\ &= \sqrt{\det \mathbf{N}_{\text{DC,MS}}^{\text{m} \rightarrow \text{o}}}. \end{aligned}$$

This leads to the result:

$$N_{\text{DC,MS}}^{\text{m} \rightarrow \text{o}} = \frac{\sqrt{[A_-^2 + 4C_g\zeta_o B_+][A_+^2 + 4C_g\zeta_o B_-]}}{2[(1 + C_g)^2 - 4C_v]}, \quad (4.17)$$

where

$$A_- = 1 + C_g - 2\sqrt{C_v}, \quad (4.18a)$$

$$A_+ = 1 + C_g + 2\sqrt{C_v}, \quad (4.18b)$$

$$B_+ = (1 + 2n_{\text{in}})(1 - \zeta_m) - 1 + 2\sqrt{C_v}, \quad (4.18c)$$

$$B_- = (1 + 2n_{\text{in}})(1 - \zeta_m) - 1 - 2\sqrt{C_v}. \quad (4.18d)$$

The noise is independent of the phase rotation angle θ of the squeezing. For the other scenarios, $\eta_{\text{DC,MS/so}}^{\text{m} \rightarrow \text{o}/\text{o} \rightarrow \text{m}}$ are the same as the transmissivity given in Eq. (4.15). But the noises are different.

$$\begin{aligned} \mathbf{N}_{\text{DC,OS}}^{\text{m} \rightarrow \text{o}} &= \text{diag} \left(\frac{1}{2} + \frac{2\zeta_o \{-2\sqrt{C_v} + C_g[-\zeta_m + 2n_{\text{in}}(1 - \zeta_m)]\}}{(1 + C_g + 2\sqrt{C_v})^2}, \right. \\ &\quad \left. \frac{1}{2} + \frac{2\zeta_o \{2\sqrt{C_v} + C_g[-\zeta_m + 2n_{\text{in}}(1 - \zeta_m)]\}}{(1 + C_g - 2\sqrt{C_v})^2} \right), \end{aligned} \quad (4.19)$$

$$\begin{aligned} \mathbf{N}_{\text{DC,MS}}^{\text{o} \rightarrow \text{m}} &= \text{diag} \left(\frac{1}{2} + \frac{2\zeta_m \{-2\sqrt{C_v} - C_g\zeta_o + 2n_{\text{in}}(1 - \zeta_m)\}}{(1 + C_g + 2\sqrt{C_v})^2}, \right. \\ &\quad \left. \frac{1}{2} + \frac{2\zeta_m \{2\sqrt{C_v} - C_g\zeta_o + 2n_{\text{in}}(1 - \zeta_m)\}}{(1 + C_g - 2\sqrt{C_v})^2} \right), \end{aligned} \quad (4.20)$$

$$\begin{aligned} \mathbf{N}_{\text{DC,OS}}^{\text{o} \rightarrow \text{m}} &= \text{diag} \left(\frac{1}{2} + \frac{2\zeta_m [C_g(-\zeta_m + 2C_v) + 2(1 - 2\sqrt{C_v})^2 n_{\text{in}}(1 - \zeta_m)]}{(1 + C_g - 2\sqrt{C_v})^2}, \right. \\ &\quad \left. \frac{1}{2} + \frac{2\zeta_m [C_g(-\zeta_m - 2C_v) + 2(1 + 2\sqrt{C_v})^2 n_{\text{in}}(1 - \zeta_m)]}{(1 + C_g + 2\sqrt{C_v})^2} \right). \end{aligned} \quad (4.21)$$

If $\zeta_o = \zeta_m = 1$, then the above equations can be greatly simplified. In this ideal case, all scenarios exhibit the same level of noise:

$$\bar{n}_{\text{DC,MS}}^{\text{m} \rightarrow \text{o}} = 0. \quad (4.22)$$

4.3 Teleportation Channel

The state generated from the cavity is a multi-mode Gaussian state, as the Hamiltonian \hat{H}_{TP} is of second order. The relationship between the input and output covariance matrices is identical to that in direct conversion, but we derive the symplectic transform \mathbf{S}_x from \mathbf{G}_{TP} . There are two cases to consider: single-mode squeezing in either the microwave or optical mode. We assume a vacuum state for the optical intrinsic mode and a thermal state with a mean photon number n_{in} for the microwave intrinsic mode. In both scenarios, the covariance matrix of the generated Gaussian state can be expressed in the following form:

$$V_{\text{om}} \equiv \begin{pmatrix} \sigma_{\text{o}} & \sigma_{\text{om}} \\ \sigma_{\text{om}}^T & \sigma_{\text{m}} \end{pmatrix}, \quad (4.23)$$

where

$$\begin{aligned} \sigma_{\text{o}} &= \frac{1}{2} \begin{pmatrix} w_1 - w_2 \sin \theta & w_2 \cos \theta \\ w_2 \cos \theta & w_1 + w_2 \sin \theta \end{pmatrix}, \\ \sigma_{\text{m}} &= \frac{1}{2} \begin{pmatrix} u_1 - u_2 \sin \theta & -u_2 \cos \theta \\ u_2 \cos \theta & u_1 + u_2 \sin \theta \end{pmatrix}, \\ \sigma_{\text{om}} &= \frac{1}{2} \begin{pmatrix} -v_2 \cos \theta & v_1 + v_2 \sin \theta \\ v_1 - v_2 \sin \theta & -v_2 \cos \theta \end{pmatrix}, \end{aligned}$$

and the parameters w_1, w_2, u_1, u_2, v_1 and v_2 are independent of θ . Next we show that from the entanglement perspective view, the θ can be chosen manually. One way to quantify the amount of entanglement is the reverse coherent information, which characterizes an achievable rate in the quantum communication.

$$\begin{aligned} \text{RCI}^{\text{m} \rightarrow \text{o}} &\equiv H(\hat{\rho}_{\text{o}}) - H(\hat{\rho}_{\text{o,m}}), \\ \text{RCI}^{\text{o} \rightarrow \text{m}} &\equiv H(\hat{\rho}_{\text{m}}) - H(\hat{\rho}_{\text{o,m}}), \end{aligned}$$

where $H(\hat{\rho}_{\text{m}})$, $H(\hat{\rho}_{\text{o}})$ and $H(\hat{\rho}_{\text{o,m}})$ are the von Neumann entropy of microwave mode, optical mode and total system, respectively, with $H(\hat{\rho}) = -\text{tr}(\hat{\rho} \log_2 \hat{\rho})$. For Gaussian states, the entropy is a function of the symplectic eigenvalues of σ_{m} , σ_{o} and V_{om} . As we can check that they are independent of θ , the entanglement of the state is independent of θ as well. So we take $\theta = \pi/2$, and apply $\pi/2$ rotation on microwave mode for further simplification. This will local operation not affect the performance of quantum teleportation. The covariance matrix can be simplified to a standard form

$$\begin{aligned} V_{\text{mo}} &= \frac{1}{2} \begin{pmatrix} u_1 - u_2 & 0 & v_1 + v_2 & 0 \\ 0 & u_1 + u_2 & 0 & v_1 - v_2 \\ v_1 + v_2 & 0 & w_1 - w_2 & 0 \\ 0 & v_1 - v_2 & 0 & w_1 + w_2 \end{pmatrix} \\ &= \frac{1}{2} \begin{pmatrix} u_q & 0 & v_q & 0 \\ 0 & u_p & 0 & -v_p \\ v_q & 0 & w_q & 0 \\ 0 & -v_p & 0 & w_p \end{pmatrix}. \end{aligned} \quad (4.24)$$

For microwave squeezing, the parameters are given by

$$u_{q/p} = 1 + \frac{8\zeta_m(C_g \pm \sqrt{C_v} + n_{\text{in}}(1 - \zeta_m))}{(1 - C_g \mp 2\sqrt{C_v})^2}, \quad (4.25a)$$

$$w_{q/p} = 1 + \frac{8C_g\zeta_o [1 \mp \sqrt{C_v} + n_{\text{in}}(1 - \zeta_m)]}{(1 - C_g \mp 2\sqrt{C_v})^2}, \quad (4.25b)$$

$$v_{q/p} = \frac{4\sqrt{C_g\zeta_m\zeta_o}(1 + C_g + 2n_{\text{in}}(1 - \zeta_m))}{(1 - C_g \mp 2\sqrt{C_v})^2}. \quad (4.25c)$$

As for optical squeezing, they are given by

$$u'_{q/p} = 1 + \frac{8\zeta_m[C_g(1 \pm \sqrt{C_v}) + (1 \pm 2\sqrt{C_v})^2 n_{\text{in}}(1 - \zeta_m)]}{(1 - C_g \pm 2\sqrt{C_v})^2}, \quad (4.26a)$$

$$w'_{q/p} = 1 + \frac{8\zeta_o[C_g(1 + n_{\text{in}}(1 - \zeta_m)) \mp \sqrt{C_v}]}{(1 - C_g \pm 2\sqrt{C_v})^2}, \quad (4.26b)$$

$$v'_{q/p} = \frac{4\sqrt{C_g\zeta_m\zeta_o}(1 + C_g + 2(1 \pm 2\sqrt{C_v})n_{\text{in}}(1 - \zeta_m))}{(1 - C_g \pm 2\sqrt{C_v})^2}, \quad (4.26c)$$

where $C_v = 4v^2/\gamma_{o/m}^2$. When $\zeta_m = \zeta_o = 1$, the symplectic eigenvalues of V_{mo} are $(1/2, 1/2)$, irrespective of whether we apply microwave or optical squeezing. To quantify the entanglement, one can examine the reverse coherent information (RCI). Similar to quantum capacity, it represents the ultimate information rate with a given level of entanglement. The RCI is determined by the symplectic eigenvalues of σ_o and σ_m ,

$$\text{RCI} = \frac{2s+1}{2} \log_2 \left(\frac{2s+1}{2} \right) - \frac{2s-1}{2} \log_2 \left(\frac{2s-1}{2} \right), \quad (4.27)$$

where

$$s = s_o = s_m = \sqrt{\frac{1}{4} + \frac{4C_g(1 + C_g)^2}{[(1 - C_g)^2 - 4C_v]^2}}. \quad (4.28)$$

Compared to direct conversion, the teleportation channel has a tunable transmissivity (or gain when ≥ 1)

$$\eta_{\text{TP}} = \kappa_q \kappa_p, \quad (4.29)$$

where κ_q and κ_p are the scaling factors of the displacement on \hat{q} and \hat{p} quadrature, respectively. As the entanglement specified by the covariance matrix is asymmetric between microwave and optical mode, the channel added noise levels differ for microwave-to-optical ('m \rightarrow o') transduction and optical-to-microwave ('o \rightarrow m') transduction, which are given by

$$N_{\text{TP}}^{\text{m} \rightarrow \text{o}} = \frac{1}{2} \sqrt{(u_q \kappa_q^2 - 2v_q \kappa_q + w_q)(u_p \kappa_p^2 - 2v_p \kappa_p + w_p)}, \quad (4.30)$$

$$N_{\text{TP}}^{\text{o} \rightarrow \text{m}} = \frac{1}{2} \sqrt{(w_q \kappa_q^2 - 2v_q \kappa_q + u_q)(w_p \kappa_p^2 - 2v_p \kappa_p + u_p)}. \quad (4.31)$$

Note that the parameters $u_{q/p}$, $v_{q/p}$ and $w_{q/p}$ have different interpretations for optical squeezing and microwave squeezing.

4.3.1 Choice of Squeezing Based on Direction of Transduction

Four different scenarios of transduction arise when one applies either optical or microwave squeezing in addition to the two directions: optical-to-microwave and microwave-to-optical transduction. For simplicity, we focus on the operational squeezing mode that best suit the direct conversion approach. Therefore, in this section we explore the preferred modality of squeezing for different transduction directions in the direct conversion protocol. While the optimal choice of squeezing for direct-conversion approach may not be optimal for teleportation-based approach, it suffices to demonstrate teleportation-based approach's advantage over direct conversion approach.

In our comparison, we assume the same set of parameters: the squeezing level C_v , the extraction efficiency ζ_m and ζ_o and the cooperativity C_g . Then, the transmissivity with optical and microwave squeezing are the same. For microwave-to-optical transduction, the difference between the noise being mixed in $N_{DC,OS}^{m \rightarrow o}$ and $N_{TP,MS}^{m \rightarrow o}$ is positive since

$$(N_{DC,OS}^{m \rightarrow o})^2 - (N_{DC,MS}^{m \rightarrow o})^2 = 16 \frac{(1 - C_g^2)C_v(1 - \zeta_o)\zeta_o}{((1 + C_g)^2 - 4C_v)^2}. \quad (4.32)$$

The physical intuition behind this is that the microwave noise will also be amplified by the squeezing on the optical side. However, for optical-to-microwave transduction, the noise being mixed in with optical squeezing may not be smaller than that with microwave squeezing. Nevertheless, as shown in Fig. 4.2, in the practical parameter region of optical-to-microwave transduction, the noise being mixed in is smaller with optical squeezing. To achieve the best performance, from now on, we will consider the microwave squeezing for microwave-to-optical transduction and optical squeezing for optical-to-microwave transduction.

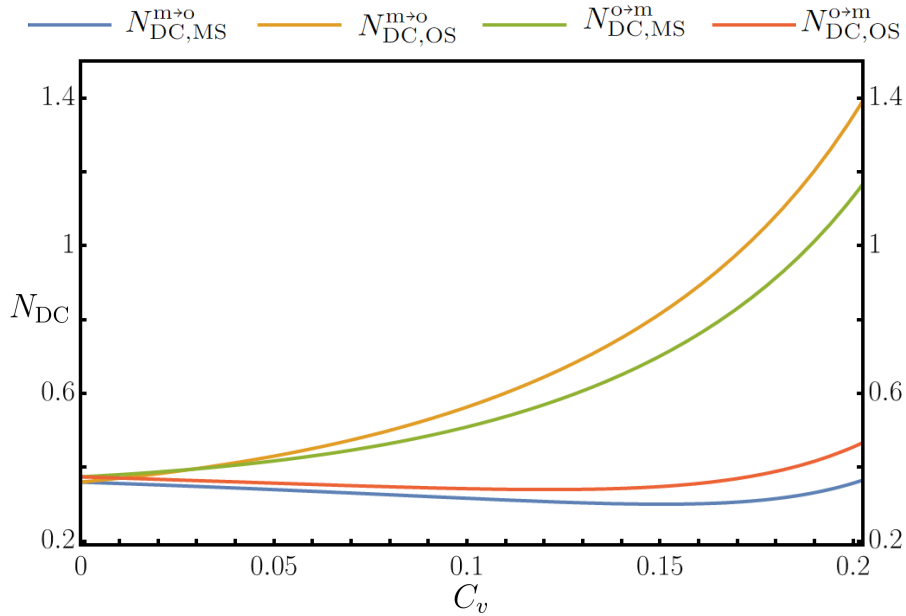


Figure 4.2: Thermal noise N_{DC} versus the squeezing level C_v with microwave thermal photon $n_{in} = 0.1$, microwave extraction efficiency $\zeta_m = 0.95$, optical extraction efficiency $\zeta_o = 0.9$ and cooperativity $C_g = 0.1$.

4.4 Fidelity Comparison

Although quantum capacity is a fundamental and accurate quantifier, achieving the quantum information rate generally necessitates specific encoding and decoding strategies, which may be challenging to implement in the near term. To compare the performance of the two approaches in systems that are closer to current technological capabilities, we first consider the fidelity between the input and output states when transducing a practical quantum state. Unlike quantum capacity, fidelity has an analytical expression and can be numerically evaluated with ease.

Assume that a single-mode Gaussian channel introduces noise mixed in as $N = \sqrt{\det[\mathbf{N}]}$ and has a transmissivity of κ^2 . The fidelity between the input and output of the channel for both the coherent state and the cat state can be calculated similarly to the methods described in Eq. (3.36) and Eq. (3.38). For the coherent state $|\alpha\rangle$,

$$\mathcal{F} = \frac{2}{1 + 2N + \kappa^2} \exp\left\{-\frac{2\alpha^2(\kappa - 1)^2}{1 + 2N + \kappa^2}\right\}. \quad (4.33)$$

And for cat state $|\text{cat}\rangle = N_{\pm}(|\alpha\rangle \pm |-\alpha\rangle)$,

$$\mathcal{F} = \frac{4N_{\pm}^4}{1 + 2N + \kappa^2} \left(e^{-\frac{2\alpha^2(1-\kappa)^2}{1+2N+\kappa^2}} + e^{-\frac{2\alpha^2(1+\kappa)^2}{1+2N+\kappa^2}} \pm 2e^{-\frac{2\alpha^2(2+2N)}{1+2N+\kappa^2}} \right. \\ \left. \pm 2e^{-\frac{2\alpha^2(2N+2\kappa^2)}{1+2N+\kappa^2}} + e^{-\frac{2\alpha^2[4N+(1+\kappa)^2]}{1+2N+\kappa^2}} + e^{-\frac{2\alpha^2[4N+(1-\kappa)^2]}{1+2N+\kappa^2}} \right). \quad (4.34)$$

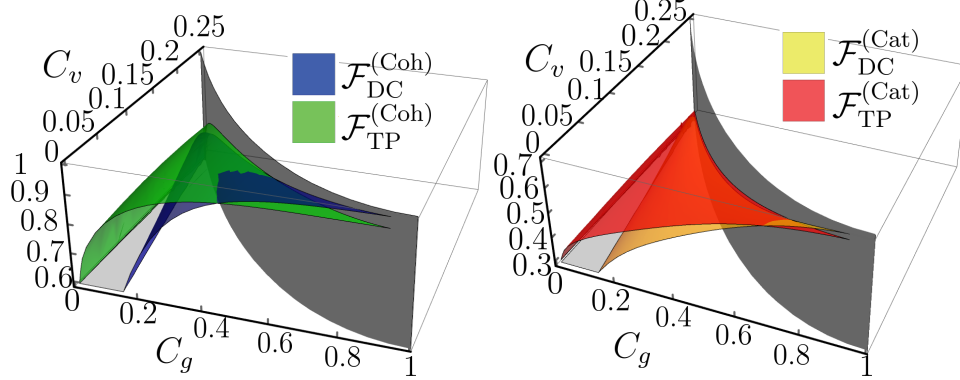


Figure 4.3: Fidelity of (a) coherent state (b) cat state after transduction when $\zeta_o = \zeta_m = 0.95$ and $n_{\text{in}} = 0.1$ for microwave-to-optical transduction involving single-mode squeezing. The amplitude is $\alpha = 2$. Green: teleportation scheme. Blue: direct conversion scheme. Dark gray surface: boundary of the stable parameter region.

Fig. 4.3 illustrates the fidelity comparison across different values of cooperativity C_g and squeezing levels C_v . In the teleportation scheme, we optimize κ_q and κ_p to maximize the fidelity of the output state. The dark gray surface in the graph represents the boundary of the stable parameter region, within which the transduction system can operate effectively. It is observed that in most of the visible parameter region, the fidelity of the teleportation-based approach (green) is higher than that of the direct conversion approach (blue). Only in the region with extremely high cooperativity does direct conversion exhibit slightly higher fidelity, though in these instances, both fidelities are very close to unity.

4.5 Capacity Comparison

In this section, we compare the quantum capacity of both the teleportation and direct conversion approaches in the context of single-mode squeezing. In regions of low cooperativity, significant single-mode squeezing is required for the direct conversion scheme to match the performance of the teleportation-based approach. The teleportation-based transduction supports nonzero rates over a broader range of extraction efficiencies compared to the direct conversion method, even when the latter operates under its optimal squeezing conditions.

In high cooperativity areas, the advantage of squeezing diminishes for both approaches due to the presence of thermal noise. However, given the additional thermal noise potentially introduced by the squeezing pump, the teleportation-based transduction approach remains the preferred method for enhancing the overall quantum information rate, measured in qubits-per-second, during transduction.

As we have demonstrated in previous sections, the input-output relation of the direct conversion and teleportation-based transduction schemes can be modeled as thermal-loss or thermal-amplification channels. Ideal transduction requires near unity transmissivity ($\eta \sim 1$) and low thermal-noise ($\bar{n} \sim 0$). While recent experiments [41] achieve high cooperativity C_g and low noise N_{DC} measured at output, the cost of such performance is a very low repetition rate, leading to orders of magnitude lower quantum information rate in qubits per second. Compared to direct conversion, the teleportation approach offers a tunable transmissivity but may introduce a higher noise level. The noise level of the teleportation-based transduction decreases with entanglement, actually $N_{TP} \sim e^{-r}$ when we take $\eta_{TP} = 1$ and a two-mode squeezed vacuum state with squeezing r for quantum teleportation.

The lower and upper bounds of the single-mode Gaussian channel are evaluated with the functions introduced in the previous chapter. The lower bound represents the achievable rate with Gaussian quantum information processing. These bounds will help us assess the performance of the transduction schemes, allowing us to determine the superior approach when the regions between the lower and upper bounds are well separated. This section is divided into two parts: the ideal extraction efficiency case in Section 4.5.1 and the practical extraction efficiency case in Section 4.5.2. In the practical case, scenarios with low cooperativity and high cooperativity are also discussed.

4.5.1 Ideal Extraction Efficiency Case

We begin the comparison between the channel capacities of the direct conversion and teleportation approaches by investigating the ideal scenario with unit extraction efficiencies $\zeta_m = \zeta_o = 1$. In this particular case, the capacity's lower bound and upper bound of the direct conversion align because $\bar{n}_{DC} = 0$, and the channel becomes a pure loss channel or quantum-limited amplification channel. Furthermore, the capacities of direct conversion in both the optical-to-microwave and microwave-to-optical transduction are identical due to the same transmissivity η_{DC} . The capacity of direct conversion, with cooperativity $C_g = 0.1$, is plotted as the blue line in Fig. 4.4 against the squeezing parameter C_v . Meanwhile, for teleportation-based quantum transduction, the tuning parameters κ_q and κ_p are optimized to attain the maximum lower bound of the quantum capacity. The optimization of the lower

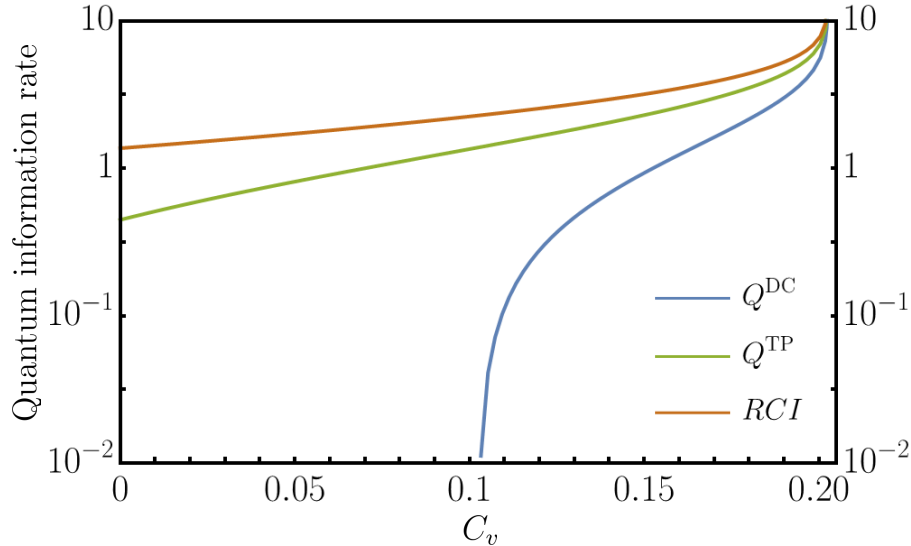


Figure 4.4: Quantum information rate of direct conversion, teleportation channel and the reverse coherent information (RCI) when $\zeta_o = \zeta_m = 1$ and $C_g = 0.1$. Q^{DC} is the exact capacity of direct conversion. Q^{TP} is the capacity lower bound of the teleportation-based approach. RCI quantifies the entanglement utilized in the teleportation-based scheme.

bound for optical-to-microwave transduction coincides with that of microwave-to-optical transduction. Since quantum teleportation utilizes the entanglement of the state, we include the reverse coherent information (RCI) as the orange curve for reference. RCI represents the asymptotic rate in quantum communication utilizing the entanglement described by V_{mo} .

As shown in Fig. 4.4, the capacity of the direct conversion is smaller than that of the teleportation at the same level of squeezing C_v , which indicates the better performance of the teleportation-based transduction. Note that the quantum information rate diverges as C_v approaches $(1 - C_g)^2/4$. This is because, in both direct conversion and teleportation, the transmissivity (η) approaches 1 and noise \bar{n} approaches 0. And the capacity is evaluated without energy constraints.

4.5.2 Practical Extraction Efficiency Case

The practical case is when the extraction efficiencies ζ_m and ζ_o are below unity. The extraction efficiencies is the ratio between the frequency of the conduction band γ_c and the total frequency of conduction band and loss frequency band $\gamma_c + \gamma_i$. In practice, the ratio is smaller than 1, while it can be tuned by operating the frequency of conduction band γ_c . The optical loss and the volume mismatching between microwave and optical mode also contribute to the total transmissivity η . While these factors are not explicitly addressed in this section, they can be effectively incorporated into the extraction efficiencies ζ_o and ζ_m . Wang et al. [50] infer that the extraction efficiencies can be tuned such that the ratio $\zeta_o/(1 - \zeta_o)$ can be within the range of 10^{-2} to 10^2 , which means that $\zeta \geq 0.9$ is achievable, ensuring the stability condition $C < 1$. On the other hand, broadband single-mode squeezing in the microwave domain, as outlined in Qiu et al. [51], can be implemented. In general, $C_v \sim 0.5$ is experimentally feasible.

To fully explore the impact of different levels of cooperativity and squeezing on the quantum information rate of the two transduction approaches, a contour plot in Fig. 4.5 is presented. Although introducing squeezing leads to more thermal noise \bar{n}_{in} , we assume the same level of noise. The gray area represents zero capacity, indicating no reliable quantum information transmission, while the green dashed line signifies the optimum squeezing C_v that maximizes the lower bound at each fixed cooperativity value C_g .

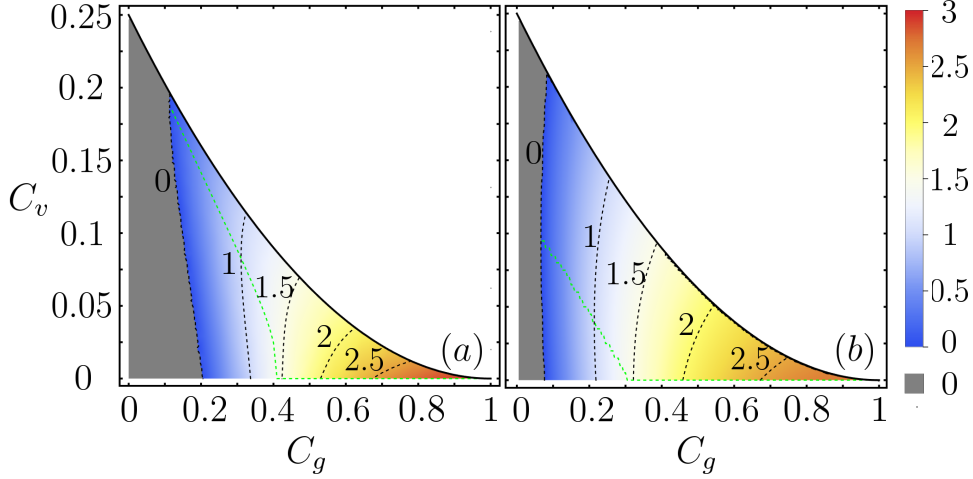


Figure 4.5: Contour of quantum information rate for microwave-to-optical transduction with $\zeta_m = \zeta_o = 0.95$ and $n_{\text{in}} = 0.1$. (a) Quantum capacity lower bound of direct conversion transduction. (b) Quantum capacity lower bound of teleportation-based transduction. The green dashed line corresponds to optimum squeezing C_v that maximizes the information rate with fixed C_g .

We observe that the teleportation approach (in sub-panel (b)) offers a larger region of non-zero rate compared to direct conversion (in sub-panel (a)), highlighting its robustness to low cooperativity. When C_g is small, choosing an optimal level of squeezing can enhance the communication rate for both direct conversion and teleportation, as evidenced by the green dashed lines. Notably, the teleportation approach requires less optimal squeezing than direct conversion. As cooperativity increases, the optimum squeezing approaches zero, indicating that squeezing does not aid in either direct conversion or teleportation. Although the results are microwave-to-optical transduction, the rate of optical-to-microwave transduction exhibits similar trends.

In the following analysis, we focus on two specific regions: the low cooperativity region and the high cooperativity region. For simplicity, we assume equal extraction efficiencies— $\zeta_m = \zeta_o = \zeta$ —in this section.

Low cooperativity

In the low cooperativity region of $C_g = 0.1$, Fig. 4.6 illustrates the quantum information rate and the effective noise N versus the squeezing level C_v for microwave-to-optical transduction and optical-to-microwave transduction. Both the lower and upper bounds of the direct conversion and teleportation channels are plotted. With chosen ζ , microwave thermal noise n_{in} and cooperativity C_g , for direct conversion, the capacity is determined solely by C_v ; while for teleportation, we optimize the

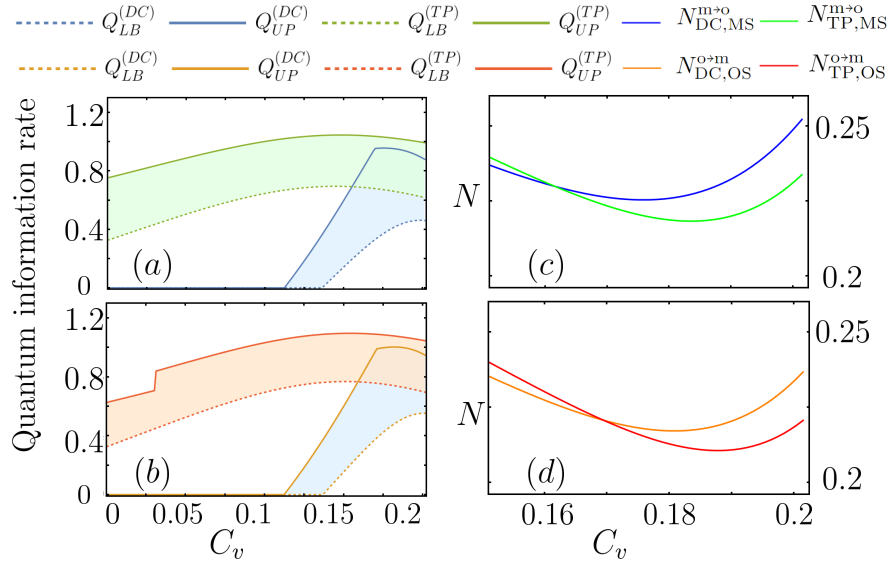


Figure 4.6: Quantum information rate and noise being mixed in versus squeezing C_v for $\zeta_m = \zeta_o = 0.975$, $n_{in} = 0.1$, and $C_g = 0.1$. (a) and (c) are microwave-to-optical transduction, (b) and (d) are optical-to-microwave transduction. In the legend, ‘LB’ indicates lower bound and ‘UB’ indicated upper bound. ‘DC’ indicates direct conversion and ‘TP’ indicates teleportation-based conversion. For the effective noise N , ‘MS’ indicates microwave squeezing and ‘OS’ indicates optical squeezing.

parameters κ_q and κ_p to maximize the lower bound and calculate the upper bound for each value of C_v .

Shown in Fig. 4.6 (a) and (b), in the small squeezing regime, the teleportation channel exhibits a non-zero capacity than direct conversion, as $\eta_{DC} < 1/2$. The capacity lower bound of the teleportation channel surpasses the capacity upper bound of the direct conversion channel when $C_v < 0.15$. For $C_v > 0.15$, the capacity region (specified by lower and upper bounds) of the two approaches overlaps. To compare their performances, we manually set $\eta_{TP} = \kappa_q \kappa_p = \eta_{DC}$ so that teleportation-based approach and the direct conversion scheme have identical transmissivity or gain, and compare the noise being mixed in. Shown in Fig. 4.6 (c) and (d), when $C_v > 0.17$, we observe that $N_{TP} < N_{DC}$, indicating that the teleportation approach can achieve the same transmissivity of direct conversion with less noise. Thus, the teleportation approach outperforms direct conversion overall.

To provide a comprehensive comparison between the two approaches in the low cooperativity region, Fig. 4.7 shows the contour plots of the lower bound of the quantum information rate versus the extraction efficiency ζ and squeezing level C_v at a fixed cooperativity of $C_g = 0.1$. By comparing both approaches, we observe that the teleportation exhibits a larger region of non-zero rate and requires less optimum squeezing C_v than the direct conversion approach for the same extraction efficiency ζ , when $C_g = 0.1$. Significantly, even without the help of any squeezing, the teleportation-based approach achieves a non-zero rate, as long as $\zeta \geq 0.9$. In contrast, the direct conversion approach requires $\zeta \geq 0.96$ to have a non-zero rate, with the help of optimal squeezing.

To maximize the rate for each extraction efficiency, we select the squeezing C_v that maximizes the lower bound of the capacity while fixing ζ , as indicated by the

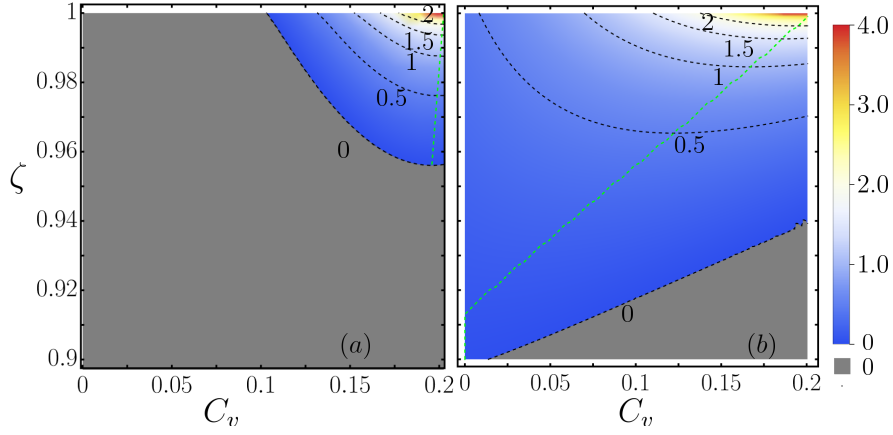


Figure 4.7: Contour of quantum information rate of microwave-to-optical transduction with $C_g = 0.1$ and $n_{\text{in}} = 0.1$. (a) Quantum capacity lower bound of direct conversion. (b) Quantum capacity lower bound of teleportation. The green dashed line corresponds to optimum squeezing C_v . The boundary of zero is obtained by rate ≤ 0.01 due to finite numerical precision.

green dashed line. The advantage of the teleportation approach over the direct conversion approach decreases as ζ approaches unity. However, in the direct conversion approach, as shown in Fig. 4.7 (a), it requires large squeezing. While in the teleportation approach, as shown in Fig. 4.7 (b), the optimum squeezing increases linearly with the extraction efficiency ζ .

Regarding the potential increase in thermal noise due to single-mode squeezing, Fig. 4.8 displays the quantum information rate relative to microwave thermal noise (n_{in}). We've optimized squeezing levels separately for direct conversion and teleportation-based transduction. Quantum information rate decreases with increasing n_{in} for both approaches. Despite the higher optimal squeezing in direct conversion, there's no significant advantage over teleportation, as indicated by overlapping region between lower bound and upper bound.

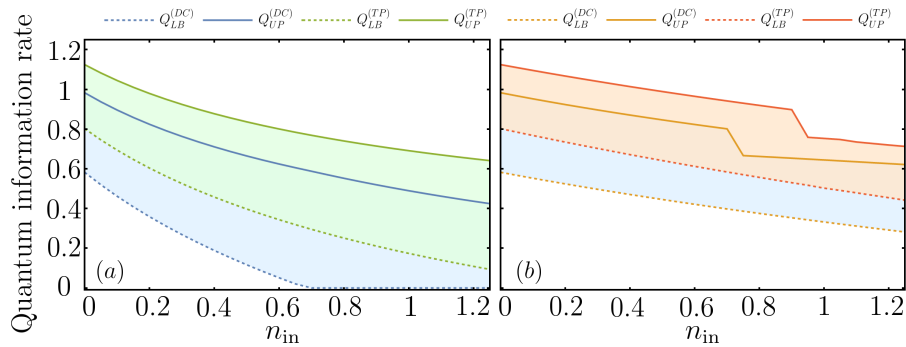


Figure 4.8: Maximum quantum information rate for optimal squeezing, versus thermal noise n_{in} when $\zeta_m = \zeta_o = 0.975$, $C_g = 0.1$. (a) Microwave-to-optical transduction, (b) Optical-to-microwave transduction.

Before concluding this part, we point out one caveat of the rate comparison in Fig. 4.7. Because we are comparing the lower bounds of both protocols, we cannot guarantee that the actual rate of the teleportation-based scheme is higher than the direct conversion scheme, similar to the situation in Ref. [44]. However, in

the presence of a noisy channel, achievable rates in the near-term are much closer to the lower bound when the channel is noisy [52], despite the exact capacity is unknown. Moreover, in Fig. 4.6 (b) we have demonstrated the advantage from noise comparison.

High cooperativity

When the cooperativity C_g is large and extraction efficiencies are non-unity, increasing the squeezing C_v does not enhance the communication rate. For direct conversion, increasing C_v to get higher η_{DC} can introduce more noise N_{DC} . The trade-off vanishes when C_g is large. In the teleportation-based approach, the noise is determined by Eq. (4.30) and Eq. (4.31) and squeezing can introduce mismatch due to thermal noise \bar{n}_{th} between u, w, v , although the entanglement between the microwave and optical mode increases. This mismatch will vanish if the entangled state is purified, i.e. $u = w = \cosh r$ and $v = \sinh r$. In contrast, for two-mode squeezing state, increasing cooperativity C_g dose not increase the mismatch. So in high cooperativity region, the benefit from squeezing also vanishes for teleportation.

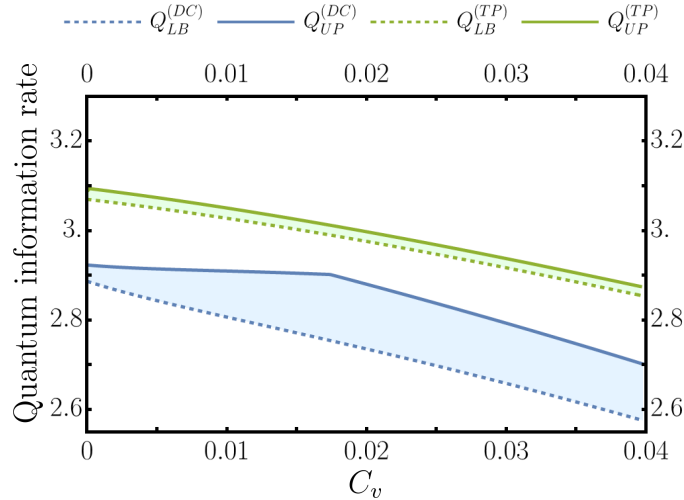


Figure 4.9: Capacity of microwave-to-optical transduction versus level of squeezing C_v for extraction efficiencies $\zeta_m = \zeta_o = 0.975$, microwave thermal noise $n_{\text{in}} = 0.1$ and cooperativity $C_g = 0.6$. Blue indicates direct conversion approach and green indicates teleportation approach. Solid and dashed curves indicate upper and lower bounds.

For instance, when $C_g = 0.6$, both the upper and lower bound decrease with C_v , as illustrated in Fig. 4.9. In this case, squeezing dose not help with the transduction rate. At the same time, the teleportation-based approach has strictly higher information rates than the direct conversion. Because the true rate lies within the green region for teleportation, strictly higher than the true rate within the blue region for direct conversion.

To gain further insights into the influence of extraction efficiency in the high cooperativity region, we present contour plots of the capacity versus C_v and ζ contour when $C_g = 0.6$ in Fig. 4.10. For each fixed ζ , we indicate the optimal squeezing level C_v that maximizes the rate in green dashed lines. In both approaches, we see that squeezing will not help unless the extraction efficiency is very close to unity. At the

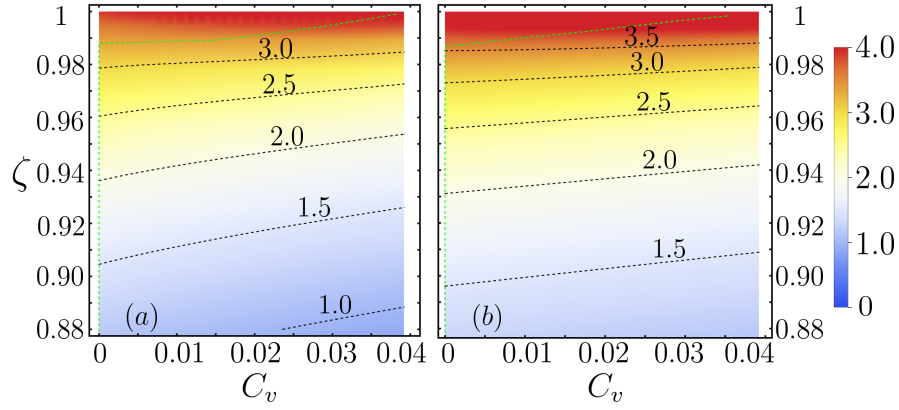


Figure 4.10: Contour of quantum information rate of microwave-to-optical transduction with $C_g = 0.6$ and $n_{\text{in}} = 0.1$. (a) Lower bound of direct conversion. (b) Lower bound of teleportation. The green dashed line corresponds to optimum squeezing C_v .

same time, the teleportation scheme still has advantage over the direct conversion in the maximum rates, despite the difference being smaller at large cooperativity.

The quantum information rate relative to microwave thermal noise (n_{in}) is shown in Fig. 4.11 when $C_g = 0.6$. When n_{in} is small, the teleportation-based transduction outperforms direct conversion because there is a clear separation between the lower bound and upper bound in (a) and (b). And when n_{in} is larger, in optical-to-microwave transduction scheme, the teleportation-based transduction still performs better than the direct conversion.

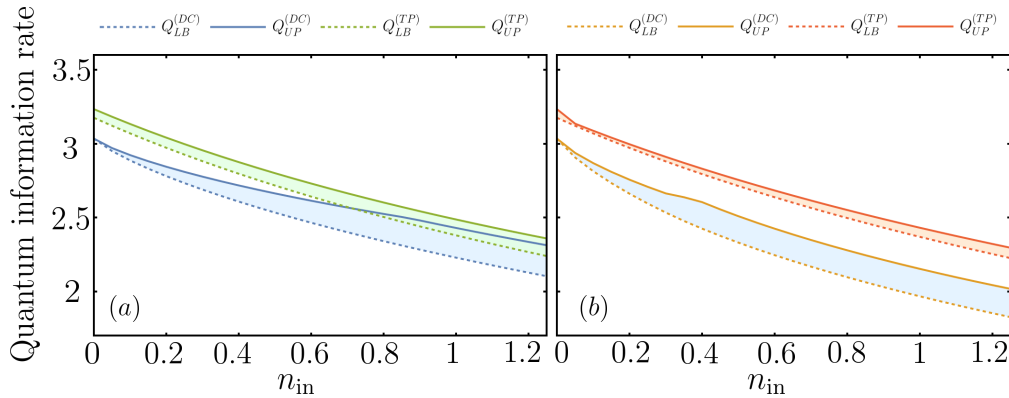


Figure 4.11: Quantum information rate versus thermal noise n_{in} when $\zeta_{\text{m}} = \zeta_{\text{o}} = 0.975$, $C_g = 0.6$. (a) Microwave-to-optical transduction, (b) Optical-to-microwave transduction.

4.6 Enhance Entanglement for Teleportation

For the teleportation-based transduction channel, the information rate depends on the Gaussian state used. To compare the teleportation channel using different entangled Gaussian states, the capacity inequality is outlined in the Theorem 29. This theorem provides insights into identifying an effective entangled state for teleportation. As observed, the additional noise introduced into the entangled state dampens the quantum capacity of the teleportation channel. Ideally, if we could purify the entangled state $\alpha \rightarrow \pi(r)$, there would be a significant boost in information rate. However, in the electro-optic transduction system, purification of a Gaussian state inevitably requires global operations on the optical side, which are challenging in the experiments due to the weak nonlinearity of light. This limitation also applies to other setups, such as opto-mechanical transduction. Therefore, we focus on increasing the entanglement between microwave and optical photons. In this closing section, I discuss several methods to enhance teleportation-based quantum transduction by augmenting the entanglement.

4.6.1 Upper Bound of Teleportation Channel

It is worthwhile to point out that the additive noise

$$\tilde{\varphi} = \sqrt{\det [\mathbf{Z}_2 \boldsymbol{\varphi}_{11} \mathbf{Z}_2^\top - 2\mathbf{Z}_2 \boldsymbol{\varphi}_{12} + \boldsymbol{\varphi}_{22}]}, \quad (4.35)$$

as stated in the Theorem 29, limits the ultimate upper bound of the teleportation channel. This is because when $r \rightarrow \infty$, the channel $\Phi(\pi(r))$ reaches its maximum capacity with $\mathbf{K} = \mathbf{I}_2$, as per Lemma 34, and the channel asymptotically approaches an identity channel since $N = e^{-r} \rightarrow 0$. In the scenario where $r \rightarrow \infty$, the teleportation channel with α can be viewed as a concatenation of an identity channel (perfect quantum teleportation) and an additive noise channel. Thus, the additive noise becomes the ultimate upper bound of the teleportation channel as we increase the Entanglement of Formation (EoF) of the state. This upper bound is illustrated in Fig. 4.12. The maximum capacity is bounded by an additive noise channel with $\varphi = 0, 0.2, 0.4$, respectively.

4.6.2 Entanglement Generation by Concatenation

As illustrated in Fig. 4.13, one approach to enhance the entanglement of the output Gaussian state is by employing the technique of concatenation, specifically through the addition of an extra cavity. The concatenation of an additional cavity introduces new dynamics to the system, potentially resulting in a more entangled and, consequently, a more efficient quantum state for teleportation and other quantum communication applications. The nuances of this process, including the impact of cavity properties and the interaction between modes, are crucial factors in the successful enhancement of entanglement.

For multiple uses of the cavities as depicted in Fig. 4.13, we assume that the initial input for the first cavity is a vacuum state. The output of the previous cavity serves as the input to the next cavity. The covariance matrix of the output after k

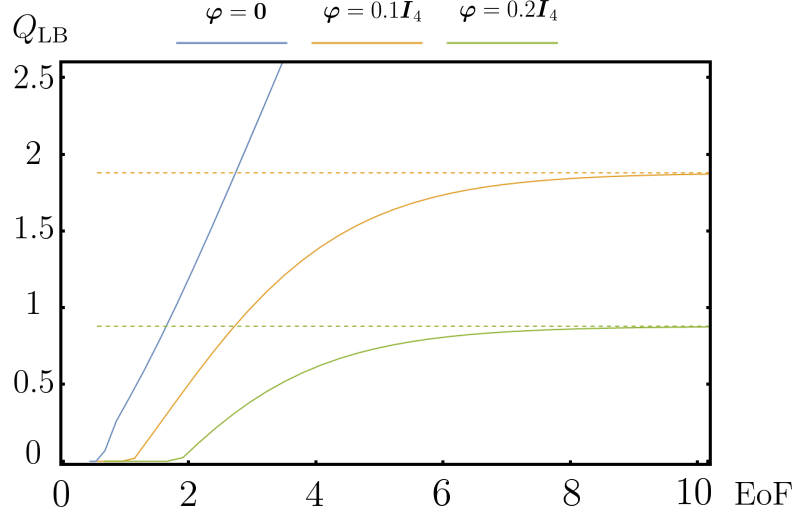


Figure 4.12: Quantum capacity of the teleportation channel versus the entanglement of formation (EoF) of the Gaussian state with covariance matrix $\alpha = \pi(r) + \varphi$. The upper bounds are obtained from additive noise in Eq. (4.35) and plotted in dashed lines. The minimum EoF required for a non-zero quantum capacity (when encoding with a coherent state) is approximately 0.389 for a pure Gaussian state $\varphi = \mathbf{0}$.

uses of the cavity is given by:

$$\mathbf{V}_{\text{out}}^{(k)} = \frac{1}{2} \mathbf{T}^{2k} + \sum_{i=0}^{k-1} \mathbf{T}^i \mathbf{N} \mathbf{T}^i, \quad (4.36)$$

where \mathbf{T} and \mathbf{N} are as defined in Eq. (4.14) and Eq. (4.16), with \mathbf{S}_x representing the transform corresponding to the two-mode squeezing operation.

As demonstrated in Fig. 4.15, with low cooperativity ($C = 0.1$), the EoF increases by concatenating cavities. Beyond a certain number of cavity uses ($k \geq k^*$), the EoF saturates due to the amplification of noise from previous cavities in subsequent ones. As shown in Fig. 4.15 (a), when the extraction efficiency is low, despite the increase in EoF, the channel might still exhibit zero quantum capacity, as 0.389 is the lower bound threshold for non-zero capacity. In high extraction efficiency scenarios shown in Fig. 4.15 (b), the EoF increases moderately. But this increase might not significantly enhance quantum capacity. Utilizing multiple cavities in parallel quantum communication could be more effective than concatenation in such cases, especially if the entanglement increases is less significant.

However, when ζ is moderate, the teleportation channel ($k = 1$) has zero quantum capacity regardless of the cooperativity. This is due to less entanglement. Whereas the concatenation approach ($k = 2$) can achieve non-zero capacity by increasing entanglement. As shown in Fig. 4.16, when $\zeta_o = \zeta_m = 0.65$, the teleportation channel with $k = 1$ has zero capacity, while with $k > 1$, it achieves non-zero capacity.

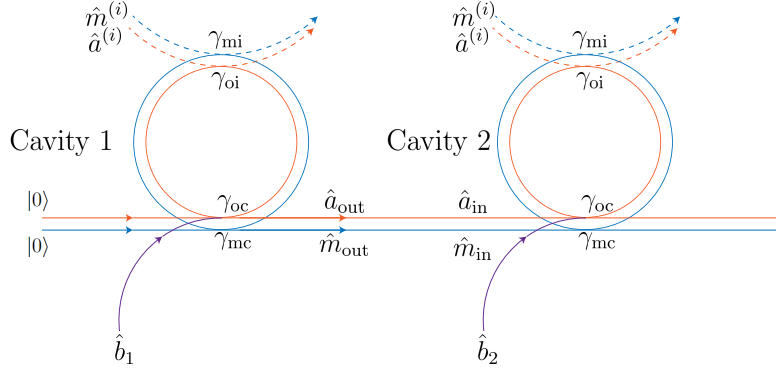


Figure 4.13: Generating entanglement by concatenating electro-optical ring cavities. The output modes from the first cavity, \hat{a}_{out} and \hat{m}_{out} , serve as the inputs for the second cavity. The strong laser pumps \hat{b}_1 and \hat{b}_2 enhance the non-linear interaction between the modes inside the cavity.

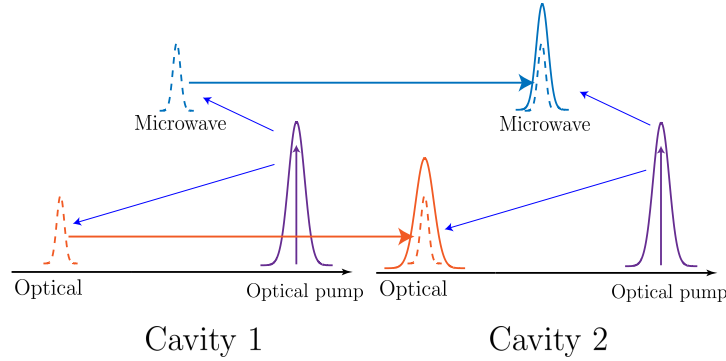


Figure 4.14: The spectrum of the microwave and optical modes in the cavity in Fig. 4.13.

4.6.3 Capacity Boost by Concatenation

When considering the quantum capacity of direct conversion and the teleportation-based transduction with $\zeta_m = \zeta_o = \zeta$, for direct conversion, the maximum value of Eq.(3.17) is achieved at $C = 1$, commonly referred to as critical coupling. Given that a single-mode Gaussian channel with $\eta \leq 1/2$ is anti-degradable, a ζ value greater than $\sqrt{1/2} \approx 0.707$ is required to achieve a non-zero quantum capacity in direct conversion scheme. Conversely, as depicted in Fig. 4.17 (a), the teleportation channel, upon optimizing κ , can exhibit a non-zero quantum capacity even for $\zeta = 0.7$. Moreover, concatenating cavities enhances not just the Entanglement of Formation (EoF) of the output state, as illustrated in Fig. 4.15 (b), but also the quantum capacity of the teleportation channel as shown in Fig. 4.17 (b). Therefore, the capacity is significantly boosted by augmenting the entanglement through the process of concatenating cavities. By strategically configuring the cavities in a concatenated setup, it is possible to optimize the entanglement levels and thus maximize the efficiency and performance of the quantum communication system.

However, while the Entanglement of Formation (EoF) increases with the number of concatenated cavities k , as illustrated in Fig. 4.15 (a), the quantum capacity lower bound (Q_{LB}) of the teleportation channel remains at zero for $\zeta \leq 0.5$. This phenomenon primarily arises from the minimal EoF and the additive noise previously discussed. The effect of this minimal entanglement on the quantum capacity is

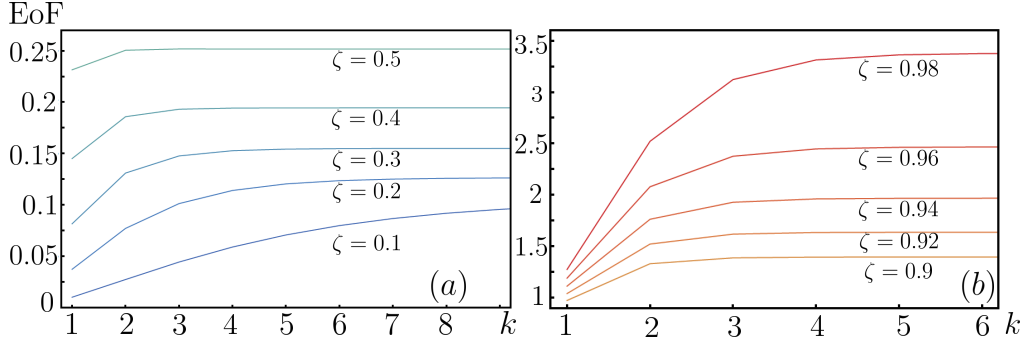


Figure 4.15: The Entanglement of Formation (EoF) of the output state for k concatenated cavities. The cooperativity $C = 0.1$, the noise $n_{\text{in}} = 0.1$ and (a) $\zeta_m = \zeta_o = \zeta \in \{0.1, 0.2, 0.3, 0.4, 0.5\}$ (b) $\zeta_m = \zeta_o = \zeta \in \{0.9, 0.92, 0.94, 0.96, 0.98\}$.

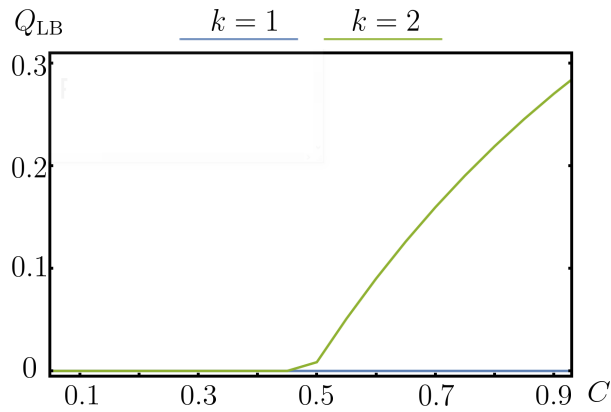


Figure 4.16: Quantum capacity of the teleportation channel versus cooperativity C with k uses of the cavity. The extraction efficiency $\zeta_o = \zeta_m = 0.65$ and $n_{\text{in}} = 0.1$.

profound: without sufficient EoF, the channel struggles to overcome the noise and achieve a non-zero capacity. This highlighted limitation underscores the critical balance between entanglement and noise in quantum communication systems.

The maximum quantum capacity achievable via cavity concatenation is depicted in Fig. 4.18. Here, we observe an enhancement in capacity in regions where the number of cavities used exceeds one ($k > 1$), revealing its potential as a viable strategy for boosting quantum capacity in teleportation channels.

4.6.4 Three Mode Teleportation

In the preceding sections, we discussed two distinct approaches to enhance the entanglement between microwave and optical oscillators. Another strategy to achieve higher entanglement is through three-mode quantum teleportation. The general scheme of teleportation and its implications are elaborated in the Theorem 23. The Hamiltonian of the cavity electro-optics, without suppressing either up-conversion or down-conversion, acts as a natural generator of three-mode entanglement involving two optical modes and one microwave mode. The Hamiltonian is expressed as:

$$\begin{aligned}\hat{H} &= \hat{H}_0 + \hbar g_1 (\hat{a}_1^\dagger \hat{m}^\dagger + \hat{a}_1 \hat{m}) + \hbar g_2 (\hat{a}_2^\dagger \hat{m} + \hat{a}_2 \hat{m}^\dagger), \\ \hat{H}_0 &= \hbar \omega_{o1} \hat{a}_1^\dagger \hat{a}_1 + \hbar \omega_{o2} \hat{a}_2^\dagger \hat{a}_2 + \hbar \omega_m \hat{m}^\dagger \hat{m}.\end{aligned}$$

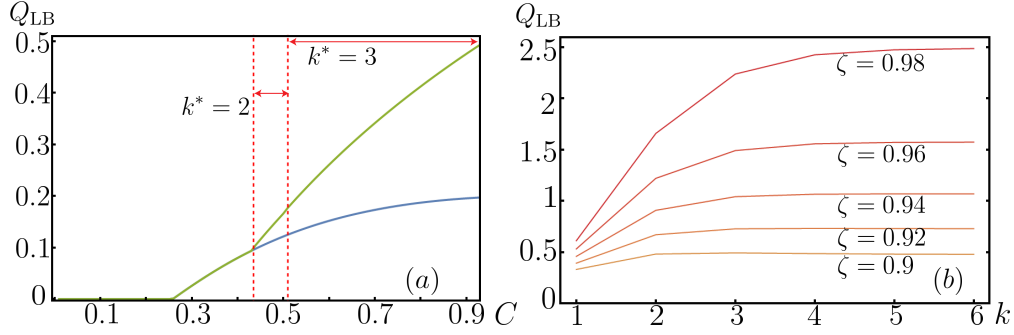


Figure 4.17: Quantum capacity lower bound Q_{LB} of the teleportation channel. (a) Capacity Q_{LB} versus the cooperativity C when $\zeta = 0.7$ and $n_{in} = 0.1$, while direct conversion has zero quantum capacity. The blue line represents $k = 1$ use of the cavity, while the green line represents multiple uses of the cavity that saturate the Q_{LB} . (b) Capacity Q_{LB} versus the number of cavities k for low cooperativity $C = 0.1$, $n_{in} = 0.1$ and $\zeta_m = \zeta_o = \zeta \in \{0.9, 0.92, 0.94, 0.96, 0.98\}$.

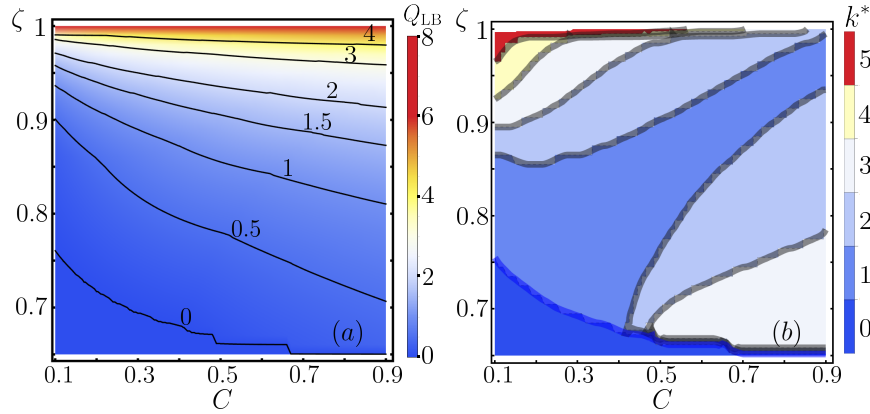


Figure 4.18: Contour plots of maximum quantum capacity and cavity number k^* versus $\zeta_m = \zeta_o = \zeta$ and cooperativity C . (a) Quantum capacity lower bound Q_{LB} of the teleportation channel. (b) The corresponding number of cavities k^* for $n_{in} = 0.1$. The gray regions indicate where the difference between k and $k + 1$ uses of cavities is less than 1%. The '0' region is where the quantum capacity is zero for any number of cavities k .

The primary challenge in this approach is to concentrate the entanglement between one optical mode and the microwave mode, through local operations involving the two optical modes. These optical modes are separated by $2\omega_m$ in the frequency domain. To couple them effectively, a strong microwave pump at $2\omega_m$ is essential, facilitating beam-splitter-like Hamiltonian interactions between the optical modes. However, given that these optical modes are generally weak and the coupling strength is constrained by the optical pump in electro-optic materials, realizing this method in the near term may be challenging.

Chapter 5

Continuous-Variable Quantum Error Correction

Quantum error correction is a crucial aspect of quantum information science, aimed at protecting quantum information from errors introduced by a quantum channel. The quantum error correction involves encoding a qubit (or an oscillator) with additional qubits (or oscillators) to safeguard the information and subsequently decoding it to recover the original message, despite the presence of errors.

The primary objective of quantum error correction is to devise a quantum code capable of shielding quantum information against various types of quantum errors. This chapter focuses on quantum error correction employing GKP states, specifically designed to correct random displacement errors. For a Gaussian channel, these errors are modeled as random additive Gaussian noise. Within the framework presented later, a general encoding using GKP states is equivalent to a general symplectic transformation. We explore different types of quantum information to be protected by GKP states, such as single GKP qubit and single oscillator, and various decoding strategies, including linear estimation and minimum mean square estimation.

In scenarios involving random displacement errors, the aim of quantum error correction is to identify an optimal quantum code—characterized by a general symplectic transform—that minimizes noise or optimizes the code distance. Various encoding types are introduced, such as the two-mode squeezing code, squeezing repetition code [53], and distributed two-mode squeezing code [54]. These codes are all examples of concatenated codes, as per the decomposition in Theorem 26. The two-mode squeezing code, for instance, involves applying two-mode squeezing transforms for all two-mode operations without single-mode operations. The squeezing repetition code uses sum gate as two-mode operation and single-mode squeezing as single-mode operation. The distributed two-mode squeezing code incorporates one two-mode squeezing and employs general beam splitters and single-mode phase rotations (passive transforms) for the remaining operations.

Due to the decomposition of a general symplectic transform, a general encoding can be interpreted as concatenated code as shown in Fig. 5.1. As illustrated in Fig. 5.1 (a), the encoding process in the last layer treats $n - 1$ oscillators as data and encodes this data into n oscillators through entanglement distribution. The local symplectic transforms on the $n - 1$ data and the relationship between this data and one additional ancilla are parameterized by the circuitry of the last layer. This process is then repeated, encoding $n - 2$ oscillators into $n - 1$ oscillators, as shown in Fig.

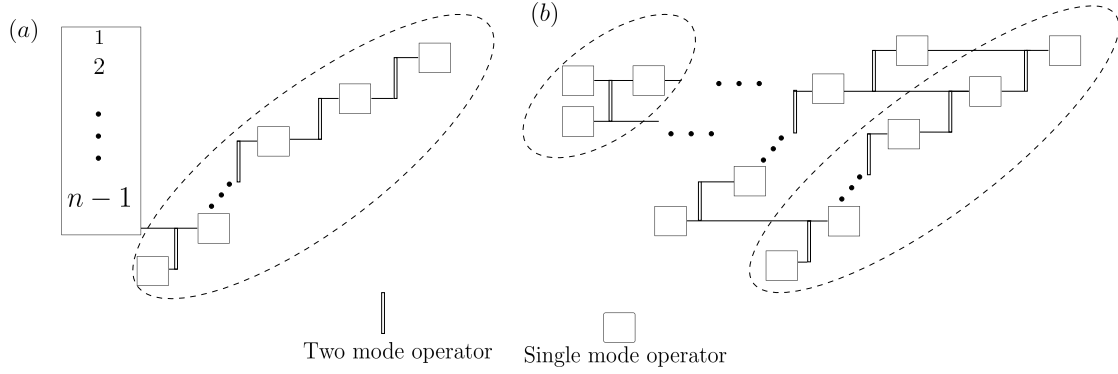


Figure 5.1: Decomposition of encoding.

5.1 (b), constructing the code recursively. Given that the code is a concatenation, the decoding process can also be designed concatenatively. We start by decoding the last oscillator from the $n - 1$ oscillators to extract its information. After the first decoding layer, the last oscillator becomes independent of the remaining oscillators. If adding more oscillators does not improve error correction, the last layer's circuit can be adjusted to the identity, preventing additional noise infiltration. This strategic design of coding and decoding layers highlights the adaptability and robustness of concatenated quantum error correction schemes in mitigating quantum errors.

5.1 Stabilizer Formalism

We begin by introducing the stabilizer formalism, a powerful framework for describing both discrete and continuous-variable quantum error correction codes. The stabilizer formalism provides a straightforward path for the experimental implementation of codewords. In this framework, the elements of the stabilizers are commuting operations. In the experiment, if we apply these stabilizers repetitively, the state of the quantum system is mapped to fully mixed states within the code space. To obtain a quantum bit (qubit) from the fully mixed state, one just measures one of the stabilizer elements. This effectively determines the state of qubit, represented by 0 or 1 according to the measurement result.

5.1.1 Stabilizer Formalism on Discrete Qubits

In the realm of discrete quantum error correction, quantum information is encoded as a qubit and the error is characterized by discrete error such as qubit flip and qubit phase flip. A qubit is expressed as:

$$|\psi\rangle = a|0\rangle + b|1\rangle = \begin{pmatrix} a \\ b \end{pmatrix},$$

where a and b are complex numbers satisfying the normalization condition $|a|^2 + |b|^2 = 1$. Operations on single qubit include the Pauli operators X, Y, Z , and operations on two qubits include the Controlled-NOT (CNOT) gate. The single qubit operators are generated by Pauli operations represented by the matrices

$$X = \begin{pmatrix} 0 & 1 \\ 1 & 0 \end{pmatrix}, \quad Y = \begin{pmatrix} 0 & -i \\ i & 0 \end{pmatrix}, \quad Z = \begin{pmatrix} 1 & 0 \\ 0 & -1 \end{pmatrix}. \quad (5.1)$$

In general, the Pauli group G_n on n qubits is the collection of all possible tensor products of Pauli operators, along with multiplicative factors of ± 1 and $\pm i$. The group G_1 , representing single qubit operations, is defined as:

$$G_1 = \{\pm I, \pm iI, \pm X, \pm iX, \pm Y, \pm iY, \pm Z, \pm iZ\},$$

whereas the Pauli group G_n for an n -qubit system is the tensor product of G_1 across all n qubits:

$$G_n = \bigotimes_{i=1}^n G_1.$$

All operators within G_1 can be represented as products of the X and Z operators, together with the constants ± 1 and $\pm i$. Therefore, we express G_1 as $G_1 = \langle X, Z \rangle$. Extending this to an n -qubit system, the Pauli group G_n is generated by independent operators X_i and Z_i :

$$G_n = \langle X_1, Z_1, \dots, X_n, Z_n \rangle.$$

The notation $X_1 Z_2$ is used to indicate an X operator acting on the first qubit and a Z operator on the second qubit, with the identity operator I applied to all remaining qubits.

The stabilizer S is a subgroup of the Pauli group G_n , characterized by the property that $-I \notin S$. The quantum states that remain invariant under all elements of S form the code space. This code space is crucial in quantum error correction, as defined in [55]:

$$\mathcal{C}(S) = \{|\psi\rangle \mid S|\psi\rangle = |\psi\rangle\}. \quad (5.2)$$

It's important to note that the exclusion of $-I$ from S is a necessary condition for the existence of a nontrivial state that is stabilized by S . This condition is equivalent to stating that all operators within S commute. From an algebraic perspective, only commuting operators can generate a stable system, while anti-commuting operators lead to the creation of subsystems.

In discrete quantum error correction, an interesting relationship exists between the number of qubits embedded in the code space and the number of generators of stabilizers. This relationship is formalized in the following lemma:

Lemma 35 *Let S be a stabilizer with $n - k$ independent generators, denoted as $S = \langle g_1, \dots, g_{n-k} \rangle$, and belonging to the Pauli group G_n . Then, the number of states stabilized by S is 2^k . Consequently, the code space defined by S is isomorphic to the state space of k qubits.*

The proof of this lemma elucidates the fundamental principles of quantum error correction in the discrete setting and is detailed in [56]. The first part comes from the fact that each g_i divides the state space by two equal parts. And the second part comes from the fact that all operators that permute the state space are Pauli operators. For example, consider the $[[3, 1, 1]]$ qubit code, defined by the stabilizer $S = \langle Z_1 Z_2, Z_2 Z_3 \rangle$. Let's start with the generator $g_1 = Z_1 Z_2$ and consider the state space of n qubits, $H^{\otimes n} = \text{span}\{|000\rangle, |001\rangle, |010\rangle, |011\rangle, |100\rangle, |101\rangle, |110\rangle, |111\rangle\}$.

Since $Z_1 Z_2$ is a Pauli operator, it only has eigenvalues of ± 1 . Thus, the states satisfying $g_1 |\psi\rangle = |\psi\rangle$ form a subspace of equal dimension to the space defined by $g_1 |\psi\rangle = -|\psi\rangle$. We can represent $H^{\otimes n}$ as $H_1 \oplus H_1^\perp$, where $H_1 = \text{span}\{|000\rangle, |001\rangle, |110\rangle, |111\rangle\}$.

Focusing on the state space H_1 and considering the operator $g_2 = Z_2 Z_3 \in S$, g_2 again divides the space evenly, resulting in $H_1 = H_2 \oplus H_2^\perp$, where $H_2 = \text{span}\{|000\rangle, |111\rangle\}$. The code space H_2 is isomorphic to a single qubit system, with logical operators defined as $\bar{X} = X_1 X_2 X_3$ and $\bar{Z} = Z_1 Z_2 Z_3$. These logical operators act such that \bar{X} maps $|000\rangle$ to $|111\rangle$, and \bar{Z} maps $|111\rangle$ to $-|111\rangle$.

The logical operators do not fix the code word $|0\rangle$ or $|1\rangle$ themselves but rather preserve the code space by permuting the code words within it. These logical operators, in conjunction with the stabilizer, form the centralizer, which fixes the entire code space. This relationship is formalized in the following definition:

Definition 36 *The centralizer of a subgroup S within the full group G is defined as $\mathcal{Z}(S) = \{g \in G \mid gs = sg, \forall s \in S\}$. In the context of stabilizer codes, the quotient group $\mathcal{Z}(S)/S$ represents the group of logical operators, denoted as $\{\bar{X}_1, \bar{Z}_1, \dots, \bar{X}_k, \bar{Z}_k\}$.*

Since the stabilizer fixes the code space, it is possible to obtain an error syndrome by measuring the stabilizer elements without disturbing the code word. The error syndrome is a set of outcomes $\{1, -1, \dots, 1\}$, corresponding to the eigenvalues $+1$ and -1 . If all outcomes are $+1$, the error syndrome indicates that no error has been detected, and we can assume the state remains error-free.

On the other hand, consider a scenario where, the measurement of s_2 yields an outcome of -1 . This error syndrome suggests that the state has deviated from the code word, necessitating the application of an appropriate corrective operation to map the state back to the code word space. In this case, the state resides in the coset of the code word $\mathcal{C}(S)$. The coset is stabilized by $\langle s_1, -s_2, \dots, s_{n-k} \rangle$. And to correct the error, we apply some logical operation to map the coset back to the code space stabilized by $\langle s_1, s_2, \dots, s_{n-k} \rangle$. The set of error operators that can be effectively corrected by the stabilizer S comprises Pauli operators $\{E_i\}$, with the condition that $E_j^\dagger E_i \notin \mathcal{Z}(S) - S$ for all i and j , as detailed in [57].

5.1.2 Stabilizer Formalism on GKP Qubits

The stabilizer formalism is similarly applicable to continuous-variable quantum error correction using GKP states, as established in [31]. GKP states can be interpreted as a symplectic lattice, further elaborated in [58, 59]. Consider a set of displacement operators defined as $\hat{D}(\sqrt{2\pi}m_i) = e^{-i\sqrt{2\pi}m_i^\top \Omega \hat{x}}$, where m_i is a $2n$ -dimensional vector, and i ranges from 1 to s . Since

$$\hat{D}(\sqrt{2\pi}m_i)\hat{D}(\sqrt{2\pi}m_j) = \hat{D}[\sqrt{2\pi}(m_i + m_j)]e^{i\pi m_i^\top \Omega m_j}, \quad (5.3)$$

$\hat{D}(\sqrt{2\pi}m_i)$ and $\hat{D}(\sqrt{2\pi}m_j)$ commute if $m_i^\top \Omega m_j \in \mathbb{Z}$. The GKP states can be formally described within the stabilizer formalism.

Definition 37 *A code space $\mathcal{C}(S)$ with a stabilizer can be defined as independent vectors m_i by follows:*

$$S(\mathbf{M}) = \langle \hat{D}(\sqrt{2\pi}m_1), \dots, \hat{D}(\sqrt{2\pi}m_s) \rangle, \quad (5.4)$$

where $m_i^\top \Omega_{2n} m_j \in \mathbb{Z}$ for all i, j . The code space includes n -mode GKP states generated by the matrix $\mathbf{M} = (m_1, \dots, m_s)$.

Writing $\mathbf{M} = (m_1, \dots, m_s)$ as matrix with columns as m_i , the set of operators is a stabilizer if

$$\mathbf{M}^\top \Omega_{2n} \mathbf{M} = A_{s \times s}, \quad (5.5)$$

where A is an anti-symmetric matrix with integer elements. GKP states can be represented as an infinite sum of eigenstates of the operators \hat{q} and \hat{p} . In the microwave frequency domain, GKP states can be prepared using a controlled displacement gate. This gate leverages the weak coupling region between a superconducting qubit and a microwave mode. Given that S is a group, the displacement operator $(-1)^{a_1 a_2 A_{12}} \hat{D}[\sqrt{2\pi}(a_1 m_1 + a_2 m_2)]$, where a_i is an integer, also constitutes an element of the stabilizer.

Thus we can conceptualize the displacement operators in the stabilizer as forming a s -dimensional lattice in the space \mathbb{R}^{2n} . This lattice is denoted as

$$\mathcal{L}(\mathbf{M}) = \left\{ \sum_{i=1}^s a_i m_i \mid a_i \in \mathbb{Z} \right\}, \quad (5.6)$$

where \mathbf{M} is the lattice generator matrix. The independence of the columns of \mathbf{M} is equivalent to the independence of the lattice basis vectors, implying that \mathbf{M} must be of full rank. Moreover, two lattices are considered identical if their generator matrices \mathbf{M}_1 and \mathbf{M}_2 can be transformed into each other through linear combinations with integer coefficients.

Lemma 38 *Two matrices \mathbf{M}_1 and \mathbf{M}_2 generate the same lattice if and only if $\mathbf{M}_1 = \mathbf{M}_2 \mathbf{N}$ for some invertible matrix $\mathbf{N}_{s \times s}$ with integer elements. The matrix \mathbf{N} satisfying these conditions is referred to as a unimodular matrix.*

Proof. The condition for generating the same lattice is that one basis can be derived from the other. Therefore, we have $\mathbf{M}_1 = \mathbf{M}_2 \mathbf{N}$ and $\mathbf{M}_2 = \mathbf{M}_1 \mathbf{N}'$ for some integer matrices \mathbf{N} and \mathbf{N}' . This leads to $\mathbf{M}_2 = \mathbf{M}_1 \mathbf{N}' = \mathbf{M}_2 \mathbf{N} \mathbf{N}'$. Given that \mathbf{M}_2 has independent columns, it must be of full rank. Consequently, $\mathbf{N} \mathbf{N}' = \mathbf{I}_s$ and $\mathbf{N}' = \mathbf{N}^{-1}$. Taking the determinant of both sides yields $\det(\mathbf{N}) \det(\mathbf{N}') = 1$. As the elements of \mathbf{N} and \mathbf{N}' are integers, so are $\det(\mathbf{N})$ and $\det(\mathbf{N}')$. Hence, $\det(\mathbf{N})$ must be either 1 or -1 . ■

Lemma 39 *Given a matrix \mathbf{M} such that $\mathbf{M}^\top \Omega_{2n} \mathbf{M}$ is an integer matrix, there exists a unimodular matrix \mathbf{N} such that*

$$\mathbf{N}^\top \mathbf{M}^\top \Omega_{2n} \mathbf{M} \mathbf{N} = \oplus_{i=1}^k \begin{pmatrix} 0 & d_i \\ -d_i & 0 \end{pmatrix} \oplus \mathbf{0}_{s-2k}. \quad (5.7)$$

A proof can be found in [60] by constructing \mathbf{N} with greatest common divisors. It can also be proved directly by the Lemma 8 with module theory. With the above Lemma, we see that the stabilizer group defined in Eq. (5.5) can be generated by a standard form

$$\{(-1)^{\phi(\tilde{m}_1)} \hat{D}(\sqrt{2\pi} \tilde{m}_1), \dots, (-1)^{\phi(\tilde{m}_s)} \hat{D}(\sqrt{2\pi} \tilde{m}_s)\}, \quad (5.8)$$

where $(-1)^{\phi(\tilde{m}_1)}$ is the sign that takes values $+1$ or -1 and

$$\tilde{\mathbf{M}}^\top \Omega_{2n} \tilde{\mathbf{M}} = \oplus_{i=1}^k \begin{pmatrix} 0 & d_i \\ -d_i & 0 \end{pmatrix} \oplus \mathbf{0}_{s-2k}. \quad (5.9)$$

Error Syndrome and Error Estimation in Standard Form

The state fixed by the stabilizer S in Eq. (5.5) is resistant to additive noise $\hat{D}(\sqrt{2\pi}\boldsymbol{\xi})$, where $\boldsymbol{\xi}$ is a $2n$ dimensional random vector. Consider a stabilizer generated by \mathbf{M} , which is in the standard form, with possible constant phase ϕ_i :

$$S = \langle e^{i\phi_1} \hat{D}(\sqrt{2\pi}m_1), \dots, e^{i\phi_{2n}} \hat{D}(\sqrt{2\pi}m_{2n}) \rangle,$$

where we assume $s = 2n$. As columns of \mathbf{M} are independent, we can represent $\boldsymbol{\xi}$ as $\sum_i a_i m_i = \mathbf{M}\mathbf{a}$. Since $\mathcal{C}(S)$ is fixed by S , in the Heisenberg picture, $\hat{D}(\sqrt{2\pi}\boldsymbol{\xi})\mathcal{C}(S)$ is fixed by

$$\begin{aligned} \hat{D}(\sqrt{2\pi}\boldsymbol{\xi})S\hat{D}^\dagger(\sqrt{2\pi}\boldsymbol{\xi}) &= \langle e^{i\phi_1} e^{i2\pi m_1^\top \Omega \boldsymbol{\xi}} \hat{D}(\sqrt{2\pi}m_1), \dots \rangle, \\ &= \langle e^{i\phi_1} e^{i2\pi d_1 a_2} \hat{D}(\sqrt{2\pi}m_1), e^{i\phi_2} e^{-i2\pi d_1 a_1} \hat{D}(\sqrt{2\pi}m_2), \dots \rangle. \end{aligned} \quad (5.10)$$

Stabilizer measurement gives us the phase value $2\pi d_1 a_2$ in module of 2π . We note that a stabilizer measurement can be physically implemented by a sum gate between the GKP qubit and a GKP ancilla [31]. The error syndrome is the set of stabilizer measurements given by

$$\begin{aligned} \mathbf{e} &= [a_2 \bmod (1/d_1), -a_1 \bmod (1/d_1), \dots, -a_{2k} \bmod (1/d_k)]^\top \\ &= \Omega(\mathbf{a} \bmod \mathbf{d}^{-1}). \end{aligned}$$

Then we have $\mathbf{a} = -\Omega\mathbf{e} + \mathbf{k}/\mathbf{d}$, where $\mathbf{k} = (k_1, \dots, k_{2n})^\top$. The relation between the error syndrome \mathbf{e} and the error $\boldsymbol{\xi}$ is

$$\boldsymbol{\xi} = \mathbf{M}\mathbf{a} = -\mathbf{M}\Omega\mathbf{e} + \mathbf{M}(\mathbf{k}/\mathbf{d}).$$

Without prior knowledge of the error distribution of $\boldsymbol{\xi}$, the random vector \mathbf{k} remains unknown. Assuming that smaller noises are more probable, we can neglect the addition of \mathbf{k} and estimate the error $\boldsymbol{\xi}$ linearly. The linear estimation is given by:

$$\tilde{\boldsymbol{\xi}} = -\mathbf{M}\Omega\mathbf{e}. \quad (5.11)$$

Error syndrome detection is performed using sum gates, which are controlled gates between the code and ancilla GKP qubits. So detecting error syndrome does not affect the output state. Post-error detection, the code space is fixed by Eq. (5.10). To correct the displacement error after error detection, we apply the displacement operation $\hat{D}(-\sqrt{2\pi}\tilde{\boldsymbol{\xi}})$, mapping the code that experienced displacement error back to the original code space fixed by Eq. (5.4).

If the absolute values of $\{a_1, \dots, a_{2n}\}$ are smaller than $\{1/d_1, \dots, 1/d_n\}$, the state is perfectly recovered. Otherwise, the actual displacement error exceeds the estimated error. After error correction, the state is displaced by $\hat{D}[\sqrt{2\pi}(\boldsymbol{\xi} + \mathbf{M}\Omega\mathbf{e})] = \hat{D}(\sqrt{2\pi}\mathbf{M}\mathbf{k}/\mathbf{d})$. Although this extra error displacement $\sqrt{2\pi}\mathbf{M}\mathbf{k}/\mathbf{d}$ commutes with the code space, it transits one code word to another. It effectively permutes the code word, thus constituting a logical error.

Given foreknowledge of the error distribution $\boldsymbol{\xi}$, it is possible to estimate \mathbf{k} based on \mathbf{e} to minimize logical errors. Assigning $\tilde{\mathbf{k}}$ according to the error distribution of $\boldsymbol{\xi}$ is also referred as post-correction. The optimal error estimation method for the post-correction is the Maximally Likelihood (ML) estimation [61]. The Minimal Energy (ME) estimation approximately solves the ML estimation and has been discussed in [61, 59, 60]. The ME estimation is also named as closest lattice point decoder and recent stimulation results are shown in [60]. However, due to the complexity of the closest vector problem and the fact that it is NP-hard, it is not further discussed here.

Centralizer and Logic Error

The centralizer of the stabilizer $S(\mathbf{M})$ consists of displacement operators that commute with the elements of $S(\mathbf{M})$. A displacement operator $\hat{D}(\sqrt{2\pi}v)$ commutes with S if $\mathbf{M}^\top \Omega v$ is an integer. To identify a set of operators that generates $\mathcal{Z}(S)$, we can set $\mathbf{M}^\top \Omega v = \pm 1$. Let \mathbf{M}_\perp generates $\mathcal{Z}(S)$. Setting

$$\mathbf{M}^\top \Omega \mathbf{M}_\perp = \Omega, \quad (5.12)$$

we find

$$\mathbf{M}_\perp = (\mathbf{M}^\top \Omega)^{-1} \Omega = \mathbf{M}(\mathbf{M}^\top \Omega \mathbf{M})^{-1} \Omega. \quad (5.13)$$

Eq.(5.10) can be generalized when \mathbf{M} is not in the standard form with this setting. For displacement error $\hat{D}(\sqrt{2\pi}\xi)$, the error syndrome associated with the generator matrix \mathbf{M} is given by

$$\mathbf{e} = \mathbf{M}^\top \Omega \xi \pmod{1}. \quad (5.14)$$

The relationship between the error syndrome and the true displacement error ξ can be found by

$$\xi = \Omega^{-1} \mathbf{M}^{-\top} (\mathbf{e} + \mathbf{k}) = -\mathbf{M}_\perp \Omega [\mathbf{e} + \mathbf{k}(\xi)], \quad (5.15)$$

where $\mathbf{k}(\xi)$ is an integer vector dependent on the value of ξ and we use Eq. (5.14). Estimating $\tilde{\xi} = -\mathbf{M}_\perp \Omega [\mathbf{e} + \tilde{\mathbf{k}}(\mathbf{e})]$ and applying the anti-displacement, after the error correction, there might be a logical error given by

$$\mathbf{v} = \xi - \tilde{\xi} = \mathbf{M}_\perp \Omega [\tilde{\mathbf{k}}(\mathbf{e}) - \mathbf{k}(\xi)].$$

The vector \mathbf{v} is a lattice point of $\mathcal{L}(\mathbf{M}_\perp)$. If it is a lattice point of \mathbf{M} as well, there is no logical error. Otherwise, there is logical error. Consider the code word $|0\dots 0\rangle$, which is the eigenstate fixed by $\{Z_i\}$ and S . When \mathbf{v} corresponds to the lattice point of \mathbf{M} . The state after error correction is still fixed by $S\{Z_i\}S^\dagger = \{Z_i\}$. Then it is the code word $|0\dots 0\rangle$. If \mathbf{v} is not a lattice point of $\mathcal{L}(\mathbf{M}_\perp)$, for example, it corresponds to X_1 . The the state after the error correction is fixed by $X_1\{Z_i\}X_1^\dagger = \{-Z_1, Z_i\}$. The code word $|0\dots 0\rangle$ becomes the code word $|10\dots 0\rangle$. The group $\mathcal{Z}(S)/S$ characterizes all the logical operators X_i, Z_i , and $\mathcal{L}(\mathbf{M}_\perp)/\mathcal{L}(\mathbf{M})$ characterizes all the logical errors. Given a stabilizer generated by \mathbf{M} , if \mathbf{M} is in standard form, the centralizer can be easily determined. Using the shorthand notation $\mathbf{D} = \text{diag}(d_1, d_1, \dots, d_n, d_n)$, we have

$$\mathbf{M}^\top \Omega \mathbf{M} = \bigoplus_{i=1}^n \begin{pmatrix} 0 & d_i \\ -d_i & 0 \end{pmatrix} = \Omega \mathbf{D},$$

$$\mathbf{M}_\perp = \mathbf{M}(\Omega \mathbf{D})^{-1} \Omega = \mathbf{M} \mathbf{D}^{-1}.$$

The stabilizer and centralizer are given by

$$S = \langle \hat{D}(\sqrt{2\pi}m_1), \dots, \hat{D}(\sqrt{2\pi}m_{2n}) \rangle. \quad (5.16)$$

$$\mathcal{Z}(S) = \langle \hat{D}(\sqrt{2\pi}m_1/d_1), \dots, \hat{D}(\sqrt{2\pi}m_{2n}/d_n) \rangle. \quad (5.17)$$

Two operators $\hat{D}(\sqrt{2\pi}a)$ and $\hat{D}(\sqrt{2\pi}b)$ anti-commute if $a^\top \Omega b$ equals $1/2$ plus an integer. Generally, the system defined by operators $\{\hat{D}(\sqrt{2\pi}m_1/d_1), \hat{D}(\sqrt{2\pi}m_2/d_1)\}$ with $(m_1/d_1)^\top \Omega (m_2/d_1) = 1/d$ forms a d -level subsystem. Therefore, the code space can be embedded into a composite system, where each subsystem is a d_i -level system. If $d_i = 2$ for all i , then the code space can host k GKP qubits. The columns of \mathbf{M}_\perp equivalently define the Pauli operators $\{X_1, Z_1, \dots, X_k, Z_k\}$.

GKP Qubit and Canonical GKP State

A canonical GKP state in an oscillator is given by

$$\mathbf{M} = \mathbf{I}_2, \quad \mathbf{M}_\perp = \mathbf{I}_2. \quad (5.18)$$

Since $\mathcal{L}(\mathbf{M}_\perp) = \mathcal{L}(\mathbf{M})$, there is no encoded qubit. The state fixed by the stabilizer is an infinite sum of q eigenstates.

$$|\square\rangle = \sum_{k=-\infty}^{\infty} |q = \sqrt{2\pi}k\rangle = \sum_{k=-\infty}^{\infty} |p = \sqrt{2\pi}k\rangle. \quad (5.19)$$

The second equality comes from the Fourier transform of the comb function.

Lemma 40 $|\psi\rangle = \sum_{k \in \mathbb{Z}} e^{ick} |q = ak + b\rangle = \sum_{k \in \mathbb{Z}} e^{ib(\frac{2\pi k}{a} - \frac{c}{a})} |p = k\frac{2\pi}{a} - \frac{c}{a}\rangle.$

Proof. We use the identities $\langle q|p\rangle = e^{-iqp}$ and $\sum_k e^{-i\omega kT} = \frac{2\pi}{T} \sum_k \delta(\omega - k\frac{2\pi}{T})$ in the calculations.

$$\begin{aligned} \sum_{k=-\infty}^{\infty} e^{ick} |q = ak + b\rangle &= \int_{\mathbb{R}} dp |p\rangle\langle p| \sum_{k=-\infty}^{\infty} e^{ick} |q = ak + b\rangle \\ &= \int_{\mathbb{R}} dp \int_{\mathbb{R}} dq |p\rangle\langle p| q\rangle \langle q| \sum_{k=-\infty}^{\infty} e^{ick} |q = ak + b\rangle \\ &= \sum_{k=-\infty}^{\infty} \int_{\mathbb{R}} dp \int_{\mathbb{R}} dq |p\rangle e^{iqp} e^{ick} \delta(q - ak - b) \\ &= \int_{\mathbb{R}} dp \sum_{k=-\infty}^{\infty} e^{ia(p+c/a)k} e^{ibp} \\ &= \int_{\mathbb{R}} dp |p\rangle \sum_{k=-\infty}^{\infty} \delta(p + c/a - 2\pi k/a) e^{ibp} \\ &= \sum_{k=-\infty}^{\infty} e^{ib(\frac{2\pi k}{a} - \frac{c}{a})} |p = k\frac{2\pi}{a} - \frac{c}{a}\rangle. \end{aligned}$$

■

A square-grid GKP qubit in an oscillator is given by

$$\mathbf{M} = \sqrt{2}\mathbf{I}_2, \quad \mathbf{M}_\perp = 1/\sqrt{2}\mathbf{I}_2.$$

As shown in Eq. (5.16) and Eq. (5.17), a qubit is encoded by the stabilizer. The logical operators are

$$X = e^{-i\sqrt{\pi}\hat{p}}, \quad Z = e^{i\sqrt{\pi}\hat{q}}.$$

The code word $|0\rangle$ and $|1\rangle$ are +1 and -1 eigenstates of Z given by

$$\begin{aligned} |0\rangle &= \sum_{k=-\infty}^{\infty} |q = 2\sqrt{\pi}k\rangle = \sum_{k=-\infty}^{\infty} |p = \sqrt{\pi}k\rangle, \\ |1\rangle &= \sum_{k=-\infty}^{\infty} |q = \sqrt{\pi} + 2\sqrt{\pi}k\rangle = \sum_{k=-\infty}^{\infty} e^{i\pi k} |p = \sqrt{\pi}k\rangle. \end{aligned}$$

In general, a GKP qubit in an oscillator can be defined by a 2-by-2 symplectic transform \mathbf{S} . Since the centralizer \mathbf{M}_\perp satisfies $\mathbf{M}_\perp^\top \Omega \mathbf{M}_\perp = 1/2\Omega$, then $\mathbf{M}_\perp = \mathbf{S}/\sqrt{2}$ for some symplectic transform \mathbf{S} . And $\mathbf{M} = \sqrt{2}\mathbf{S}$. When $\mathbf{S} = \mathbf{I}_2$, the GKP qubit is encoded in a square lattice \mathcal{L}_\square . When $\mathbf{S} = \text{diag}(r, 1/r)$, it is a rectangular lattice. And

$$\mathbf{S} = \frac{\sqrt{2}}{3^{\frac{1}{4}}} \begin{pmatrix} 1 & -1/2 \\ 0 & \sqrt{3}/2 \end{pmatrix}, \quad (5.20)$$

for the hexagonal lattice \mathcal{L}_\triangle . If a Gaussian transform $\hat{U}_\mathbf{S}$ is applied on a square-grid GKP qubit, the code space is fixed by $\hat{U}_\mathbf{S} \hat{U}_\mathbf{S}^\dagger$. From Eq. (1.10), the displacement operator transforms according to

$$e^{-i\sqrt{2\pi}m^\top \Omega \mathbf{S}^{-1} \hat{\mathbf{x}}} = e^{-i\sqrt{2\pi}m^\top \mathbf{S}^\top \Omega \hat{\mathbf{x}}} = e^{-i\sqrt{2\pi}(Sm)^\top \Omega \hat{\mathbf{x}}}.$$

Therefore a single GKP qubit encoded in an oscillator can be obtained from a GKP qubit in a square lattice and a symplectic transform \mathbf{S} .

Equivalent Code

In the previous sections, we observed that the error syndrome of a code is $-\mathbf{M}^\top \Omega \boldsymbol{\xi} \pmod{1}$, and the logical error after the error correction is determined by $\mathcal{L}(\mathbf{M}_\perp)/\mathcal{L}(\mathbf{M})$. Thus, two codes with generator matrices \mathbf{M}_1 and \mathbf{M}_2 are equivalent for correcting displacement errors if they generate the same lattice. Two equivalent codes may not have the same error syndrome, since when $\mathbf{M} \rightarrow \mathbf{M}\mathbf{N}$, then

$$\mathbf{e} = -\mathbf{M}^\top \Omega \boldsymbol{\xi} \pmod{1} \rightarrow \mathbf{e}' = -\mathbf{N}^\top \mathbf{M}^\top \Omega \boldsymbol{\xi} \pmod{1}.$$

Two equivalent codes may not have the same stabilizer S or code words. For example, consider a GKP qubit encoded in an oscillator with different stabilizers S_1 and S_2 given by

$$\begin{aligned} S_1 &= \langle e^{i2\sqrt{\pi}\hat{p}}, e^{-i2\sqrt{\pi}\hat{q}} \rangle, \\ S_2 &= \langle e^{i2\sqrt{\pi}\hat{p}}, -e^{-i2\sqrt{\pi}\hat{q}} \rangle. \end{aligned}$$

The centralizers are the same with logical operator given by

$$X = e^{i\sqrt{\pi}\hat{p}}, \quad Z = e^{-i\sqrt{\pi}\hat{q}}.$$

The code words $|0\rangle$ and $|1\rangle$ are obtained by +1 and -1 eigenstates of Z and S . The code words with stabilizer S_1 are

$$\begin{aligned} |0\rangle &= \sum_k |q = 2\sqrt{\pi}k\rangle = \sum_k |p = \sqrt{\pi}k\rangle, \\ |1\rangle &= \sum_k |q = 2\sqrt{\pi}k + \sqrt{\pi}\rangle = \sum_k e^{i\pi k} |p = \sqrt{\pi}k\rangle. \end{aligned}$$

And the code words with the stabilizer S_2 are

$$\begin{aligned} |0\rangle &= \sum_k |q = 2\sqrt{\pi}k + \sqrt{\pi}/2\rangle = \sum_k e^{i\pi k/2} |p = \sqrt{\pi}k\rangle, \\ |1\rangle &= \sum_k |q = 2\sqrt{\pi}k + 3\sqrt{\pi}/2\rangle = \sum_k e^{i3\pi k/2} |p = \sqrt{\pi}k\rangle. \end{aligned}$$

From Lemma 39, for any code with generator matrix \mathbf{M} , we can find an equivalent code with generator matrix $\tilde{\mathbf{M}} = \mathbf{M}\mathbf{N}$ such that $\tilde{\mathbf{M}}$ is in standard form. Therefore, it is sufficient to consider all matrices with \mathbf{M} in standard form, and the centralizer is given by $\mathbf{M}\mathbf{D}^{-1}$. For GKP qubit codes, we can summarize the stabilizer formalism in group structure as

$$\begin{aligned} \text{Logical Operators: } & \mathcal{Z}(S)/S, \\ \text{Logical Errors: } & \mathcal{L}(\mathbf{M}_\perp)/\mathcal{L}(\mathbf{M}). \end{aligned}$$

Another equivalence arises from considering homogeneous noises ξ . We say the distribution of the noise $P(\xi)$ has some symmetry \mathbf{Q} if $P(\mathbf{Q}\xi) = P(\xi)$. For homogeneous noise ξ , all \mathbf{Q} in the set $\text{Sp}(2n) \cap \text{O}(2n)$ do not change the probability density function (PDF) of the error distribution. In other words, rotating ξ by any \mathbf{Q} does not change the PDF. Two codes have the same performance if $\mathbf{M} \rightarrow \mathbf{Q}^{-1}\mathbf{M}$. Therefore for the homogeneous noise, two codes with generator matrices \mathbf{M}_1 and \mathbf{M}_2 are equivalent if they satisfy

$$\mathbf{M}_1 = \mathbf{Q}\mathbf{M}_2\mathbf{N}, \quad (5.21)$$

where $\mathbf{Q} \in \text{Sp}(2n) \cap \text{O}(2n)$ and \mathbf{N} is a unimodular matrix.

5.1.3 $[[n,k]]$ GKP Qubit Code

In this part, we discuss the $[[n,k]]$ GKP qubit code and show examples of the $[[n,k]]$ code. With the framework above, all equivalent codes can be generated by some symplectic transform. Consider a generator matrix \mathbf{M} with $s = 2n$ independent generators of stabilizer. When its normal form $\tilde{\mathbf{M}} = \mathbf{M}\mathbf{N}$ has $d_1 = d_2 \dots = d_{2k} = 2$ and $d_{2k+1} = \dots = d_{2n} = 1$, the stabilizer encodes k GKP qubits in n oscillators. Since

$$\tilde{\mathbf{M}}_\perp = \tilde{\mathbf{M}}[(1/2\mathbf{I}_{2k}) \oplus \mathbf{I}_{2n-2k}], \quad \tilde{\mathbf{M}}_\perp^\top \Omega \tilde{\mathbf{M}}_\perp = [(1/2\Omega_{2k}) \oplus \Omega_{2n-2k}],$$

the logical operator X_i, Z_i of the k qubits are given by the first $2k$ columns of $\tilde{\mathbf{M}}_\perp$.

Definition 41 A generator matrix \mathbf{M} encodes k qubits into n oscillators if its standard form $\tilde{\mathbf{M}}$ satisfies

$$\tilde{\mathbf{M}}^\top \Omega \tilde{\mathbf{M}} = (2\Omega_{2k}) \oplus (\Omega_{2n-2k}). \quad (5.22)$$

A code defined above can be generated by a symplectic transform \mathbf{S} . Indeed, one can find \mathbf{S} such that

$$\tilde{\mathbf{M}} = \mathbf{S}(\sqrt{2}\mathbf{I}_{2k} \oplus \mathbf{I}_{2n-2k}), \quad (5.23a)$$

$$\tilde{\mathbf{M}}_\perp = \mathbf{S} \left(\frac{1}{\sqrt{2}}\mathbf{I}_{2k} \oplus \mathbf{I}_{2n-2k} \right), \quad (5.23b)$$

$$\mathbf{B} = \mathbf{S}/\sqrt{2}. \quad (5.23c)$$

The basis \mathbf{B} corresponds to the whole Pauli group of n GKP qubits. $\mathcal{L}(\tilde{\mathbf{M}}_\perp)$ is a subgroup of $\mathcal{L}(\mathbf{B})$, so the k qubits code can be embedded to n qubits code.

Conversely, with a basis \mathbf{B} such that $\mathbf{B}^\top \boldsymbol{\Omega} \mathbf{B} = \frac{1}{2} \mathbf{I}_{2n}$, we can construct an $[[n, k]]$ code in different ways. The first approach is by scaling the basis. For this approach,

$$\begin{aligned} \mathbf{M} &= \mathbf{B} \left[(2\mathbf{I}_{2k}) \oplus \sqrt{2}\mathbf{I}_{2n-2k} \right], \\ \mathbf{M}^\top \boldsymbol{\Omega} \mathbf{M} &= (2\boldsymbol{\Omega}_{2k}) \oplus (\boldsymbol{\Omega}_{2n-2k}). \end{aligned}$$

The second approach is from the discrete variable code. In this approach, the basis \mathbf{B} is usually a direct product such as $\mathbf{B} = \frac{1}{\sqrt{2}} \mathbf{I}_{2n}$ for square-grid qubits and

$$\mathbf{B} = 3^{-1/4} \bigoplus_{i=1}^n \begin{pmatrix} 1 & -1/2 \\ 0 & \sqrt{3}/2 \end{pmatrix},$$

for hexagonal-grid qubits. Then one can effectively define a Pauli group with Pauli operators and identity

$$\begin{aligned} \{X_1, Z_1, \dots\} &= \{\hat{D}(\sqrt{2\pi}b_1), \hat{D}(\sqrt{2\pi}b_2), \dots\}, \\ \hat{\mathbf{1}} &= \langle \hat{D}(2\sqrt{2\pi}b_1), \hat{D}(2\sqrt{2\pi}b_2), \dots \rangle. \end{aligned}$$

An $[[n, k]]$ GKP qubit code can be obtained by an $[[n, k, d]]$ quantum qubit code with Pauli operators defined above. For example, $[[3, 1, 1]]$ qubit code has stabilizer $S = \langle Z_1 Z_2, Z_2 Z_3 \rangle$. The corresponding $[[3, 1]]$ GKP qubit code can be constructed by

$$\mathbf{M} = (b_2 + b_4, b_4 + b_6, 2b_1, b_2, 2b_3, 2b_5),$$

where $2b_1, b_2, 2b_3, 2b_5$ are chosen in any way such that the columns of \mathbf{M} are independent from each other. The first column corresponds to $Z_1 Z_2$ and the second column corresponds to $Z_2 Z_3$. To verify that the \mathbf{M} encodes 1 qubit, we calculate

$$\mathbf{M}^\top \boldsymbol{\Omega} \mathbf{M} = \begin{pmatrix} 0 & 0 & -1 & 0 & -1 & 1 \\ 0 & 0 & 0 & 0 & -1 & -1 \\ 1 & 0 & 0 & 1 & 0 & 0 \\ 0 & 0 & -1 & 0 & 0 & 0 \\ 1 & 1 & 0 & 0 & 0 & 0 \\ -1 & 1 & 0 & 0 & 0 & 0 \end{pmatrix} = \mathbf{A}.$$

Since $\det[\mathbf{A}] = d_1^2 d_2^2 d_3^2 = 4$, then (d_1, d_2, d_3) has to be $(1, 1, 2)$. Indeed, the generator matrix gives a $[[3, 1]]$ code.

5.2 Error Model

The quantum random displacement error channel for an n bosonic system is given by

$$\Phi_{P(\boldsymbol{\xi})}(\hat{\rho}) = \int_{\mathbb{R}^{2n}} d^{2n}\boldsymbol{\xi} P(\boldsymbol{\xi}) \hat{W}(\boldsymbol{\xi}) \hat{\rho} \hat{W}^\dagger(\boldsymbol{\xi}), \quad (5.24)$$

where $P(\boldsymbol{\xi})$ is the PDF of the random displacement $\boldsymbol{\xi}$. It is easy to verify that the channel is completely positive and trace-preserving. Moreover, concatenating two random displacement channels results in another random displacement channel.

$$\begin{aligned}
\Phi_{P_1(\boldsymbol{\xi})} \circ \Phi_{P_2(\boldsymbol{\xi})}(\hat{\rho}) &= \int_{\mathbb{R}^{2n}} d^{2n}\boldsymbol{\xi}_1 \int_{\mathbb{R}^{2n}} d^{2n}\boldsymbol{\xi}_2 P_1(\boldsymbol{\xi}_1) P_2(\boldsymbol{\xi}_2) \hat{W}(\boldsymbol{\xi}_1 + \boldsymbol{\xi}_2) \hat{\rho} \hat{W}^\dagger(\boldsymbol{\xi}_1 + \boldsymbol{\xi}_2) \\
&= \int_{\mathbb{R}^{2n}} d^{2n}\boldsymbol{\xi}_1 \int_{\mathbb{R}^{2n}} d^{2n}\boldsymbol{\xi} P_1(\boldsymbol{\xi}_1) P_2(\boldsymbol{\xi} - \boldsymbol{\xi}_1) \hat{W}(\boldsymbol{\xi}) \hat{\rho} \hat{W}^\dagger(\boldsymbol{\xi}) \\
&= \int_{\mathbb{R}^{2n}} d^{2n}\boldsymbol{\xi} [P_1 * P_2(\boldsymbol{\xi})] \hat{W}(\boldsymbol{\xi}) \hat{\rho} \hat{W}^\dagger(\boldsymbol{\xi}) \\
&= \Phi_{P_1 * P_2}(\hat{\rho}),
\end{aligned} \tag{5.25}$$

where $P_1 * P_2$ is the PDF of the convolution of two random variables. When passing through a random displacement channel, the characteristic function transforms as follows:

$$\begin{aligned}
\chi_{\Phi(\hat{\rho})}(\mathbf{t}) &= \text{Tr}[\hat{W}(\mathbf{t}) \int_{\mathbb{R}^{2n}} d^{2n}\mathbf{t}_1 P(\mathbf{t}_1) \hat{W}(\mathbf{t}_1) \hat{\rho} \hat{W}^\dagger(\mathbf{t}_1)] \\
&= \text{Tr}[\int_{\mathbb{R}^{2n}} d^{2n}\mathbf{t}_1 P(\mathbf{t}_1) e^{i\mathbf{t}_1^\top \mathbf{N} \mathbf{t}} \hat{\rho} \hat{W}(\mathbf{t})] \\
&= \tilde{P}(\mathbf{t}) \chi_{\hat{\rho}}(\mathbf{t}),
\end{aligned} \tag{5.26}$$

where $\tilde{P}(\mathbf{t}) = \int_{\mathbb{R}^{2n}} d^{2n}\mathbf{t}_1 P(\mathbf{t}_1) e^{i\mathbf{t}_1^\top \mathbf{N} \mathbf{t}}$ is the Fourier transform of $P(\mathbf{t})$. For a Gaussian channel with $\mathbf{T} = \mathbf{I}_{2n}$ and $\mathbf{d} = \mathbf{0}$, the channel is a random displacement channel with $P(\mathbf{t}) \propto e^{-\frac{1}{2}\mathbf{t}^\top \mathbf{N}^{-1} \mathbf{t}}$. If $\mathbf{N} = \text{diag}(\sigma_1^2, \sigma_1^2, \dots, \sigma_n^2)$, the multi-mode Gaussian channel is called independent additive white Gaussian noise (AWGN) channels, denoted as $\bigotimes_{\ell=1}^n \Phi_{\sigma_\ell^2}$. On the other hand, a general Gaussian channel can be transformed into independent AWGN channels by concatenating the general Gaussian channel with pre-processing and post-processing Gaussian channel. The pre-processing and post-processing can be quantum limited, i.e., the environment is in a vacuum state. As mentioned in subsection 1.2.3 and the Ref. [17], if the environment is vacuum, the channel is degradable. In the single-mode case, it is a pure amplification or pure loss channel and has a quantum capacity given by $\log\left(\frac{k}{|1-k|}\right)$.

Lemma 42 *Any multi-mode Gaussian channel characterized by \mathbf{T} , \mathbf{N} , and \mathbf{d} can be transformed into a product of independent AWGN channels, via Gaussian pre-processing only, post-processing only, or both Gaussian pre-processing and post-processing.*

Proof. Without loss of generality, we can assume $\mathbf{d} = \mathbf{0}$, since applying a displacement $\hat{D}(-\mathbf{d})$ first can cancel this term. The multi-mode Gaussian channel transforms the characteristic function as

$$\chi_{\Phi(\hat{\rho})}(\mathbf{t}) = \chi_{\hat{\rho}}(\mathbf{T}^\top \mathbf{t}) \exp\left(-\frac{1}{2}\mathbf{t}^\top \mathbf{N} \mathbf{t}\right). \tag{5.27}$$

We can concatenate this Gaussian channel with a Gaussian channel having $\mathbf{T}' = \mathbf{T}^{-1}$ and \mathbf{N}' . The concatenation can be pre-concatenation or post-concatenation. The resulting channel becomes AWGN channels with additive noise $\mathbf{T}^{-1} \mathbf{N} \mathbf{T}^{-\top} + \mathbf{N}' = \text{diag}(\sigma_1^2, \sigma_1^2, \dots, \sigma_n^2) = \boldsymbol{\Sigma}$. From Lemma 9, the Gaussian channel with $\mathbf{T}' = \mathbf{T}^{-1}$

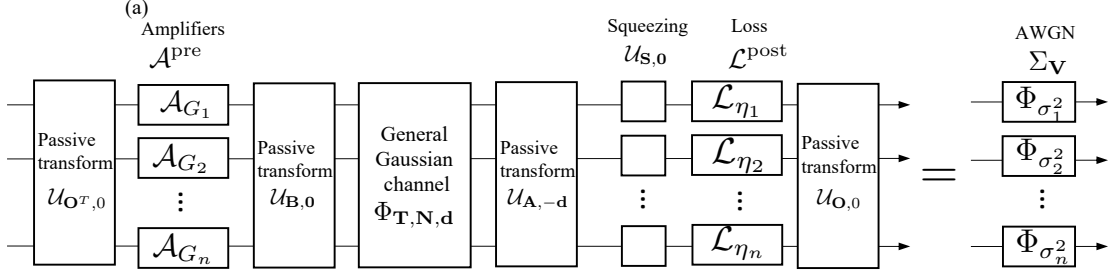


Figure 5.2: Schematic of the general Gaussian channel reduction scheme to a product of additive white Gaussian noise (AWGN) channels.

and \mathbf{N}' can be constructed by a symplectic transform \mathbf{S} between the system A and environment D as long as it satisfies:

$$\mathbf{N}' \pm \frac{i}{2}(\mathbf{\Omega} - \mathbf{T}^{-1}\mathbf{\Omega}\mathbf{T}^{-\top}) \geq 0,$$

which simplifies to

$$\mathbf{T}\mathbf{\Sigma}\mathbf{T}^{\top} - \mathbf{N} \pm \frac{i}{2}(\mathbf{\Omega} - \mathbf{T}\mathbf{\Omega}\mathbf{T}^{\top}) \geq 0.$$

Given \mathbf{T}' , this requirement can be met when \mathbf{N}' is sufficiently large. Another approach requires both pre-processing and post-processing as shown in Fig. 5.2. By singular value decomposition, $\mathbf{T} = \mathbf{A}^{-1}\mathbf{G}\mathbf{B}^{-1}$, where \mathbf{A} and \mathbf{B} are symplectic and orthogonal matrices, and \mathbf{G} is a positive diagonal matrix. Applying the general beam splitter \mathbf{B} and \mathbf{A} before and after the Gaussian channel, the concatenated channel has transmissivity $\mathbf{G} = \bigoplus_{k=1}^{2n} G'_k$ and noise $\mathbf{A}\mathbf{N}\mathbf{A}^{\top}$. Single-mode squeezing before the concatenated channel further transforms \mathbf{G} to $\mathbf{G}' = \text{diag}(G_1, G_1, \dots, G_n, G_n)$. By Williamson's theorem, a symplectic transform \mathbf{S}_B exists such that $\mathbf{S}_B\mathbf{A}\mathbf{N}\mathbf{A}^{\top}\mathbf{S}_B^{\top}$ is diagonalized. Applying this transform in the post-processing, we get transmissivity $\mathbf{G}' = \text{diag}(G_1, G_1, \dots, G_n, G_n)$ and noise $\mathbf{N}' = (\sigma'_1, \sigma'_1, \dots, \sigma'_n)$. In the final step, for $G_k > 1$, we post-process with a pure-loss channel $\eta_k = 1/G_k^2$ on the k -th mode; while for $G_k < 1$, we pre-process with a quantum-limited amplifier with gain $k = 1/G_k^2$ on the k -th mode. ■

Due to the reduction, in the rest of the context, we assume our channel is independent AWGN channels. We denote the PDF of the $2n$ -dimensional multivariate Gaussian distribution as

$$g(\mathbf{\Sigma}, \mathbf{x} - \mathbf{\mu}) = \frac{1}{(2\pi)^n \sqrt{\det \mathbf{\Sigma}}} \exp \left(-\frac{1}{2}(\mathbf{x} - \mathbf{\mu})^{\top} \mathbf{\Sigma}^{-1}(\mathbf{x} - \mathbf{\mu}) \right), \quad (5.28)$$

where $\mathbf{x} = (x_1, \dots, x_{2n})^{\top}$, $\mathbf{\Sigma}$ is the covariance matrix, and $\mathbf{\mu}$ is the mean vector. The channel model is then given by

$$\Phi(\hat{\rho}) = \int_{\mathbb{R}^{2n}} d^{2n}\mathbf{\xi} g \left[\bigoplus_{i=1}^n (\sigma_i^2 \mathbf{I}_2), \mathbf{\xi} \right] e^{-i\mathbf{\xi}^{\top} \mathbf{\Omega} \hat{\mathbf{x}}} \hat{\rho} e^{i\mathbf{\xi}^{\top} \mathbf{\Omega} \hat{\mathbf{x}}}. \quad (5.29)$$

In the realm of quantum error correction with $[[n, k]]$ GKP qubit code, the heterogeneous Gaussian noise plays a pivotal role. As detailed in Section 5.1.3, the

construction of any such code is equivalent to a specific symplectic transform \mathbf{S} . We can interpret this transform as correlating random noises, which can be represented as:

$$\mathbf{S}^{-1} \left(\bigoplus_{i=1}^n \sigma_i^2 \mathbf{I}_2 \right) \mathbf{S}^{-\top}.$$

In this scenario, we use the GKP ancillas to capture the correlated noises and predict the noise that occurs on the data.

The symmetry of these channels is given by single phase rotations, signifying that when \mathbf{S} is modified to $(\mathbf{R}(\theta) \oplus \mathbf{I}_{2n-2})\mathbf{S}$, the PDF of the random noises remains unaltered. This is mathematically expressed as:

$$\mathbf{R}(\theta)^{-1}(\sigma_i^2 \mathbf{I}_2) \mathbf{R}(\theta)^{-\top} = \sigma_i^2 \mathbf{I}_2.$$

Consequently, codes that differ by single phase rotations are equivalent to each other in this context. Furthermore, in scenarios where the channel noise is homogeneous, the symmetry extends to encompass any beam splitter transform \mathbf{B} . This is mathematically expressed as:

$$\mathbf{B}^{-1}(\sigma^2 \mathbf{I}_{2n}) \mathbf{B}^{-\top} = \sigma^2 \mathbf{I}_{2n}.$$

5.3 Quantum Error Correction on Oscillators

Quantum error correction is essential for robust quantum information processing with noisy devices. As bosonic quantum systems play a crucial role in quantum sensing, communication, and computation, it is important to design error correction codes suitable for these systems against various different types of noises. While most efforts aim at protecting qubits encoded into the infinite dimensional Hilbert space of a bosonic mode, Ref. [52] proposed an error correction code to maintain the infinite-dimensional-Hilbert-space nature of bosonic systems by encoding a single bosonic mode into multiple bosonic modes. Enabled by Gottesman-Kitaev-Preskill (GKP) states as ancilla, the code overcomes the no-go theorem of Gaussian error correction.

This section aims to explore the methods and principles of quantum error correction specifically tailored for oscillators. The data is a set of oscillators experiencing small displacement errors in the continuous region (q, p) when going through AWGN channels. Hence, the performance of this quantum error correction strategy is measured by the reduction in the variance of the error after the error correction process has been applied. A generalized error correction code to the scenario with general heterogeneous Gaussian noises is provided to protect an oscillator. When the noises are correlated, they can be reduced to independent and heterogeneous noises by Williamson theorem through a suitable bosonic transform and this transform can be absorbed to encoding. Next, the encoding of k data oscillators by n oscillators is discussed. The primary objective is to safeguard k oscillators using $M = n - k$ GKP states.

5.3.1 GKP-Gaussian Error Correction and the Lower Bound

To correct the AWGN noises, Ref. [52] adopts an approach of combining GKP grid states and Gaussian operations, to go beyond the no-go theorem for Gaussian Quantum Error Correction (QEC) [62]. There, an independent and identical distributed (iid) noise model is adopted to exemplify the basic principle; A general framework that extends Ref. [52]’s approach to the multi-mode general AWGN channels is depicted in Fig. (5.3), the QEC scheme applies a general zero-displacement Gaussian unitary $\hat{U}_{\mathbf{E},0}$, described by the symplectic transform \mathbf{E} , on the input state $\hat{\rho}$ and $n - 1$ GKP ancilla to obtain an entangled n -mode non-Gaussian state. After passing through the AWGN channels $\Sigma_{\mathbf{V}}$, the output goes through the inverse of the Gaussian unitary $\hat{U}_{\mathbf{E}^{-1},0}$. Finally, one simultaneously measures the momentum and position quadratures (up to module $\sqrt{2\pi}$) of the $n - 1$ GKP ancilla modes via GKP-assisted measurements. Based on the measurement results, one applies a displacement on the data mode to obtain an approximation of the original input $\hat{\rho}$.

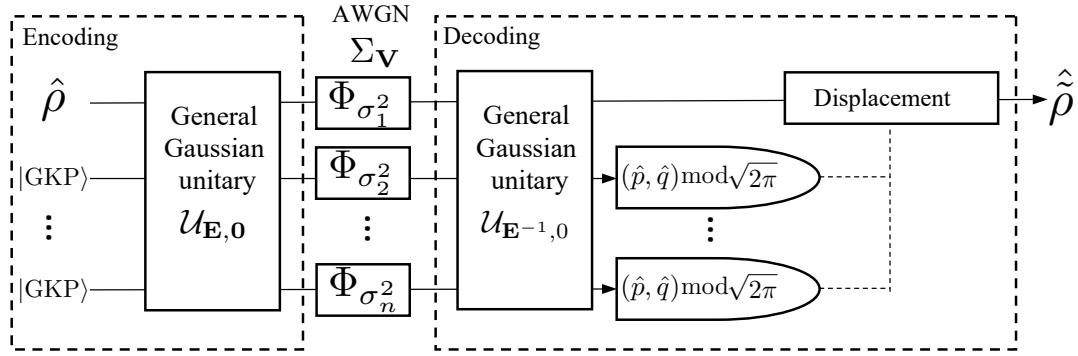


Figure 5.3: The general multi-mode GKP-Gaussian code. The notation \mathcal{U} denotes the channel that a unitary transform \hat{U} incurs.

The intuition behind the QEC design is that the channel concatenation,

$$\mathcal{U}_{\mathbf{E}^{-1},0} \circ \Sigma_{\mathbf{V}} \circ \mathcal{U}_{\mathbf{E},0} = \Sigma_{\mathbf{E}^{-1}\mathbf{V}(\mathbf{E}^{-1})^T}, \quad (5.30)$$

correlates the errors on different modes in a controlled way. As AWGN channels can be interpreted as random displacements via Eq. (5.30), measuring the displacements on the $n - 1$ ancilla will lead to a good estimation of the displacement error remaining on the data mode. The crucial contribution of the GKP grid state is to enable the joint measurement of displacements on both quadratures, up to a module $\sqrt{2\pi}$ ambiguity, so that the joint estimation of both quadrature displacements is possible. In the above scheme, we have delayed all measurement till the end; in general, one can consider performing measurements and displacements in between the Gaussian gates. However, due to the Gaussian nature of the unitaries, the displacements conditioned on the measurement results can always be pushed until the end, and even largely avoided via post-processing on the measurement results. Indeed, only the displacements on the data mode is necessary in general.

To judge the performance of a QEC scheme, as AWGN noises apply random displacements, we can consider the STDs of the random displacement errors after the decoding procedure. In general, the STD $\sigma_{L,q}$ on the position quadrature and the STD $\sigma_{L,p}$ on the momentum quadrature can be unequal, therefore we define the

average logical noise STD $\sigma_L = \sqrt{(\sigma_{L,q}^2 + \sigma_{L,p}^2)/2}$. Regardless of the error correction scheme, for a noise model described in Eq. (5.29), one can prove a lower bound of the noise STD

$$\sigma_L^2 \geq \frac{1}{e} \prod_{\ell=1}^n \frac{\sigma_\ell^2}{1 - \sigma_\ell^2} > \frac{1}{e} \prod_{\ell=1}^n \sigma_\ell^2, \quad (5.31)$$

which generalizes Eq. (12) of Ref. [52] to the multi-mode case. Note we will only consider $0 < \sigma_\ell < 1$, as the case of zero noise is trivial and channels with $\sigma_\ell > 1$ will be discarded due to zero quantum capacity.

5.3.2 Concatenated TMS and SR Code with Linear Estimator

Although lower and upper bound can be derived from quantum capacity, an error correction scheme needs a specific encoding and decoding, corresponding to the general Gaussian unitary \mathbf{E} and the error estimation in the general GKP-Gaussian error correction scheme. In this part, we consider protecting one oscillator by $n - 1$ square-grid canonical GKP states. The multi-mode concatenation of GKP-two-mode-squeezing (TMS) code and the GKP-squeezing-repetition (SR) code are provided. The concatenated Two-Mode Squeezing (TMS) and Squeezed Repetition (SR) codes implement linear estimation for error correction, which is principally based on the main peak of the output PDF from the previous layer's error correction. These codes effectively handle heterogeneous noise, characterized by the covariance matrix $\mathbf{V} = \bigoplus_{i=1}^n \sigma_i^2 \mathbf{I}_2$.

In the initial layer of error correction, we commence by correlating the last two canonical square-grid GKP states, which facilitates the protection of one GKP state using the other. This initial step plays a crucial role in significantly reducing the noise. Subsequently, this error correction process is reiterated through $n - 1$ layers, each further enhancing the noise reduction. As we proceed through the layers, the efficacy of the error correction progressively increases. Although the PDF after the error correction in k layers is no longer the Gaussian function, we can still express the covariance matrix as:

$$\mathbf{V}_{(k)} = \left(\bigoplus_{i=1}^{n-k-1} \sigma_i^2 \mathbf{I}_2 \right) \oplus (\tilde{\sigma}_{(k)}^2 \mathbf{I}_2),$$

where $\tilde{\sigma}_{(k)}$ is the reduced noise level after k layers of error correction. Notably, $\tilde{\sigma}_{(k)}$ is expected to be smaller than the initial noise levels $\sigma_n, \dots, \sigma_{n-k}$, reflecting the cumulative effect of the error correction process. In regions where $\sigma_i < 1$, which are essential for maintaining non-zero quantum capacity for single-use of the channel, the error reduction asymptotically approaches $\sigma_1^2 \cdots \sigma_n^2$.

Numerical analyses reveal that optimally tailoring the error correction procedures for each specific noise model significantly enhances the noise reduction capability. Employing a global optimization strategy allows these concatenated codes to achieve optimal scaling in relation to the input noise level. Conversely, a greedy optimization approach tends to result in less efficient scaling. These findings highlight the critical importance of developing error correction strategies that are finely tuned to the specific characteristics of the noise model in concatenated TMS and SR codes.

Two-mode TMS Code

We begin with the two-mode case ($n = 2$) of the noise model in Eq. (5.29), where the noise covariance matrix $\mathbf{V} = \text{Diag}(\sigma_1^2, \sigma_1^2, \sigma_2^2, \sigma_2^2)$ for a data mode and a single GKP ancilla. In a GKP-TMS-code, the symplectic transform of the encoding

$$\mathbf{E} = \begin{pmatrix} \sqrt{G}\mathbf{I}_2 & \sqrt{G-1}\mathbf{Z}_2 \\ \sqrt{G-1}\mathbf{Z}_2 & \sqrt{G}\mathbf{I}_2 \end{pmatrix},$$

corresponds to a TMS operation, where $\mathbf{I}_2 = \text{Diag}(1, 1)$ and $\mathbf{Z}_2 = \text{Diag}(1, -1)$. The random displacement $\mathbf{z} = (z_q^{(1)}, z_p^{(1)}, z_q^{(2)}, z_p^{(2)})$ of the output AWGN channels now has the covariance matrix

$$\mathbf{V}_z = (\mathbf{E})^{-1}\mathbf{V}(\mathbf{E}^{-1})^T = \begin{pmatrix} [G\sigma_1^2 + (G-1)\sigma_2^2]\mathbf{I}_2 & -\sqrt{G(G-1)}(\sigma_1^2 + \sigma_2^2)\mathbf{Z}_2 \\ -\sqrt{G(G-1)}(\sigma_1^2 + \sigma_2^2)\mathbf{Z}_2 & [G\sigma_2^2 + (G-1)\sigma_1^2]\mathbf{I}_2 \end{pmatrix}.$$

The joint PDF of $\mathbf{z} = (z_q^{(1)}, z_p^{(1)}, z_q^{(2)}, z_p^{(2)})$ is given by

$$\begin{aligned} P(z_q^{(1)}, z_p^{(1)}, z_q^{(2)}, z_p^{(2)}) &= \frac{1}{(2\pi)^2 |\mathbf{V}_z|^{\frac{1}{2}}} \exp\left(-\frac{1}{2} \mathbf{z}^T \mathbf{V}_z^{-1} \mathbf{z}\right) \\ &= \frac{1}{(2\pi)^2 \sigma_1^2 \sigma_2^2} \exp\left\{-\frac{1}{2\sigma_1^2 \sigma_2^2} \left\{ [(G-1)\sigma_1^2 + G\sigma_2^2] (z_q^{(1)2} + z_q^{(2)2}) \right. \right. \\ &\quad \left. \left. + [G\sigma_1^2 + (G-1)\sigma_2^2] (z_p^{(1)2} + z_p^{(2)2}) + 2\sqrt{G(G-1)}(\sigma_1^2 + \sigma_2^2)(z_q^{(1)}z_q^{(2)} - z_p^{(1)}z_p^{(2)}) \right\} \right\}. \end{aligned}$$

Then we obtain the conditional distribution given by:

$$\begin{aligned} P(z_q^{(1)}, z_p^{(1)} | z_q^{(2)}, z_p^{(2)}) &= \frac{P(z_q^{(1)}, z_p^{(1)}, z_q^{(2)}, z_p^{(2)})}{\int_{-\infty}^{\infty} P(z_q^{(1)}, z_p^{(1)}, z_q^{(2)}, z_p^{(2)}) dz_q^{(1)} dz_p^{(1)}} \\ &= \frac{(G-1)\sigma_1^2 + G\sigma_2^2}{2\pi\sigma_1^2\sigma_2^2} \exp\left\{-\frac{1}{2\sigma_1^2\sigma_2^2} \left\{ \left[\sqrt{(G-1)\sigma_1^2 + G\sigma_2^2} z_q^{(1)} + \sqrt{\frac{G(G-1)}{(G-1)\sigma_1^2 + G\sigma_2^2}} (\sigma_1^2 + \sigma_2^2) z_q^{(2)} \right]^2 \right. \right. \\ &\quad \left. \left. + \left[\sqrt{(G-1)\sigma_1^2 + G\sigma_2^2} z_p^{(1)} - \sqrt{\frac{G(G-1)}{(G-1)\sigma_1^2 + G\sigma_2^2}} (\sigma_1^2 + \sigma_2^2) z_p^{(2)} \right]^2 \right\} \right\}. \end{aligned}$$

Here, we have two types of estimators $(\bar{z}_q^{(1)}, \bar{z}_p^{(1)})$ based on the measurement result $(z_q^{(2)}, z_p^{(2)})$. The first is the maximum likelihood estimator (MLE)

$$(\bar{z}_q^{(1)}, \bar{z}_p^{(1)}) = \arg_{(z_q^{(1)}, z_p^{(1)})} \max P(z_q^{(1)}, z_p^{(1)} | z_q^{(2)}, z_p^{(2)}).$$

The second approach is to minimize the variance, which leads to using the average as the estimator as

$$(\bar{z}_q^{(1)}, \bar{z}_p^{(1)}) = \langle (z_q^{(1)}, z_p^{(1)}) \rangle_{P(\cdot, \cdot | z_q^{(2)}, z_p^{(2)})}.$$

The above estimations are the same in two-mode case because the PDF, $P(z_q^{(1)}, z_p^{(1)} | z_q^{(2)}, z_p^{(2)})$, is Gaussian. Therefore, we get

$$\begin{aligned} \bar{z}_q^{(1)} &= \langle z_q^{(1)} \rangle_{P(\cdot, \cdot | z_q^{(2)}, z_p^{(2)})} = -\frac{\sqrt{G(G-1)}(\sigma_1^2 + \sigma_2^2)}{(G-1)\sigma_1^2 + G\sigma_2^2} z_q^{(2)}, \\ \bar{z}_p^{(1)} &= \langle z_p^{(1)} \rangle_{P(\cdot, \cdot | z_q^{(2)}, z_p^{(2)})} = \frac{\sqrt{G(G-1)}(\sigma_1^2 + \sigma_2^2)}{(G-1)\sigma_1^2 + G\sigma_2^2} z_p^{(2)}. \end{aligned} \tag{5.32}$$

Now the probability density functions of logical quadrature noises ξ_q and ξ_p can be derived from the joint PDF. Since the measurements on $|\text{GKP}\rangle$ state have the module $\sqrt{2\pi}$ uncertainty, the corrected quadrature noises are given by

$$\begin{aligned}\xi_q &= z_q^{(1)} - \bar{z}_q^{(1)} \\ &= z_q^{(1)} + \frac{\sqrt{G(G-1)}(\sigma_1^2 + \sigma_2^2)}{(G-1)\sigma_1^2 + G\sigma_2^2} R_{\sqrt{2\pi}}(z_q^{(2)}), \\ \xi_p &= z_p^{(1)} - \bar{z}_p^{(1)} \\ &= z_p^{(1)} - \frac{\sqrt{G(G-1)}(\sigma_1^2 + \sigma_2^2)}{(G-1)\sigma_1^2 + G\sigma_2^2} R_{\sqrt{2\pi}}(z_p^{(2)}).\end{aligned}$$

We can get the joint PDF $P(z_q^{(1)}, z_q^{(2)})$ of random variables $z_q^{(1)}$ and $z_q^{(2)}$, as

$$\begin{aligned}\frac{1}{2\pi\sigma_1\sigma_2} \exp \left\{ -\frac{1}{2\sigma_1^2\sigma_2^2} \left\{ [(G-1)\sigma_1^2 + G\sigma_2^2]z_q^{(2)2} + [G\sigma_1^2 + (G-1)\sigma_2^2]z_q^{(1)2} \right. \right. \\ \left. \left. + 2\sqrt{G(G-1)}(\sigma_1^2 + \sigma_2^2)z_q^{(1)}z_q^{(2)} \right\} \right\}.\end{aligned}$$

Then the PDF of ξ_q is given by:

$$\begin{aligned}Q(\xi_q) &= \int_{-\infty}^{\infty} dz_q^{(1)} \int_{-\infty}^{\infty} dz_q^{(2)} P(z_q^{(1)}, z_q^{(2)}) \\ &\times \delta \left[\xi_q - z_q^{(1)} - \frac{\sqrt{G(G-1)}(\sigma_1^2 + \sigma_2^2)}{(G-1)\sigma_1^2 + G\sigma_2^2} R_{\sqrt{2\pi}}(z_q^{(2)}) \right] \\ &= \sum_{n \in \mathbb{Z}} b_n F_{\frac{\sigma_1\sigma_2}{\sqrt{(G-1)\sigma_1^2 + G\sigma_2^2}}}(\xi_q + \mu_n),\end{aligned}$$

where the coefficients and the means are

$$\begin{aligned}b_n &= \int_{(n-\frac{1}{2})\sqrt{2\pi}}^{(n+\frac{1}{2})\sqrt{2\pi}} dz F_{\sqrt{(G-1)\sigma_1^2 + G\sigma_2^2}}(z), \\ \mu_n &= \frac{\sqrt{G(G-1)}(\sigma_1^2 + \sigma_2^2)}{(G-1)\sigma_1^2 + G\sigma_2^2} \sqrt{2\pi}n,\end{aligned}\tag{5.33}$$

and F_σ is the PDF of a zero-mean Gaussian distribution with a variance σ^2 . Following the same steps, we can also show that the residue noise ξ_p obey the same statistics as ξ_q . The output variance is therefore

$$\sigma_L^2 = \frac{\sigma_1^2\sigma_2^2}{(G-1)\sigma_1^2 + G\sigma_2^2} + \sum_{n \in \mathbb{Z}} b_n \mu_n^2.\tag{5.34}$$

We also derive the asymptotic expressions of the optimal gain that minimizes the output variance when both σ_1 and σ_2 are small. The leading order of the above noise variance can be obtained as

$$\begin{aligned}\sigma_L^2 &\simeq \frac{\sigma_1^2\sigma_2^2}{(G-1)\sigma_1^2 + G\sigma_2^2} \\ &+ \frac{2\pi G(G-1)(\sigma_1^2 + \sigma_2^2)^2}{[(G-1)\sigma_1^2 + G\sigma_2^2]^2} \text{Erfc} \left(\frac{\sqrt{\pi}}{2\sqrt{(G-1)\sigma_1^2 + G\sigma_2^2}} \right).\end{aligned}\tag{5.35}$$

For a fixed gain G and $\sigma_2 < \sigma_1$, Eq. (5.35) leads to

$$\sigma_L^2 \simeq \frac{\sigma_1^2 \sigma_2^2}{\sigma_G^2} + \frac{2\pi G(G-1)(\sigma_1^2 + \sigma_2^2)}{\sigma_G^4} \text{Erfc}\left(\frac{\sqrt{\pi}}{2\sigma_G}\right), \quad (5.36)$$

where

$$\sigma_G^2 = (G-1)\sigma_1^2 + G\sigma_2^2. \quad (5.37)$$

The above equation decreases as σ_G increases as long as $\sigma_G > 0.7$, when $\sigma_1^2 + \sigma_2^2$ and G are fixed. In the small noise limit, we have $\sigma_G \gg 1$ and this condition is satisfied. Therefore, when $\sigma_2 < \sigma_1 \ll 1$, we have

$$\begin{aligned} \sigma_G(\sigma_1, \sigma_2)^2 &= (G-1)\sigma_1^2 + G\sigma_2^2 \\ &< (G-1)\sigma_2^2 + G\sigma_1^2 = \sigma_G(\sigma_2, \sigma_1)^2. \end{aligned}$$

So we can switch the two channels to get a smaller STD of the output noise, then adjust the gain G for a even smaller STD of the output noise after switching. Numerical results show that the optimal $G \gg 1$ when both σ_1 and σ_2 are small. Thus, $G \approx G-1$ and $G(G-1)(\sigma_1^2 + \sigma_2^2)^2 \approx [(G-1)\sigma_1^2 + G\sigma_2^2]^2$. Also the argument inside the Erfc function is much larger than 1. With $x \equiv 1/\sigma_G^2$, Eq. (5.35) can be further simplified to

$$\sigma_L^2 = f(x) \equiv \sigma_1^2 \sigma_2^2 x + 2\pi \text{Erfc}\left(\frac{\sqrt{\pi x}}{2}\right).$$

The optimum x^* can be found by solving

$$f'(x^*) = \sigma_1^2 \sigma_2^2 + 2\pi \left[-\frac{1}{2\sqrt{x^*}} \exp\left(-\frac{\pi x^*}{4}\right) \right] = 0,$$

which leads to

$$x^* = \frac{4}{\pi} \ln\left(\frac{\pi}{\sigma_1^2 \sigma_2^2 \sqrt{x^*}}\right). \quad (5.38)$$

We solve Eq. (5.38) by plugging in x^* iteratively,

$$\begin{aligned} x^* &= \frac{4}{\pi} \ln\left(\frac{\pi}{\sigma_1^2 \sigma_2^2 \sqrt{x}}\right) \\ &= \frac{4}{\pi} \ln\left(\frac{\pi}{\sigma_1^2 \sigma_2^2}\right) - \frac{2}{\pi} \ln(x^*) \\ &= \frac{4}{\pi} \ln\left(\frac{\pi}{\sigma_1^2 \sigma_2^2}\right) - \frac{2}{\pi} \ln\left[\frac{4}{\pi} \ln\left(\frac{\pi}{\sigma_1^2 \sigma_2^2}\right) - \frac{2}{\pi} \ln(x^*)\right] \\ &\approx \frac{4}{\pi} \ln\left(\frac{\pi}{\sigma_1^2 \sigma_2^2}\right) - \frac{2}{\pi} \ln\left(\frac{4}{\pi}\right) - \frac{2}{\pi} \ln\left[\ln\left(\frac{\pi}{\sigma_1^2 \sigma_2^2}\right)\right] \\ &\approx \frac{4}{\pi} \ln\left(\frac{\pi^{3/2}}{2\sigma_1^2 \sigma_2^2}\right). \end{aligned} \quad (5.39)$$

Then the optimal gain and the output noise are given by

$$\begin{aligned}
G^* &= \frac{1/x^* + \sigma_1^2}{\sigma_1^2 + \sigma_2^2} = \frac{\frac{\pi}{4} \left[\ln \left(\frac{\pi^{3/2}}{2\sigma_1^2\sigma_2^2} \right) \right]^{-1} + \sigma_1^2}{\sigma_1^2 + \sigma_2^2}, \\
\sigma_L^{*2} &\simeq \sigma_1^2\sigma_2^2x^* + 2\pi \operatorname{Erfc} \left(\frac{\sqrt{\pi x}}{2} \right) \\
&\approx \sigma_1^2\sigma_2^2x^* + \frac{4}{\sqrt{x^*}} \exp \left(-\frac{\pi x^*}{4} \right) \\
&\approx \frac{4\sigma_1^2\sigma_2^2}{\pi} \left\{ \ln \left(\frac{\pi^{3/2}}{2\sigma_1^2\sigma_2^2} \right) + \left[\ln \left(\frac{\pi^{3/2}}{2\sigma_1^2\sigma_2^2} \right) \right]^{-\frac{1}{2}} \right\} \\
&\approx \frac{4\sigma_1^2\sigma_2^2}{\pi} \ln \left(\frac{\pi^{3/2}}{2\sigma_1^2\sigma_2^2} \right).
\end{aligned} \tag{5.40}$$

As numerical results show that $\sigma_L(\sigma_1, \sigma_2)$ is smaller when $\sigma_1 < \sigma_2$, we get the asymptotic curve for $\sigma_L = t\sigma_1$ ($t < 1$) under this approximation by

$$t^2 = \frac{4\sigma_2^2}{\pi} \ln \left(\frac{\pi^{3/2}}{2\sigma_1^2\sigma_2^2} \right).$$

Two-mode SR Code

In a GKP-SR code, the encoding Gaussian unitary is composed of three single-mode squeezing operations and a two-mode SUM gate, leading to the overall symplectic transform

$$\mathbf{E} = \begin{pmatrix} \kappa/G & 0 & 0 & 0 \\ 0 & G/\kappa & 0 & -G \\ G & 0 & G/\kappa & 0 \\ 0 & 0 & 0 & \kappa/G \end{pmatrix}, \tag{5.41}$$

which is parameterized by κ and G . The decoding procedure is similar to the GKP-TMS code, where a linear estimator is devised and a displacement operation is applied on the data mode accordingly, leading to the output noise PDFs as

$$Q^{(2)}(x) = \sum_{n \in \mathbb{Z}} b_n F_{\kappa\sigma_1/G}(x + \kappa\sigma_1/\sigma_2\sqrt{2\pi}n), \tag{5.42a}$$

$$P^{(2)}(x) = \sum_{n \in \mathbb{Z}} b_n F_{\kappa\sigma_1/G}(x + \kappa\sqrt{2\pi}n), \tag{5.42b}$$

where

$$b_n = \int_{(n-\frac{1}{2})\sqrt{2\pi}}^{(n+\frac{1}{2})\sqrt{2\pi}} dz F_{G\sigma_2/\kappa}(z), \tag{5.43}$$

$$\kappa^2 = \left(\sqrt{G^8\sigma_1^4 + 4G^4\sigma_2^4 - G^4\sigma_1^2} \right) / 2\sigma_2^2. \tag{5.44}$$

The κ is chosen to balance the variances of each Gaussian peak to $\kappa\sigma_1/G$ in the noise PDF. Note that when $G \rightarrow 0$, we have $\mathbf{E} \rightarrow \mathbf{I}$ approaches the identity, which

corresponds to no error-correction. The variances of the output noise after error-correction can be obtained as

$$\sigma_{L,q}^2 = (\kappa\sigma_1/G)^2 + \sum_{n \in \mathbb{Z}} b_n^2 (\kappa\sigma_1/\sigma_2)^2 2\pi n^2, \quad \sigma_{L,p}^2 = (\kappa\sigma_1/G)^2 + \sum_{n \in \mathbb{Z}} b_n^2 \kappa^2 2\pi n^2. \quad (5.45)$$

Similar to the GKP-TMS code, here we optimize the parameter G to obtain the minimum average noise σ_L^* . When both σ_1 and σ_2 are small, asymptotically we have

$$\sigma_L^{*2} \approx \frac{4\bar{\sigma}^4}{\pi} \ln \left[\frac{\pi^{3/2}}{2\bar{\sigma}^4} \right] + \frac{4\bar{\sigma}^4}{\pi} \ln \left(\frac{\sigma_1^2 + \sigma_2^2}{2\sigma_1^2} \right), \quad (5.46)$$

which is identical to Eq. (5.40) in the leading-order, up to a next-order correction that disappears when $\sigma_1 = \sigma_2$. When $\sigma_1 \neq \sigma_2$, while to the leading-order the GKP-TMS code is symmetric between the two channels, the GKP-SR code is asymmetric: Eq. (5.46) shows that we will choose the order $\sigma_2 \leq \sigma_1$ to minimize σ_L^* —we want to use the less noisy channel for GKP ancilla, in contrary to the GKP-TMS code.

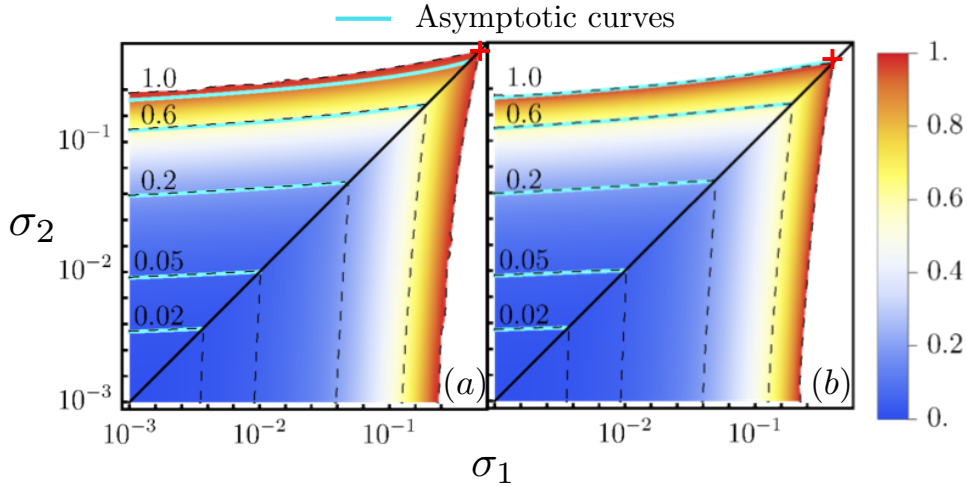


Figure 5.4: Contours of the error-correction ratio $\sigma_L^*/\min[\sigma_1, \sigma_2]$ for (a) GKP-two-mode squeezing code and (b) GKP-squeezing-repetition code. The end points marked by the red crosses are $\sigma_1 = \sigma_2 \simeq 0.56$ for (a) and $\sigma_1 = \sigma_2 \simeq 0.41$ for (b).

The performance of TMS code and SR code in the two mode case are shown in Fig. 5.6. These plots show the ratio $\sigma_L^*/\min(\sigma_1, \sigma_2)$ versus the input STDs σ_1, σ_2 . In Fig. 5.4(a) and (b), the asymptotic results (cyan curves) agree well with the numerical results. The agreements are good when both σ_1 and σ_2 are small as expected from the asymptotic analysis $\sigma_1, \sigma_2 \rightarrow 0$.

Concatenated TMS Code

A common technique in QEC code design is concatenation—each element in a single error-correction circuit layer can be further error-corrected by another layer of circuit, and thereby the noise is further suppressed. As the number of concatenation layers increases, the logical noise can usually be reduced to an arbitrary small amount. Fig. 5.6(a) shows the $(u+1)$ -th layer of encoding, where a two-mode code is applied on the logical mode at the u -th layer (with noise STD $\sigma_L^{(u)}$) and another

GKP ancilla mode (with noise STD σ_u). Thereby, one can further reduce the average noise STD to $\sigma_L^{(u+1)}$.

For concatenated TMS code with linear decoder, it can be shown that the output PDF is a sum of Gaussian functions by mathematical induction. At the $(u+1)$ -th layer, the noises are independent random variables $(\xi_q^{(1)}, \xi_p^{(1)}, \xi_q^{(2)}, \xi_p^{(2)})$, which correspond to the new mode introduced and a second mode from the u -th layer. The new mode has a Gaussian noise PDF

$$Q(\xi_q^{(1)}) = P(\xi_p^{(1)}) = F_{\sigma_u}(\xi_{q,p}^{(1)}).$$

By mathematical induction, we suppose the second mode from the u -th layer has a PDF as a sum of Gaussian functions

$$Q(\xi_q^{(2)}) = P(\xi_p^{(2)}) = \sum_{k \in \mathbb{Z}} b_k F_{\sigma^{(u)}}(\xi_{q,p}^{(2)} + t_k), \quad (5.47)$$

where $F_\sigma(\cdot)$ is the PDF of a zero-mean Gaussian distribution with STD σ and $\sum_{k \in \mathbb{Z}} b_k = 1$ are normalized. We also assume that the coefficients are symmetric

$$b_k = b_{-k}, \quad t_k = -t_{-k}.$$

Following the same procedures of the two-mode squeezing code with heterogeneous independent noises, we have the joint PDF of q and p

$$\begin{aligned} P_{12}(\boldsymbol{\xi}) &= F_{\sigma_u}(\xi_q^{(1)}) F_{\sigma_u}(\xi_p^{(1)}) \sum_{k_1, k_2 \in \mathbb{Z}} b_{k_1} b_{k_2} F_{\sigma^{(u)}}(\xi_q^{(2)} + t_{k_1}) F_{\sigma^{(u)}}(\xi_p^{(2)} + t_{k_2}), \\ P'_{12}(\mathbf{z}) &= P_{12}(\mathbf{S}\boldsymbol{\xi}) = F_{\sigma_u}(\sqrt{G}z_q^{(1)} + \sqrt{G-1}z_q^{(2)}) F_{\sigma_u}(\sqrt{G}z_p^{(1)} - \sqrt{G-1}z_p^{(2)}) \times \\ &\quad \sum_{k_1, k_2 \in \mathbb{Z}} b_{k_1} b_{k_2} F_{\sigma^{(u)}}(\sqrt{G-1}z_q^{(1)} + \sqrt{G}z_q^{(2)} + t_{k_1}) F_{\sigma^{(u)}}(-\sqrt{G-1}z_p^{(1)} + \sqrt{G}z_p^{(2)} + t_{k_2}). \end{aligned}$$

By separating q and p and reformulating them, we are able to find the estimators of $z_q^{(1)}$ and $z_p^{(1)}$ in terms of the second mode.

$$P'_{12,q}(z_q^{(1)}, z_q^{(2)}) = \sum_{k \in \mathbb{Z}} b_k F_{\sigma_u}(\sqrt{G}z_q^{(1)} + \sqrt{G-1}z_q^{(2)}) F_{\sigma^{(u)}}(\sqrt{G-1}z_q^{(1)} + \sqrt{G}z_q^{(2)} + t_k), \quad (5.48a)$$

$$P'_{12,p}(z_p^{(1)}, z_p^{(2)}) = \sum_{k \in \mathbb{Z}} b_k F_{\sigma_u}(\sqrt{G}z_p^{(1)} - \sqrt{G-1}z_p^{(2)}) F_{\sigma^{(u)}}(-\sqrt{G-1}z_p^{(1)} + \sqrt{G}z_p^{(2)} + t_k). \quad (5.48b)$$

Eq. (5.48a) can be reformulated to:

$$\begin{aligned} P'_{12,q}(z_q^{(1)}, z_q^{(2)}) &= \sum_{k \in \mathbb{Z}} b_k \frac{1}{2\pi\sigma_u\sigma^{(u)}} \exp \left\{ -\frac{G\sigma^{(u)^2} + (G-1)\sigma_u^2}{2\sigma_u^2\sigma^{(u)^2}} \left[z_q^{(1)} + \right. \right. \\ &\quad \left. \left. \frac{\sqrt{G(G-1)}(\sigma_u^2 + \sigma^{(u)^2})}{(G-1)\sigma_u^2 + G\sigma^{(u)^2}} \left(z_q^{(2)} + \frac{\sigma_u^2}{\sqrt{G}(\sigma_u^2 + \sigma^{(u)^2})} t_k \right) \right]^2 \right\} \exp \left\{ -\frac{(z_q^{(2)} + \sqrt{G}t_k)^2}{2[(G-1)\sigma_u^2 + G\sigma^{(u)^2}]} \right\}. \end{aligned} \quad (5.49)$$

We choose the linear estimator by MLE on the main peak of Eq. (5.49),

$$\begin{aligned}\bar{z}_q^{(1)} &= -A_q R_{\sqrt{2\pi}}(z_q^{(2)}), \\ \bar{z}_p^{(1)} &= A_q R_{\sqrt{2\pi}}(z_p^{(2)}),\end{aligned}\tag{5.50}$$

where we have introduced the following notations to make things more compact,

$$A_q = \frac{\sqrt{G(G-1)}(\sigma_u^2 + \sigma^{(u)^2})}{(G-1)\sigma_u^2 + G\sigma^{(u)^2}},\tag{5.51a}$$

$$\sigma^{(u+1)} = \frac{\sigma_u \sigma^{(u)}}{\sigma_3},\tag{5.51b}$$

$$\sigma_3 = \sqrt{(G-1)\sigma_u^2 + G\sigma^{(u)^2}}.\tag{5.51c}$$

After the correction, the additive noise of q is a sum of two random variables

$$\begin{aligned}\xi'_q &= z_q^{(1)} - \bar{z}_q^{(1)} = z_q^{(1)} + A_q R_{\sqrt{2\pi}}(z_q^{(2)}), \\ Q(\xi'_q) &= \int_{-\infty}^{\infty} dz_q^{(1)} \int_{-\infty}^{\infty} dz_q^{(2)} P'_{12,q}(z_q^{(1)}, z_q^{(2)}) \\ &\times \delta[\xi'_q - z_q^{(1)} - A_q R_{\sqrt{2\pi}}(z_q^{(2)})].\end{aligned}$$

Finally we have the PDF for ξ'_q :

$$\begin{aligned}Q(\xi'_q) &= \sum_{k,\ell \in \mathbb{Z}} \left[b_k \int_{(\ell-\frac{1}{2})\sqrt{2\pi}}^{(\ell+\frac{1}{2})\sqrt{2\pi}} F_{\sigma_3}(z_3 + \sqrt{G}t_k) dz_3 \right] \\ &\times F_{\sigma^{(u+1)}} \left[\xi'_q + A_q(\sqrt{2\pi}\ell + \frac{\sigma_u^2}{\sqrt{G}(\sigma_u^2 + \sigma^{(u)^2})}t_k) \right] \\ &\equiv \sum_{k,\ell \in \mathbb{Z}} b_{k,\ell} F_{\sigma^{(u+1)}}(\xi'_q + t_{k,\ell}).\end{aligned}\tag{5.52}$$

Similarly, the PDF for ξ'_p is given by:

$$\begin{aligned}P(\xi'_p) &= \sum_{k,\ell \in \mathbb{Z}} \left[b_k \int_{(\ell-\frac{1}{2})\sqrt{2\pi}}^{(\ell+\frac{1}{2})\sqrt{2\pi}} F_{\sigma_3}(z_3 + \sqrt{G}t_k) dz_3 \right] \\ &\times F_{\sigma^{(u+1)}} \left[-\xi'_p + A_q(\sqrt{2\pi}\ell + \frac{\sigma_u^2}{\sqrt{G}(\sigma_u^2 + \sigma^{(u)^2})}t_k) \right] \\ &\equiv \sum_{k,\ell \in \mathbb{Z}} b_{k,\ell} F_{\sigma^{(u+1)}}(\xi'_p - t_{k,\ell}).\end{aligned}\tag{5.53}$$

From the assumption in Eq. (5.47), we see that $b_{k,\ell} = b_{-k,-\ell}$ and $t_{k,\ell} = -t_{-k,-\ell}$. Therefore the PDFs after the $(u+1)$ -round are still symmetric. The $Q(\xi'_q)$ and $P(\xi'_p)$ have the same form of function. And the function is a sum of Gaussian functions. As we know at the bottom layer, the assumption of Eq. (5.47) is true; therefore, by induction we have proven that in all layers, the PDFs satisfy the form in Eq. (5.47). Let us perform asymptotic analyses by assuming $\sigma_u \gg \sigma^{(u)}$. This is usually a good approximation after the first layer of concatenation. Then $\sigma^{(u+1)} \approx \sigma^{(u)}/\sqrt{G-1}$. The leading term $\sigma^{(u+1)}$ decreases with $\sigma^{(u)}$. By induction,

we should expect the order $(n, n-1, \dots, 3, 1, 2)$ works well. Note that in the first layer, $(1, 2)$ is better than $(2, 1)$. Next we show that the QEC code reduces the noise to a level of $\sigma^{(u+1)} \sim \prod_{k=0}^u \sigma_u$ asymptotically. On the one hand, we would like to take $\sigma_3 = c\sqrt{2\pi}$ for $c \ll 1$ so that the integral in Eq. (5.52) takes most of its values around the origin. On the other hand, the smaller σ_3 , the larger $\sigma^{(u+1)}$ is. Thus σ_3 is bounded and $\sigma^{(u+1)} = \sigma^{(u)}\sigma_u/(c\sqrt{2\pi}) \sim \sigma^{(u)}\sigma_u$ after optimizing G . By induction, it is expected that $\sigma^{(u+1)} \sim \prod_{k=0}^u \sigma_u$.

Concatenated SR Code

The update rule of the noise characters at each layer for the GKP-SR code with linear decoder is obtained with similar derivation. In particular, it can be shown that the noise after an arbitrary number of error-correction layers has a PDF composed of a sum of Gaussian functions. Let's first start with the symplectic transform of the GKP-SR code. As shown in Fig. 5.5, the corresponding symplectic transform of

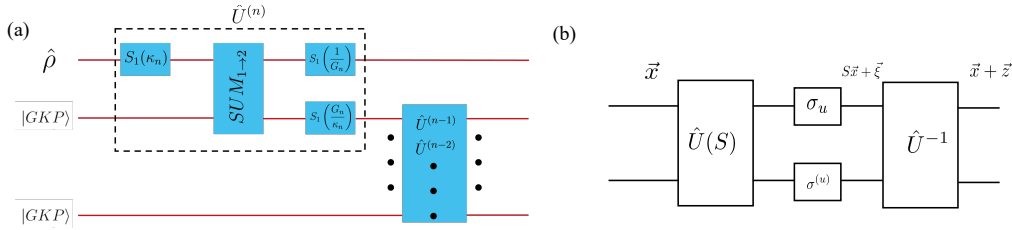


Figure 5.5: Schematic plots. (a) Encoding of the GKP-SR code. (b) The model of two channels.

the unitary \hat{U} is

$$S = \begin{pmatrix} \frac{\kappa}{G_{u+1}} & 0 & 0 & 0 \\ 0 & \frac{G_{u+1}}{\kappa} & 0 & -G_{u+1} \\ G_{u+1} & 0 & \frac{G_{u+1}}{\kappa} & 0 \\ 0 & 0 & 0 & \frac{\kappa}{G_{u+1}} \end{pmatrix}. \quad (5.54)$$

We prove the conclusion by mathematical induction. Consider the $(u+1)$ -th layer of error-correction, where the noise input from the u -th layer has its PDF composed of a sum of Gaussian distributions, i.e.,

$$\begin{aligned} P_2^{(u)}(\xi_q^{(2)}, \xi_p^{(2)}) &= Q^{(u)}(\xi_q^{(2)}) \times P^{(u)}(\xi_p^{(2)}), \\ Q^{(u)}(\xi_q^{(2)}) &= \sum_{k \in \mathbb{Z}} b_{k,q}^{(u)} F_{\sigma^{(u)}}(\xi_q^{(2)} - t_{k,q}^{(u)}), \\ P^{(u)}(\xi_p^{(2)}) &= \sum_{k \in \mathbb{Z}} b_{k,p}^{(u)} F_{\sigma^{(u)}}(\xi_p^{(2)} - t_{k,p}^{(u)}), \end{aligned}$$

where $F_{\sigma}(\cdot)$ is the zero-mean Gaussian PDF with STD σ . We have assumed the q and p quadratures can in general have different means $\{t_{k,q}^{(u)}\}$ and $\{t_{k,p}^{(u)}\}$. The superposition coefficients $b_{n,q}^{(u)}$ and $b_{n,p}^{(u)}$ of the quadratures can be different. Here we

will also assume the symmetry in the mathematical induction

$$b_{k,q}^{(u)} = b_{-k,q}^{(u)}, \quad t_{k,q}^{(u)} = -t_{-k,q}^{(u)}, \quad (5.56a)$$

$$b_{k,p}^{(u)} = b_{-k,p}^{(u)}, \quad t_{k,p}^{(u)} = -t_{-k,p}^{(u)}, \quad (5.56b)$$

for $k = 0, \pm 1, \pm 2, \dots$. Note that

$$t_{0,q}^{(u)} = t_{0,p}^{(u)} = 0. \quad (5.57)$$

In the $(u+1)$ -th layer, we introduce an additional mode, which goes through an AWGN channel with variance σ_u^2 . The PDF of the additional noise $(\xi_q^{(1)}, \xi_p^{(1)})$ is therefore

$$P_1(\xi_q^{(1)}, \xi_p^{(1)}) = F_{\sigma_u}(\xi_q^{(1)}) \times F_{\sigma_u}(\xi_p^{(1)}).$$

This results in the overall noise PDF as a product

$$P_{12}(\vec{\xi}) = P_1(\xi_q^{(1)}, \xi_p^{(1)}) \times P_2^{(u)}(\xi_q^{(2)}, \xi_p^{(2)}).$$

From the noise transformation $\vec{z} = S^{-1}\vec{\xi}$, before the measurement the joint noise PDF can be obtained from

$$\begin{aligned} P'_{12}(\vec{z}) &= P_{12}(S\vec{z}) \\ &= F_{\sigma_u}\left(\frac{\kappa}{G_{u+1}}z_1\right) F_{\sigma_u}\left(\frac{G_{u+1}}{\kappa}z_2 - G_{u+1}z_4\right) \times \\ &\quad \sum_{k_1 \in \mathbb{Z}} b_{k_1,q}^{(u)} F_{\sigma^{(u)}}\left(G_{u+1}z_1 + \frac{G_{u+1}}{\kappa}z_3 - t_{k_1,q}^{(u)}\right) \times \\ &\quad \sum_{k_2 \in \mathbb{Z}} b_{k_2,p}^{(u)} F_{\sigma^{(u)}}\left(\frac{\kappa}{G_{u+1}}z_4 - t_{k_2,p}^{(u)}\right). \end{aligned}$$

It can be seen from the above equation that at the output side, z_1 only correlates with z_3 and z_2 only correlates with z_4 . We may write the joint PDFs of position and momentum separately, for example,

$$\begin{aligned} P'_{12,q}(z_1, z_3) &= F_{\sigma_u}\left(\frac{\kappa}{G_{u+1}}z_1\right) \sum_{k=0,\pm 1,\dots} b_{k,q}^{(u)} F_{\sigma^{(u)}}\left(G_{u+1}z_1 + \frac{G_{u+1}}{\kappa}z_3 - t_{k,q}^{(u)}\right) \\ &= \frac{1}{2\pi\sigma_u\sigma^{(u)}} b_{0,q}^{(u)} \exp\left\{-\frac{1}{2}\left\{\frac{1}{\sigma_3^2}[z_1 + A_q z_3]^2 + \frac{1}{\sigma_4^2}(z_3)^2\right\}\right\} \end{aligned} \quad (5.58a)$$

$$\begin{aligned} &+ \frac{1}{2\pi\sigma_u\sigma^{(u)}} \sum_{k=\pm 1,\dots} b_{k,q}^{(u)} \exp\left\{-\frac{1}{2}\left\{\frac{1}{\sigma_3^2}\left[z_1 + A_q\left(z_3 - \frac{\kappa}{G_{u+1}}t_{k,q}^{(u)}\right)\right]^2\right.\right. \\ &\quad \left.\left.+ \frac{1}{\sigma_4^2}\left(z_3 - \frac{\kappa}{G_{u+1}}t_{k,q}^{(u)}\right)^2\right\}\right\}. \end{aligned} \quad (5.58b)$$

Here we have introduced the notations

$$\sigma_3 \equiv \frac{G_{u+1}\sigma_u\sigma^{(u)}}{\sqrt{\kappa^2\sigma^{(u)2} + G_{u+1}^4\sigma_u^2}}, \quad \sigma_4 \equiv \frac{\sqrt{\kappa^2\sigma^{(u)2} + G_{u+1}^4\sigma_u^2}}{G_{u+1}}, \quad A_q \equiv \frac{G_{u+1}^4\sigma_u^2}{\kappa(\kappa^2\sigma^{(u)2} + G_{u+1}^4\sigma_u^2)}. \quad (5.59)$$

We have separated the PDF into two parts, the first part is the main peak in Eq. (5.58a), and the second part is the rest of the peaks in Eq. (5.58b). To correct error, we measure the GKP state of the second mode to infer about the noises z_3, z_4 , from which we produce estimates of z_1, z_2 and the corresponding corrections on the noise of the first mode. Denote the measurement results \tilde{z}_3, \tilde{z}_4 . Let's focus on the main peak in Eq. (5.58a), the linear estimation give

$$\bar{z}_1 = -A_q \tilde{z}_3. \quad (5.60)$$

It turns out that choosing this estimator will also simplify the update rule significantly. Considering the ambiguity in the measurement result \tilde{z}_3 due to the GKP state, after applying a displacement $-\bar{z}_1$ to reduce the noise, we have the residual noise

$$\xi'_q = z_1 - \bar{z}_1 = z_1 + A_q R_{\sqrt{2\pi}}(z_3).$$

The PDF of the position quadrature of the output in the $(u+1)$ -th layer is given by

$$\begin{aligned} Q^{(u+1)}(\xi'_q) &= \int_{-\infty}^{\infty} dz_1 \int_{-\infty}^{\infty} dz_3 P'_{12,q}(z_1, z_3) \times \delta[\xi'_q - z_1 - A_q R_{\sqrt{2\pi}}(z_3)] \\ &= \sum_{k, \ell \in \mathbb{Z}} b_{k,q}^{(u)} F_{\sigma_3} \left(\xi'_q + A_q (\ell \sqrt{2\pi} - \frac{\kappa}{G_{u+1}} t_{k,q}^{(u)}) \right) \\ &\quad \times \int_{(\ell - \frac{1}{2})\sqrt{2\pi}}^{(\ell + \frac{1}{2})\sqrt{2\pi}} dz_3 F_{\sigma_4} \left(z_3 - \frac{\kappa}{G_{u+1}} t_{k,q}^{(u)} \right). \end{aligned}$$

Note that if one does not choose this estimator in Eq. (5.60), then in the above equation, one will have additional cross terms as $\xi'_q z_3$. This coupling leads to non-Gaussian function of ξ'_q in general. The output PDF can be calculated in a similar way using the mean value of the main peak as

$$P^{(u+1)}(\xi'_p) = \sum_{k, \ell \in \mathbb{Z}} b_{k,p}^{(u)} F_{\frac{\kappa \sigma_u}{G_{u+1}}} \left(\xi'_p - \kappa \ell \sqrt{2\pi} \right) \times \int_{(\ell - \frac{1}{2})\sqrt{2\pi}}^{(\ell + \frac{1}{2})\sqrt{2\pi}} dz_3 F_{\frac{G_{u+1} \sigma_u}{\kappa}} \left(z_3 - \frac{G_{u+1}}{\kappa} t_{k,p}^{(u)} \right).$$

The κ is chosen to balance the variances of the main peaks of both quadratures:

$$\frac{\kappa \sigma_u}{G_{u+1}} = \frac{G_{u+1} \sigma_u \sigma^{(u)}}{\sqrt{\kappa^2 \sigma^{(u)2} + G_{u+1}^4 \sigma_u^2}} \Rightarrow \kappa^2 = \frac{\sqrt{G_{u+1}^8 \sigma_u^4 + 4 G_{u+1}^4 \sigma^{(u)4}} - G_{u+1}^4 \sigma_u^2}{2 \sigma^{(u)2}}. \quad (5.61)$$

With this choice of κ , the PDFs are simplified to the following,

$$\begin{aligned}
Q^{(u+1)}(\xi'_q) &= \sum_{k, \ell \in \mathbb{Z}} b_{k,q}^{(u)} F_{\frac{\kappa \sigma_u}{G_{u+1}}} \left[\xi'_q + \kappa \frac{\sigma_u}{\sigma^{(u)}} (\ell \sqrt{2\pi} - \frac{\kappa}{G_{u+1}} t_{k,q}^{(u)}) \right] \\
&\quad \times \int_{(\ell - \frac{1}{2})\sqrt{2\pi}}^{(\ell + \frac{1}{2})\sqrt{2\pi}} dz_3 F_{\frac{G_{u+1}\sigma^{(u)}}{\kappa}} (z_3 - \frac{\kappa}{G_{u+1}} t_{k,q}^{(u)}) \\
&\equiv \sum_{k' \in \mathbb{Z}} b_{k',q}^{(u+1)} F_{\sigma_{u+1}} (\xi'_q - t_{k',q}^{(u+1)}), \\
P^{(u+1)}(\xi'_p) &= \sum_{k, \ell \in \mathbb{Z}} b_{k,p}^{(u)} F_{\frac{\kappa \sigma_u}{G_{u+1}}} \left(\xi'_p - \kappa \ell \sqrt{2\pi} \right) \times \int_{(\ell - \frac{1}{2})\sqrt{2\pi}}^{(\ell + \frac{1}{2})\sqrt{2\pi}} dz_3 F_{\frac{G_{u+1}\sigma^{(u)}}{\kappa}} (z_3 - \frac{G_{u+1}}{\kappa} t_{k,p}^{(u)}) \\
&\equiv \sum_{k' \in \mathbb{Z}} b_{k',p}^{(u+1)} F_{\sigma_{u+1}} (\xi'_p - t_{k',p}^{(u+1)}).
\end{aligned} \tag{5.62}$$

We indeed see that the PDFs of both quadratures on the $(u+1)$ -th layer of error correction are composed of a sum of Gaussian functions. The new set of Gaussian functions have an identical STD $\sigma_{u+1} = \kappa \sigma_u / G_{u+1}$, but different means $\{t_{k',q}^{(u+1)}\}$, $\{t_{k',p}^{(u+1)}\}$ and weights $\{b_{k',q}^{(u+1)}\}$, $\{b_{k',p}^{(u+1)}\}$. We can reorder the Gaussian functions into the following series,

$$\begin{aligned}
b_{(k,\ell),q}^{(u+1)} &= b_{k,q}^{(u)} \int_{(\ell - \frac{1}{2})\sqrt{2\pi}}^{(\ell + \frac{1}{2})\sqrt{2\pi}} dz_3 F_{\frac{G_{u+1}\sigma^{(u)}}{\kappa}} (z_3 - \frac{\kappa}{G_{u+1}} t_{k,q}^{(u)}), \\
t_{(k,\ell),q}^{(u+1)} &= -\kappa \frac{\sigma_u}{\sigma^{(u)}} (\ell \sqrt{2\pi} - \frac{\kappa}{G_{u+1}} t_{k,q}^{(u)}), \\
b_{(k,\ell),p}^{(u+1)} &= b_{k,p}^{(u)} \int_{(\ell - \frac{1}{2})\sqrt{2\pi}}^{(\ell + \frac{1}{2})\sqrt{2\pi}} dz_3 F_{\frac{G_{u+1}\sigma^{(u)}}{\kappa}} (z_3 - \frac{G_{u+1}}{\kappa} t_{k,p}^{(u)}), \\
t_{(k,m),p}^{(u+1)} &= \kappa \ell \sqrt{2\pi}, \\
(k, \ell) &\Rightarrow k'.
\end{aligned} \tag{5.63}$$

Now that we have proven the sum of Gaussian function part, next, we show the symmetry of Eq. (5.56a) also holds at the $(u+1)$ -th layer, which makes $Q^{(u+1)}(\xi'_q)$ and $P^{(u+1)}(\xi'_p)$ even functions. Note that the (k, ℓ) term and the $(-k, -\ell)$ term match based on the given assumptions of Eq. (5.56a). To be explicit, $b_{(k,\ell),q|p}^{(u+1)} = b_{(-k,-\ell),q|p}^{(u+1)}$ and $t_{(k,\ell),q|p}^{(u+1)} = -t_{(-k,-\ell),q|p}^{(u+1)}$ give rise to $b_{k',q|p}^{(u+1)} = b_{k',q|p}^{(u+1)}$ and $t_{k',q|p}^{(u+1)} = t_{k',q|p}^{(u+1)}$. To complete the proof, we only need to verify that all assumptions are true at the $u = 0$ -th round. In that case, we have

$$\begin{aligned}
Q^{(0)}(\xi_q) &= F_{\sigma_0}(\xi_q), \\
P^{(0)}(\xi_p) &= F_{\sigma_0}(\xi_p),
\end{aligned}$$

which are indeed compositions of Gaussian functions, and the main peak (the only peak) has zero means. Also both functions are even functions. Therefore, we have completed the proof. The update rule can be used to evaluate the overall effects of the error correction. From the above argument, we may calculate the variance

of $Q^{(u+1)}(\xi_q)$ and $P^{(u+1)}(\xi_p)$ in terms of σ_u , $\sigma^{(u)}$ and G_{u+1} easily since they are zero-mean.

$$\begin{aligned}\text{Var}_q^{(u+1)} &= \left(\frac{\kappa\sigma_u}{G_{u+1}}\right)^2 + \sum_n b_{n,q}^{(u)} (t_{n,q}^{(u)})^2, \\ \text{Var}_p^{(u+1)} &= \left(\frac{\kappa\sigma_u}{G_{u+1}}\right)^2 + \sum_n b_{n,p}^{(u)} (t_{n,p}^{(u)})^2.\end{aligned}\tag{5.64}$$

Similar to the TMS code with heterogeneous independent AWGN, we derive the asymptotic curves for SR code in the same way. In the case of $n = 2$, the PDFs in both channels are exactly Gaussian. Let the STD be σ_1 for the channel transferring data mode and σ_2 for ancilla mode. Therefore, Eqs.(5.62) reduce to:

$$Q(\xi'_q) = \sum_{n \in \mathbb{Z}} b_n F_{\sigma^{(2)}}(\xi'_q - \kappa \frac{\sigma_1}{\sigma_2} n \sqrt{2\pi}), \tag{5.65}$$

$$P(\xi'_p) = \sum_{n \in \mathbb{Z}} b_n F_{\sigma^{(2)}}(\xi'_p - \kappa n \sqrt{2\pi}), \tag{5.66}$$

where $\sigma^{(2)} = \kappa\sigma_1/G$ and $b_n = \int_{(n-\frac{1}{2})\sqrt{2\pi}}^{(n+\frac{1}{2})\sqrt{2\pi}} F_{G\sigma_2/\kappa}(x) dx$. From Eq. (5.61), when $G \gg 1$, $\kappa \approx \sigma_2/\sigma_1$. Let's take the sum over $n = 0, \pm 1$ to obtain the asymptotic result. Since $b_{\pm 1} \approx \text{Erfc}(\sqrt{\pi}/2G\sigma_1)/2$, using our definition for the total output noise we have:

$$\begin{aligned}2\sigma_L^2 &\equiv \text{Var}_p + \text{Var}_q \\ &= \frac{2\sigma_1^2\sigma_2^2}{G^2\sigma_1^2} + 2\pi \left(1 + \frac{\sigma_2^2}{\sigma_1^2}\right) \text{Erfc}\left(\frac{\sqrt{\pi}}{2G\sigma_1}\right).\end{aligned}\tag{5.67}$$

Let $x = 1/G^2\sigma_1^2$, then we need to solve the minimization of the function

$$f(x) = \sigma_1^2\sigma_2^2x + 2\pi \left(1 + \frac{\sigma_2^2}{\sigma_1^2}\right) \text{Erfc}\left(\frac{\sqrt{\pi x}}{2}\right).$$

We find the optimum x^* by fixing the derivative to be 0 and then get the approximate value by solving the equation iteratively.

$$\begin{aligned}x^* &= \frac{4}{\pi} \ln \left[\frac{\sqrt{\pi}}{4\sigma_1^2\sigma_2^2/(1 + \sigma_2^2/\sigma_1^2)\sqrt{x^*}} \right] \\ &\approx \frac{4}{\pi} \ln \left[\frac{\pi^{3/2}}{4\sigma_1^2\sigma_2^2/(1 + \sigma_2^2/\sigma_1^2)} \right].\end{aligned}$$

Therefore, we have the approximate σ_L^2 and also the asymptotic curves for $\sigma_L = t\sigma_2$ as

$$\sigma_L^2 \approx \frac{4\sigma_1^2\sigma_2^2}{\pi} \ln \left[\frac{\pi^{3/2}}{4\sigma_1^2\sigma_2^2/(1 + \sigma_2^2/\sigma_1^2)} \right], \tag{5.68}$$

$$t^2 = \frac{4\sigma_1^2}{\pi} \ln \left[\frac{\pi^{3/2}}{4\sigma_1^2\sigma_2^2/(1 + \sigma_2^2/\sigma_1^2)} \right]. \tag{5.69}$$

The performance of the concatenated codes is shown in Fig. 5.6. Fig. 5.6(a) shows the $(u + 1)$ -th layer of encoding, where a two-mode code is applied on the logical mode at the u -th layer (with noise STD $\sigma_L^{(u)}$) and another GKP ancilla mode (with

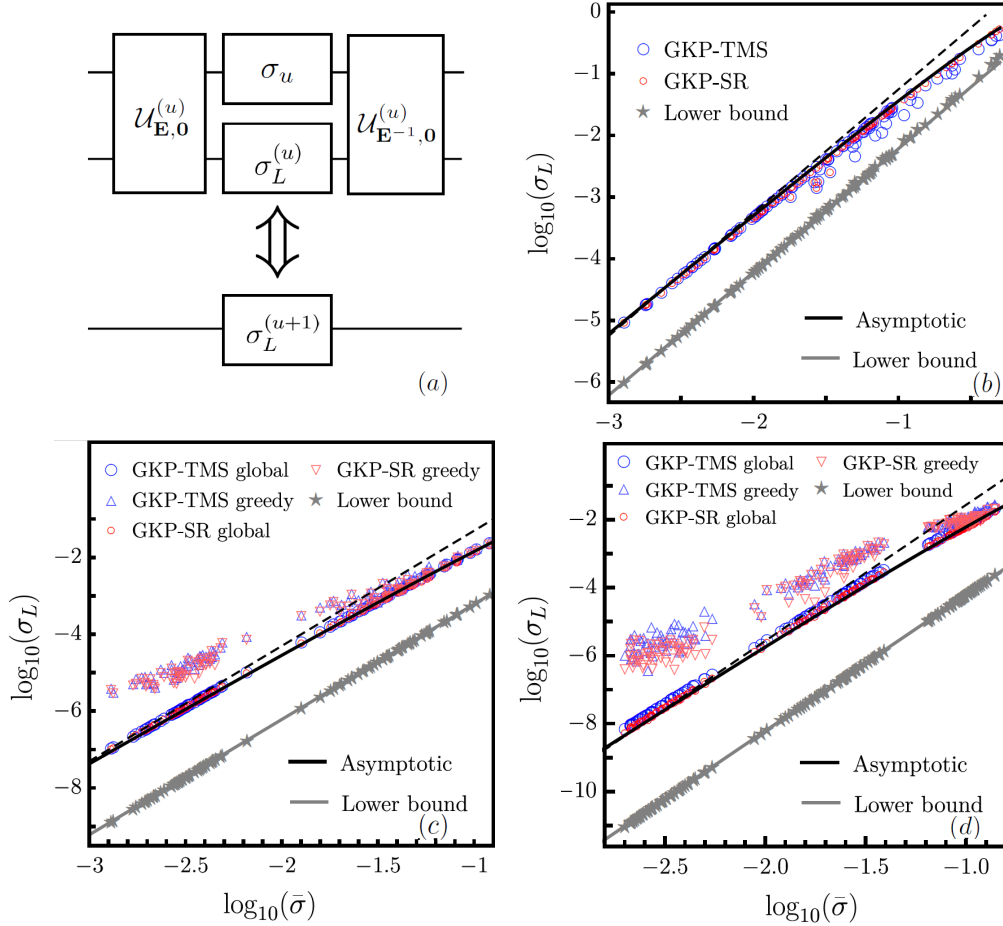


Figure 5.6: (a) Schematic of the concatenation of codes. (b-d) The corrected noise STD σ_L^* vs $\bar{\sigma}$ in a logarithmic scale. The number of modes equals two (b), three (c) and four (d). Asymptotic results (black solid lines) are obtained from Eq. (5.71) for comparison. The black dashed lines show the scaling of $\sigma_L^* \sim \bar{\sigma}^n$, with $n = 2, 3, 4$ in (b)(c)(d). The lower bound (gray solid lines and stars) comes from Ineq. (5.31).

noise STD σ_u). Thereby, one can further reduce the average noise STD to $\sigma_L^{(u+1)}$. For example, in the initial layer ($u = 2$), the mode with noise STD $\sigma_L^{(2)} \equiv \sigma_1$ is encoded with a mode with noise STD σ_2 ; after the error-correction, the reduced noise has a variance $(\sigma_L^{(3)})^2 \simeq v(\sigma_1^2, \sigma_2^2)$ to the leading-order, as given in Eq. (5.40). Naively, one can simply use Eq. (5.40) recursively to obtain the leading-order logical noise in multiple layers of error-correction. For example, for the three-mode case of $u = 4$ with σ_1, σ_2 at the bottom layer, we have

$$\begin{aligned} \sigma_L^{(4)2} &\simeq v(\sigma_3^2, \sigma_L^{(3)2}) \simeq v(\sigma_3^2, v(\sigma_2^2, \sigma_1^2)) \\ &= \frac{16\bar{\sigma}^6}{\pi^2} \ln\left(\frac{\pi^{3/2}}{2\sigma_1^2\sigma_2^2}\right) \ln\left[\frac{\pi^{5/2}}{8\bar{\sigma}^6} / \ln\left(\frac{\pi^{3/2}}{2\sigma_1^2\sigma_2^2}\right)\right], \end{aligned} \quad (5.70)$$

which is not symmetric between σ_ℓ 's. Therefore, an optimization over the different orders of the noisy channels in the encoding is necessary. To obtain a qualitative understanding, we consider a rough estimation using the geometric mean $\bar{\sigma}$.

$$\sigma_L^{(u)2} \simeq v(\sigma_{u-1}^2, \sigma_L^{(u-1)2}), u \geq 3, \quad (5.71)$$

which is exact to the leading-order for the special case of $u = 3$. In Fig. 5.6, Eq. (5.71) is shown as the solid black curves for comparison. It verifies the scaling $\sigma^{(u)} \sim \bar{\sigma}^{u-1}$ when the noise STDs are small.

However, things are more complicated due to the non-Gaussian noise PDF. In the two-mode case, the initial displacement noise PDF is Gaussian, and becomes non-Gaussian after a single layer of error-correction. Therefore, a more accurate analysis is necessary to evaluate the performance of a concatenated code design. Formally, for the noise model described by Eq. (5.29), an n -layer concatenation of the two-mode codes is described by two vectors. First, the set of parameters $\mathbf{G} = (G_1, \dots, G_{n-1})$ determines the encoding operations. Second, a permutation vector $\mathbf{\Pi} = (P_1, \dots, P_n)$ denotes the order of channels $\{\Phi_{\sigma_\ell^2}\}_{\ell=1}^n$ being utilized: at the u -th layer, the additional mode goes through the channel $\Phi_{\sigma_{P_u}^2}$. Without loss of generality, we consider the noises in the channels to be ordered from small to large as $\sigma_1 \leq \sigma_2 \leq \dots \leq \sigma_n$. For example, the reverse order $\mathbf{\Pi} = (n, n-1, \dots, 3, 2, 1)$ describes the following procedure: the mode at the bottom layer experiences the the least noisy channel $\Phi_{\sigma_1^2}$, and then after the encoding with all other modes layer by layer, interacts with the data mode that goes through the most noisy channel $\Phi_{\sigma_n^2}$ as indicated by the case of Fig. 5.6(a).

With the encoding specified above, after performing the displacement based on estimators similar to the two-mode case, it turns out that the residue noise PDF is a symmetric sum of Gaussian functions. For the GKP-TMS code, the PDFs of both quadratures at the $(u+1)$ -th layer are identical,

$$P(\xi') = \sum_{k, \ell \in \mathbb{Z}} b_{k, \ell} F_{\sigma^{(u+1)}}(\xi' - t_{k, \ell}), \quad (5.72)$$

where the parameters $b_{k, \ell}$, $\sigma^{(u+1)}$ and $t_{k, \ell}$ depend on parameters \mathbf{G} and $\mathbf{\Pi}$. Therefore, we can keep track of the noise PDF efficiently, via a recursion.

For a concatenated scheme over the noise model in Eq. (5.29), we can choose the parameter \mathbf{G} and the order $\mathbf{\Pi}$ of the n channels to minimize the output noise STD

$$\sigma_L(\mathbf{G}, \mathbf{\Pi}) = \sqrt{(\sigma^{(n+1)})^2 + \sum_{k, \ell \in \mathbb{Z}} b_{k, \ell} t_{k, \ell}^2}. \quad (5.73)$$

for the GKP-TMS code or a similar formula for the GKP-SR code. For n channels, there are $n!$ choices of orders. For each order $\mathbf{\Pi}$, we may optimize the parameter \mathbf{G} through a multi-parameter global optimization to obtain $\sigma_L^*(\mathbf{\Pi}) = \min_{\mathbf{G}} \sigma_L(\mathbf{G}, \mathbf{\Pi})$. Alternatively, one can adopt a greedy strategy: at the u -th layer ($3 \leq u \leq n+1$) one minimizes $\sigma^{(u)}$ over a single parameter G_{u-2} at this layer. We denote the greedy minimum as $\sigma_L^*(\mathbf{\Pi})$. Overall, a global scheme involves a joint optimization problem of $n-1$ parameters; while the greedy scheme only involves a single-parameter optimizing problem for $n-1$ times. To understand the performance of the codes, we numerically evaluate the variances for random samples. We have considered random samples of three types—“realistic”, “asymptotic” and “mixed”—to incorporate the generic properties of noises. The realistic samples take all $\log_{10}(\sigma_s)$ uniform in range $[-2, -0.7]$ to represent cases that are practically relevant; the asymptotic samples take all $\log_{10}(\sigma_s)$ uniform in range $[-3, -2]$ to probe the asymptotic performances; while the mixed samples take $\log_{10}(\sigma_s)$ uniform in each of the three different ranges: $[-4, -3]$, $[-3, -2]$ and $[-2, -1]$, to represent the case where noises are very different across the different channels.

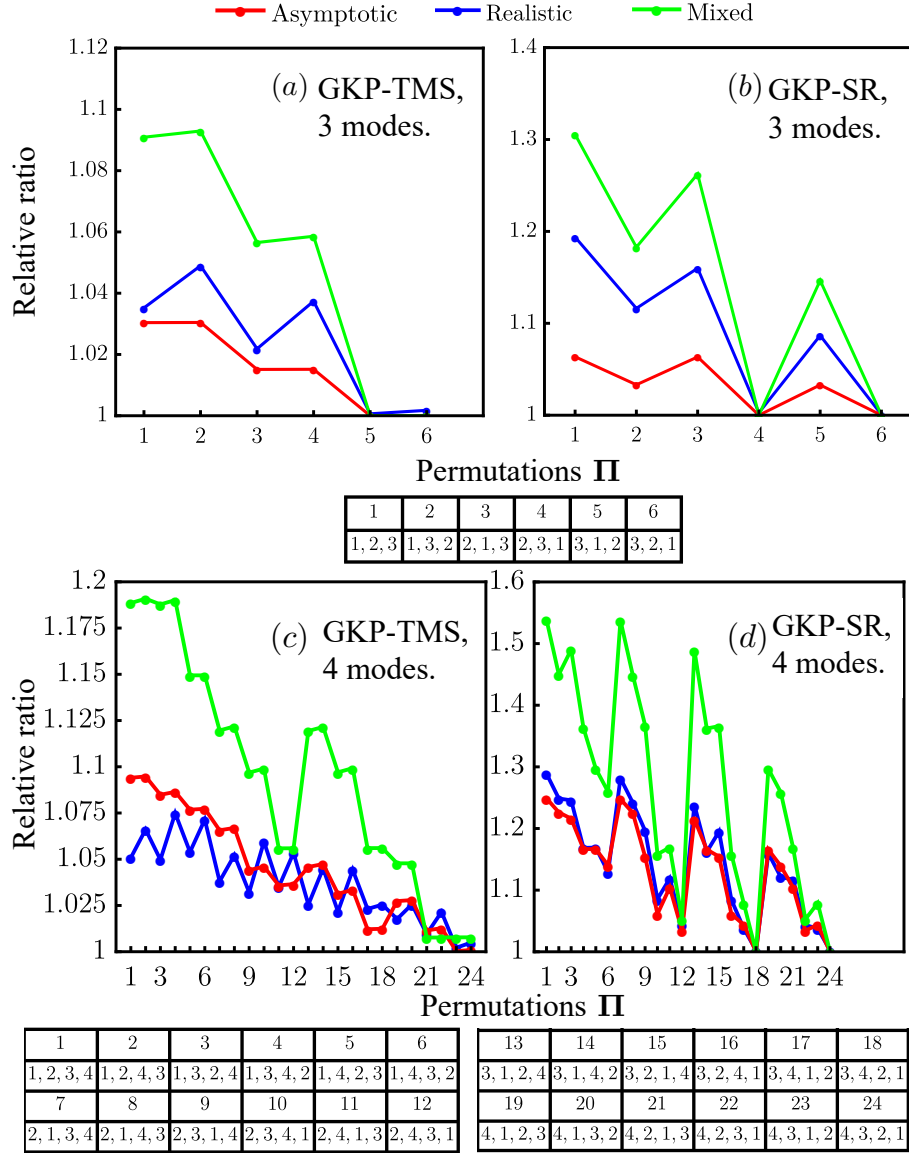


Figure 5.7: Average relative ratios $\sigma_L^*(\Pi) / \min_{\Pi} \sigma_L^*(\Pi)$ versus permutation Π for GKP-TMS and GKP-SR codes with three and four modes. The data set σ_i is generated randomly.

Now we further look into the global minimized noise $\sigma_L^*(\mathbf{\Pi})$ as a function of the order $\mathbf{\Pi}$. For example, using random samples, we calculate their relative ratios of $\sigma_L^*(\mathbf{\Pi})/\min_{\mathbf{\Pi}} \sigma_L^*(\mathbf{\Pi})$ for each permutation $\mathbf{\Pi}$. To represent the general case, we take the sample average for each permutation and plot the average relative ratios in Fig. 5.7. Although fluctuations occur among some permutations, an average value close to or equal to unity indicates an optimal permutation. For the 4-mode cases in Fig. 5.7 (d), the relative ratios are generally greater when the most noisy channel is put on the bottom, such as orders 1, 3, 7 and 13. While relative ratios are smaller when the least noisy channel is put on the bottom, such as orders 12, 18 and 24. We see that in most cases the reverse order $\mathbf{\Pi} = (n, n-1, \dots, 2, 1)$ gives a relative ratio of unity, therefore is the optimal order of permutation in most cases being considered, for both GKP-TMS and GKP-SR codes. After the global optimization of the encoding parameter \mathbf{G} , the differences between permutations are generally small, typically less than one order of magnitude, considering that the noise can be suppressed to many orders of magnitude smaller than the original noise. Indeed, suppose one optimizes over the entire Gaussian encoding unitary $\hat{U}_{\mathbf{E}, \mathbf{0}}$ in Fig. 5.3, the permutations of the noisy channels will not affect the overall performance, as Gaussian unitary enables the arbitrary swapping between modes. Below, we give some intuition about the different permutations.

For the two-mode case of the GKP-TMS code, the numerical results show that the order $\mathbf{\Pi} = (1, 2)$ works better than the other order $\mathbf{\Pi} = (2, 1)$. This is caused by effects from the side peaks beyond the main Gaussian peak in the noise distributions. As to multi-mode concatenation, because $\sigma_u \gg \sigma^{(u)}$ is true after the first layer, we can ignore the effects of side peaks in the noise distribution of higher-order concatenations i.e., $\sigma_L^{(u+1)} \approx \sigma^{(u+1)}$, then $\sigma_L^{(u+1)} \approx \sigma^{(u+1)} \approx \sigma^{(u)}/\sqrt{G-1}$ as shown in last paragraph of Section 5.3.2. So we prefer to put the less noisy channel on the bottom. Intuitively, the order $\mathbf{\Pi} = (n, n-1, \dots, 1, 2)$ should work better. Indeed, although the reverse order has good performances, the orders $(3, 1, 2)$ and $(4, 3, 1, 2)$ are in fact as good as, if not slightly better than, the reverse orders $(3, 2, 1)$ and $(4, 3, 2, 1)$ respectively. At the bottom layer, one can utilize the order $(1, 2)$ identical to the two-mode case; while for the higher-order layers, the non-Gaussian distribution complicates the situation and the reversed orders turn out to have better performances.

For the two-mode case of the GKP-SR code, the numerical results show that the order $\mathbf{\Pi} = (2, 1)$ works better. Similarly, for higher orders, if we ignore the effects of side peaks, we have $\sigma_L^{(u+1)} \approx \sigma^{(u+1)} \approx \sigma^{(u)}/G$. So the order $\mathbf{\Pi} = (n, n-1, \dots, 2, 1)$ is expected to work better intuitively. Since our asymptotic analysis does not include the effect of side peaks after the first layer, when the differences between σ 's are small, other orders may work as good or even slightly better sometimes.

5.3.3 Mode-wise Decomposition and MMSE Estimation

In the previous sections, we introduced concatenated codes for heterogeneous noises. However, if the noises are homogeneous, i.e., $\sigma_1 = \dots = \sigma_n$, the code may be significantly simplified. In this section, we derive the optimal oscillator-to-oscillator codes within the GKP stabilizer codes for homogeneous noises. An arbitrary GKP-stabilizer code is effectively simplified to a generalized GKP two-mode-squeezing (TMS) code.

The optimal encoding strategy minimizes the geometric mean error, achieved through GKP-TMS codes with optimized GKP lattices and TMS gains. In the decoding phase, the minimum mean square error (MMSE) estimator is utilized. It outperforms the linear estimator by minimizing residual noise on data modes more effectively. While linear estimation leads to a break-even point of additive noise at $\sigma_{\text{lin}}^* \sim 0.558$, MMSE estimation pushes this threshold to $\sigma_{\text{MMSE}}^* = 0.605(5)$. This value is at the edge of the best break-even region for arbitrary GKP codes, which ranges from 0.607 to 0.707, as derived from our quantum capacity analyses.

In the single-mode data and ancilla scenario, the optimal code design for minimizing geometric mean error is efficiently solvable. Numerical evidence suggests that a hexagonal GKP lattice is optimal, surpassing the previously favored square lattice. The multimode case presents more complex challenges in identifying the optimal lattice. For two-mode data and ancilla, the D4 lattice—a 4-dimensional dense-packing lattice—proves superior to direct product of 2-dimensional lattices. This indicates that high-dimensional lattices potentially offer better performance than low-dimensional ones in GKP-stabilizer codes.

Besides the results on the optimal code design, the code reduction also allows us to prove a more general version of the no-threshold-theorem of Ref. [63], where the original proof relies on explicit maximum likelihood error decoder based on GKP-type syndrome information. Our proof is based on a simple, classical information-theoretical argument; moreover, our no-threshold-theorem applies to all GKP-stabilizer codes, and more generally, even when the GKP ancilla are replaced by general non-Gaussian states.

Reduction of Encoding for iid Channel

Lemma 43 *By local symplectic transform Λ_d and Λ_a , a multi-mode pure Gaussian state is generated by two-mode squeezings.*

$$\mathbf{S}\mathbf{S}^\top = (\Lambda_d \oplus \Lambda_a)[\oplus_{i=1}^k \mathbf{S}_{G_i} \oplus \mathbf{I}_{2N-4k}](\Lambda_d \oplus \Lambda_a)^\top. \quad (5.74)$$

The proof of the mode-wise entanglement is provided in Ref. [64]. We can apply the lemma to the iid AGN channel. Because after some encoding \mathbf{S} , the channel has noise given by covariance matrix $\mathbf{V} = \sigma^2 \mathbf{S}^{-1} \mathbf{S}^{-\top}$. In other words, we can decompose a general GKP-stabilizer code into TMS operations and local symplectic operations; see Fig. 5.8 (a-b) for a visual aid of the lemma for the $k = N/2$ case. The local Gaussian unitary U_{Λ_d} and its inverse are applied on the data modes, while the local Gaussian unitary U_{Λ_a} and its inverse are applied on the ancilla modes. Consequently, the encoding and decoding can be taken as simple product of TMS operations.

The above lemma reduces the number of parameters in code description from $2n^2$ to $2k^2 + 2(n-k)^2$ in the leading order. In fact, as we will explain later, coherent data processing (via Λ_d) only reshapes the residual noise; it does not aid in error

correction. Hence a further reduction to $2(n - k)^2$ is permissible. Moreover, the generally multimode entangling operations between data and ancilla are now given by standard TMS operations with N to-be-determined gain parameters G_i .

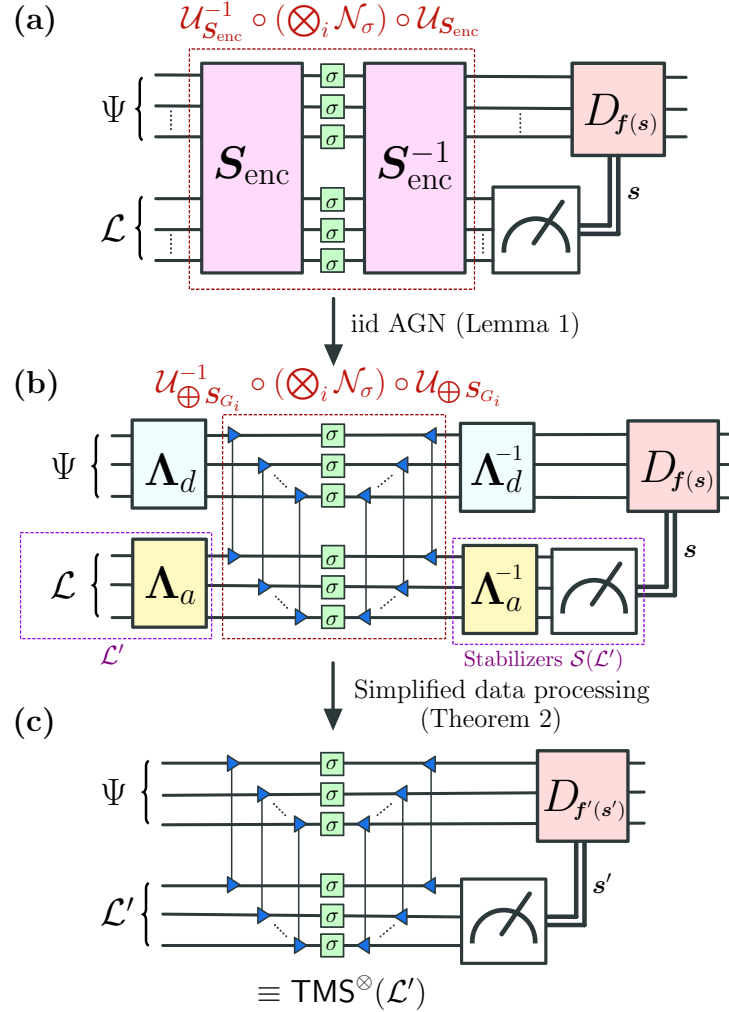


Figure 5.8: Illustration of GKP-stabilizer code reduction (here, $M = N$). (a) A general GKP-stabilizer code with encoding S_{enc} and an ancillary GKP lattice \mathcal{L} . The syndromes s are extracted from stabilizer measurements on the ancillary lattice \mathcal{L} and inform the corrective displacements on the data $D_{f(s)}$. (b) Reduction of the GKP stabilizer code to a set of TMS operations between the data and ancilla modes, up to local symplectic transformations Λ_d and Λ_a . (c) Coherent data processing via Λ_d does not change the performance of the code. Acting on the initial ancillary lattice \mathcal{L} by a symplectic transformation Λ_a produces another lattice \mathcal{L}' . Thus, a general GKP-stabilizer code reduces to a direct product of TMS codes with a GKP ancillary lattice \mathcal{L}' , $\text{TMS}^\otimes(\mathcal{L}')$.

Lemma 44 (Sufficiency of $\text{TMS}^\otimes(\mathcal{L})$) *For an iid AGN channel, in terms of the geometric mean error after the error correction, ${}^{2N}\sqrt{\det[\mathbf{V}_{\text{out}}]}$, on the data modes, the most general GKP-stabilizer code can be completely reduced to a direct product of TMS codes with a general (potentially multimode) ancillary lattice state \mathcal{L} , defined as $\text{TMS}^\otimes(\mathcal{L})$.*

Proof. Lemma 44 is a consequence of Lemma 43, together with the fact that (1) a local symplectic transformation Λ_a on the initial ancillary lattice \mathcal{L} defines a new lattice \mathcal{L}' and (2) coherent pre- and post-processing of the data modes do not increase code performance. To show (2), using the geometric mean $\bar{\sigma}_{\text{GM}}^2 = \sqrt[2N]{\det[\mathbf{V}_{\text{out}}]}$ as a performance metric, first observe that we can push data noise processing via Λ_d^{-1} after the corrective displacement D_f by simply redefining our error estimator $f' \equiv \Lambda_d f$, i.e., $D_f \circ \mathcal{U}_{\Lambda_d^{-1}} = \mathcal{U}_{\Lambda_d^{-1}} \circ D_{\Lambda_d f}$. Just after corrective displacements (but prior to data processing), the residual error covariance matrix on the data modes is \mathbf{V}_{out} and transforms to $\mathbf{V}'_{\text{out}} = \Lambda_d^{-1} \mathbf{V}_{\text{out}} \Lambda_d^{-\top}$ after data processing. However, the geometric mean is invariant under symplectic transformations; in other words, $\det[\mathbf{V}'_{\text{out}}] = \det[\mathbf{V}_{\text{out}}]$. Thus, the performance of the code (as quantified by the geometric mean error) only depends on the gain parameters of the TMS operations, the ancillary lattice state, and the error estimator for corrective displacements—not on Λ_d . ■

We note that the reduction does not work for non-pure Gaussian state or heterogeneous Gaussian noise. In general, we need to consider the whole symplectic group. Next, a few examples of code reductions (consequences of Lemma 43) are provided by specifying the local symplectic matrices Λ_d and Λ_a discussed in Lemma 43.

In the two-mode case, we reduce the GKP-squeezed-repetition code, $\mathcal{S}_{\text{Sq-Rep}}^{[2]}$, to a GKP-TMS code. The local symplectic transform Λ_d is a single-mode squeezer $\Lambda_d = \text{diag}(\sqrt[4]{2}\lambda, 1/\sqrt[4]{2}\lambda)$ and $\Lambda_a = \Lambda_d^{-1}$. Applying Λ_a and Λ_d , we obtain TMS with gain $G = (\sqrt{2} + 1)/2$. Hence, the two-mode squeezed repetition code is equivalent to a TMS code of fixed gain $G = (\sqrt{2} + 1)/2$ and an ancilla rectangular GKP (with dimensions specified by the squeezing parameter λ).

Consider one data mode and two ancilla modes. We can show that a downward staircase concatenation of the TMS code $\mathcal{S}_{G_1, G_2}^{\text{down}} = (\mathbf{I}_2 \oplus \mathcal{S}_{G_2})(\mathcal{S}_{G_1} \oplus \mathbf{I}_2)$ is equivalent to an upward staircase concatenation $\mathcal{S}_{G_a, G_{12}}^{\text{up}} = (\mathcal{S}_{G_{12}} \oplus \mathbf{I}_2)(\mathbf{I}_2 \oplus \mathcal{S}_{G_a})$ with to be determined gains G_a and G_{12} . The data mode is already in normal form, hence $\Lambda_d = \mathbf{I}_2$. The local symplectic transform on the ancilla modes is given by an inverse TMS transformation, $\Lambda_a = \mathcal{S}_{G_a}^{-1}$, with gain $G_a = G_2 G_1 / (1 + G_2(G_1 - 1))$. Applying Λ_d and Λ_a then reduces the staircase encoding to TMS between the first and second modes with gain $G_{12} = 1 + G_2(G_1 - 1)$.

The three-mode squeezed-repetition code can also be reduced. The squeezed-repetition code has encoding matrix

$$\mathcal{S}_{\text{Sq-Rep}}^{[3]} = \begin{pmatrix} 1/\lambda^2 & 0 & 0 & 0 & 0 & 0 \\ 0 & \lambda^2 & 0 & -\lambda & 0 & 0 \\ 1 & 0 & \lambda & 0 & 0 & 0 \\ 0 & 0 & 0 & 1/\lambda & 0 & -\lambda \\ \lambda^2 & 0 & \lambda^3 & 0 & \lambda & 0 \\ 0 & 0 & 0 & 0 & 0 & 1/\lambda \end{pmatrix}; \quad (5.75)$$

see Fig. 5.9(c) for a circuit diagram. By squeezing the data mode via $\Lambda_d = \mathbf{Sq}(\lambda(\lambda^2 + \lambda^4)^{\frac{1}{4}})$ and applying a two-mode ancilla transformation Λ_a , which is lengthy to show, we end up with TMS between the first and the second mode with gain $G_{12} = (\sqrt{1/\lambda^2 + 1} + 1)/2$.

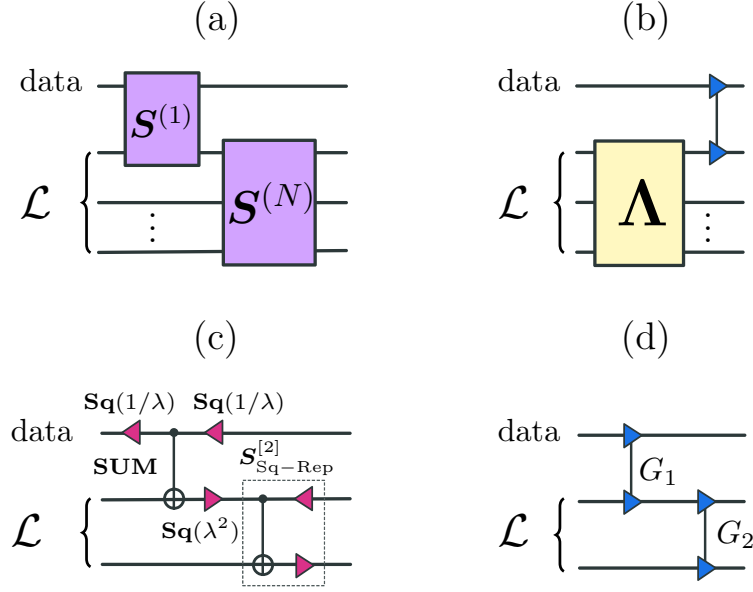


Figure 5.9: Circuit diagrams for concatenated codes. (a) General definition of a concatenated code. Data couples to an ancilla via $S^{(1)}$. Adding more layers leads to further error suppression. (b) Equivalent representation using TMS code reduction. Most operations in a concatenated code can be done offline on the ancillae and the ancillae can be coupled to the data at the end via TMS. (c) Example of a three mode concatenated squeezed repetition code. (d) Example of a three mode concatenated TMS code.

Metric of performance

On the decoding side, an inverse Gaussian unitary described by S_{enc}^{-1} is first applied to disentangle the data and the ancilla. Then one measures the ancilla system to perform error correcting displacement operations $D_{f(s)}$ based on the measurement results s . Here, f is a vector function (i.e., $f : \mathbb{R}^{2M} \rightarrow \mathbb{R}^{2k}$) that takes the syndromes s as input and provides an estimate for the error displacements on the data. The corrective displacements aim to cancel the additive noise on the data. Due to the analog nature of the errors, such a cancellation is never perfect, and there will be residual, random displacements ξ_d on the output data modes.

To quantify the error correction performance, we evaluate the covariance matrix V_{out} of the residue displacements ξ_d , despite the distribution of ξ_d being non-Gaussian after decoding. Note that, prior to encoding, one may also apply a Gaussian unitary U_{S_d} and then apply the inverse $U_{S_d}^{-1}$ after the final decoding step. Pre- and post-processing transform the residue noise covariance matrix as $S_d^{-1} V_{\text{out}} S_d^{-\top}$. Such an operation is considered ‘free’ and should not improve the performance of the error correction. Therefore, we consider the geometric mean (GM) error

$$\bar{\sigma}_{\text{GM}}^2 \equiv \sqrt[2N]{\det V_{\text{out}}}, \quad (5.76)$$

as the figure of merit to benchmark code performance, which is necessarily invariant under symplectic operations on the data. Moreover, the GM error has information theoretic roots, as it relates to a lower bound on the quantum capacity for the additive non-Gaussian noise channel of a multimode GKP code. Given the geometric

mean error of general additive noise $\bar{\sigma}_{\text{GM}}^2$, the quantum capacity of the N -mode additive noise channel $C_{\mathcal{Q}} \geq \max \left[0, N \log_2 \left(\frac{1}{e\bar{\sigma}_{\text{GM}}^2} \right) \right]$.

As an alternative simpler metric, we also consider the root-mean-square (RMS) error,

$$\bar{\sigma}_{\text{RMS}}^2 \equiv \frac{\text{Tr}\{\mathbf{V}_{\text{out}}\}}{2N}. \quad (5.77)$$

The RMS error is only invariant under orthogonal symplectic (e.g., linear optical) transformations on the data. However, it is easier to evaluate and provides an upper bound for the GM error, $\bar{\sigma}_{\text{RMS}}^2 \geq \bar{\sigma}_{\text{GM}}^2$.

No Threshold for Finite Squeezing

Combining the reduction of the code and the classical capacity theorem, it can be shown that if the squeezing is finite, we cannot suppress the noise to an arbitrary amount. This phenomena is referred as no threshold theorem. Although the derivation is based on the iid noises, it can be extended to heterogeneous noises by taking $\sigma = \min\{\sigma_1, \dots, \sigma_n\}$.

Consider iid AGN noise $\boldsymbol{\xi} = (\boldsymbol{\xi}_d, \boldsymbol{\xi}_a)$ for the displacement errors on N data modes and M ancilla modes. After the encoding (and decoding) transformations $\mathbf{S}_{\text{enc}} (\mathbf{S}_{\text{enc}}^{-1})$, the correlated noises are $(\mathbf{x}_d, \mathbf{x}_a) = \mathbf{S}_{\text{enc}}^{-1} \boldsymbol{\xi} \sim \mathcal{N}(0, \mathbf{V}_x)$, where $\mathbf{V}_x = \sigma^2 \mathbf{S}_{\text{enc}}^{-1} \mathbf{S}_{\text{enc}}^{-\top}$. Since all encoding can be reduced to TMS up to local transformations via Lemma 43, we need only consider \mathbf{V}_x as a direct sum of N correlated two-mode blocks (plus an identity block on the remaining $M - N$ ancilla modes), which has qq and pp correlations between data and ancilla arising from two-mode squeezing (but zero qp correlations). Therefore, to analyze general properties of the code, we can focus our attention on one data-ancilla mode pair and one quadrature at a time. Let q_{a_i} be the $(2i-1)$ th element of \mathbf{x}_a (where $i = 1, 2, \dots, N$) that is correlated with q_{d_i} of \mathbf{x}_d via TMS with gain G_i , and let $\tilde{q}_{d_i} \equiv \tilde{q}_{d_i}(q_{a_i})$ be the estimation of the data noise given knowledge of the ancilla noise, which we can extract from, e.g., syndrome measurements. Although perfect knowledge of the ancilla noise is not generally available, we assume that it is in order to place an ultimate lower bound. The estimation variance of a generic random variable X , given side information Y , is lower bounded by a function of the conditional differential entropy $S(X|Y)$ via $\mathbb{E}[(X - \tilde{X}(Y))^2] \geq \exp[2S(X|Y)]/2\pi e$. In our current setting, $S(q_{d_i}|q_{a_i}) = \ln\left(\frac{2\pi e\sigma^2}{2G_i - 1}\right)/2$, which is limited by the finite squeezing to correlate the noises. Therefore,

$$\mathbb{E}[(q_{d_i} - \tilde{q}_{d_i})^2] \geq \frac{\sigma^2}{2G_i - 1}. \quad (5.78)$$

If the TMS has a finite squeezing level G_i , then having a larger number of ancilla modes (or an arbitrary ancilla state) will not further help error correction. This implies a universal no-threshold theorem for a wide variety of codes based on Gaussian encoding—including but not limited to GKP-stabilizer codes.

Theorem 45 (No threshold for finite squeezing) *For N data modes and arbitrary number of ancilla modes, the residual error for any oscillators-to-oscillators code using Gaussian encoding is lower bounded by*

$$\text{Tr}(\mathbf{V}_{\text{out}}) \geq \sum_{i=1}^N \frac{2\sigma^2}{2G_i - 1}, \quad (5.79)$$

where \mathbf{V}_{out} is the covariance matrix for the residual output error of the code, G_i are the two-mode squeezing gains of the encoding after code reduction [see Lemma 43 and Lemma 44], and σ^2 is the variance of the iid AGN channels.

Proof. The proof follows by summing over the individual variances (left hand side) of Eq. (5.78), which is less than or equal to the trace of the residual output covariance matrix, \mathbf{V}_{out} . The factor of two is due to the fact that the q and p quadratures of the i th mode contribute equally to the sum due to the structure of two-mode squeezing.

■

If we place a tolerance on the output error $\varepsilon \geq \text{Tr}(\mathbf{V}_{\text{out}})$, Theorem 45 implies that the (average) gain G must scale as $G \sim N\sigma^2/\varepsilon$ for the error to stay below tolerance, which is independent of the number of ancilla modes M used in the code. Thus, we cannot make ε arbitrarily small with a finite amount of squeezing even if we increase the number of ancilla modes; this is the essence of the no-threshold theorem for oscillator-to-oscillator codes. The proof follows from the general code reduction Lemma 44 (see also Lemma 43) and a simple, classical data-processing argument. Furthermore, we do not require the ancilla modes to be prepared in GKP states and the decoding strategy does not enter into our proof.

Minimum Mean Square Error (MMSE) estimation

To evaluate the random displacement error, we consider Minimum Mean Square Error estimation, which is constructed to minimize the RMS error of Eq. (5.77) (as RMS error is the square root of mean square error). The encoding symplectic transform \mathbf{S}_{enc} correlates the additive noise between the data and the ancilla. Let the covariance matrix of the AGN be \mathbf{V}_ξ . The error correlation is described by

$$\mathbf{V}_x = \mathbf{S}_{\text{enc}}^{-1} \mathbf{V}_\xi \mathbf{S}_{\text{enc}}^{-\top}. \quad (5.80)$$

The additive noise on the ancilla \mathbf{x}_a can be extracted by measuring the stabilizers of the ancilla canonical GKP states. This leads to an error syndrome $\mathbf{s} \in [-\sqrt{\pi}/2, \sqrt{\pi}/2]^{2(n-k)}$, from which we can estimate the additive noise on the data \mathbf{x}_d . As shown in Eq. (5.14), for a general lattice with generator matrix \mathbf{M} , we have $\mathbf{s} = R_{\sqrt{2\pi}}(\mathbf{M}^\top \boldsymbol{\Omega} \mathbf{x}_a)$, where $R_{\sqrt{2\pi}}$ is the element-wise modulus of $\sqrt{2\pi}$ and $\mathbf{x}_a = \boldsymbol{\xi}$ is the random noise of the ancilla.

This error syndrome gives us some information about the random displacement error of data \mathbf{x}_d since \mathbf{x}_d and \mathbf{x}_a are correlated by two-mode squeezing transforms. The joint probability density distribution of the data and the error syndrome, $P(\mathbf{x}_d, \mathbf{s})$, is not a Gaussian distribution but a sum of Gaussian distributions. The MMSE minimizes $\bar{\sigma}_{\text{RMS}}^2$ in Eq. (5.77), and the estimator can be derived from the conditional distribution $P(\mathbf{x}_d|\mathbf{s})$ via $\mathbf{f}_{\text{MMSE}}(\mathbf{s}) = \int_{\mathbb{R}^{2k}} d\mathbf{x}_d \mathbf{x}_d P(\mathbf{x}_d|\mathbf{s})$ leading to the following theorem

Theorem 46 *For a GKP-stabilizer code with GKP lattice state \mathcal{L} described by generator matrix \mathbf{M} , the minimum mean square estimation (MMSE) for an error syndrome \mathbf{s} is given by*

$$\begin{aligned} \mathbf{f}_{\text{MMSE}}(\mathbf{s}) &= - \frac{\sum_{\mathbf{n}} \mathbf{V}_d^{-1} \mathbf{V}_{da}(\mathbf{s} - \mathbf{n}\sqrt{2\pi}) e^{(\sqrt{2\pi}\mathbf{n}^\top \mathbf{V}_{d|a} \mathbf{s} - \pi \mathbf{n}^\top \mathbf{V}_{d|a} \mathbf{n})}}{\sum_{\mathbf{m}} e^{(\sqrt{2\pi}\mathbf{m}^\top \mathbf{V}_{d|a} \mathbf{s} - \pi \mathbf{m}^\top \mathbf{V}_{d|a} \mathbf{m})}}, \end{aligned} \quad (5.81)$$

where $\mathbf{m}, \mathbf{n} \in \mathbb{Z}^{2M}$ sum over all integer vectors, and the matrices \mathbf{V}_{da} , \mathbf{V}_d and \mathbf{V}_a are defined through the equation

$$\begin{pmatrix} \mathbf{V}_d & \mathbf{V}_{da} \\ \mathbf{V}_{da}^T & \mathbf{V}_a \end{pmatrix}^{-1} \equiv (\mathbf{I}_{2N} \oplus \mathbf{M}^\top \boldsymbol{\Omega}) \mathbf{V}_x (\mathbf{I}_{2N} \oplus (\mathbf{M}^\top \boldsymbol{\Omega})^\top). \quad (5.82)$$

and $\mathbf{V}_{d|a} = \mathbf{V}_a - \mathbf{V}_{da}^T \mathbf{V}_d^{-1} \mathbf{V}_{da}$.

Proof. In the QEC protocol, the original noise covariance matrix $\mathbf{V}_\xi = \bigoplus_{i=1}^{N+M} \sigma_i^2 \mathbf{I}_2$ is transformed into

$$\mathbf{V}_x^{-1} = \mathbf{S}_{\text{enc}}^\top \mathbf{V}_\xi^{-1} \mathbf{S}_{\text{enc}},$$

via the encoding symplectic transform \mathbf{S}_{enc} and decoding symplectic transform $\mathbf{S}_{\text{enc}}^{-1}$. Let the additive noise on the data and ancilla be

$$\mathbf{x}_d = (x_1^{(q)}, x_1^{(p)}, \dots, x_k^{(q)}, x_k^{(p)})^\top, \quad \mathbf{x}_a = (x_{k+1}^{(q)}, x_{k+1}^{(p)}, \dots, x_n^{(q)}, x_n^{(p)})^\top,$$

which are random variables following the joint distribution

$$P(\mathbf{x}_d, \mathbf{x}_a) = g[\mathbf{V}_x, (\mathbf{x}_d, \mathbf{x}_a)]. \quad (5.83)$$

We define the interval $\mathcal{I} \equiv [-\sqrt{\pi/2}, \sqrt{\pi/2}]$, and the error syndrome

$$\mathbf{s} = R_{\sqrt{2\pi}}(\mathbf{M}^\top \boldsymbol{\Omega} \mathbf{x}_a) \in \mathcal{I}^{2k}.$$

To get the joint distribution of \mathbf{x}_d and \mathbf{s} , we first rewrite Eq. (5.83) as

$$P(\mathbf{x}_d, \mathbf{M}^\top \boldsymbol{\Omega} \mathbf{x}_a) = g \left[\begin{pmatrix} \mathbf{V}_d & \mathbf{V}_{da} \\ \mathbf{V}_{da}^T & \mathbf{V}_a \end{pmatrix}^{-1}, (\mathbf{x}_d, \mathbf{M}^\top \boldsymbol{\Omega} \mathbf{x}_a) \right],$$

where we have defined the covariance matrix in the block form

$$\begin{pmatrix} \mathbf{V}_d & \mathbf{V}_{da} \\ \mathbf{V}_{da}^T & \mathbf{V}_a \end{pmatrix}^{-1} \equiv (\mathbf{I}_{2N} \oplus \mathbf{M}^\top \boldsymbol{\Omega}) \mathbf{V}_x (\mathbf{I}_{2N} \oplus (\mathbf{M}^\top \boldsymbol{\Omega})^\top). \quad (5.84)$$

and used the property $g(\boldsymbol{\Sigma}, \mathbf{x}) = g(\mathbf{L}\boldsymbol{\Sigma}\mathbf{L}^\top, \mathbf{L}\mathbf{x})$ for some invertible matrix \mathbf{L} . From here, the distribution of the error and syndrome can be solved as

$$P(\mathbf{x}_d, \mathbf{s}) = \int_{\mathbb{R}^{2M}} d(\mathbf{M}^\top \boldsymbol{\Omega} \mathbf{x}_a) P(\mathbf{x}_d, \mathbf{M}^\top \boldsymbol{\Omega} \mathbf{x}_a) \sum_{\mathbf{k}} \delta(\mathbf{s} - \mathbf{M}^\top \boldsymbol{\Omega} \mathbf{x}_a - \mathbf{k}\sqrt{2\pi}) \quad (5.85a)$$

$$= \sum_{\mathbf{k}} g\left((\mathbf{I}_{2N} \oplus \mathbf{M}^\top \boldsymbol{\Omega}) \mathbf{V}_x (\mathbf{I}_{2N} \oplus (\mathbf{M}^\top \boldsymbol{\Omega})^\top), (\mathbf{x}_d, \mathbf{s} - \mathbf{k}\sqrt{2\pi})\right) \quad (5.85b)$$

$$= \sum_{\mathbf{k}} g(\mathbf{V}_d^{-1}, \mathbf{x}_d + \mathbf{V}_d^{-1} \mathbf{V}_{da}(\mathbf{s} - \mathbf{k}\sqrt{2\pi})) g(\mathbf{V}_{d|a}^{-1}, \mathbf{s} - \mathbf{k}\sqrt{2\pi}). \quad (5.85c)$$

where we sum over all vector of integers $\mathbf{k} \in \mathbb{Z}^{2M}$, $\delta(\cdot)$ is the Dirac delta function and $\mathbf{V}_{d|a} = \mathbf{V}_a - \mathbf{V}_{da}^T \mathbf{V}_d^{-1} \mathbf{V}_{da}$. From (5.85a) to (5.85b), we integrate over \mathbf{x}_a . From (5.85b) to (5.85c), we adopt the block form of Eq. (5.84) and separate the joint distribution into two parts.

The PDF of the syndrome measurement result can be obtained by integrating over \mathbf{x}_d ,

$$P(\mathbf{s}) = \int_{\mathbb{R}^{2k}} d\mathbf{x}_d P(\mathbf{x}_d, \mathbf{s}) = \sum_{\mathbf{k}} g(\mathbf{V}_{d|a}^{-1}, \mathbf{s} - \mathbf{k}\sqrt{2\pi}).$$

The PDF of the conditional distribution is therefore

$$\begin{aligned} P(\mathbf{x}_d|\mathbf{s}) &= P(\mathbf{x}_d, \mathbf{s})/P(\mathbf{s}) \\ &= \frac{\sum_{\mathbf{n}} g(\mathbf{V}_d^{-1}, \mathbf{x}_d + \mathbf{V}_d^{-1}\mathbf{V}_{da}(\mathbf{s} - \mathbf{n}\sqrt{2\pi})) g(\mathbf{V}_{d|a}^{-1}, \mathbf{s} - \mathbf{n}\sqrt{2\pi})}{\sum_{\mathbf{m}} g(\mathbf{V}_{d|a}^{-1}, \mathbf{s} - \mathbf{m}\sqrt{2\pi})}. \end{aligned}$$

The MMSE estimator is obtained by evaluating the mean of the conditional distribution

$$\begin{aligned} \mathbf{f}_{\text{MMSE}}(\mathbf{s}) &= \int_{\mathbb{R}^{2k}} d\mathbf{x}_d \mathbf{x}_d P(\mathbf{x}_d|\mathbf{s}) \\ &= \frac{-\sum_{\mathbf{n}} \mathbf{V}_d^{-1}\mathbf{V}_{da}(\mathbf{s} - \mathbf{n}\sqrt{2\pi}) g(\mathbf{V}_{d|a}^{-1}, \mathbf{s} - \mathbf{n}\sqrt{2\pi})}{\sum_{\mathbf{m}} g(\mathbf{V}_{d|a}^{-1}, \mathbf{s} - \mathbf{m}\sqrt{2\pi})} \\ &= \frac{-\sum_{\mathbf{n}} \mathbf{V}_d^{-1}\mathbf{V}_{da}(\mathbf{s} - \mathbf{n}\sqrt{2\pi}) \exp\{\sqrt{2\pi}\mathbf{n}^\top \mathbf{V}_{d|a}\mathbf{s} - \pi\mathbf{n}^\top \mathbf{V}_{d|a}\mathbf{n}\}}{\sum_{\mathbf{m}} \exp\{\sqrt{2\pi}\mathbf{m}^\top \mathbf{V}_{d|a}\mathbf{s} - \pi\mathbf{m}^\top \mathbf{V}_{d|a}\mathbf{m}\}}, \end{aligned}$$

where $\mathbf{n}, \mathbf{m} \in \mathbb{Z}^{2M}$. ■

Given an error syndrome \mathbf{s} extracted from a general GKP ancilla in a QEC protocol, the element at the i th row and j th column of the output covariance matrix \mathbf{V}_{out} for N data modes is given as

$$\begin{aligned} [\mathbf{V}_{\text{out}}]_{ij} &= \int_{\mathbb{R}^{2k}} d\mathbf{x}_d \int_{\mathbb{J}^{2M}} d\mathbf{s} (\mathbf{x}_d - \tilde{\mathbf{x}}_d)_{i \times j} P(\mathbf{x}_d, \mathbf{s}) \\ &= \sum_{\mathbf{k}} \int_{\mathbb{J}^{2M}} d\mathbf{s} \int_{\mathbb{R}^{2k}} d\mathbf{x}_d (\mathbf{x}_d - \tilde{\mathbf{x}}_d)_{i \times j} g(\mathbf{V}_d^{-1}, \mathbf{x}_d + \mathbf{V}_d^{-1}\mathbf{V}_{da}(\mathbf{s} - \mathbf{k}\sqrt{2\pi})) g(\mathbf{V}_{d|a}^{-1}, \mathbf{s} - \mathbf{k}\sqrt{2\pi}) \\ &= \sum_{\mathbf{k}} \int_{\mathbb{J}^{2M}} d\mathbf{s} \left([\mathbf{V}_d^{-1}]_{ij} g(\mathbf{V}_{d|a}^{-1}, \mathbf{s} - \mathbf{k}\sqrt{2\pi}) + g(\mathbf{V}_{d|a}^{-1}, \mathbf{s} - \mathbf{k}\sqrt{2\pi}) \left\{ \tilde{\mathbf{x}}_d + [\mathbf{V}_d^{-1}\mathbf{V}_{da}(\mathbf{s} - \mathbf{k}\sqrt{2\pi})] \right\}_{i \times j} \right) \\ &= [\mathbf{V}_d^{-1}]_{ij} + \sum_{\mathbf{k}} \int_{\mathbb{J}^{2M}} d\mathbf{s} g(\mathbf{V}_{d|a}^{-1}, \mathbf{s} - \mathbf{k}\sqrt{2\pi}) \left\{ \tilde{\mathbf{x}}_d + [\mathbf{V}_d^{-1}\mathbf{V}_{da}(\mathbf{s} - \mathbf{k}\sqrt{2\pi})] \right\}_{i \times j} \\ &= [\mathbf{V}_d^{-1}]_{ij} + \sum_{\mathbf{k}} 2\pi \int_{\mathbb{J}^{2M}} d\mathbf{s} g(\mathbf{V}_{d|a}^{-1}, \mathbf{s} - \mathbf{k}\sqrt{2\pi}) \left[\frac{\sum_{\mathbf{n}} \mathbf{V}_d^{-1}\mathbf{V}_{da}(\mathbf{n} - \mathbf{k}) g(\mathbf{V}_{d|a}^{-1}, \mathbf{s} - \mathbf{n}\sqrt{2\pi})}{\sum_{\mathbf{m}} g(\mathbf{V}_{d|a}^{-1}, \mathbf{s} - \mathbf{m}\sqrt{2\pi})} \right]_{i \times j}. \end{aligned}$$

where we use the notation $\mathbf{x}_{i \times j} = \mathbf{x}_i \mathbf{x}_j$, as the product of vector component i and j and have expanded and simplified by using the fact that

$$\int_{\mathbb{R}^{2M}} d\mathbf{x}_d (\mathbf{x}_i - \boldsymbol{\mu}_i)(\mathbf{x}_j - \boldsymbol{\mu}_j) \frac{\det(\mathbf{V}_d)^{\frac{1}{2}}}{(2\pi)^N} \exp\left\{-\frac{1}{2}(\mathbf{x} - \boldsymbol{\tau})^\top \mathbf{V}_d(\mathbf{x} - \boldsymbol{\tau})\right\} = [\mathbf{V}_d^{-1}]_{ij} + (\boldsymbol{\mu}_i - \boldsymbol{\tau}_i)(\boldsymbol{\mu}_j - \boldsymbol{\tau}_j).$$

The MMSE estimation exhibits a notable property: both the estimation function and the output covariance matrix after error correction remain invariant under a basis transform of the GKP lattice, expressed as $\mathbf{M} \rightarrow \mathbf{M}\mathbf{N}^\top$. This invariance contrasts with the linear estimation, which depends on the choice of lattice basis.

This unique property of the MMSE captures the fundamental nature of the lattice description inherent to GKP states. Consequently, this allows for the utilization of any basis within the lattice $\mathcal{L}(\mathbf{M})$ for effective error correction. The flexibility afforded by the MMSE in choosing a lattice basis significantly enhances the practicality and adaptability of error correction strategies.

Theorem 47 (Invariance of MMSE) *Consider a generator matrix \mathbf{M} and a change of basis by a unimodular matrix \mathbf{N} , which defines another generator matrix $\mathbf{M}' = \mathbf{M}\mathbf{N}^\top$. Let $\mathbf{s} = R_{\sqrt{2\pi}}(\mathbf{M}^\top \Omega \mathbf{x}_a)$ be the error syndrome and consider the MMSE estimator $\tilde{\mathbf{x}}_d(\mathbf{s}) = \mathbf{f}_{\text{MMSE}}(\mathbf{s})$. Likewise, let $\mathbf{s}' = R_{\sqrt{2\pi}}(\mathbf{N}\mathbf{M}^\top \Omega \mathbf{x}_a)$ be the error syndrome in the new basis and the corresponding MMSE estimator $\tilde{\mathbf{x}}'_d(\mathbf{s}') = \mathbf{f}_{\text{MMSE}}(\mathbf{s}')$. Then, $\tilde{\mathbf{x}}'_d(\mathbf{s}') = \tilde{\mathbf{x}}_d(\mathbf{s})$ and $[\mathbf{V}_{\text{out}}]_{ij} = [\mathbf{V}'_{\text{out}}]_{ij}$. While the linear estimator, given by considering only the $\mathbf{n} = \mathbf{0}$ element in the sum of Eq. (5.81),*

$$\mathbf{f}_{\text{Linear}}(\mathbf{s}) = -\mathbf{V}_d^{-1} \mathbf{V}_{da} \mathbf{s}, \quad (5.86)$$

and its output covariance matrix are not invariant under the change of basis.

We aim to prove the theorem through a series of step-by-step calculations. To facilitate this, we first introduce some necessary lemmas and then proceed with the proof.

Lemma 48 (Invariance of the joint PDF) *Consider a generator matrix \mathbf{M} and a change of lattice basis by a unimodular matrix \mathbf{N} , which defines another generator matrix $\mathbf{M}' = \mathbf{M}\mathbf{N}^\top$. Let $\mathbf{s} = R_{\sqrt{2\pi}}(\mathbf{M}^\top \Omega \mathbf{x}_a)$ be the error syndrome and consider the joint PDF $P(\mathbf{x}_d, \mathbf{s})$. Likewise, let $\mathbf{s}' = R_{\sqrt{2\pi}}(\mathbf{M}'^\top \Omega \mathbf{x}_a) = R_{\sqrt{2\pi}}(\mathbf{N}\mathbf{M}^\top \Omega \mathbf{x}_a)$ be the error syndrome in the new basis and the corresponding joint PDF $P'(\mathbf{x}_d, \mathbf{s}')$. Then, $P'(\mathbf{x}_d, \mathbf{s}') = P(\mathbf{x}_d, \mathbf{s})$.*

Proof. From properties of modulo operations, we have that

$$R_{\sqrt{2\pi}}(\mathbf{N}^{-1} \mathbf{s}') = R_{\sqrt{2\pi}}(\mathbf{N}^{-1} \mathbf{N} \mathbf{M}^\top \Omega \mathbf{x}_a) = \mathbf{s},$$

as both \mathbf{N} and \mathbf{N}^{-1} are matrices of integers. Therefore $\mathbf{N}^{-1} \mathbf{s}' = \mathbf{s} + \boldsymbol{\ell}_{\mathbf{N}^{-1} \mathbf{s}'}$ for some vector of integers $\boldsymbol{\ell}_{\mathbf{N}^{-1} \mathbf{s}'}$ determined by $\mathbf{N}^{-1} \mathbf{s}'$. The joint PDF for the data \mathbf{x}_d and the error syndrome \mathbf{s}' in the new basis is then

$$P'(\mathbf{x}_d, \mathbf{s}') = \sum_{\mathbf{k}} g \left\{ [\mathbf{I}_{2N} \oplus (\mathbf{N}\mathbf{M}^\top \Omega)] \mathbf{V}_x [\mathbf{I}_{2N} \oplus (\mathbf{N}\mathbf{M}^\top \Omega)^\top], (\mathbf{x}_d, \mathbf{s}' - \mathbf{k}\sqrt{2\pi}) \right\} \quad (5.87a)$$

$$= \sum_{\mathbf{k}} g \left\{ [\mathbf{I}_{2N} \oplus (\mathbf{M}^\top \Omega)] \mathbf{V}_x [\mathbf{I}_{2N} \oplus (\mathbf{M}^\top \Omega)^\top], (\mathbf{x}_d, \mathbf{N}^{-1}(\mathbf{s}' - \mathbf{k}\sqrt{2\pi})) \right\} \quad (5.87b)$$

$$= \sum_{\mathbf{k}'} g \left\{ [\mathbf{I}_{2N} \oplus (\mathbf{M}^\top \Omega)] \mathbf{V}_x [\mathbf{I}_{2N} \oplus (\mathbf{M}^\top \Omega)^\top], (\mathbf{x}_d, \mathbf{N}^{-1} \mathbf{s}' - \mathbf{k}'\sqrt{2\pi}) \right\} \quad (5.87c)$$

$$= \sum_{\mathbf{k}'} g \left\{ [\mathbf{I}_{2N} \oplus (\mathbf{M}^\top \Omega)] \mathbf{V}_x [\mathbf{I}_{2N} \oplus (\mathbf{M}^\top \Omega)^\top], (\mathbf{x}_d, \mathbf{s} - (\mathbf{k}' - \boldsymbol{\ell}_{\mathbf{N}^{-1} \mathbf{s}'})\sqrt{2\pi}) \right\} \quad (5.87d)$$

$$= \sum_{\mathbf{k}''} g \left\{ (\mathbf{I}_{2N} \oplus [\mathbf{M}^\top \Omega]) \mathbf{V}_x [\mathbf{I}_{2N} \oplus (\mathbf{M}^\top \Omega)^\top], (\mathbf{x}_d, \mathbf{s} - \mathbf{k}''\sqrt{2\pi}) \right\} \quad (5.87e)$$

$$= P(\mathbf{x}_d, \mathbf{s}). \quad (5.87f)$$

(5.87a) follows directly from the Eq. (5.85c). To move from (5.87b) to (5.87c), we use the fact that \mathbf{N}^{-1} is a unimodular matrix and acting with \mathbf{N}^{-1} on an integer vector simply changes the summation index, $\mathbf{N}^{-1}\mathbf{k} \rightarrow \mathbf{k}'$. In (5.87d), we use $\mathbf{N}^{-1}\mathbf{s}' = \mathbf{s} + \ell_{\mathbf{N}^{-1}\mathbf{s}'}\sqrt{2\pi}$. And in (5.87e), we change the summation index, which is over all integer vectors in \mathbb{Z}^{2M} . ■

Lemma 49 *Given a vector $\mathbf{s} \in \mathbb{R}^{2M}$, a unimodular matrix \mathbf{N} , and a function $J(\mathbf{s})$, it follows that*

$$\int_{\mathfrak{J}^{2M}} J(\mathbf{s}) d(R_{\sqrt{2\pi}}(\mathbf{N}\mathbf{s})) = \int_{\mathfrak{J}^{2M}} J(\mathbf{s}) d\mathbf{s}. \quad (5.88)$$

Proof. For brevity, we use the shorthand $R()$ for the modulo function $R_{\sqrt{2\pi}}()$. Given a unimodular matrix \mathbf{N} , the function $f : \mathbf{s} \rightarrow R(\mathbf{N}\mathbf{s})$ is a bijection from \mathfrak{J}^{2M} to \mathfrak{J}^{2M} , as we can find the inverse function $f^{-1} : R(\mathbf{N}\mathbf{s}) \rightarrow \mathbf{s}$ by $\mathbf{s} = R(\mathbf{N}^{-1}R(\mathbf{N}\mathbf{s}))$. We can then divide the region \mathfrak{J}^{2M} into sub regions $A_{\mathbf{k}} = \{\mathbf{x} \in \mathfrak{J}^{2M} | \mathbf{N}\mathbf{x} - \mathbf{k}\sqrt{2\pi} \in \mathfrak{J}^{2M}\}$. There are finite number of these regions since \mathbf{N} and \mathbf{x} are finite. Let $B_{\mathbf{k}} = \{f(\mathbf{x}) | \mathbf{x} \in A_{\mathbf{k}}\}$ be the image of $A_{\mathbf{k}}$. Then $\mathbf{x} \in A_{\mathbf{k}}$ is equivalent to $f(\mathbf{x}) \in B_{\mathbf{k}}$ by the bijective map” f and thus

$$\begin{aligned} \int_{\mathfrak{J}^{2M}} J(\mathbf{s}) d(f(\mathbf{s})) &= \sum_{\mathbf{k}} \int_{B_{\mathbf{k}}} J(\mathbf{s}) d(f(\mathbf{s})) \\ &= \sum_{\mathbf{k}} \int_{B_{\mathbf{k}}} J(\mathbf{s}) d(\mathbf{N}\mathbf{s} - \mathbf{k}\sqrt{2\pi}) \\ &= \sum_{\mathbf{k}} \int_{A_{\mathbf{k}}} J(\mathbf{s}) d\mathbf{s} \\ &= \int_{\mathfrak{J}^{2M}} J(\mathbf{s}) d\mathbf{s}, \end{aligned}$$

where we use $|\mathbf{N}| = 1$ from the second line to the third line. ■

Now, we begin the proof of the Theorem 47.

Proof. From Lemma 48, we have that $P(\mathbf{x}_d, \mathbf{s}) = P'(\mathbf{x}_d, \mathbf{s}')$. Since $P(\mathbf{s}) = P'(\mathbf{s}')$, then $P(\mathbf{x}_d | \mathbf{s}) = P'(\mathbf{x}_d | \mathbf{s}')$ for the conditional distribution, such that

$$\begin{aligned} \tilde{\mathbf{x}}'_d(\mathbf{s}') &= \int_{\mathbb{R}^{2k}} d\mathbf{x}_d \mathbf{x}_d P'(\mathbf{x}_d | \mathbf{s}') \\ &= \int_{\mathbb{R}^{2k}} d\mathbf{x}_d \mathbf{x}_d P(\mathbf{x}_d | \mathbf{s}) \\ &= \tilde{\mathbf{x}}_d(\mathbf{s}). \end{aligned}$$

Therefore, the estimators are the same under a basis change. Consider the output covariance matrix in the new basis \mathbf{V}'_{out} ,

$$\begin{aligned} [\mathbf{V}'_{\text{out}}]_{ij} &= \int_{\mathbb{R}^{2k}} d\mathbf{x}_d \int_{\mathfrak{J}^{2M}} d\mathbf{s}' [\mathbf{x}_d - \tilde{\mathbf{x}}'_d(\mathbf{s}')]_{i \times j} P'(\mathbf{x}_d, \mathbf{s}') \\ &= \int_{\mathbb{R}^{2k}} d\mathbf{x}_d \int_{\mathfrak{J}^{2M}} d\mathbf{s}' [\mathbf{x}_d - \tilde{\mathbf{x}}_d(\mathbf{s})]_{i \times j} P(\mathbf{x}_d, \mathbf{s}) \\ &= \int_{\mathbb{R}^{2k}} d\mathbf{x}_d \int_{\mathfrak{J}^{2M}} d(R_{\sqrt{2\pi}}(\mathbf{N}\mathbf{s})) (\mathbf{x}_d - \tilde{\mathbf{x}}_d(\mathbf{s}))_{i \times j} P(\mathbf{x}_d, \mathbf{s}) \\ &= \int_{\mathbb{R}^{2k}} d\mathbf{x}_d \int_{\mathfrak{J}^{2M}} d\mathbf{s} (\mathbf{x}_d - \tilde{\mathbf{x}}_d(\mathbf{s}))_{i \times j} P(\mathbf{x}_d, \mathbf{s}) \\ &= [\mathbf{V}_{\text{out}}]_{ij}. \end{aligned}$$

We have used Lemmas 47 and 48 to go from the first equality to the second equality and used the relation $\mathbf{s}' = R_{\sqrt{2\pi}}(\mathbf{N}\mathbf{s})$ and Lemma 49 to go from the third equality to the fourth equality. The final equality follows by definition of the covariance matrix.

On the other hand, the linear estimation may not be invariant under a lattice basis transformation.

$$\mathbf{f}_{\text{Linear}}(\mathbf{s}) = -\mathbf{V}_d^{-1}\mathbf{V}_{da}\mathbf{s}, \quad \mathbf{f}_{\text{Linear}}(\mathbf{s}') = -\mathbf{V}_d^{-1}\mathbf{V}_{da}\mathbf{s}' = -\mathbf{V}_d^{-1}\mathbf{V}_{da}R_{\sqrt{2\pi}}(\mathbf{N}\mathbf{s}),$$

and $\mathbf{f}_{\text{Linear}}(\mathbf{s}) \neq \mathbf{f}_{\text{Linear}}(\mathbf{s}')$. As a consequence, the output covariance matrix for linear estimation may also change under a change of lattice basis. To show this explicitly, let us first write the output covariance matrix \mathbf{V}_{out} in full,

$$\begin{aligned} [\mathbf{V}_{\text{out}}]_{ij} &= \int_{\mathbb{R}^{2N}} d\mathbf{x}_d \int_{\mathcal{I}^{2M}} d\mathbf{s} (\mathbf{x}_d - \mathbf{f}_{\text{Linear}}(\mathbf{s}))_{i \times j} P(\mathbf{x}_d, \mathbf{s}) \\ &= \sum_{\mathbf{k}} \int_{\mathcal{I}^{2M}} d\mathbf{s} \int_{\mathbb{R}^{2N}} d\mathbf{x}_d (\mathbf{x}_d - \mathbf{f}_{\text{Linear}}(\mathbf{s}))_{i \times j} g[\mathbf{V}_d^{-1}, \mathbf{x}_d + \mathbf{V}_d^{-1}\mathbf{V}_{da}(\mathbf{s} - \mathbf{k}\sqrt{2\pi})] \\ &\quad \times g(\mathbf{V}_{d|a}^{-1}, \mathbf{s} - \mathbf{k}\sqrt{2\pi}) \\ &= \sum_{\mathbf{k}} \int_{\mathcal{I}^{2M}} d\mathbf{s} [\mathbf{V}_d^{-1}]_{ij} g(\mathbf{V}_{d|a}^{-1}, \mathbf{s} - \mathbf{k}\sqrt{2\pi}) \\ &\quad + \left[-\mathbf{V}_d^{-1}\mathbf{V}_{da}\mathbf{s} + \mathbf{V}_d^{-1}\mathbf{V}_{da}(\mathbf{s} - \mathbf{k}\sqrt{2\pi}) \right]_{i \times j} g(\mathbf{V}_{d|a}^{-1}, \mathbf{s} - \mathbf{k}\sqrt{2\pi}) \\ &= [\mathbf{V}_d^{-1}]_{ij} + \sum_{\mathbf{k}} 2\pi [\mathbf{V}_d^{-1}\mathbf{V}_{da}\mathbf{k}]_{i \times j} \int_{\mathcal{I}^{2M}} d\mathbf{s} g(\mathbf{V}_{d|a}^{-1}, \mathbf{s} - \mathbf{k}\sqrt{2\pi}), \end{aligned}$$

where we have used the expression of $P(\mathbf{x}_d, \mathbf{s})$ in (5.85c) in the first step. This covariance matrix depends on the basis choice of the GKP state. The explicit calculation is presented in Ref.[65]. ■

Optimal Single-mode Code

In this subsection, we focus on the single-mode code. This approach involves encoding one oscillator using another single-mode GKP state by two-mode squeezing transform. The conclusion is that the optimal single-mode code is given by two-mode squeezing and the single-mode hexagonal GKP state. The gain of the two-mode squeezing depends on the strength of the error level σ .

First we show the symmetry of the single mode lattice and that the single mode lattice can be generated by a single mode squeezing and a phase rotation. We can have the same lattice \mathcal{L} with different choices of bases. In particular, the generator matrices \mathbf{M}_1 and \mathbf{M}_2 generate the same lattice if there exist a unimodular matrix \mathbf{N} (i.e. a matrix with integer entries and $\det \mathbf{N} = 1$) such that

$$\mathbf{M}_1^\top = \mathbf{N}\mathbf{M}_2^\top.$$

The generator matrix that gives a single-mode canonical GKP state is given by

$$\mathbf{M}^\top \Omega \mathbf{M} = \Omega.$$

Therefore, by Bloch-Messiah decomposition of the symplectic matrix, the \mathbf{M} can be written as

$$\mathbf{M} = \mathbf{R}(\phi)\mathbf{S}\mathbf{q}(r)\mathbf{R}(\theta),$$

(θ, r)	$(\frac{\pi}{4}, \sqrt[4]{3})$	$(0.16\pi, 2.095)$	$(0.11\pi, 3.021)$	$(0.18\pi, 3.385)$
\mathbf{N}	$\begin{pmatrix} 1 & 0 \\ 0 & 1 \end{pmatrix}$	$\begin{pmatrix} -2 & -1 \\ 1 & 0 \end{pmatrix}$	$\begin{pmatrix} 2 & -1 \\ 1 & 0 \end{pmatrix}$	$\begin{pmatrix} 1 & -2 \\ 1 & -1 \end{pmatrix}$

Table 5.1: Equivalent representations of a hexagonal lattice. \mathbf{N} is a unimodular matrix that relates the lattice basis vectors.

where $\mathbf{R}(\theta)$ and $\mathbf{R}(\phi)$ are 2×2 rotation matrices and $\mathbf{Sq}(r)$ is the single-mode squeezing. The term $\mathbf{R}(\phi)$ can be omitted because different instances of $\mathbf{R}(\phi)$ represent equivalent code. Fixing r , it is easy to see that two bases

$$\begin{aligned} \mathbf{M}_1 &= \mathbf{Sq}(r)\mathbf{R}(\theta), \\ \mathbf{M}_2 &= \mathbf{Sq}(r)\mathbf{R}(\theta + \pi/2), \end{aligned}$$

are the same lattice since $\mathbf{M}_2^\top = \mathbf{R}(\frac{\pi}{2})\mathbf{M}_1^\top$ and $\mathbf{R}(\frac{\pi}{2})$ is a unimodular matrix. Furthermore, it is easy to show that

$$\begin{aligned} \mathbf{M}_1 &= \mathbf{Sq}(r)\mathbf{R}(\theta), \\ \mathbf{M}_2 &= \mathbf{Sq}(r)\mathbf{R}(-\theta), \end{aligned}$$

present the same lattice under a reflection about the x -axis. Combining the above symmetries, we conclude that two bases

$$\begin{aligned} \mathbf{M}_1 &= \mathbf{Sq}(r)\mathbf{R}(\theta), \\ \mathbf{M}_2 &= \mathbf{Sq}(r)\mathbf{R}(\pi/2 - \theta), \end{aligned}$$

correspond to the same lattice. A generator matrix for the hexagonal lattice can be written as

$$\mathbf{M}_\square = \frac{\sqrt{2}}{3^{1/4}} \begin{pmatrix} 1 & -\frac{1}{2} \\ 0 & \frac{\sqrt{3}}{2} \end{pmatrix},$$

By the Bloch-Messiah decomposition,

$$\mathbf{M}_\square = \mathbf{R}\left(-\frac{\pi}{6}\right)\mathbf{Sq}(3^{1/4})\mathbf{R}\left(\frac{\pi}{4}\right), \quad (5.89)$$

where $\mathbf{Sq}(3^{1/4}) = \text{diag}(3^{1/4}, 3^{-1/4})$. Due to rotation symmetry, we have the same lattice from \mathbf{M}'_\square if

$$\begin{aligned} \mathbf{M}'_\square &\equiv \mathbf{Sq}(r)\mathbf{R}(\theta) \\ &= \mathbf{R}(\phi)\mathbf{M}_\square\mathbf{N}^\top, \end{aligned} \quad (5.90)$$

where \mathbf{N} is a unimodular matrix. For $\mathbf{N} \neq \mathbf{I}$, the squeezing value $r \geq 3^{1/4}$; see Table 5.1. Examples of two-mode symplectic lattice are shown in Fig. 5.10.

To obtain the best two-mode GKP-stabilizer code, one simply needs to optimize the parameters (r, θ) and the TMS gain, alongside choosing an optimal estimator \mathbf{f}_{MMSE} as the decoding strategy. In Fig. 5.11(a), we plot the contour of the RMS error $\bar{\sigma}_{\text{RMS}}^2$ for an MMSE decoder optimized over the TMS gain G for each point (r, θ) . We find four equal minimum points for $\bar{\sigma}_{\text{RMS}}^2$, which turn out to be equivalent

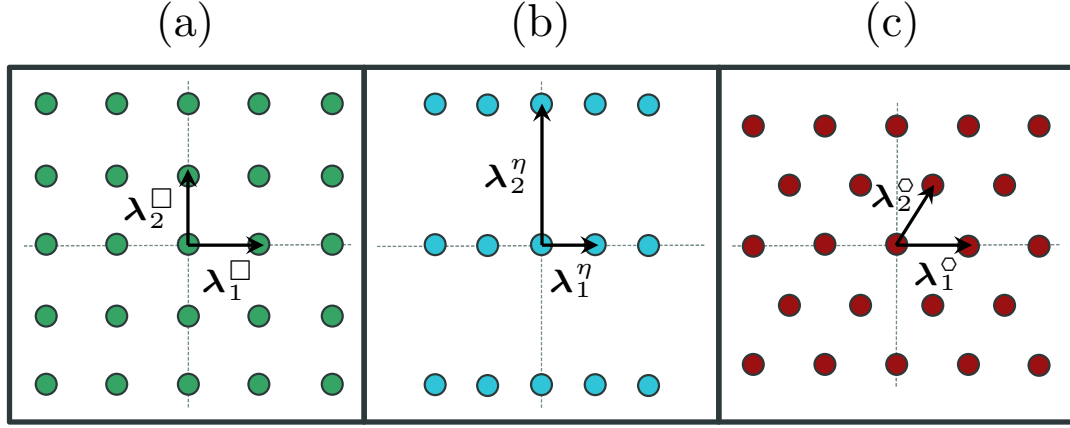


Figure 5.10: Illustration of two-dimensional lattices with basis vectors denoted: (a) Square, (b) Rectangular, (c) Hexagonal. Any two-dimensional symplectically integral lattice can be generated from the square lattice by rotation and squeezing.

lattice representations of the hexagonal lattice as listed in Table 5.1. Meanwhile, the square lattice has $r = 1$ with θ arbitrary (represented by the green line); the rectangular lattice has $\theta = 0$ and r changes the shape of the rectangle (represented by the blue line). The square and rectangular lattices are strictly sub-optimal.

In Fig. 5.11(b), we plot the GM error $\bar{\sigma}_{\text{GM}}^2$ in (r, θ) parameter space for the same optimized gain values of Fig. 5.11(a). The two subplots are very similar, with some deviations at the left-bottom corner due to the large squeezing of a rectangular lattice which induces asymmetry between q and p quadratures. The hexagonal lattices again minimize the output noise. Moreover, for the hexagonal lattices, $\bar{\sigma}_{\text{GM}}^2 \approx \bar{\sigma}_{\text{RMS}}^2$ up to our numerical precision, which is a strong indicator that—even if we minimize the GM error instead—the hexagonal lattice is still optimal.

Multimode Codes

Although the mode-wise decomposition simplifies the encoding to two-mode squeezing transforms, optimization is still challenging since $|\text{Sp}(2M, \mathbb{R})| = 2M^2 + M$ parameters need to be optimized in general for the ancilla GKP lattice. Nevertheless, as we will show in this section with a few examples, going to higher-dimensional lattices may indeed improve the performance of oscillators-to-oscillators codes.

Below, we first give a lower bound on the output noise for a general multimode GKP code, then discuss break-even points. Finally, we evaluate the performance of $N = M = 2$ multimode GKP stabilizer codes for various lattice configurations (e.g., square, hexagonal, and D4) and estimation strategies (e.g., linear estimation versus MMSE).

By information theoretic arguments, we are able to find lower bounds for the RMS and GM errors, $\bar{\sigma}_{\text{RMS}}$ and $\bar{\sigma}_{\text{GM}}$, for a general multimode GKP code, with M ancilla modes and k data modes, in terms of the variances σ_i^2 of the AGN channels $\bigotimes_i \mathcal{N}_{\sigma_i}$. In particular, for iid AGN, we show that $\bar{\sigma}_{\text{RMS}} \geq \bar{\sigma}_{\text{GM}} \geq \sigma_{\text{LB}}$, where

$$\sigma_{\text{LB}} \equiv \frac{1}{\sqrt{e}} \left(\frac{\sigma^2}{1 - \sigma^2} \right)^{\frac{k+M}{2k}}. \quad (5.91)$$

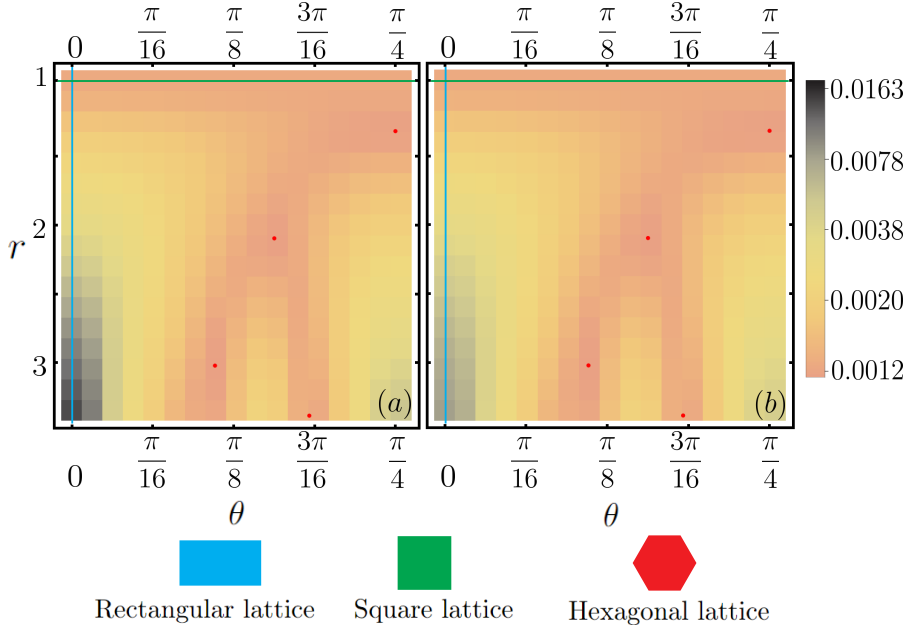


Figure 5.11: Output noise for a single-mode ($N = M = 1$) GKP stabilizer code. Input noise variance is $\sigma^2 = 10^{-2}$. We optimize the TMS gain G for each point (r, θ) . (a) RMS error $\bar{\sigma}_{\text{RMS}}^2$, (b) GM error $\bar{\sigma}_{\text{GM}}^2$. For the square lattice (green line), $\bar{\sigma}_{\text{RMS}}^2 = 1.25129(5) \times 10^{-3}$ and $\bar{\sigma}_{\text{GM}}^2 = 1.25129(5) \times 10^{-3}$. The four hexagonal lattice points (red dots) have the same output noises of $\bar{\sigma}_{\text{RMS}}^2 = 1.15575(5) \times 10^{-3}$ for RMS error and $\bar{\sigma}_{\text{GM}}^2 = 1.15575(5) \times 10^{-3}$ for GM error. Only the range $\theta \in [0, \pi/4]$ is considered due to symmetry.

For single-layer codes ($k = M$), there is at best quadratic error suppression, exactly similar to the $N = M = 1$ GKP codes discussed in Ref. [52]. Higher order error suppression can be obtained for codes with $M > k$ —with the output standard deviation scaling as $\sim \sigma^{1+\frac{M}{k}}$ per Eq. (5.91). The break-even point in the error correction refers to $\sigma_{\text{LB}} = \sigma$. In this case, the error correction process does not reduce the additive noise at all. Since a bosonic pure-loss channel with transmittance $\eta \in [0, 1]$ can be converted via pre-amplification to an AGN channel with variance $\sigma^2 = 1 - \eta$, and $\eta > 1/2$ is necessary for non-zero quantum capacity, we have $\sigma^2 < 1/2$. On the other hand, taking $\sigma_{\text{LB}}/\sigma = 1$ in Eq. (5.91) we have

$$\sigma\sqrt{e} = \left(\frac{\sigma^2}{1 - \sigma^2} \right)^{\frac{k+M}{2k}} < 1,$$

so the break-even point $\sigma^* < 1/\sqrt{e} = 0.607$. As this is obtained from lower bound, the true break-even point is larger than this value. Hence, the break-even point σ^* (η^*) for multimode GKP codes lies within $.607 \leq \sigma^* \leq .707$. As shown for multimode ($k = M = 2$) GKP stabilizer codes and MMSE estimation with AGN error, we numerically find break-even points near $1/\sqrt{e} \approx .607$. We remark that linear estimation strategies have a lower break-even point of .558 [52].

As shown in Fig. 5.12, we compare the reduction ratio $\sigma_{\text{GM}}/\sigma$ for different $k = M = 2$ codes. In our optimization process, we chose equal gains for the two-mode squeezing transforms, specifically setting $G_1 = G_2$. This equalization effectively correlates the two data with the two-mode GKP state. Considering the

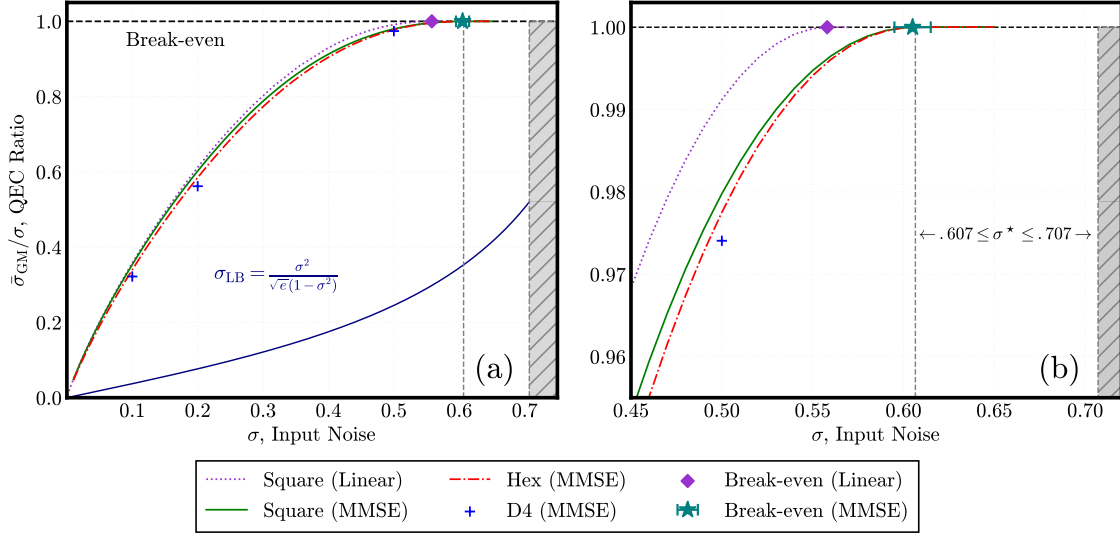


Figure 5.12: Quantum error correction (QEC) ratio between output noise and input noise of a single-layer, multimode ($N = M = 2$) GKP TMS code $\text{TMS}^{\otimes 2}(\mathcal{L})$ for different lattices \mathcal{L} (Square, Hexagonal, D4) and estimation strategies (linear, MMSE). The square code with linear estimation (dotted purple) agrees with the original GKP TMS code presented in Ref. [52]. Grey hatched region is forbidden by information theoretic arguments. While the break-even point of the linear estimation with square lattice $\sigma \simeq 0.558$ (purple diamond), the break-even point of the MMSE estimation $\sigma = 0.605(5)$ for both square and hexagonal lattices (green star). For D4 lattice, we narrowed the break-even point to $0.60 - 0.61$, which is consistent with square and hexagonal lattices.

noise as independent and identically distributed and with $G_1 = G_2$, it's pertinent to note that the local symplectic transform, which is instrumental in generating the ancilla lattice, can be further deconstructed into mode-wise decomposition. This leads to the complete optimization of the ancilla lattice involving one two-mode squeezing transform and two single-mode transforms, encompassing a total of seven parameters.

Given the computational intensity of these calculations, a complete optimization of the entire lattice was deemed impractical. Instead, our results focus on three specific lattice configurations: the direct product of square GKP lattices, the direct product of hexagonal GKP lattices, and the D4 lattice. For error estimation, we employed both linear estimation and the Minimum Mean Square Error (MMSE) approach. We observe that MMSE estimation outperforms linear estimation for identical lattice configurations. Furthermore, among the lattices tested, the D4 lattice performs better than the hexagonal lattice, which in turn performs better than the square lattice. This hierarchy in performance is likely attributed to that the D4 lattice is more efficient in spherical compacting.

It is also noteworthy that the D4 lattice requires certain two-mode squeezing operations for its generation. This aspect of the D4 lattice suggests that encoding two data with two-mode GKP state offers a more advantageous scenario than protecting a single data point with one ancilla, thus illustrating a quantum advantage in communication scenarios.

The break-even point value $\sigma_{\text{MMSE}}^* \approx .605(5)$ for MMSE agrees with the lower

bound on the break-even point ($.607 \leq \sigma^* \leq .707$) for general GKP codes discussed in the previous parts. It is an open question whether this can be pushed further or not.

5.4 Quantum Error Correction on GKP Qubit

This section delves into quantum error correction for GKP qubits encoded within n oscillators. Unlike the QEC for oscillators, here the quantum information is represented by discrete variables in the form of GKP qubits.

A critical aspect of evaluating the performance of quantum error correction codes is the 'code distance'. This quantifier, independent of the decoder's characteristics, serves as a key metric for assessing the effectiveness of a QEC code. For practical error correction, an estimation process or a decoder is essential. In this context, the linear estimation approach (also referred as passive error correction) for decoding is discussed. Then the GKP qubit code within the independent and identically distributed (iid) channel model is discussed. And the code can be simplified by the mode-wise decomposition and the symmetry of the channel itself.

Within this framework, we introduce the Distributed Two-Mode Squeezing (dtms) code. A notable feature of the dtms code is its ability to minimize active inline Gaussian operations. This efficiency stems from the analysis of the channel model, underscoring the adaptability of the dtms code to various encodings of qubits into oscillators. In terms of code distance, our proposed dtms qubit codes demonstrate comparable efficiency to those identified in Ref. [60]. However, a significant advantage of our approach lies in its considerably more straightforward construction, offering a practical and efficient solution for quantum error correction in GKP qubits.

5.4.1 Code Distance

When encoding discrete information into a multimode GKP state, we need some generic method of characterizing the performance of the resulting code. One natural figure of merit is the so-called *GKP code distance* [31], which gives a relative measure of how large a displacement error needs to be in order to enact a logical error on the code space. For simplicity, we focus on qubits code ($d = 2$). The extension to qudits is straightforward ($d > 2$).

Definition 50 (GKP Pauli distance) *Consider a GKP qubit code $\mathcal{C}(S)$ associated to a $2N$ -dimensional lattice \mathcal{L} with the generator matrix \mathbf{M} . The GKP Pauli distance for the logical operator $J \in \{\hat{X}_L, \hat{Y}_L, \hat{Z}_L\}$ is given by*

$$\mathfrak{D}_J \equiv \sqrt{2\pi} \times \min_{\mathbf{a} \in \mathbb{Z}^{2N}} \|\mathbf{m}_J - \mathbf{M}\mathbf{a}\|, \quad (5.92)$$

where $\mathbf{m}_J \in \mathcal{L}(\mathbf{M}_\perp)/\mathcal{L}(\mathbf{M})$ is a Pauli displacement vector corresponding to the logical Pauli operation $J \in S(\mathbf{M}_\perp)/S(\mathbf{M})$. The GKP code distance \mathfrak{D} is defined as

$$\mathfrak{D} \equiv \min_{J \in \{X, Y, Z\}} \mathfrak{D}_J. \quad (5.93)$$

The Pauli distances are invariant under a beam splitter transform $\mathbf{B} \in \text{Sp}(2n) \cap O(2n)$. Since

$$\|\mathbf{B}(\mathbf{m}_J - \mathbf{M}\mathbf{a})\| = \|\mathbf{m}_J - \mathbf{M}\mathbf{a}\|.$$

For iid Gaussian noise with variance σ^2 , one can roughly estimate the probability of error by code distance. When a random displacement error $\hat{D}(\boldsymbol{\xi})$ occurs, from Eq. (5.15)

$$\boldsymbol{\xi} = -\sqrt{2\pi}\mathbf{M}_\perp\boldsymbol{\Omega}[\mathbf{e} + \mathbf{k}(\boldsymbol{\xi})].$$

There is Pauli logical error J when the projection of $\boldsymbol{\xi}$ along the direction \mathbf{m}_J is between the odd integer values of \mathbf{k} . Due to the rotation symmetry of iid noise, we can rotate $\boldsymbol{\xi}$ by \mathbf{B} so that its projection on \mathbf{m}_J is along the first axis of Cartesian Coordinate. Then

$$\begin{aligned}\bar{p}_J &= \sum_{n \in \mathbb{Z}} \int_{\mathfrak{D}_J(2n+1)-\mathfrak{D}_J/2}^{\mathfrak{D}_J(2n+1)+\mathfrak{D}_J/2} dx g(\sigma^2, x) \\ &= \sum_{n \in \mathbb{Z}} \frac{1}{2} \left[\operatorname{erfc} \left(\frac{(1+4n)\mathfrak{D}_J}{2\sqrt{2}\sigma^2} \right) - \operatorname{erfc} \left(\frac{(3+4n)\mathfrak{D}_J}{2\sqrt{2}\sigma^2} \right) \right],\end{aligned}\quad (5.94)$$

where

$$\operatorname{erfc}(x) = 1 - \operatorname{erf}(x) = 1 - \frac{2}{\sqrt{\pi}} \int_0^x dt e^{-t^2}, \quad (5.95)$$

is the complementary error function, which decreases exponentially when its argument increases. And the \bar{p}_J decreases with the code distance.

Consider a single GKP qubit encoded in \mathbf{M} . Given the PDF $P(\boldsymbol{\xi})$ of random displacement error $\hat{D}(\boldsymbol{\xi})$, the error syndrome

$$\mathbf{e} = R_{\sqrt{2\pi}}(\mathbf{M}^\top \boldsymbol{\Omega} \boldsymbol{\xi}) = \mathbf{M}^\top \boldsymbol{\Omega} \boldsymbol{\xi} + \mathbf{k}(\boldsymbol{\xi})\sqrt{2\pi},$$

where $\mathbf{k}(\boldsymbol{\xi}) = \frac{1}{\sqrt{2\pi}}[\mathbf{M}^\top \boldsymbol{\Omega} \boldsymbol{\xi} - R_{\sqrt{2\pi}}(\mathbf{M}^\top \boldsymbol{\Omega} \boldsymbol{\xi})]$ is a function of $\boldsymbol{\xi}$. Since \mathbf{k} is a random variable associated with $\boldsymbol{\xi}$, we can estimate $\mathbf{k}(\boldsymbol{\xi})$ by $\tilde{\mathbf{k}}(\mathbf{e}) = \mathbf{f} \circ R_{\sqrt{2\pi}}(\boldsymbol{\xi})$. Then there is no error if $\mathbf{k}(\boldsymbol{\xi}) - \tilde{\mathbf{k}}$ is $(2\mathbb{Z}, 2\mathbb{Z}, \mathbb{Z}, \dots, \mathbb{Z})$. Let R_I be all the regions when $\mathbf{k}(\boldsymbol{\xi}) - \tilde{\mathbf{k}}$ is $(2\mathbb{Z}, 2\mathbb{Z}, \mathbb{Z}, \dots, \mathbb{Z})$. Similarly

$$R_X : \text{when } \mathbf{k}(\boldsymbol{\xi}) - \tilde{\mathbf{k}} = (2\mathbb{Z} + 1, 2\mathbb{Z}, \mathbb{Z}, \dots, \mathbb{Z}), \quad (5.96a)$$

$$R_Z : \text{when } \mathbf{k}(\boldsymbol{\xi}) - \tilde{\mathbf{k}} = (2\mathbb{Z}, 2\mathbb{Z} + 1, \mathbb{Z}, \dots, \mathbb{Z}), \quad (5.96b)$$

$$R_Y : \text{when } \mathbf{k}(\boldsymbol{\xi}) - \tilde{\mathbf{k}} = (2\mathbb{Z} + 1, 2\mathbb{Z} + 1, \mathbb{Z}, \dots, \mathbb{Z}). \quad (5.96c)$$

Then with the estimation \mathbf{f} , the probabilities of no error and Pauli errors are given by

$$\begin{aligned}p_I &= \int_{\boldsymbol{\xi} \in R_I} d\boldsymbol{\xi} P(\boldsymbol{\xi}), & p_X &= \int_{\boldsymbol{\xi} \in R_X} d\boldsymbol{\xi} P(\boldsymbol{\xi}), \\ p_Z &= \int_{\boldsymbol{\xi} \in R_Z} d\boldsymbol{\xi} P(\boldsymbol{\xi}), & p_Y &= \int_{\boldsymbol{\xi} \in R_Y} d\boldsymbol{\xi} P(\boldsymbol{\xi}).\end{aligned}$$

For the linear estimation (passive decoder in [61]), the estimation function $\tilde{\mathbf{k}}(\mathbf{e}) = 0$. In this case, the R_I is all the regions where $\mathbf{k}(\boldsymbol{\xi})$ is $(2\mathbb{Z}, 2\mathbb{Z}, \mathbb{Z}, \dots, \mathbb{Z})$. Define a new random variable $\boldsymbol{\xi}' = \mathbf{M}^\top \boldsymbol{\Omega} \boldsymbol{\xi}$, with the PDF

$$P'(\boldsymbol{\xi}') = \int_{R^{2n}} d\boldsymbol{\xi} P(\boldsymbol{\xi}) \delta(\boldsymbol{\xi}' - \mathbf{M}^\top \boldsymbol{\Omega} \boldsymbol{\xi}) = \frac{1}{|\det \mathbf{M}|} P(\boldsymbol{\Omega}^{-1} \mathbf{M}^{-\top} \boldsymbol{\xi}'). \quad (5.97)$$

There is no error if $\xi' - R_{\sqrt{2\pi}}(\xi')$ is $\sqrt{2\pi}(2\mathbb{Z}, 2\mathbb{Z}, \mathbb{Z}, \dots, \mathbb{Z})$. Thus the probability of no error is given by

$$p_I = \sum_{n_1, n_2 \in \mathbb{Z}} \int_{2n_1\sqrt{2\pi}-\sqrt{\pi/2}}^{2n_1\sqrt{2\pi}+\sqrt{\pi/2}} d\xi'_1 \int_{2n_2\sqrt{2\pi}-\sqrt{\pi/2}}^{2n_2\sqrt{2\pi}+\sqrt{\pi/2}} d\xi'_2 \int_{\mathbb{R}^{2n-2}} \xi'_{2n-2} P'(\xi'). \quad (5.98)$$

We can apply the above results to the Gaussian noise with covariance matrix $\Sigma = \oplus_{i=1}^n (\sigma_i^2 \mathbf{I}_2)$. And assume that the $[[n, 1]]$ code is generated by the symplectic transform \mathbf{S} . Then $\mathbf{M} = \mathbf{S}(\sqrt{2}\mathbf{I}_2 \oplus \mathbf{I}_{2n-2})$ and $\mathbf{M}_\perp = \mathbf{S}(1/\sqrt{2}\mathbf{I}_2 \oplus \mathbf{I}_{2n-2})$. We obtain the following expressions

$$p_I = \int_{-\frac{1}{2}\sqrt{\pi}+2\sqrt{\pi}k_1}^{\frac{1}{2}\sqrt{\pi}+2\sqrt{\pi}k_1} d\xi_1 \int_{-\frac{1}{2}\sqrt{\pi}+2\sqrt{\pi}k_2}^{\frac{1}{2}\sqrt{\pi}+2\sqrt{\pi}k_2} d\xi_2 \int_{\mathbb{R}^{2n-2}} d^{2n-2} \xi_{2n-2} g(\mathbf{S}^\top \Sigma \mathbf{S}, \xi), \quad (5.99a)$$

$$p_X = \int_{-\frac{1}{2}\sqrt{\pi}+2\sqrt{\pi}k_1}^{\frac{3}{2}\sqrt{\pi}+2\sqrt{\pi}k_1} d\xi_1 \int_{-\frac{1}{2}\sqrt{\pi}+2\sqrt{\pi}k_2}^{\frac{1}{2}\sqrt{\pi}+2\sqrt{\pi}k_2} d\xi_2 \int_{\mathbb{R}^{2n-2}} d^{2n-2} \xi_{2n-2} g(\mathbf{S}^\top \Sigma \mathbf{S}, \xi), \quad (5.99b)$$

$$p_Z = \int_{-\frac{1}{2}\sqrt{\pi}+2\sqrt{\pi}k_1}^{\frac{1}{2}\sqrt{\pi}+2\sqrt{\pi}k_1} d\xi_1 \int_{\frac{1}{2}\sqrt{\pi}+2\sqrt{\pi}k_2}^{\frac{3}{2}\sqrt{\pi}+2\sqrt{\pi}k_2} d\xi_2 \int_{\mathbb{R}^{2n-2}} d^{2n-2} \xi_{2n-2} g(\mathbf{S}^\top \Sigma \mathbf{S}, \xi), \quad (5.99c)$$

$$p_Y = \int_{\frac{1}{2}\sqrt{\pi}+2\sqrt{\pi}k_1}^{\frac{3}{2}\sqrt{\pi}+2\sqrt{\pi}k_1} d\xi_1 \int_{\frac{1}{2}\sqrt{\pi}+2\sqrt{\pi}k_2}^{\frac{3}{2}\sqrt{\pi}+2\sqrt{\pi}k_2} d\xi_2 \int_{\mathbb{R}^{2n-2}} d^{2n-2} \xi_{2n-2} g(\mathbf{S}^\top \Sigma \mathbf{S}, \xi). \quad (5.99d)$$

The above results only apply to the passive estimation. And the optimal estimation that minimizes the logical error is the Maximal Likelihood estimation [61], in which the random integer variable \mathbf{k} is estimated as well given probability distribution $P(\xi)$.

5.4.2 Distributed Two Mode Squeezing Code

In this section, the mode-wise decomposition is applied to simplify the $[[n, k]]$ code for iid Gaussian noise. Then we take a further step on streamlining GKP-based quantum error correction via minimizing the active inline Gaussian operations. Inspired by continuous-variable distributed quantum sensing, we propose the *distributed two-mode squeezing codes (dtms)* that employ only a single active element (a two-mode squeezer) per data mode and balanced arrays of variable beamsplitters.

As an example, for a single qubit encoded into 4 modes, we find a dtms- $[[4, 1]]$ code with a single two-mode squeezing operation of $< 7\text{dB}$ that outperforms the conventional concatenated GKP- $[[4, 1, 2]]$ qubit code. In terms of code distance, our proposed qubit codes achieve comparable performance to the codes identified (via generic numerical search) in Ref. [60], while offering a significantly simplified construction. The proposed code in small size is suitable for quantum repeaters and quantum sensor networks.

Code Reduction for iid Noise

Since any $[[n, k]]$ code can be generated by some \mathbf{S} , applying \mathbf{S} to canonical GKP oscillators to generate the code can instead be viewed as applying \mathbf{S}^{-1} to the channel without further encoding. So let consider the $[[n, k]]$ code with \mathbf{S} that correlates the noise of iid Gaussian noise. By the mode-wise decomposition,

$$\mathbf{S}^{-1}(\sigma^2 \mathbf{I}_{2n}) \mathbf{S}^{-\top} = \sigma^2 (\mathbf{S}_A \oplus \mathbf{S}_B)^{-1} (\text{TMS}) (\mathbf{S}_A \oplus \mathbf{S}_B)^{-\top}.$$

Then we can effectively generate the $[[n, k]]$ code by taking $\mathbf{S} = \oplus_i \mathbf{S}_{G_i}(\mathbf{S}_A \oplus \mathbf{S}_B)$, where \mathbf{S}_{G_i} corresponds to two-mode squeezing transform. Applying a general beam splitter \mathbf{Q} on \mathbf{S} does not change the code performance since this is equivalent to reshaping the covariance matrix of the noise to

$$\mathbf{Q}^{-1} \sigma^2 \mathbf{I}_{2n} \mathbf{Q}^{-\top} = \sigma^2 \mathbf{I}_{2n}.$$

In fact, any two-mode transforms in Definition 25 can be decomposed in the way $\mathbf{Q}\mathbf{S}_G(\mathbf{S}_A \oplus \mathbf{S}_B)$. When the two-mode transform is beam splitter, then $G = 1$. When the two-mode transform is two-mode squeezing and anti two-mode squeezing, then $G = G$. And when the two-mode transform is sum gate, then $G = (\sqrt{2} + 1)/2$ with two identical single-mode squeezing transforms with $r = 2^{1/4}$.

If n is even and we take identical $n/2$ two-mode squeezing transforms to correlates these oscillators, then $\mathbf{S} = (\oplus_{i=1}^{n/2} \mathbf{S}_G)(\mathbf{S}_A \oplus \mathbf{S}_B)$. The covariance matrix transforms to

$$\sigma^2 \begin{pmatrix} \mathbf{S}_A^{-1} & \mathbf{0} \\ \mathbf{0} & \mathbf{S}_B^{-1} \end{pmatrix} \begin{pmatrix} (2G-1)\mathbf{I}_n & 2\sqrt{G(G-1)}\mathbf{Z}_n \\ 2\sqrt{G(G-1)}\mathbf{Z}_n & (2G-1)\mathbf{I}_n \end{pmatrix} \begin{pmatrix} \mathbf{S}_A^{-\top} & \mathbf{0} \\ \mathbf{0} & \mathbf{S}_B^{-\top} \end{pmatrix},$$

where $\mathbf{Z}_n = \oplus_n \mathbf{Z}_2$. We can further apply the mode-wise decomposition to local symplectic transform $\mathbf{S}_A^{-1}\mathbf{S}_A^{-\top}$. When the local symplectic transform \mathbf{S}_A is a beam splitter, then the code is equivalent to the code generated by $\mathbf{S} = (\oplus_{i=1}^{n/2} \mathbf{S}_G)(\mathbf{I}_A \oplus \mathbf{S}_B)$.

Algorithm 51 (dtms code) *A distributed two-mode squeezing (dtms) code is given by k two-mode squeezing \mathbf{S}_{G_i} with tunable gain G_i and two configurable beamsplitter arrays \mathbf{A} and \mathbf{B} . The generator matrix*

$$\mathbf{M} = (\oplus_{i=1}^k \mathbf{S}_{G_i} \oplus \mathbf{I}_{2N-4k})(\mathbf{A} \oplus \mathbf{B})(\sqrt{2}\mathbf{I}_{2k} \oplus \mathbf{I}_{2N-2k}). \quad (5.100)$$

And the logic Pauli operator of the encoded k GKP qubits

$$X_i = \hat{D}(\sqrt{2\pi}m_{2i-1}/2), \quad (5.101)$$

$$Z_i = \hat{D}(\sqrt{2\pi}m_{2i}/2), \quad (5.102)$$

where m_i is the i -th column of \mathbf{M} .

In our algorithm, the local symplectic transforms are beam splitter arrays without squeezing. In general, local symplectic transform \mathbf{S}_A and \mathbf{S}_B may have squeezing. The fixed local symplectic transform \mathbf{S}_A can be viewed as the inner code that encodes k qubits into k oscillators. The two-mode squeezing transforms \mathbf{S}_{G_i} correlates the data and the other correlated GKP states generated by \mathbf{S}_B . To minimize the inline active squeezing, we take only one nontrivial two-mode squeezing and the two local symplectic transforms as general beam splitters. Then the dtms code is given by

$$\mathbf{M} = (\mathbf{S}_G \oplus \mathbf{I}_{2N-4})(\mathbf{A} \oplus \mathbf{B})(\sqrt{2}\mathbf{I}_{2k} \oplus \mathbf{I}_{2N-2k}), \quad (5.103a)$$

$$\mathbf{S} = (\mathbf{S}_G \oplus \mathbf{I}_{2N-4})(\mathbf{A} \oplus \mathbf{B}). \quad (5.103b)$$

As will be shown later, this simplified setup can still perform well.

The circuit to generate the code is shown in the Fig. 5.13 (a). A beam splitter array \mathbf{A} can be decomposed in layers as in the Theorem 27. Only the first layer

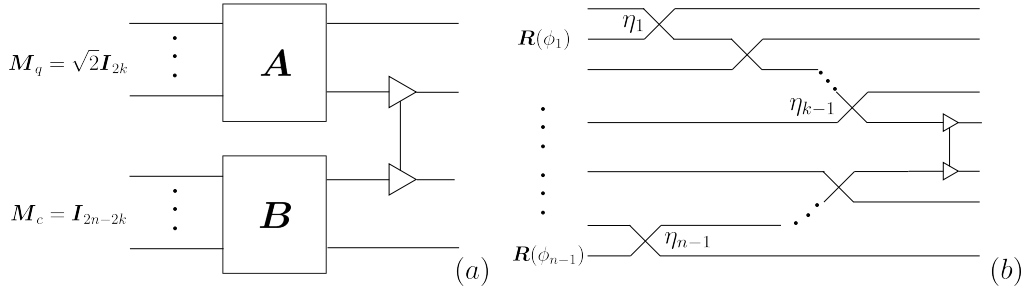


Figure 5.13: The circuit of dtms code. (a) An $[[n, k]]$ code is generated by $\mathbf{A} \in \cap \text{Sp}(2k) \cap O(2k)$, $\mathbf{B} \in \text{Sp}(2n - k) \cap O(2n - 2k)$. (b) The reduction of circuit in (a) due to the commutation relation.

characterizes the beam splitter array \mathbf{A} , as the other layers commute with the channel and cancel out with symmetry \mathbf{Q} . Then we have the reduction in the Fig. 5.13 (b). The number of phase rotations can be reduced to $n - 1$ due to the commutation relation between the phase rotation and the beam splitter (two-mode squeezing) transform as shown in the Fig. 5.14

To understand how the code works, we can analyze the iid additive noise $\sigma^2 \mathbf{I}_{2N}$ correlated by the symplectic transform in Eq. (5.103b). Treating square-grid GKP qubits subjected to the correlated noise $\mathbf{S}^{-1}(\sigma^2 \mathbf{I}_{2N})\mathbf{S}^{-\top}$, after the two-mode squeezing, the $N - k$ channels are then characterized by the noises $\sigma^2[(2G - 1)\mathbf{I}_2] \oplus \mathbf{I}_{2N-4k}$. Next, we distribute the first amplified k noises across the entire $N - k$ channels using a general beam splitter \mathbf{B} . This results in the correlated noises for the $N - k$ channels:

$$\sigma^2 \mathbf{B}^{-1} \{[(2G - 1)\mathbf{I}_2] \oplus \mathbf{I}_{2N-4k}\} \mathbf{B}^{-\top}. \quad (5.104)$$

For instance, \mathbf{B} could be a balanced beam splitter, evenly distributing one amplified noise to $N - 1$ channels. The diagonal elements of Eq. (5.104) are then $\sigma^2(2G - 1)/(N - 1)$. Detecting $N - 1$ smaller noises $\sigma^2(2G - 1)/(N - 1)$ is more effective than detecting one larger noise $\sigma^2(2G - 1)$ due to the spread of the noises.

The advantage of selecting \mathbf{S}_B as a beam splitter array lies in its simplicity and its potential for reduction in the case of iid channels. The total number of

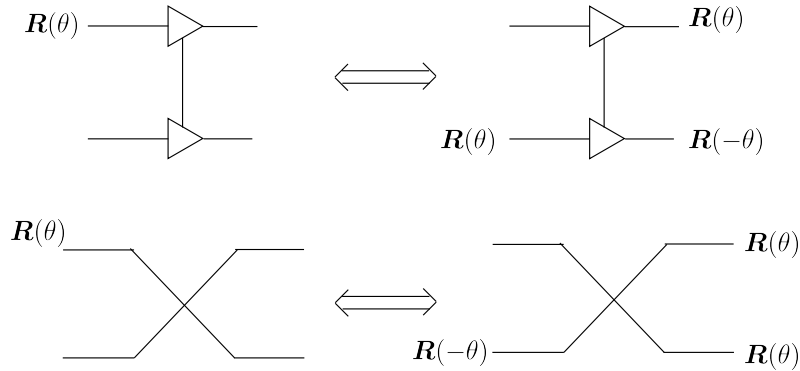


Figure 5.14: For two-mode beam splitter and two-mode squeezing, the phase rotation on the left hand side can be transformed to the phase rotations to the right hand side.

parameters for the encoding strategy is $2n - 2$. As this code strategy is derived from the analysis of the iid Gaussian noise model, it is applicable to other quantum codes (non-GKP code) in bosonic quantum systems experiencing random displacement Gaussian noise.

Code Distance of $[[n,1]]$ dtms Code

Consider a GKP qubit encoded by N oscillators. We set $\mathbf{A} = \mathbf{I}_2$, indicating that the GKP qubit is a square-grid GKP qubit. And the other $N - 1$ oscillators are initially in square-grid canonical GKP states. The distributed two-mode squeezing (dtms) code is characterized by a two-mode squeezing operation combined with a general beam splitter \mathbf{B} applied to $N - 1$ square-grid canonical GKP states. Let

$$\mathbf{B} = \begin{pmatrix} \tilde{\mathbf{B}} \\ \mathbf{B}' \end{pmatrix},$$

where $\tilde{\mathbf{B}}$ is a $2 \times 2(N - 1)$ sub-matrix of \mathbf{B} . Note that $\tilde{\mathbf{B}}\tilde{\mathbf{B}}^\top = \mathbf{I}_{2k}$. When there is no single-phase rotation, we can write $\tilde{\mathbf{B}}$ in the block form as

$$\tilde{\mathbf{B}} = \left(\pm\sqrt{\eta_1}\mathbf{I}_2, \pm\sqrt{(1-\eta_1)\eta_2}\mathbf{I}_2, \dots, \pm\sqrt{(1-\eta_1)\dots(1-\eta_{N-2})}\mathbf{I}_2 \right),$$

where $\eta_i = |\cos \theta_i|^2$. A balanced beam splitter without single phase rotations can be obtained by taking $\eta_1 = (1 - \eta_1)\eta_2 = \dots = (1 - \eta_1)\dots(1 - \eta_{N-2})$. Solving this recursively, we obtain $\eta_{N-2} = 1/2$, ..., $\eta_1 = 1/(N - 1)$ and

$$\tilde{\mathbf{B}} = 1/\sqrt{N-1} (\pm\mathbf{I}_2, \dots, \pm\mathbf{I}_2).$$

Adding phases leads to the block form as

$$\tilde{\mathbf{B}} = \left[\sqrt{\eta_1}\mathbf{R}(\phi_1), \dots, \sqrt{(1-\eta_1)\dots(1-\eta_{N-2})}\mathbf{R}(\phi_{n-1}) \right]. \quad (5.105)$$

The generator matrix of the $[[N, 1]]$ code is obtained from

$$\mathbf{M} = (\mathbf{S}_G \oplus \mathbf{I}_{2N-4})(\mathbf{I}_2 \oplus \mathbf{B})(\sqrt{2}\mathbf{I}_2 \oplus \mathbf{I}_{2N-2}),$$

Then

$$\mathbf{M} = \begin{pmatrix} \sqrt{2G}\mathbf{I}_2 & \sqrt{G-1}\mathbf{Z}_2\tilde{\mathbf{B}} \\ \sqrt{2(G-1)}\mathbf{Z}_2 & \sqrt{G}\tilde{\mathbf{B}} \\ \mathbf{0} & \mathbf{B}' \end{pmatrix}.$$

For iid noise, the code has the same performance as $\mathbf{B}^\top \mathbf{M}$ since \mathbf{B} is a beam splitter array in the symmetry $\text{Sp}(2n) \cap O(2n)$. An equivalent form of \mathbf{M} is given by

$$\begin{aligned} \tilde{\mathbf{M}} &= \mathbf{B}^\top \mathbf{M} \\ &= \begin{pmatrix} \sqrt{2G}\mathbf{I}_2 & \sqrt{G-1}\mathbf{Z}_2\tilde{\mathbf{B}} \\ \sqrt{2(G-1)}\tilde{\mathbf{B}}^\top \mathbf{Z}_2 & (\sqrt{G-1})\tilde{\mathbf{B}}^\top \tilde{\mathbf{B}} + \mathbf{I}_{2N-2} \end{pmatrix}. \end{aligned} \quad (5.106)$$

We see that only the sub block $\tilde{\mathbf{B}}$ plays the role in the code. As we will explore in greater detail later, it is feasible to choose

$$\tilde{\mathbf{B}} = \frac{1}{\sqrt{N-1}} (\mathbf{R}(\phi) \quad \cdots \quad \mathbf{R}(\phi)),$$

to achieve a balanced code. This specific code design, while potentially not the optimal solution among all possible general beam splitters \mathbf{B} , still offers significant advantages. The logical Pauli operators for this code can be obtained by the columns of the dual matrix \mathbf{M}_\perp , which are given by

$$(p_X \ p_Z) = \left(\frac{\sqrt{G/2} \mathbf{I}_2}{\sqrt{(G-1)/2} \tilde{\mathbf{B}}^\top \mathbf{Z}_2} \right). \quad (5.107)$$

It is important to note that the code's distance and performance remain unchanged when $\phi_i \rightarrow \phi_i + \pi/2$. Therefore, we can restrict the range of ϕ_i to $0 \leq \phi_i < \pi/2$.

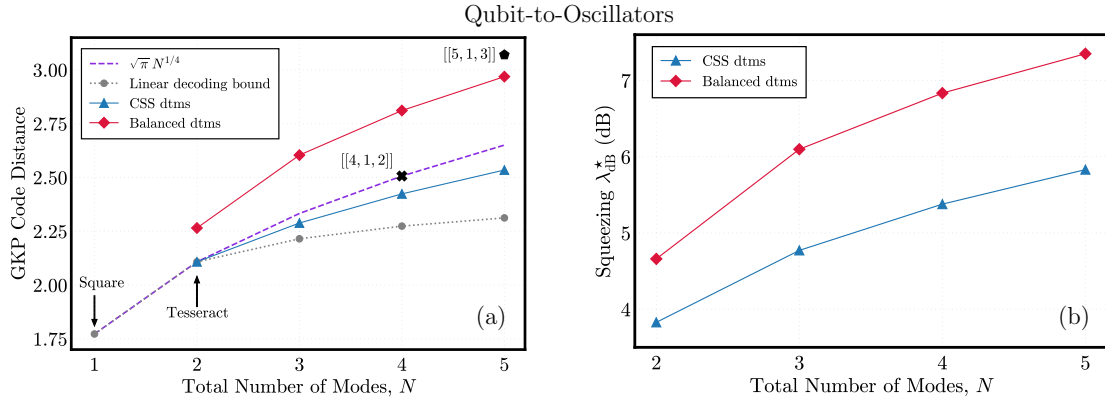


Figure 5.15: (a) Code distance $\mathfrak{D}_{\text{dtms}}$ for dtms qubit code. Assorted codes from the literature are shown for reference: Square, Tesseract, Square- $[[4, 1, 2]]$, Square- $[[5, 1, 3]]$, and scaling of GKP-surface-type codes $\sim N^{1/4}$. Linear decoding bound inferred from two-stage linear decoder. (b) Optimized squeezing for dtms qubit code. Two-mode squeezing gain G^* converted to equivalent single-mode squeezing $\lambda_{\text{dB}}^* = 20 \log_{10}(\sqrt{G^*} + \sqrt{G^* - 1})$.

The code distance is numerically calculated by searching for the closest lattice point that minimizes the distance, as defined in Eq. (5.92). The LLL lattice reduction algorithm is employed to obtain a reduced lattice basis for the generator matrix specified in Eq. (5.106). Babai's algorithm is then used to find an approximate lattice point. Since Babai's algorithm might not return the true closest point, a brute-force search is conducted around the approximate point with a cutoff l , considering $(2N)^{2l+1}$ points to get the true distance. The closest lattice point problem is NP-hard, and this algorithm takes exponential time with increasing code dimension N .

First of all, we consider a CSS-type code where the phase rotations $\phi_i = 0$. In this scenario, the generator matrix can be divided into independent q and p sections, satisfying:

$$\mathfrak{D}_X = \mathfrak{D}_Z = \mathfrak{D}_Y / \sqrt{2}. \quad (5.108)$$

The code distance \mathfrak{D}_X is computed numerically for the q section. The lattice in this case has N dimensions. By optimizing the beam splitter array η_i and the two-mode squeezing G with a cutoff $l = 4$, the code distance is maximized over $N - 1$ parameters. This optimization is further validated by ensuring that the code distance remains consistent when $l = 5$. The results are presented in Fig. 5.15 (a)

with blue triangles. We numerically find that the optimal values for the beam splitter parameters are approximately $\eta_1 = 1/\sqrt{N-1}$, ..., $\eta_{N-1} = 1/\sqrt{2}$. This suggests that a balanced beam splitter array, which evenly splits the modes, outperforms the other beam splitter configurations.

Next, we introduce $N-1$ phase rotations into the balanced beam splitter array. This non-CSS-type code correlates the q and p sections, leading to a $2N$ -dimensional lattice. With a cutoff $l = 3$, we compute the code distance as:

$$\min\{\mathfrak{D}_X, \mathfrak{D}_Y, \mathfrak{D}_Z\}.$$

By optimizing phase rotations, we can further increase the code distance. Compared to the CSS-type code with a balanced beam splitter array, phase rotations increase \mathfrak{D}_X and \mathfrak{D}_Z while decreasing \mathfrak{D}_Y . Thus, the code distance increases. Numerical optimization suggests that equal phase rotations, $\phi_1 = \dots = \phi_{N-1} = \phi$, balance the code distances effectively. This can be explained as in the optimal case, interchanging any two GKP ancillas, thus interchanging any two blocks of Eq. (5.105), does not change the code distance. Hence, in our numerical search, only two parameters G and ϕ are optimized to achieve a balanced code. These results are depicted in Fig. 5.15 (a) with red diamonds.

When $G = 1$, there is no correlation between the qubit and the other canonical GKP states. The code distance is given by the $\sqrt{2\pi}$ multiplies the norm of the column vector in Eq. (5.107), which is $\sqrt{(2G-1)\pi}$. When G increases, the code distance increases until to a turning point so that the true distance is $\|p_J - \mathbf{M}\mathbf{k}\|$, where \mathbf{k} is non-zero. With the *smallest* optimized gain $G(n)$, the code distance can be inferred from

$$\mathfrak{D} = \sqrt{(2G(n)-1)\pi}. \quad (5.109)$$

With optimized gain G , the code distances obtained from the above equation are shown as curves with different colors in Fig. 5.15.

Comparing to the code in Ref [60], Lin et al numerically optimized codes over all symplectic matrices $\mathbf{S} \in \text{Sp}(2n)$, which has $n^2 + n$ parameters. The optimized code needs to be constructed by Bloch-Messiah decomposition, which requires n active squeezings and a general n -dimension beam splitter array. The optimization could also lead to local optima. Our code design, based on a specific beam splitter array and having only 2 parameters, avoids such complexities. Although our results do not surpass the $[[5, 1, 3]]$ code, our approach requires only 1 active squeezing between two modes. Additionally, our balanced code design demonstrates larger distances compared to the Tesseract code and the $[[4, 1, 2]]$ code in lower dimensions. Moreover, the dtms code can be easily extended to a larger number of modes n , making it a versatile and practical choice for code design.

[[4,2]] dtms Code

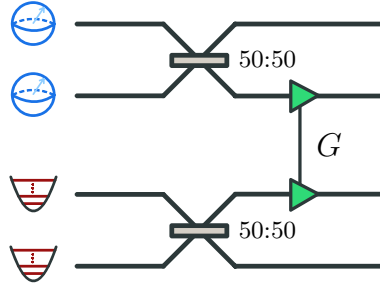


Figure 5.16: Encoding schematic for the $[[4,2]]$ -dtms code.

The dtms code can be straightforwardly extended to a $[[n,k]]$ code. Here, we provide an example of a dtms code encoding 2 GKP qubits. By distributing one two-mode squeezing to 2 GKP qubits and 2 canonical GKP states, we obtain a CSS-type dtms- $[[4,2]]$ code with a generator matrix

$$\mathbf{M}_{[[4,2]]} = (\mathbf{S}_{G=2} \oplus \mathbf{I}_2)[\mathbf{B}(1/2) \oplus \mathbf{B}(1/2)](\sqrt{2}\mathbf{I}_4 \oplus \mathbf{I}_4), \quad (5.110)$$

where

$$\mathbf{B}(1/2) = \frac{1}{\sqrt{2}} \begin{pmatrix} \mathbf{I}_2 & -\mathbf{I}_2 \\ \mathbf{I}_2 & \mathbf{I}_2 \end{pmatrix},$$

is the two-mode balanced beam splitter. We calculate the code distance numerically. The code distance is $\sqrt{2\pi}$, which is the same as the conventional $[[4,2,2]]$ code. However, this code design requires less squeezing. With the smallest optimum gain $G(n)$, the code distance of the dtms $[[n,2]]$ can be inferred as

$$\mathfrak{D} = \sqrt{G(n)\pi}. \quad (5.111)$$

Bibliography

- [1] S. Roman. *Advanced Linear Algebra*. Graduate Texts in Mathematics. Springer New York, 2007.
- [2] Arvind, B Dutta, N Mukunda, and R Simon. The real symplectic groups in quantum mechanics and optics. *Pramana*, 45(6):471–497, dec 1995.
- [3] Brian Hall. *Lie Groups, Lie Algebras, and Representations*, volume 222. Springer Nature, Cham, second edition. edition, 2015.
- [4] Alexander S. Holevo. *Quantum Systems, Channels, Information*. De Gruyter, Berlin, Boston, 2013.
- [5] R. Simon, N. Mukunda, and Biswadeb Dutta. Quantum-noise matrix for multimode systems: $U(n)$ invariance, squeezing, and normal forms. *Phys. Rev. A*, 49:1567–1583, Mar 1994.
- [6] John Williamson. On the algebraic problem concerning the normal forms of linear dynamical systems. *American Journal of Mathematics*, 58(1):141–163, 1936.
- [7] W. Forrest Stinespring. Positive functions on c^* -algebras. *Proceedings of the American Mathematical Society*, 6(2):211–216, 1955.
- [8] Man-Duen Choi. Completely positive linear maps on complex matrices. *Linear Algebra and its Applications*, 10(3):285–290, 1975.
- [9] F Caruso, V Giovannetti, and A S Holevo. One-mode bosonic gaussian channels: a full weak-degradability classification. *New Journal of Physics*, 8(12):310–310, dec 2006.
- [10] Alexander S. Holevo. Bounds for the quantity of information transmitted by a quantum communication channel. *Problems Inform. Transmission*, pages 3–11, 1973.
- [11] A. S. Holevo and R. F. Werner. Evaluating capacities of bosonic gaussian channels. *Phys. Rev. A*, 63:032312, Feb 2001.
- [12] I. Devetak and P. W. Shor. The capacity of a quantum channel for simultaneous transmission of classical and quantum information, 2004.
- [13] Seth Lloyd. Capacity of the noisy quantum channel. *Phys. Rev. A*, 55:1613–1622, Mar 1997.

-
- [14] I. Devetak. The private classical capacity and quantum capacity of a quantum channel. *IEEE Transactions on Information Theory*, 51(1):44–55, 2005.
 - [15] Stefano Pirandola, Riccardo Laurenza, Carlo Ottaviani, and Leonardo Banchi. Fundamental limits of repeaterless quantum communications. *Nat. Commun.*, 8:15043, 2017.
 - [16] Marco Fanizza, Farzad Kianvash, and Vittorio Giovannetti. Estimating quantum and private capacities of gaussian channels via degradable extensions. *arXiv:2103.09569*, 2021.
 - [17] F Caruso, V Giovannetti, and A S Holevo. One-mode bosonic gaussian channels: a full weak-degradability classification. *New Journal of Physics*, 8(12):310–310, dec 2006.
 - [18] Charles H. Bennett, Gilles Brassard, Claude Crépeau, Richard Jozsa, Asher Peres, and William K. Wootters. Teleporting an unknown quantum state via dual classical and einstein-podolsky-rosen channels. *Phys. Rev. Lett.*, 70:1895–1899, Mar 1993.
 - [19] T. C. Ralph and P. K. Lam. Teleportation with bright squeezed light. *Phys. Rev. Lett.*, 81:5668–5671, Dec 1998.
 - [20] Michael Reck, Anton Zeilinger, Herbert J. Bernstein, and Philip Bertani. Experimental realization of any discrete unitary operator. *Phys. Rev. Lett.*, 73:58–61, Jul 1994.
 - [21] Spyros Tserkis, Sho Onoe, and Timothy C. Ralph. Quantifying entanglement of formation for two-mode gaussian states: Analytical expressions for upper and lower bounds and numerical estimation of its exact value. *Phys. Rev. A*, 99:052337, May 2019.
 - [22] M. M. Wolf, G. Giedke, O. Krüger, R. F. Werner, and J. I. Cirac. Gaussian entanglement of formation. *Physical Review A*, 69(5), may 2004.
 - [23] Mankei Tsang. Cavity quantum electro-optics. *Phys. Rev. A*, 81:063837, Jun 2010.
 - [24] Mankei Tsang. Cavity quantum electro-optics. ii. input-output relations between traveling optical and microwave fields. *Phys. Rev. A*, 84:043845, Oct 2011.
 - [25] Alfredo Rueda, Florian Sedlmeir, Michele C. Collodo, Ulrich Vogl, Birgit Stiller, Gerhard Schunk, Dmitry V. Strekalov, Christoph Marquardt, Johannes M. Fink, Oskar Painter, Gerd Leuchs, and Harald G. L. Schwefel. Efficient microwave to optical photon conversion: an electro-optical realization. *Optica*, 3(6):597–604, Jun 2016.
 - [26] Linran Fan, Chang-Ling Zou, Risheng Cheng, Xiang Guo, Xu Han, Zheng Gong, Sihao Wang, and Hong X. Tang. Superconducting cavity electro-optics: A platform for coherent photon conversion between superconducting and photonic circuits. *Science Advances*, 4(8):eaar4994, 2018.

-
- [27] Rishabh Sahu, William Hease, Alfredo Rueda, Georg Arnold, Liu Qiu, and Johannes M. Fink. Quantum-enabled operation of a microwave-optical interface. *Nature Communications*, 13(1):1276, Mar 2022.
 - [28] C. W. Gardiner and M. J. Collett. Input and output in damped quantum systems: Quantum stochastic differential equations and the master equation. *Phys. Rev. A*, 31:3761–3774, Jun 1985.
 - [29] Leonard Mandel and Emil Wolf. *Optical Coherence and Quantum Optics*. Cambridge University Press, 1995.
 - [30] Jing Wu, Chaohan Cui, Linran Fan, and Quntao Zhuang. Deterministic microwave-optical transduction based on quantum teleportation. *Phys. Rev. Appl.*, 16:064044, Dec 2021.
 - [31] Daniel Gottesman, Alexei Kitaev, and John Preskill. Encoding a qubit in an oscillator. *Physical Review A*, 64(1), jun 2001.
 - [32] Kyungjoo Noh and Christopher Chamberland. Fault-tolerant bosonic quantum error correction with the surface–gottesman-kitaev-preskill code. *Phys. Rev. A*, 101:012316, Jan 2020.
 - [33] Takaya Matsuura, Hayata Yamasaki, and Masato Koashi. Equivalence of approximate gottesman-kitaev-preskill codes. *Phys. Rev. A*, 102:032408, Sep 2020.
 - [34] Frédéric Grosshans and Philippe Grangier. Quantum cloning and teleportation criteria for continuous quantum variables. *Phys. Rev. A*, 64(1):010301, 2001.
 - [35] Yuntao Xu, Ayed Al Sayem, Linran Fan, Sihao Wang, Risheng Cheng, Chang-Ling Zou, Wei Fu, Likai Yang, Mingrui Xu, and Hong X Tang. Bidirectional electro-optic conversion reaching 1% efficiency with thin-film lithium niobate. *arXiv preprint arXiv:2012.14909*, 2020.
 - [36] Charles H Bennett, David P DiVincenzo, and John A Smolin. Capacities of quantum erasure channels. *Phys. Rev. Lett.*, 78(16):3217, 1997.
 - [37] Michael M Wolf, David Pérez-García, and Geza Giedke. Quantum capacities of bosonic channels. *Phys. Rev. Lett.*, 98(13):130501, 2007.
 - [38] Johannes Majer, JM Chow, JM Gambetta, Jens Koch, BR Johnson, JA Schreier, L Frunzio, DI Schuster, Andrew Addison Houck, Andreas Wallraff, et al. Coupling superconducting qubits via a cavity bus. *Nature*, 449(7161):443–447, 2007.
 - [39] Y Zhang, M Menotti, K Tan, VD Vaidya, DH Mahler, LG Helt, L Zatti, M Liscidini, B Morrison, and Z Vernon. Squeezed light from a nanophotonic molecule. *Nat. Commun.*, 12(1):1–6, 2021.
 - [40] Jing Wu, Linran Fan, and Quntao Zhuang. Teleportation-based microwave-to-optical quantum transduction: The limited role of single-mode squeezing. *Phys. Rev. A*, 109:022619, Feb 2024.

-
- [41] Rishabh Sahu, William Hease, Alfredo Rueda, Georg Arnold, Liu Qiu, and Johannes M Fink. Quantum-enabled operation of a microwave-optical interface. *Nature communications*, 13(1):1276, 2022.
 - [42] Liu Qiu, Rishabh Sahu, William Hease, Georg Arnold, and Johannes M Fink. Coherent optical control of a superconducting microwave cavity via electro-optical dynamical back-action. *Nature Communications*, 14(1):3784, 2023.
 - [43] R Sahu, L Qiu, W Hease, G Arnold, Y Minoguchi, P Rabl, and JM Fink. Entangling microwaves with light. *Science*, 380(6646):718–721, 2023.
 - [44] Changchun Zhong, Mingrui Xu, Aashish Clerk, Hong X. Tang, and Liang Jiang. Quantum transduction is enhanced by single mode squeezing operators. *Phys. Rev. Res.*, 4:L042013, Oct 2022.
 - [45] Changchun Zhong, Zhixin Wang, Changling Zou, Mengzhen Zhang, Xu Han, Wei Fu, Mingrui Xu, S Shankar, Michel H Devoret, Hong X Tang, et al. Proposal for heralded generation and detection of entangled microwave–optical-photon pairs. *Phys. Rev. Lett.*, 124(1):010511, 2020.
 - [46] Manuel A Castellanos-Beltran, KD Irwin, GC Hilton, LR Vale, and KW Lehnert. Amplification and squeezing of quantum noise with a tunable josephson metamaterial. *Nature Physics*, 4(12):929–931, 2008.
 - [47] EP Menzel, R Di Candia, F Deppe, P Eder, L Zhong, M Ihmig, M Haeberlein, A Baust, E Hoffmann, D Ballester, et al. Path entanglement of continuous-variable quantum microwaves. *Physical Review Letters*, 109(25):250502, 2012.
 - [48] M Malnou, DA Palken, Leila R Vale, Gene C Hilton, and KW Lehnert. Optimal operation of a josephson parametric amplifier for vacuum squeezing. *Physical Review Applied*, 9(4):044023, 2018.
 - [49] Robert W Boyd. *Nonlinear optics*. Academic press, 2020.
 - [50] Changqing Wang, Ivan Gonin, Anna Grassellino, Sergey Kazakov, Alexander Romanenko, Vyacheslav P. Yakovlev, and Silvia Zorzetti. High-efficiency microwave-optical quantum transduction based on a cavity electro-optic superconducting system with long coherence time. *npj Quantum Information*, 8(1):149, Dec 2022.
 - [51] Jack Y. Qiu, Arne Grimsmo, Kaidong Peng, Bharath Kannan, Benjamin Lienhard, Youngkyu Sung, Philip Krantz, Vladimir Bolkhovskiy, Greg Calusine, David Kim, Alex Melville, Bethany M. Niedzielski, Jonilyn Yoder, Mollie E. Schwartz, Terry P. Orlando, Irfan Siddiqi, Simon Gustavsson, Kevin P. O’Brien, and William D. Oliver. Broadband squeezed microwaves and amplification with a josephson travelling-wave parametric amplifier. *Nature Physics*, 19(5):706–713, May 2023.
 - [52] Kyungjoo Noh, S. M. Girvin, and Liang Jiang. Encoding an oscillator into many oscillators. *Phys. Rev. Lett.*, 125:080503, Aug 2020.
 - [53] Jing Wu and Quntao Zhuang. Continuous-variable error correction for general gaussian noises. *Phys. Rev. Appl.*, 15:034073, Mar 2021.

-
- [54] Anthony J. Brady, Jing Wu, and Quntao Zhuang. Safeguarding oscillators and qudits with distributed two-mode squeezing, 2024.
 - [55] Daniel Gottesman. Stabilizer codes and quantum error correction, 1997.
 - [56] Min-Hsiu Hsieh. Entanglement-assisted coding theory, 2008.
 - [57] Michael A. Nielsen and Isaac L. Chuang. *Quantum Computation and Quantum Information: 10th Anniversary Edition*. Cambridge University Press, 2010.
 - [58] James William Harrington. *Analysis of Quantum Error-Correcting Codes: Symplectic Lattice Codes and Toric Codes*. PhD thesis, California Institute of Technology, 2004.
 - [59] Jonathan Conrad, Jens Eisert, and Francesco Arzani. Gottesman-kitaev-preskill codes: A lattice perspective. *Quantum*, 6:648, feb 2022.
 - [60] Mao Lin, Christopher Chamberland, and Kyungjoo Noh. Closest lattice point decoding for multimode gottesman-kitaev-preskill codes, 2023.
 - [61] Christophe Vuillot, Hamed Asasi, Yang Wang, Leonid P. Pryadko, and Barbara M. Terhal. Quantum error correction with the toric gottesman-kitaev-preskill code. *Phys. Rev. A*, 99:032344, Mar 2019.
 - [62] Julien Niset, Jaromír Fiurášek, and Nicolas J. Cerf. No-go theorem for gaussian quantum error correction. *Phys. Rev. Lett.*, 102:120501, Mar 2009.
 - [63] Lisa Hänggeli and Robert König. Oscillator-to-oscillator codes do not have a threshold. *IEEE Trans. Inf. Theory*, 68(2):1068–1084, 2021.
 - [64] Alonso Botero and Benni Reznik. Modewise entanglement of Gaussian states. *Phys. Rev. A*, 67:052311, May 2003.
 - [65] Jing Wu, Anthony J. Brady, and Quntao Zhuang. Optimal encoding of oscillators into more oscillators. *Quantum*, 7:1082, August 2023.